Linearized radiative transfer theory : a general discrete ordinate approach to the calculation of radiances and analytic weighting functions, with application to atmospheric remote sensing

Citation for published version (APA):
Spurr, R. J. D. (2001). *Linearized radiative transfer theory : a general discrete ordinate approach to the calculation of radiances and analytic weighting functions, with application to atmospheric remote sensing*. [Phd Thesis 1 (Research TU/e / Graduation TU/e), Applied Physics and Science Education]. Technische Universiteit Eindhoven. https://doi.org/10.6100/IR545442

DOI:
10.6100/IR545442

Document status and date:
Published: 01/01/2001

Document Version:
Publisher's PDF, also known as Version of Record (includes final page, issue and volume numbers)

Please check the document version of this publication:

• A submitted manuscript is the version of the article upon submission and before peer-review. There can be important differences between the submitted version and the official published version of record. People interested in the research are advised to contact the author for the final version of the publication, or visit the DOI to the publisher's website.
• The final author version and the galley proof are versions of the publication after peer review.
• The final published version features the final layout of the paper including the volume, issue and page numbers.

Link to publication

General rights
Copyright and moral rights for the publications made accessible in the public portal are retained by the authors and/or other copyright owners and it is a condition of accessing publications that users recognise and abide by the legal requirements associated with these rights.

- Users may download and print one copy of any publication from the public portal for the purpose of private study or research.
- You may not further distribute the material or use it for any profit-making activity or commercial gain
- You may freely distribute the URL identifying the publication in the public portal.

If the publication is distributed under the terms of Article 25fa of the Dutch Copyright Act, indicated by the "Taverne" license above, please follow below link for the End User Agreement:

www.tue.nl/taverne

Take down policy
If you believe that this document breaches copyright please contact us at:

openaccess@tue.nl

providing details and we will investigate your claim.

Download date: 04. Oct. 2023

Linearized Radiative Transfer Theory

A General Discrete Ordinate Approach to the Calculation of Radiances and Analytic Weighting Functions, with Application to Atmospheric Remote Sensing

Robert James Duncan Spurr

Linearized Radiative Transfer Theory

A General Discrete Ordinate Approach to the Calculation of Radiances and Analytic Weighting Functions, with Application to Atmospheric Remote Sensing

PROEFSCHRIFT

ter verkrijging van de graad van doctor
aan de Technische Universiteit Eindhoven
op gezag van de Rector Magnificus prof.dr. M. Rem,
voor een commissie aangewezen door het College voor
Promoties in het openbaar te verdedigen
op maandag 28 mei 2001 om 16.00 uur

door

Robert James Duncan Spurr

geboren te London, U. K.

Dit proefschrift is goedgekeurd door de promotoren:

prof.dr. H. Kelder
prof.dr. K. Stamnes

Copromotor:
dr. P. Stammes

Druk: KNMI (Koninklijk Nederlands Meteorologisch Instituut)

CIP-DATA LIBRARY TECHNISCHE UNIVERSITEIT EINDHOVEN

Spurr, Robert James Duncan

Linearized Radiative Transfer Theory: A General Discrete Ordinate Approach to the Calculation of Radiances and Analytic Weighting Functions, with Application to Atmospheric Remote Sensing / by Robert J. D. Spurr. - Eindhoven : Technische Universiteit Eindhoven, 2001. - Proefschrift
ISBN 90-386-1789-5
NUGI 812
Trfw.: stralingstransport / remote sensing / ozon / optimal estimation
Subject headings: radiative transfer / remote sensing / ozone / optimal estimation

DEDICATION

To the memory of my parents

Geoffrey Spurr
and
Olive Mary Spurr

and also to

Diane Imrey

...this most excellent canopy, the air, look you
this brave o'erhanging firmament, this majestical
roof fretted with golden fire,...

HAMLET, Act II, Scene II
William Shakespeare

Spielen denn meine Sinne noch zu sehr mit Licht?

Gebet, Buch der Bilder
Rainer Maria Rilke

Contents

Chapter 1

Introduction

1.1. Background and motivation

1.1.1. Remote sensing in the Earth's atmosphere

In recent years a growing consensus is emerging that human activities on our planet are contributing to climate change. In order to understand the chemical and physical processes that govern atmospheric balance and to assess the anthropological impact on climate, it is essential to determine the distributions of atmospheric constituents and to monitor these distributions on a long-term global basis. In-situ measurements from ground-based instruments can give detailed local information about the atmosphere. However, only passive remote-sensing instruments on satellites can generate the kind of global record necessary for monitoring atmospheric constituents on a long-term basis.

Many determinations of atmospheric constituents are made from observations of radiance spectra of scattered, reflected and absorbed sunlight (UV, visible and near infrared) or from attenuated thermal emission spectra (infrared and beyond to radio waves). Scattering is produced by molecules and various types of aerosol (including clouds). Molecular scattering cross-sections are characterized by the Rayleigh λ^{-4} law, with aerosol scattering typically showing a much less strong dependence on wavelength ($\sim \lambda^{-1}$). The angular distribution of molecular scattering has a $(1+\cos^2\Theta)$ dependence on angle of scatter Θ; aerosol scattering distributions are much more variable, often exhibiting strong peaks in the forward direction. Molecular scattering dominates in the UV (ultra violet), with aerosols replacing molecules as the major source of scattered light in the visible and near infrared. Thermal emission becomes important for wavelengths in excess of 2.4 microns. Molecular scattering has two parts - the Cabannes line which accounts for 96% of scattering events, and the 4% inelastic rotational-Raman component which is considered responsible for the Ring effect ("filling in" of Fraunhofer lines in the earthshine spectra).

For constituents that also absorb light, the scattering is non-conservative. The combination of scattering and absorption is termed the attenuation or extinction. Virtually all aerosols show some absorption, though in the case of water-droplet clouds in the UV and visible, this is very small. The degree of aerosol absorption is often characteristic of the aerosol type; for example, sooty particles produced in biomass-burning and other combustion events are strongly absorbing and the presence of such aerosols can be detected from backscatter measurements in the UV. In general, the molecular scattering and aerosol scattering and absorption signatures are slowly varying with wavelength. In the UV and visible, there is little information on aerosol properties to be gleaned from a single radiance spectrum. Another contribution to the radiance spectrum is due to reflection by the surface. In general the (bidirectional) surface reflection property is also smoothly dependent on wavelength, though its angular distribution can vary enormously, particularly over a faceted sea-surface.

Of much greater significance is the selective absorption of sunlight by atmospheric gases. Molecular absorption is a quantum physics phenomenon involving discrete transfers of energy to excited quantum states; the frequencies of such transitions are characteristic for each molecule. In the infrared, molecular excitation states are vibrational and rotational; transitions show up as sharply defined lines which often occur in groups (bands). The strength or intensity of these lines is an indication of the opacity of the atmosphere; a great deal of information about molecular abundances can be deduced from high-resolution measurements taken over such absorption bands. Absorption is so strong in certain bands (particularly CO_2 and H_2O in parts of the infrared) that the atmosphere is actually opaque.

Though O_2 and N_2 make up the vast majority of air molecules, they are not significant as far as line spectroscopy in the infrared (>1000 nm) is concerned. However there are three well-defined

O_2 absorption bands in the near infrared, of which the O_2 *A* band around 760 nm is prominent. H_2O (water vapor) also has a number of absorption bands in the visible and near infrared. At higher photon energies in the UV and visible, transitions to excited electronic states become available. Electronic band systems are not so well-defined, largely because of superimposed vibrational fine structure. O_3 is the most important trace species here; the well-known Huggins bands in the soft UV show moderately-resolved structure, whereas the hard-UV Hartley bands and the weak Chappuis bands in the visible are nearly continuous.

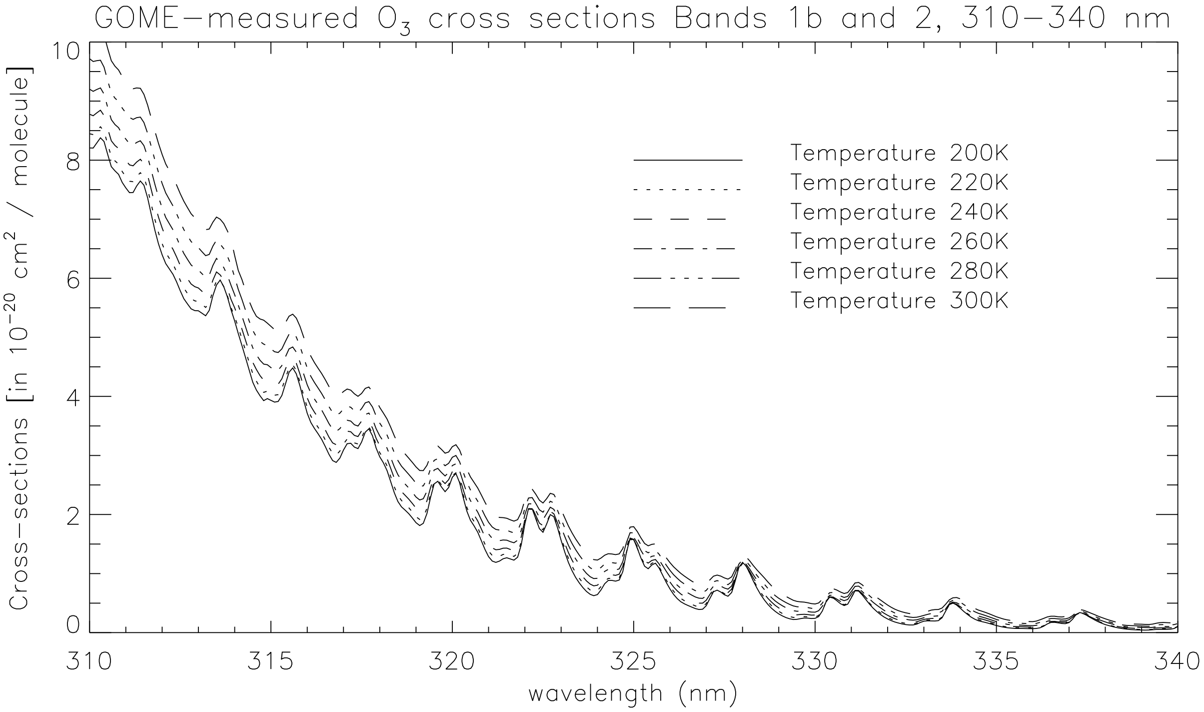

Figure 1.1: Ozone absorption cross sections in the Huggins bands for six temperatures as indicated; derived from measurements made with the GOME instrument during the pre-flight calibration phase.

In this work, we will focus on the Hartley-Huggins O_3 absorption bands in our consideration of ozone profile retrieval. Figure 1.1 displays O_3 absorption cross sections in the Huggins bands from 310 to 340 nm; the temperature dependence of the cross sections is evident. These cross sections were measured during the pre-flight calibration of the GOME instrument in 1994 (for details on instrument specifics for GOME and other instruments considered in this thesis, see Appendix A). Despite the comparative lack of fine structure in these UV/visible bands, a lot of information can be deduced from a backscatter instrument with moderate spectral resolution. Several other chemically important trace species have absorption signatures in the UV/visible, including NO_2, HCHO, BrO, OClO and SO_2; atmospheric opacities for these species are generally small.

An example from the GOME instrument will illustrate the kind of spectral features to be expected in the UV, visible and near infrared parts of the earthshine backscatter spectrum. In Figure 1.2, we show two parts of a reflectivity spectrum taken by GOME on 27 September 1997 for a scene over Borneo in South East Asia; this snapshot was taken at the time of a notable biomass burning event. The reflectivity $R(\lambda)$ is defined by:

$$R(\lambda) = \frac{\pi}{\mu_\odot} \cdot \frac{I(\lambda)}{F(\lambda)}, \tag{1.1}$$

in terms of the earthshine radiance $I(\lambda)$, the solar irradiance $F(\lambda)$ as measured by GOME (perpendicular to the solar direction), and the solar zenith angle cosine $\mu_\odot$. In this example, reflectivity values were obtained by simple division of earthshine radiance measurements with nearest-neighbor (in wavelength) solar irradiances; normally the two spectra have slightly different wavelength calibrations. The solar zenith angle was ~20.6°, and the earthshine spectrum was taken for the direct nadir footprint. The read-out time was 1.5 seconds; this limits the data to wavelengths above 307 nm. [Because of signal-to-noise limitations, measurements in the range 240 to 307 nm are normally taken every 12 seconds].

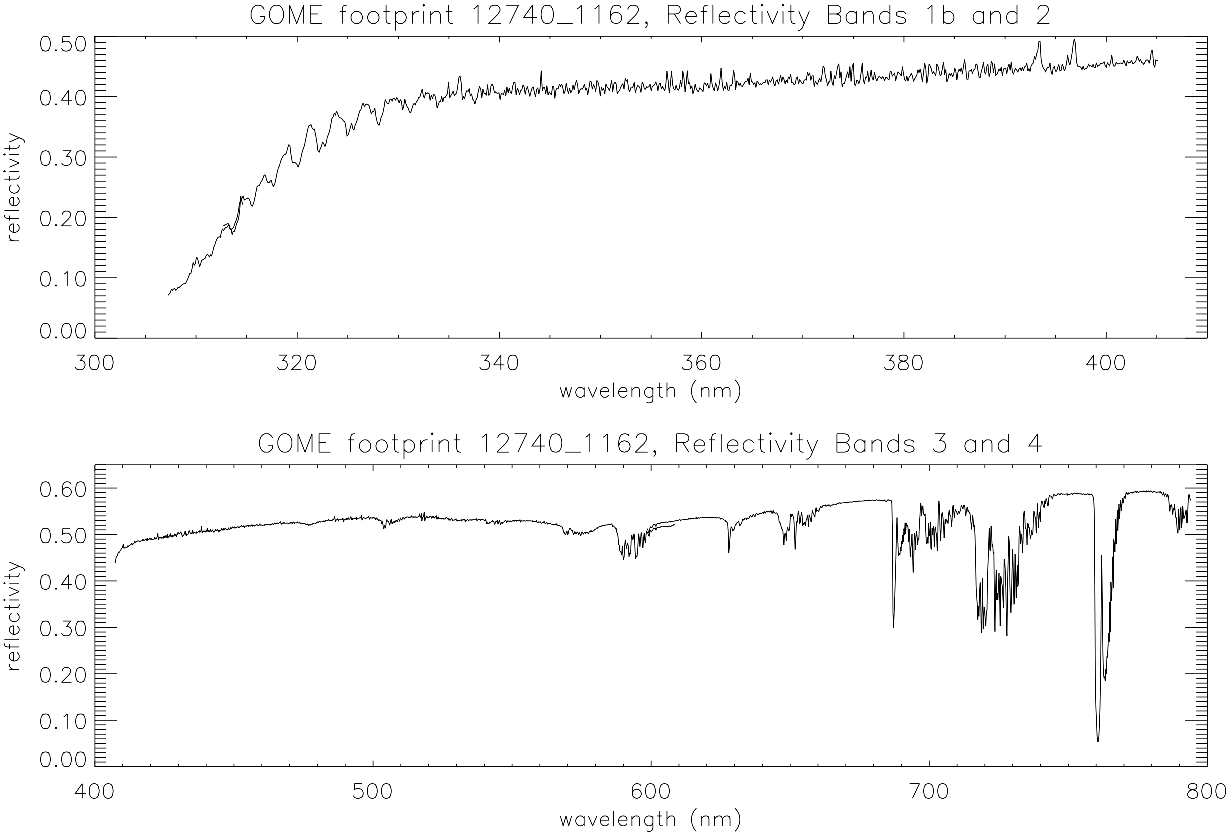

Figure 1.2: GOME reflectivity spectrum for orbit 12740 on 27 September 1997, pixel number 1162, for a scene over Borneo during a biomass burning event. Note the overlap regions near 313 nm (Bands 1b/2), 400 nm (Bands 2/3), and 600 nm (Bands 3/4).

A number of features are of interest. In the top panel for Bands 1b and 2 (307 to 410 nm), the Huggins-bands O_3 absorption features are prominent for wavelengths up to 340 nm; below 307 nm, increasingly strong O_3 absorption in the Hartley bands limits the penetration of UV radiation through the atmosphere (virtually no photons reach the surface at 300 nm). The Ca II Fraunhofer lines are also noticeable at 393.4 nm and 396.8 nm.

In the lower panel of Figure 1.2 for Bands 3 and 4 covering the visible and near infrared near-infrared parts of the spectrum, the O_2 *A* band shows as a deep absorption feature in the 760-770 nm range. The weaker O_2 *B* and γ bands appear at 687.1 and 628 nm respectively, along with several H_2O bands centered around 590 nm, 650 nm and 720 nm. The shallow dip from 500 to 650 nm is characteristic of Chappuis band O_3 absorption. Some of the fine structures in the UV are due to NO_2 absorption, others to inelastic Rotational-Raman scattering; features due to other minor trace species are too small to pick out by eye. Beyond 340 nm, gas absorption is generally weak with the exception of H_2O and O_2. For this particular spectrum the continuum level from 340 to 790 nm is relatively flat; this is characteristic of situations with strongly scattering layers in the lower atmosphere (in this case the extensive smoke pall from forest burning).

1.1.2. Retrieval of atmospheric constituents

The process of deducing constituent distributions from observations of the Earth's atmosphere is termed retrieval. We confine our attention to observations of radiance spectra. At a basic level, retrieval consists of making simulations of the earthshine backscatter for wavelengths in a spectral window and matching them with a sample of measurements in the window. Since the dependence of the backscatter on any given atmospheric parameter is usually complex, this matching has to be done by a suitable optimization (fitting) process. Formally we write $\mathbf{Y} = F(\mathbf{X})$ for the relation between simulated measurement vector $\mathbf{Y}$ and state vector $\mathbf{X}$ of constituent parameters to be retrieved; F is the *forward model*, which encompasses our understanding of the physics behind the measurement process. Retrieval involves the solution of the formal inverse problem $\mathbf{X} = F^{-1}(\mathbf{Y})$.

In general, forward models depend in a complex and non-linear manner on the state vector. Provided the non-linearity of this dependence is not excessive, the inverse problem can proceed iteratively using a series of linear inversion steps. The *linearization* of the forward model about state vector $\mathbf{X}_0$ is given by

$$\mathbf{Y} - \mathbf{Y}_0 = \mathbf{K}(\mathbf{X} - \mathbf{X}_0), \tag{1.2}$$

where the matrix $\mathbf{K}$ is the set of *weighting functions* (partial derivatives $\partial\mathbf{Y}/\partial\mathbf{X}$ of the radiances with respect to the elements of the state vector $\mathbf{X}$) evaluated at $\mathbf{X}_0$, and $\mathbf{Y}_0 = F(\mathbf{X}_0)$ is the simulated measurement vector at that point. The matrix $\mathbf{K}$ is a map from the space of state vectors $\mathbf{X}$ to the space of measurements, subject to the presence of measurement errors. The linear inversion by *optimal estimation* is based on Bayes' theorem, which expresses the posterior probability density function (*pdf*) $P(\mathbf{X}|\mathbf{Y})$ for state $\mathbf{X}$ given measurement $\mathbf{Y}$, as the product of the prior *pdf* $P(\mathbf{X})$ for $\mathbf{x}$ and the conditional *pdf* $P(\mathbf{Y}|\mathbf{X})$ for $\mathbf{Y}$ given $\mathbf{X}$. The last quantity requires the forward model and measurement error statistics. The optimal estimate is the state which maximizes $P(\mathbf{X}|\mathbf{Y})$; in other words, the MAP (maximum *a posteriori*) estimate [1].

For the measurement vector $\mathbf{Y}_{meas}$, it is usual to assume Gaussian statistics with error covariance matrix $\mathbf{S}_{meas}$. If the prior *pdf* $P(\mathbf{X})$ is Gaussian with mean value $\mathbf{X}_a$ (the *a priori* state vector) and error covariance matrix $\mathbf{S}_a$, then the posterior *pdf* is also Gaussian. In this case, it is straightforward to show that by linearizing about state vector $\mathbf{X}_n$, the optimal estimate for $\mathbf{X}_{n+1}$ is given by:

$$\mathbf{X}_{n+1} = \mathbf{X}_n + \mathbf{G}_n^{-1}\left[\mathbf{K}_n^T\mathbf{S}_{meas}^{-1}(\mathbf{Y}_{meas} - \mathbf{Y}_n) - \mathbf{S}_a^{-1}(\mathbf{X}_n - \mathbf{X}_a)\right]; \tag{1.3}$$

$$\mathbf{G}_n = \mathbf{S}_a^{-1} + \mathbf{K}_n^T\mathbf{S}_{meas}^{-1}\mathbf{K}_n. \tag{1.4}$$

(Subscript "T" denotes matrix transpose). The iteration is stopped when a suitable convergence criterion has been satisfied (for example, relative changes in the elements of the state vector from one iteration to the next are all below a prescribed small threshold). $\mathbf{G}_n$ is known as the information matrix or the solution error covariance matrix, and it is the principal source of diagnostic information about the quality and accuracy of the retrieval. Optimal estimation is the most widely-used method of inversion in the field of atmospheric measurements. Other fitting methods include the Levenberg-Marquardt algorithm [2] which is a modified form of non-linear least squares fitting, and the Phillips-Tikhonov regularization scheme [3].

In the above formalism, the accuracy of the retrieval depends not only on errors resulting from the measurement process but also on uncertainties concerning the *a priori* estimate. Additional sources of error may be included in the retrieval; these are “model parameter” errors (due to uncertainties in atmospheric quantities used in the forward model but not retrieved) and “forward model” errors due to systematic bias inherent in the forward model. A vector **b** of model parameter errors may also be assumed to have Gaussian statistics with error covariance $\mathbf{S}_b$, in which case the term $\mathbf{K}_b^T \mathbf{S}_b^{-1} \mathbf{K}_b$ must be added at each iteration step to the matrix **G**. $\mathbf{K}_b$ are weighting functions with respect to model parameters **b**; in general they will depend on the current guess for the retrieval vector $\mathbf{X}_n$. For further details on the niceties of inverse methods in atmospheric retrieval problems, see the works of Rodgers [4, 1].

The discussion here is quite general, and applicable to any atmospheric retrieval. The point is clear - an iterative fitting method with linear inversion will require a forward model that must simultaneously generate both simulated radiance measurements and matrices of weighting functions with respect to state vector elements. Additional weighting functions will be required if we are to consider model parameter uncertainties. The major part of the forward model is the theoretical radiative transfer (RT) calculation of the light field at the entrance of the instrument; the lesser (but still important) part is the instrument response function which takes the RT results and generates simulated measurements as actually detected by the instrument. The response function is instrument specific; we shall be concerned in this thesis with the RT modeling.

For the simulation of backscattered light in an anisotropic multi-layer medium requiring a full multiple scatter RT treatment, the derivation of weighting functions is a major consideration. Traditionally, weighting functions have been determined using finite difference estimates typified by

$$K_{FD}(\xi) \simeq \frac{Y(\xi[1+\varepsilon_{FD}]) - Y(\xi[1-\varepsilon_{FD}])}{2\varepsilon_{FD}}. \tag{1.5}$$

where the two simulated backscatter radiances $Y(\xi[1 \pm \varepsilon_{FD}])$ are calculated by applying perturbations $\pm\varepsilon_{FD}$ to parameter ξ which is either an element of the state vector **X** to be retrieved or an element of the model parameter vector **b**. Definition (1.5) requires two separate RT simulations for each vector element; in a complex multi-parameter retrieval problem, the number of radiance simulations will multiply ten-fold and more. This can be prohibitively expensive on computer resources. There is also the question of accuracy; finite difference estimates rely in an rather arbitrary way on the choice of perturbation ε_{FD} (indeed some weighting functions are very poorly estimated by such simple finite difference schemes).

What is required here is a *linearized radiative transfer model* that will be called just once at each iteration step and that will generate all necessary weighting function matrices at the same time as the simulated measurements. The model should produce weighting functions that are as accurately calculated as the simulated radiances, without the need for numerical estimates. This is then the motivation for this thesis - to produce just such a linearized RT model, one that can be used in all generality for a wide range of atmospheric retrieval problems based on backscatter earthshine measurements. The large part of this thesis is concerned with the theoretical and practical development of such a model (to be called LIDORT). We now discuss O_3 profile retrieval in more detail; this will serve to introduce the kind of output that the LIDORT model is capable of producing.

1.1.3. Introduction to O_3 profile retrieval from space

In this work, the main application of the RT model is to the retrieval of O_3 profiles from nadir viewing remote sensing instruments such as GOME [5], GOME-2 [6], SCIAMACHY [7] and OMI [8].

The spectrum of measurements covers the O_3 Hartley-Huggins bands from 270 nm to 340 nm. Retrieval state vector **X** will consist of O_3 profile elements, either in the form of volume mixing ratios at selected levels or in the form of partial (Umkehr) column densities, plus a small number of additional parameters such as the surface albedo, the total aerosol optical depth and the total NO_2 column density. [NO_2 is the most important interfering trace species absorbing in this part of the UV spectrum].

The radiative transfer part of the forward model should calculate simulated backscatter radiances and associated weighting functions with respect to O_3 profile elements. We illustrate RT model output for this application in Figure 1.3; all results were generated using the LIDORT model developed in this thesis. In the top panel, backscatter sun-normalized radiances have been calculated at a relatively fine spectral resolution for a direct-nadir view and for solar zenith angle 50°. A clear sky atmosphere with O_3 absorption and Rayleigh and background aerosol scattering was assumed; the surface albedo was 0.1. The Huggins-bands absorption features are evident; the general shape of this curve is similar to the corresponding part of Figure 1.2 (top panel), though the general level of backscattered light is much lower in the simulation because of the clear sky assumption.

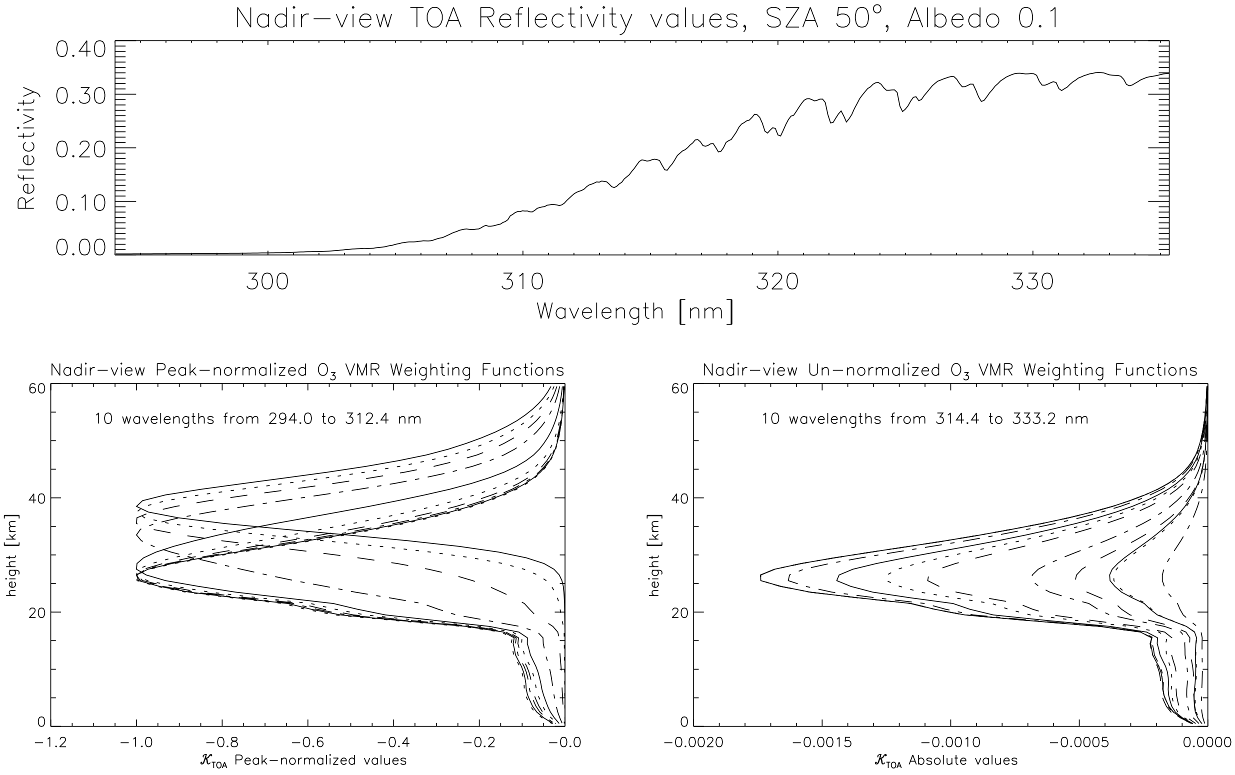

Figure 1.3: (top panel) Simulated reflectivity spectrum for a clear sky scenario for a spectral range 295-335 nm; solar zenith angle 50°, direct nadir view; (lower panels) O_3 volume mixing ratio weighting functions for a selection of wavelengths.

The lower panels show weighting functions with respect to O_3 volume mixing ratio, calculated at a fine vertical resolution of 1 km. The wavelength range has been divided into two halves. The lower left panel contains weighting functions for 10 wavelengths from 294.2 to 312.4 nm, with values normalized to the peak sensitivity in the stratosphere. The lower right panel shows absolute weighting functions for 10 wavelengths from 314.4 to 333.3 nm. For decreasing wavelengths in the UV below $\sim$314 nm (lower left panel) the increasingly strong O_3 absorption in the Hartley bands progressively raises the scattering penetration depth. Sensitivity to O_3 absorption has a maximum value at increasingly high pressure levels as one moves further into the UV. Beyond 314 nm, this height-dependent sensitivity disappears; the peak sensitivity remains at the same level, becoming increasingly weaker as the absorption falls off at higher wavelengths. The clear dependence of penetration depth with wavelength allows O_3 profiles to be retrieved accurately in the stratosphere.

In the lower right panel, the relative sensitivity in the troposphere is greater for higher wavelengths; this effect depends not only on solar zenith angle and surface albedo, but also on the temperature distribution in the troposphere (through the temperature dependence of the Huggins bands cross sections). This indicates that retrieval accuracy and vertical resolution in the troposphere might be improved by extending the upper limit of the fitting window to include these wavelengths. This is a major issue for instruments such as GOME which measure this part of the spectrum; we will return to this question in Chapter 5.

Initial feasibility studies for ozone profile retrieval were based on single scatter RT models [9]. The first algorithm to return profiles on an operational basis was developed for the BUV instrument [10]; this work was then extended to the SBUV, SBUV-2 and SSBUV instruments (for a summary of these developments, see [11]). This “BUV-type algorithm” uses optimal estimation and relies on look-up tables of simulated radiances calculated with a dedicated pseudo-spherical radiation code [12]; all weighting functions are estimated by finite differences. SBUV has 12 spectral channels and 12 profile elements are retrieved; with only limited spectral information, accurate profiles of O_3 that are relatively free from prior influences are restricted to the pressure range 1-20 mbar.

The GOME instrument has more spectral information than SBUV; it has a resolution of $\sim$0.2 nm in the range 240 - 350 nm. Signal to noise is severely restricted below 305 nm due to strong O_3 absorption; measurements below this threshold are taken with a longer read-out (12 seconds). A number of groups have looked at the retrieval of O_3 profile data from GOME [13, 14, 15, 16]; most use optimal estimation with *a priori* O_3 profiles taken from a suitable climatology [17]. The retrieval proceeds in two stages. A preliminary BUV-type retrieval is done for the short-wavelength pixels below about 307 nm - this produces a stratospheric profile representative of the large air-mass scanned during the 12-second read-out. The second step uses measurements in the Hartley-Huggins bands with shorter read-out times (typically 1.5 seconds) and wavelengths out to 335 nm. The initially-retrieved stratospheric profile is used as *a priori* for this second stage; complete atmosphere profiles can then be retrieved for the smaller footprints. It is customary to include surface albedo and total aerosol optical thickness as additional retrieved parameters. In an operational algorithm, the retrieval is improved by including a fitting parameter for an additional “Ring spectrum” that characterizes the signature due to inelastic Rotational-Raman scattering (this spectrum is present at every wavelength, but is seen most clearly in the partly filled-in Fraunhofer lines of the backscatter spectrum). The Ring spectrum can be determined either by using a simple semi-empirical method [18] or by simulations based on appropriate radiative transfer modeling [19, 20].

Despite some years of study for the GOME project, there are a number of unresolved issues regarding the O_3 profile retrieval. The GOME retrieval has been plagued by measurement uncertainties. With the wide wavelength range and the use of measurements taken by two different serial read-out detectors, the radiometric accuracy is critical. This has been seriously compromised in recent times owing to the degradation of the instrument more than 5 years after launch. A second major source of measurement error has been the polarization sensitivity of the GOME measurements [21, 22]. The question of tropospheric sensitivity has not been investigated in any systematic way, nor has the issue of fitting window optimization. Some studies have been carried out to test the effect of temperature profile and aerosol optical thickness model parameter errors, but the forward model error assessment has received little attention (this includes the neglect of polarization in the radiative transfer model). We address many of these issues in Chapters 4 and 5.

1.1.4. A note on DOAS-type retrievals

The DOAS (Differential Optical Absorption Spectroscopy) fitting method relies on a drastic simplification of the forward model. Trace gas absorption is expressed in terms of the Beer-Lambert law

$$I_\lambda(s,\Omega) = I_\lambda(0)\mathrm{e}^{-\tau_s(\lambda)} \tag{1.6}$$

for intensity I_λ at wavelength λ, and for a straight-line path with direction Ω and total length s through the atmosphere. The path opacity $\tau_s(\lambda)$ is simply the slant path column density $C_g(s,\Omega)$ of gas g multiplied by the appropriate trace gas absorption cross section $\sigma_g(\lambda)$ at wavelength λ.

For GOME, $I_\lambda(0)$ is usually taken to be the measured extraterrestrial solar spectrum. Leaving aside issues to do with wavelength calibration of the solar and earthshine spectra, then from the extinction law (1.6) and the definition of $\tau_s(\lambda)$, we see that the natural logarithm of the earthshine reflectivity spectrum may be fitted to a reference trace gas absorption cross section using linear regression. This is the basic DOAS fitting for the slant column density $C_g(s,\Omega)$. Smooth features in the reflectivity spectrum due to aerosol absorption and scattering, molecular scattering and surface reflectance properties are filtered out with a low-order polynomial in wavelength. For more details on DOAS fitting, see the review article by Platt [23]. Note that it is also possible to use non-linear least squares fitting to fit reflectivity directly against cross section reference spectra [24]. In both cases, division by a suitable Air Mass Factor (AMF) will convert the slant result $C_g(s,\Omega)$ to a vertical column density V_g independent of path direction Ω. This AMF conversion is normally a full radiative transfer computation, a pure simulation that is divorced from the fitting process.

DOAS has been used for ground-based instruments to detect column distributions of trace species such as O_3 and NO_2, HCHO and OClO and BrO (see [23] and references therein). The use of DOAS with GOME measurements represents the first application of the method to remote sensing instruments; the primary focus has been on total O_3 column amounts [25]. Besides O_3, a number of other trace species column abundances have been recorded. NO_2 [7], HCHO [26, 27] and BrO [24, 28, 29] have all been measured by GOME on a global basis, and OClO [30] and SO_2 [31] for special scenarios. Related techniques have been used to derive H_2O abundances [32, 33]. SCIAMACHY, GOME-2 and OMI will also employ this technique in various forms. See also the discussion in the Summary and Outlook section.

1.2. Radiative transfer aspects

In section 1.2.1 we discuss general aspects of radiative transfer theory as they apply to the work presented here. Following this background material, we summarize the discrete ordinate solution to the radiative transfer equation (RTE). In section 1.2.3 we introduce the linearization of the discrete ordinate model; this theme is the “Red Line” that runs through the thesis.

1.2.1. Requirements in a planetary atmosphere

In general, a planetary atmosphere is inhomogeneous in both the vertical and horizontal directions. In this work, we will not consider a full three-dimensional treatment of the radiative transfer equation (RTE) in such an atmosphere. We take the atmosphere to be stratified, that is, composed of a number of homogeneous horizontal layers. The radiation field will then depend on a single vertical coordinate (the vertical optical depth τ or the altitude) and the two directional variables μ (cosine of the polar angle) and ϕ (azimuth angle with respect to a given direction). Radiative transfer in planetary atmospheres is dominated by two light sources - thermal emission and the solar collimated beam. In order to compute the radiation field $I(\tau,\mu,\phi)$ in the presence of a solar beam, we need to specify the direction $(-\mu_0,\phi_0)$ of the beam at the top of the atmosphere and the incident solar flux $\pi F_\odot$ perpendicular to this direction.

We need also a wavelength grid at which the radiation field is to be found, plus a specification of the optical properties of all atmospheric constituents at these wavelengths. This includes not only the bulk properties such as the scattering and absorption cross sections of particulates in the atmosphere (molecules and aerosols), but also a knowledge of their angular distribution of scattering (phase functions). Finally the wavelength dependence and angular distribution of the surface reflectance must be specified. For atmospheric thermal emission sources in local thermodynamic equilibrium, we require black-body Planck functions and an indication of their dependence on vertical optical depth; thermal emission is assumed isotropic. Kirchhoff's relation between reflectance and emittance will hold at surface boundary.

The stratification assumption allows RTE solutions to be determined in each layer. The complete radiation field is then put together by means of a set of boundary conditions, namely: (1) the downward diffuse radiation at the top of the atmosphere (TOA) is zero in the absence of thermal emission sources; (2) at each intermediate layer boundary, the radiance is continuous in all polar (elevation) and azimuthal directions; and (3) the upwelling radiance at the bottom of the atmosphere is a known function of the incident downwelling radiance, the dependence being expressed in terms of the reflectance property of the surface. The simplest stratification assumes a plane-parallel medium that neglects any sphericity due to the earth's curvature. Plane-parallel RT models are valid for a wide range of atmospheric problems. It is well known that this assumption breaks down for large solar zenith angles, and also for wide off-nadir viewing angles. It has been shown that for viewing angles close to nadir, the plane-parallel assumption is good to about 2% for solar zenith angles up to about 75° (see for example [34]).

The emphasis in this work is on nadir-viewing remote sensing applications from space; the plane-parallel assumption is in general too restrictive to be applied on a consistent basis to simulations of earthshine radiation. To allow for curvature effects, the simplest approach assumes that the attenuation of the direct solar beam is computed in a spherical-shell atmosphere, but that line-of-sight attenuation and all scattering events continue to be treated for a plane-parallel medium. This is the *pseudo-spherical approximation*; it has been shown to be valid close-to-nadir viewing for solar zenith angles up to 90° [35]. In this work we also consider a sphericity correction for line-of-sight viewing some distance from the nadir; attenuation in these directions is also treated for a curved stratified atmosphere, and the radiation field is integrated along the line-of-sight direction instead of the nadir direction assumed for the ordinary pseudo-spherical calculation.

Two further corrections will be used in this work. The first is the delta-M scaling procedure [36, 34] which is useful for dealing with phase function angular distributions which are sharply peaked in the forward direction. The delta-M transformation replaces the original phase function by a delta-function forward peak plus a smoother anisotropic residual; this results in a scaling (reduction) of the optical depth and other optical properties. The second correction replaces approximate forms for the single scatter contributions to the radiation field with more exact results based on precise specifications of the phase function. The combination of these two corrections is the Nakajima-Tanaka single scatter correction [37].

There are a number of different methods of solving the RTE in a multi-layer multiply-scattering atmosphere, ranging from Monte-Carlo methods [38] through finite-difference techniques [39, 40] to doubling and adding [41]. For a review of techniques, see the work by Lenoble [42]. Virtually all these solution methods are intensity-only models, in that they generate only the radiance spectrum and associated integrated quantities such as flux and mean intensity which are required for heating-rate and radiative forcing simulations.

The generation of radiance derivatives in anisotropic scattering media has received much less attention. The GOMETRAN finite-difference RT model was the first to generate simultaneous fields of radiance derivatives without the need for finite difference approximations; GOMETRAN was developed by Rozanov and co-workers [40, 43, 44] for the GOME instrument. The present work reports on the development of a generalized approach to weighting function derivation from the standpoint of discrete ordinate tradiative transfer heory. Very recently, and again within the context of ozone profile retrieval, perturbation methods have been applied to the Gauss-Seidel radiative transfer formalism to generate analytic weighting functions [45].

For a given wavelength, light is properly described by a four-vector $\{I, Q, U, V\}$ of Stokes parameters. I is the intensity (radiance), and the customary polarization quantities (degree of linear polarization, degree of circular polarization, direction of linear polarization) may be expressed in terms of these Stokes parameters. For definitions, see [46] and [47]. Vector RT models are complex, hard to implement and require large amounts of CPU time for their execution; most atmospheric RT simulations have used the scalar intensity-only approximation. There have been very few remote sensing instrument measuring polarized light, though this situation is changing. The intensity should properly be calculated as the first component of the Stokes vector using a vector model; the scalar-only assumption can lead to significant sources of error [48]. In this work, we develop linearization and weighting function analysis for the scalar-only discrete ordinate radiative transfer equations. This is a logical step to take before tackling the more complex problem of a vector model linearization (research on this development has in fact already started). For further remarks on this paragraph, see Chapter 6, Section 3.2.

Scattering will be regarded as non-conservative in this work; the case of conservative scattering (no absorption) requires special mathematical treatment; it is never realized in practical situations in the Earth's atmosphere. We do not consider non-coherent (or inelastic) scattering, which involves a certain proportion of photons changing frequency as a result of the scattering process. In the atmosphere, Rotational-Raman (RR) scattering by air molecules results in a spectrum of discrete lines on either side of the central Cabannes line. RR scattering contributions to earthshine radiance have been modeled to first-order [20, 19], but there is still no comprehensive RT treatment of combined elastic and inelastic scattering.

1.2.2. The discrete ordinate method

The discrete ordinate method of solving the radiative transfer equation in a scattering medium is one of the oldest. It dates back to the pioneering work of Chandrasekhar in the 1940s [49]; he elevated the field of radiative transfer to a branch of mathematical physics in its own right. Chandrasekhar's book "Radiative Transfer" [46] is still an essential source text for scientists in this discipline.

For the diffuse radiance $I(\tau,\mu,\phi)$ (excluding the direct solar beam) in direction (μ,ϕ) and at optical depth τ, the form of the integro-differential RTE used in this thesis is:

$$\mu\frac{dI(\tau,\mu,\phi)}{d\tau} = I(\tau,\mu,\phi) - J(\tau,\mu,\phi) \tag{1.7}$$

$$J(\tau,\mu,\phi) = \frac{\omega}{4\pi}\int_{-1}^{1} d\mu' \int_{0}^{2\pi} d\phi' P(\mu,\phi;\mu',\phi') I(\tau,\mu',\phi') + \frac{\omega}{4\pi} P(\mu,\phi;-\mu_0,\phi_0) F_\odot \mathrm{e}^{-\tau_{spher}(\tau)}, \tag{1.8}$$

where $P(\mu,\phi;\mu',\phi') = P(\Theta_s)$ is the phase function for scattering, which depends on scattering angle Θ_s, and ω is the single scattering albedo. The scattering angle is given in terms of (incident and scattered) directional variables through the usual relation:

$$\cos\Theta_s = -\mu\mu' + \sqrt{(1-\mu^2)\left(1-\mu'^2\right)}\cos\left(\phi-\phi'\right). \tag{1.9}$$

The source function $J(\tau,\mu,\phi)$ comprises the scattered diffuse light term (the multiple scatter integral), the scattered light from the direct solar beam, and a thermal emission contribution (omitted here). $\tau_{spher}(\tau)$ is the slant path optical depth of the solar beam to the point of scatter, calculated in a curved atmosphere (the pseudo-spherical approximation).

In common with a number of other radiative transfer solution methods, the azimuth dependence of the radiation field is expressed as a Fourier cosine series in the relative azimuth angle:

$$I(\tau,\mu,\phi) = \sum_{m=0}^{2N-1} I^m(\tau,\mu)\cos m(\phi_0-\phi). \tag{1.10}$$

This requires the phase function to be expanded in a finite series of Legendre polynomials in the cosine of the angle of scatter; the expansion coefficients are termed the phase function moments. This reduces the problem to the solution of the Fourier components $I^m(\tau,\mu)$. The discrete ordinate approach involves the use of a numerical quadrature scheme to approximate the integral over polar directions in dealing with the multiple scatter source term. It is customary to use a double-Gauss scheme, with quadrature abscissae and weights $\{\mu_i, w_i\}, i = 1,\ldots,N$ defined separately for the upwelling and downwelling hemispheres. The integer $2N$ is the total number of streams. The RTE is then reduced further to the solution of a set of coupled linear first-order differential equations for the stream components $I^m(\tau,\mu_i)$:

$$\mu_i\frac{dI^m(\tau,\mu_i)}{d\tau} = I^m(\tau,\mu_i) - \sum_{j=\pm 1}^{j=\pm N} w_j \Pi^m(\mu_i,\mu_j) I^m(\tau,\mu_j) - Q^m(\mu_i) e^{-\tau_{spher}(\tau)}, \tag{1.11}$$

$$Q^m(\mu_i) = \frac{F_\odot}{2}(2-\delta_{m0})\Pi^m(\mu_i,-\mu_0), \quad \Pi^m(\mu,\mu') = \frac{\omega}{2}\sum_{l=m}^{2N-1}\beta_l P_l^m(\mu) P_l^m(\mu'). \tag{1.12}$$

with β_l denoting the Legendre expansion phase function moments, and $P_l^m(\mu)$ the associated Legendre polynomials in argument μ.

Homogeneous solutions are obtained by solving (1.11) without the solar beam term; in the general case, the modern way uses eigensolution methods (see for example [34]). Particular solutions in the presence of the solar term may be obtained by substitution methods (essentially trying a solution of the same form) or by the use of an infinite-medium Green's function technique [50]. Both particular solution methods have been implemented in the present work. Once this set of differential equations is solved, the boundary conditions are invoked in order to establish the integration constants arising from the solution. The stream components $I^m(\tau,\mu_i)$ may then be written down for any optical depth. To establish the solution away from the quadrature streams, the source function integration technique (again developed by Chandrasekhar) is used. This is essentially a smart interpolation; it ensures that radiances at arbitrary μ satisfy continuity requirements at the boundaries.

Analytic two-stream solutions of the discrete ordinate equations have been worked out in detail and applied to a number of atmospheric and ocean scenarios (for a summary, see [34]). A limited number of analytic 4-stream solutions have also developed [51]. With the advent of large and powerful computers in the 1970s, it became possible to develop multiple scattering RT models for multi-layer atmospheres. This was done for the 2N-stream plane-parallel discrete ordinate model by Knut Stamnes and co-workers in a series of papers from 1980 onwards [52, 53, 54, 55, 56, 57], culminating in the release of the DISORT plane-parallel radiative transfer package in 1988 [58]. DISORT is the most widely used RT code available to the atmospheric community. It is a generic scattering formalism that does not require direct specification of atmospheric constituent inputs and their optical properties at the microphysical level. Instead, it is only necessary to specify three optical inputs for each layer - the total single scattering albedo, the vertical optical thickness and the total phase function moments.

The philosophy behind the DISORT work was to build a general-purpose and flexible radiative transfer package that could be used in a wide variety of atmospheric applications. The model applies to a plane-parallel medium and includes both thermal and solar beam sources. The model is called as a subroutine within an environment which the user tailors to his or her specific needs. The user will then create the DISORT inputs from the set of atmospheric constituents and parameters appropriate to the application. A pseudo-spherical version SDISORT has been developed [35], but unfortunately this has not been packaged as a general-purpose tool in the same manner as DISORT itself. The delta-M scaling is standard in DISORT. A second version of the code incorporates the single scatter correction procedure of Nakajima-Tanaka [37].

1.2.3. Linearizing discrete ordinate theory: an introduction to LIDORT

As noted in Section 1.1.2, forward models used in iterative retrieval applications should be able to generate weighting functions. These are partial derivatives of the radiance field with respect to parameters that will either be retrieved (elements of the state vector) or parameters that will contribute to uncertainties in the retrieval. Weighting functions are also expressed in terms of Fourier components; the definitions are:

$$K_\xi\left(\tau,\mu,\phi_0-\phi\right)=\sum_{m=0}^{2N-1}K_\xi^m(\tau,\mu)\cos m\left(\phi_0-\phi\right); \tag{1.13}$$

$$K_\xi^m(\tau,\mu)=\xi\frac{\partial I^m(\tau,\mu)}{\partial\xi} \quad \text{or} \quad K_\xi^m(\tau,\mu)=\lim_{\varepsilon\to 0}\frac{I^m(\tau,\mu,\xi[1+\varepsilon])-I^m(\tau,\mu,\xi)}{\varepsilon}. \tag{1.14}$$

The parameter ξ may be anything from temperature to O_3 volume mixing ratio or logarithm of the column abundance, or aerosol scattering or extinction or asymmetry parameter. It can even be the surface albedo. Recalling that the key inputs to a discrete ordinate model are the optical depth grid, total single scattering albedos and total phase function moments, it is only necessary to first establish the derivatives of these inputs with respect to ξ. Once this is done, chain-rule differentiation of the discrete ordinate radiances will yield the required weighting functions. Thus $\partial\omega/\partial\xi$, $\partial\tau/\partial\xi$ and $\partial\beta_l/\partial\xi$ are additional inputs required to generate weighting functions. As this thesis will show, the entire discrete ordinate solution is explicitly differentiable at all places; no numerical approximations are required. The level of accuracy (controlled largely by the number of streams) is the same for radiance and weighting functions.

The first approach (Chapter 2 of this thesis) to the calculation of weighting functions used first-order perturbation analysis; weighting functions are determined by relaxing the perturbation in (1.14) (second part). This approach was first developed first for an analytic two-stream solution, then extended to the general $2N$-stream plane-parallel RT model. It was necessary to break down the entire radiance solution in a multi-layer atmosphere into its component parts, and apply perturbation methods to each part. The second approach (Chapter 3 of this thesis) was to generate radiance derivatives (1.14) by direct explicit differentiation of the radiance field. This was done in the pseudo-spherical treatment, and extended to produce output at arbitrary optical depth and direction.

On the basis of the linearization analysis, the numerical model LIDORT (LInearized Discrete Ordinate Radiative Transfer) has been developed and tested. The philosophy adopted for LIDORT is the same as that for DISORT - to make a general-purpose and flexible radiative transfer package that could be used in a wide variety of atmospheric applications, not just for simulating intensity, but also for generating weighting functions that are necessary in so many retrieval applications. Like DISORT, LIDORT is a subroutine called from a user-defined environment. LIDORT too is a scattering formalism; it does not need to know the number and nature of the atmospheric gases and particulates. Validation of LIDORT is straightforward: radiances may be compared directly with DISORT and SDISORT output, while weighting functions are validated using the finite-difference estimation (1.5) and choosing ε_{FD} small enough.

Chapters 4 and 5 of the present work are concerned with the application of the linearized discrete ordinate radiative transfer theory in the context of ozone profile retrieval from nadir viewing remote sensing instruments such as GOME.

1.3. Scope of the thesis

1.3.1. Main goals of the work

The main goals of this work are:

1. To carry out a complete linearization of the discrete ordinate radiative transfer solution in a multiply scattering multi-layer medium, with the purpose of deriving analytically accurate weighting functions.

2. To develop a generalized radiative transfer forward model package (LIDORT) for the simultaneous and accurate generation of radiances and weighting function fields, for use in a wide variety of atmospheric retrieval applications.

3. In the context of an O_3 profile retrieval algorithm for nadir viewing space-borne instruments measuring backscatter UV spectra, to investigate the accuracy of radiance and weighting function output from 4 and 6 stream versions of LIDORT.

4. Using an O_3 profile retrieval algorithm based on 4-stream LIDORT, to carry out an error assessment and some sensitivity studies of the retrieval.

The work was divided into four stages:

1. The determination of analytic derivatives was first carried out for a plane-parallel atmosphere for the TOA upwelling radiation field. This was done using perturbation analysis. This stage is reported in Chapter 2 and resulted in the first LIDORT model.

2. Using direct differentiation of the discrete ordinate solution, the weighting function analysis was generalized to include the pseudo-spherical treatment of the direct beam, and to produce output anywhere in the atmosphere. The sphericity correction was developed at this stage. This stage is reported in Chapter 3 and resulted in the second LIDORT model.

3. This covers the third goal above. TOA upwelling analytic radiances and derivatives were worked out for 4 and 6 stream models and compared to 20-stream LIDORT output for a wide range of scenarios in the UV spectral range. This stage includes incorporation of the Nakajima-Tanaka single scatter correction.

4. This covers the fourth goal. Using optimal estimation methods, an examination was made of temperature sensitivity and upper wavelength limits for the O_3 profile retrieval algorithm. The error assessment was carried out for forward model errors, measurement errors due to polarization correction and model parameter errors such as temperature profile and aerosol optical thickness uncertainties.

1.3.2. Thesis contents

In Chapter 2, we apply first-order perturbation analysis to the discrete ordinate TOA upwelling radiance solution in a multiply-scattering multi-layer plane-parallel atmosphere. The homogeneous and particular solutions in a given layer are examined and their first-order perturbations determined. A new formalism is developed for the linearization of the eigenvalue equation that governs the homogeneous solution. The boundary value problem is then subject to the perturbation analysis, and this yields the perturbed values of the integration constants; from these ingredients, weighting functions at the discrete ordinate (quadrature) streams can be evaluated. A further step is then taken to develop TOA weighting functions at arbitrary polar directions by applying the perturbation methods to the post-processing source function integration which delivers radiances in these directions. A general bidirectional treatment of the surface boundary condition is given; isotropic surface thermal emission is included. In addition to the solar beam source, perturbation analysis is applied to the particular solution pertinent to atmospheric thermal emission source terms; the treatment assumes a polynomial dependence of the emission on optical depth.

Radiance output is validated against DISORT. Examples of weighting functions are presented for a 5-layer test atmosphere; they are validated against finite difference estimates. A second example is presented for a realistic terrestrial atmosphere with Rayleigh/aerosol scattering and O_3 absorption in the Hartley-Huggins band region of the UV spectrum; weighting functions for profiles of O_3 volume mixing ratio and temperature are given. Peak values of weighting functions in the UV below 320 nm are shown to possess the dependence of scattering penetration depth on wavelength that is a cornerstone of the BUV retrieval algorithm for O_3 profiles. A comparison with the GOMETRAN model output is presented. This work resulted in the first version of the LIDORT model, and release of a User's Guide (Version 1.1).

In Chapter 3 we extend the linearization analysis to cover the generation of weighting function output at arbitrary optical depth and viewing geometry, and to develop the analysis for a pseudo-spherical model. The emphasis is changed from perturbation methods to direct differentiation; the linearization operator is introduced. A number of parameterizations for the pseudo-spherical attenuation of the direct solar beam are presented and their respective accuracies discussed. The Green's function particular solution is developed for the first time in a multi-layer atmosphere for the pseudo-spherical treatment; the more traditional particular solution method due to Chandrasekhar is treated in parallel. Derivatives and weighting function generation are worked out for the pseudo-spherical average secant treatment; this requires some care in dealing with parameter dependencies from different layers (cross-layer derivative terms are largely absent in the plane-parallel situation). The post-processing function is extended to generate upwelling and downwelling output of radiance and weighting functions anywhere in the atmosphere. This allows the model to be used for ground-based retrievals.

Validation of radiances is done against DISORT (plane-parallel) and SDISORT (pseudo-spherical). A sphericity correction is developed for modeling TOA upwelling output at the wide-angle off-nadir line-of-sight angles typical of GOME-2 and OMI viewing situations; this involves the use of multiple scatter output from LIDORT in conjunction with more precise calculations of atmospheric upwelling single scattering along the line-of-sight. Examples are presented for a 60-layer atmosphere with Rayleigh and aerosol scattering and O_3 absorption. Plane-parallel and pseudo-spherical radiance and weighting function output are compared for a number of viewing geometries. The effect of refraction is investigated. Examples are also presented showing the effect of the sphericity correction; it is shown that this correction is essential for GOME-2 and OMI. This paper is the template for Version 2.1 of the numerical package LIDORT.

Chapters 2 and 3 are the "concept papers". Chapter 4 is a major investigation of the forward model accuracy required for the application of LIDORT to the O_3 profile retrieval algorithm. In particular we are interested in the use of 4 and 6 stream models for performance enhancement in fast-delivery retrieval. The formalism developed in the previous two chapters is re-examined, with special emphasis placed on the development of analytic homogeneous and particular solutions obtainable with the use of low stream numbers. It is shown that additional weighting functions may be obtained with respect to quantities such as the aerosol asymmetry parameter which affect the angular distribution of scattering; this opens up the model to a wider range of potential aerosol retrieval problems. A post-processing function is developed using the Nakajima-Tanaka single scatter correction; this uses an exact form of the phase function, but with transmittance calculations evaluated in an atmosphere with a (delta-M) scaled optical depth grid. This single scatter term is then combined with a multiple scatter calculation from LIDORT to generate more accurate output. The sphericity correction from Chapter 3 is extended to incorporate the NT correction.

With the same reference atmosphere as that used in the previous chapter, 4 and 6 stream TOA upwelling output is compared with accurate 20-stream LIDORT results for a wide range of viewing geometries. The wavelength range 299-335 nm is covered. The effect of cloud optical thickness is examined for a cloud layer. Other scenarios involving optically thick layers superimposed on the clear sky reference atmosphere are investigated (Saharan dust, volcanic, polluted boundary layer). Radiance error limits are established for all scenarios. It is shown that the 4-stream radiance error is generally in the range 1.5-2.0% for most scenarios; the NT procedure does not always improve the accuracy. 6 stream accuracies in radiance are in general a factor of 3 better; the NT correction is very successful for 6 streams. Weighting function errors are restricted to $\pm 2\%$ in the 6 stream case. Wide-angle sphericity-corrected output is examined in detail for the four instruments listed in Appendix A; without this correction GOME-2 and OMI output can be 5-8% in error at swath extremes. This research resulted in the current version of LIDORT (V2.3), and an updated User's Guide to Version 2.3.

Chapter 5 presents results using the operational O_3 profile algorithm under development at KNMI for the GOME-2 instrument. We review the main points of optimal estimation theory, concentrating on the classification and derivation of error sources and on the singular value decomposition (SVD) of the weighting function matrix. This allows a clear interpretation of the sources of information in the retrieval. We define the degrees of freedom for signal (DFS) diagnostic as a measure of retrieval precision. The 4 stream LIDORT RT model from Chapter 4 is used in the forward model. Synthetic measurement data is created on a 34-layer grid using LIDORT simulations together with a high resolution solar spectrum; noise and instrument response characteristics are taken for the GOME-2 instrument. The state vector profile is a series of partial O_3 column densities; *a priori* values are taken from a suitable O_3 climatology. Surface albedo is retrieved simultaneously.

We use the DFS diagnostic to investigate profile precision and tropospheric profile resolution based on the temperature dependence of the Huggins-band O_3 cross-sections; the increase in DFS from cold to warm tropospheric regimes is most apparent in the 313-322 nm range. Absolute values of DFS depend on scenario variables such as solar zenith angle and albedo, and also on the degree of regularization in the retrieval. The DFS is also used to optimize the choice of an upper wavelength limit for the fitting; it is shown that the inclusion of wavelengths above 322 nm does little to increase its value.

We look at the effect of forward model errors on the O_3 profiles due to the assumption of a low number of streams used in the discrete ordinate solutions; 4/20 stream errors are shown to be unacceptably large for wavelengths in excess of 320 nm. Using output from a polarization RT model, we quantify the profile error due to the neglect of polarization in the RT modeling. We look at profile accuracy as a function of calibration errors on GOME radiances due to the implementation of polarization correction algorithms; this is shown to be a major source of error for tropospheric profile elements. We investigate the effect of model parameter errors on the retrieval, concentrating on temperature and aerosol optical thickness uncertainties. For aerosols, the optical thickness of the lowest tropospheric layer is a critical source of error for the retrieval of the lowest O_3 profile element. It is shown that temperature errors are significant everywhere in the atmosphere; stringent requirements on temperature uncertainty are needed to minimize this source or error in the overall profile accuracy.

Appendix A contains brief details on the four instruments GOME, GOME-2 SCIAMACHY and OMI that are featured in this thesis. We note the spectral ranges and resolutions, the footprint and swath dimensions, and the nominal read-out times. The main target constituents are listed for each instrument. Brief remarks are made about calibration issues and (with the exception of OMI) the polarization devices. Appendix B contains some notes on the construction and layout of the LIDORT numerical software package. The scope of LIDORT Version 2.3 is summarized, and the directory structure of the package is outlined along with short descriptions of the functions of the main modules. Further details may be found in the User's Guide to LIDORT Version 2.3.

Chapter 2

A linearized discrete ordinate radiative transfer model for atmospheric remote sensing retrieval

This chapter has been published in the Journal of Quantitative Spectroscopy and Radiative Transfer, **68**, 689-735, 2001, and was co-authored by T.P. Kurosu and K.V. Chance.

Abstract

The radiative transfer forward model simulation of intensities and associated parameter derivatives (weighting functions) is a vital part of the retrieval of earth atmospheric constituent information from measurements of backscattered light. The discrete ordinate method is the most commonly used approach for the determination of solutions to the radiative transfer equation. In this paper, we carry out an internal perturbation analysis of the complete discrete ordinate solution in a plane-parallel multi-layered multiply-scattering atmosphere. Perturbations in layer atmospheric quantities will translate into small changes in the single-scatter albedos and optical depth values. In addition, we consider perturbations in layer thermal emission source terms and in the surface albedo. It is shown that the solution of the boundary value problem for the perturbed intensity field leads in a natural way to the weighting function associated with the parameter causing the perturbation. We have developed a numerical model LIDORT (LInearized Discrete Ordinate Radiative Transfer) for the simultaneous generation of backscatter intensities and weighting function output at arbitrary elevation angles, for a user-defined set of atmospheric variations. Results for a 5-layer test atmosphere with two scatterers and thermal emission terms are shown. Intensities are validated against benchmark discrete ordinate results, while weighting functions are checked for consistency against finite difference results based on external perturbations. A second example is presented for a 60-layer terrestrial atmosphere with molecular and aerosol scattering and ozone trace gas absorption in the UV spectral range; weighting functions are shown to correspond closely with results derived from another radiative transfer model.

2.1. Introduction

2.1.1. Background and rationale

The derivation of atmospheric constituent distributions and surface properties from surface-based, airborne and satellite remote sensing instruments plays a vital role in monitoring the earth's atmosphere and understanding the chemical and physical processes therein. A common feature of all retrievals is the need for an accurate forward model for the generation of synthetic quantities such as radiances, fluxes and weighting functions. The model should include a full treatment of all orders of scattering. Accurate multiple-scatter forward models are also critical for addressing problems in stellar and planetary atmospheres.

The retrieval process will generate estimates of a number of atmospheric parameter distributions which together constitute the *state vector* $\mathbf{X}$ of parameters to be retrieved. The retrieval is the formal inverse of the forward problem $\mathbf{Y} = F(\mathbf{X})$, where $\mathbf{Y}$ is the vector of synthetic measurements and F is a function describing the attenuation of solar and/or thermal emission radiation in the atmosphere by means of absorption, scattering and reflection of light. This function is specified by a radiative transfer model. In most cases, F has a complex dependence on the atmospheric parameters $\mathbf{X}$, and the inverse problem is often solved with a non-linear iterative scheme based on likelihood estimation. Uncertainties in the retrieval will depend not only on the accuracy of the instrumental measurements but also on uncertainties inherent in the modeling of the atmosphere and on assumptions made about the accuracy of any *a priori* information.

Non-linear least squares fitting [2] has been and continues to be a standard technique for many remote sensing problems, for example the global fitting of limb emission spectra [59]. The optimal estimation retrieval algorithm [60, 4] has found much use in constituent profile retrieval from backscatter and emission measurements. In particular, we note the application of this method to ozone profile retrieval from nadir backscatter measurements made by instruments such as SBUV [11] and GOME [13, 14, 15]. A number of related retrieval techniques are used in the remote sensing context, including Phillips-Tikhonov regularization [3], and Chahine inversion [61]. In order to illustrate the retrieval requirement for forward model synthetic measurements and associated weighting functions, we give an example for the optimal estimation approach [60, 4].

The solution of the inverse problem $\mathbf{X} = F^{-1}(\mathbf{Y})$ is constrained by the existence of an independent *a priori* state vector $\mathbf{X}_a$ with error covariance $\mathbf{S}_a$. Assuming Gaussian statistics with error covariance $\mathbf{S}_m$ associated with measurement vector $\mathbf{Y}_m$, the optimization minimizes with respect to $\mathbf{X}$ the functional

$$\Phi = (X - X_a)^T S_a^{-1} (X - X_a) + (Y - F(X))^T S_m^{-1} (Y - F(X)). \tag{2.1}$$

The T-superscript denotes matrix transpose. If the forward model is linearized about the state $\mathbf{X}_n$:

$$F(X) = F(X_n) + K_n(X - X_n) + O(X - X_n)^2, \tag{2.2}$$

then the estimate for the next guess of the state vector is given by

$$X_{n+1} = X_a + G^{-1} K_n^T S_m^{-1} \left[(Y_{meas} - Y_n) - K_n (X_a - X_n) \right], \tag{2.3}$$

where

$$G = K_n^T S_m^{-1} K_n + S_a^{-1}. \tag{2.4}$$

Here, $\mathbf{Y}_n = F(\mathbf{X}_n)$ is the synthetic measurement computed from a forward model calculation based on atmospheric state vector $\mathbf{X}_n$, and $\mathbf{K}_n$ is the Jacobean matrix of forward model parameter derivatives (also known as weighting functions) evaluated at $\mathbf{X}_n$. $\mathbf{K}_n$ represents the responses of the simulated intensity to small changes in atmospheric parameters that make up state vector $\mathbf{X}_n$. (Henceforth we use the term "weighting functions" for $\mathbf{K}_n$). The starting point for the state vector iteration is often taken to be the *a priori* value. For optimal estimation and other iterative retrieval algorithms, it is clear that the radiative transfer model must generate the set $\{\mathbf{Y}_n, \mathbf{K}_n\}$ for each state vector estimate $\mathbf{X}_n$.

In many circumstances, a simplified model of atmospheric light attenuation can be used, for which weighting functions can be determined in a straightforward manner from explicit expressions. Thus for example in solar occultation viewing, extinction of the line-of-sight solar beam predominates over atmospheric backscatter, which is ignored in the forward model (see for example [61] for SAGE II retrieval). However for instruments measuring backscattered light in the UV, visible and near infrared regions, multiple scattering of light in the earth's atmosphere is an important physical process that cannot be neglected. Although accurate values for $\mathbf{Y}_n$ for multiple scattering scenarios have been determined from a variety of radiative transfer (RT) solution methods (see [42] for a summary of techniques), less attention has been paid to the calculation of weighting functions $\mathbf{K}_n$.

Finite difference approximations to $\mathbf{K}_n$ have often been derived by using *external* perturbations. Here, two independent simulations of the atmospheric attenuation are made, one for an unperturbed atmosphere, the other for an atmosphere in which a single parameter has been changed by a small amount; the intensities are subtracted and divided by the parameter change. This process must be repeated for each parameter to be retrieved, and at every iteration step of the retrieval. In addition to the time-consuming nature of this approach, the accuracy depends in a rather *ad hoc* manner on the magnitude of the external perturbation. This is particularly evident when the optical properties depend in a complex non-linear fashion on the atmospheric parameter in question (for example, temperature).

The main purpose of this paper is the development of a forward model LIDORT (LInearized Discrete Ordinate Radiative Transfer) that will generate quickly and accurately any desired set of backscatter weighting functions in a multi-layered atmosphere with anisotropic scatterers, as well as the backscatter intensity field. The model is based on the discrete ordinate method for the solution of the radiative transfer equation (RTE). This method has a long history, from the pioneering work of Chandrasekhar in the 1940s [46, 49] to the DISORT package developed by Stamnes and co-workers in the 1980s [58]. DISORT in particular has been widely used in atmospheric radiative transfer applications, and has recently been installed in MODTRAN [62] to provide a reliable scattering formalism.

The discrete ordinate approach uses optical depth as the vertical coordinate; scattering properties are specified by means of layer single-scatter albedos and phase functions. The method reduces the full RTE to a set of coupled *linear* first-order differential equations. We show that first-order perturbation analysis may be carried out explicitly on the discrete ordinate solutions to these equations. Furthermore, we show that the boundary condition problem applied to the *perturbed* intensity field generates in a natural way the complete field of first-order parameter derivatives. Analytic expressions may be developed for all weighting functions, which can then be calculated rapidly and to the same level of accuracy as the (unperturbed) backscattered intensity.

We look at the following general scenario pertinent to satellite retrieval applications in the earth's atmosphere. We confine our attention to intensity and weighting function output for upwelling radiation at the top of the atmosphere (TOA). The atmosphere will be assumed plane-parallel, with each layer treated as homogeneous and possessing several non-conservative scattering particulates. Two sources of light will be considered – the beam source (prototype for solar illumination) and an isotropic thermal emission source. No diffuse light is incident on the top of the atmosphere. The atmosphere is bounded below by a reflecting surface with a known bi-directional or Lambertian reflection function. The lower boundary may also have a thermal emission property (assumed isotropic). The scope of the plane-parallel DISORT package [58] covers this scenario, and this version of DISORT will be used as the standard for validating the backscatter intensity results. Polarization effects are not included.

For weighting function derivation, we need to know how variations in layer atmospheric quantities will be manifested as changes to the layer single-scatter albedos and optical thickness values. We will not consider changes to phase function angular distributions (although this is in principle possible in the perturbation analysis). The effect of atmospheric parameter variations will also be included in the thermal emission source term. For the surface property, we will consider perturbations of the total surface albedo (but not the angular distribution of the bi-directional reflectance) and the surface emission term. These assumptions will allow a wide variety of weighting functions to be derived, including those with respect to layer trace gas concentrations, layer temperatures and pressures, cloud and aerosol scattering and extinction coefficients, molecular scattering coefficients, and thermal emission coefficients.

As part of the algorithm development for the GOME satellite instrument [5], a weighting function analysis has been carried out on the GOMETRAN RT model developed for this instrument [43]. This model uses altitude rather than optical depth as the vertical coordinate, and the RTE for a multi-layered atmosphere is solved using finite differences for the altitude derivatives. This transforms the complete problem to a linear matrix algebra system [39, 40], which is then subject to first-order perturbation theory for the generation of weighting function output. As is often the case with altitude finite-differencing, great care must be taken with the choice of vertical grid. This version of GOMETRAN has been used in some studies of ozone profile retrieval from GOME nadir backscatter measurements using optimal estimation methods [14, 15].

2.1.2. Overview of the paper

In Section 2.2 we recapitulate the discrete ordinate solution for the backscattered intensity. Following the basic RTE definitions (Section 2.2.1), the description falls into two parts: (1) solution of the discrete ordinate differential equations for the homogeneous and particular integrals for each layer, the component solutions being evaluated at the computational quadrature angles (Section 2.2.2); (2) the intensity field derivation using appropriate boundary conditions at the top and bottom of the atmosphere, plus continuity of the field at intermediate layer boundaries, to fix the constants of integration; the solution is completed using the *post-processing function*, that is, the derivation of intensities for arbitrary (user-defined) zenith angles using the source function integration method (Section 2.2.3). This exposition follows closely the DISORT description [58]. Although much of this material is familiar (see for example [58] or [34]), the exposition given here is designed to illuminate the perturbation analysis that follows.

In Section 2.3.1 we introduce some definitions and rules for the first-order perturbation analysis of the discrete ordinate solution. In Section 2.3.2 we apply these rules to the layer homogeneous and particular solutions of the perturbed RTE. This is followed by a description of the boundary conditions required for the perturbed intensity field (Section 2.3.3). Section 2.3.4 outlines the derivation of analytic expressions for TOA weighting functions with respect to layer parameters for both the discrete ordinate stream angles and the post-processed off-quadrature directions; the TOA albedo weighting functions are treated in Section 2.3.5. The whole of Section 2.3 is designed to give an overall summary and description of the weighting function analysis without going into excessive mathematical detail. Most of the algebraic manipulations have been placed in Appendices 2.6.1, 2.6.2 and 2.6.3.

An analytic formulation of the discrete ordinate solution for a single layer was first developed by Chandrasekhar [46, 49] using the full-space quadrature scheme over the interval $(-1,1)$. It turns out that a complete analytic perturbation analysis can also be developed with this quadrature scheme. This approach is not as flexible or as powerful as the "double" quadrature eigenproblem method used in DISORT and the present work. The original Chandrasekhar solution and the corresponding perturbation analysis are presented for completeness in Appendix 2.6.4.

In Section 2.4 we consider the numerical model LIDORT developed from the theory in Sections 2.2 and 2.3, and provide two examples of weighting function simulations. Following some discussion of the model and its implementation (Section 2.4.1 to Section 2.4.3), the first example treats a 5-layer atmosphere with two scatterers and beam and thermal source terms; this scenario will illustrate the principles behind the weighting function derivations. In Section 2.4.5, we examine a realistic scenario involving a 60-layer terrestrial atmosphere with both molecular (Rayleigh) and aerosol scattering, and including ozone absorption, for a number of wavelengths in the UV region. In both examples, we check the LIDORT weighting function output by comparing with external finite-difference values obtained from independently-calculated intensities based on perturbed atmospheric parameters. In addition, values of intensity in all cases are checked against DISORT results for the same scenarios. Finally, we show that the weighting function results in Section 2.4.5 are consistent with values computed from the GOMETRAN model [43] for the same scenario.

In Section 2.5 following the summary, we remark on future developments for LIDORT. These include (i) additional options to output weighting function fields at arbitrary optical depths and stream angles, for both upwelling and downwelling directions; (ii) the generation of mean-value output (fluxes, mean intensities); (iii) the treatment of the direct beam attenuation in a curved atmosphere; and (iv) a vectorization of the model for the treatment of fully-polarized light. The first three developments have been carried out, and will be the subject of a second paper (R. Spurr, in preparation).

2.2. The discrete ordinate solution

2.2.1. Radiative transfer equation (RTE)

The equation of radiative transfer for the diffuse intensity field I in a plane-parallel scattering medium may be written

$$\mu\frac{dI(\tau,\mu,\phi)}{d\tau}=I(\tau,\mu,\phi)-J(\tau,\mu,\phi). \tag{2.5}$$

The scattering is assumed to be completely coherent (no redistribution among wavelengths), so that Equation (2.5) is valid for a monochromatic intensity field. The optical depth coordinate τ is measured perpendicular to the medium boundaries with $\tau=0$ at TOA, and the direction is specified through μ (absolute value of the cosine of the zenith angle) and ϕ (azimuth angle). In this paper, the source term J is defined to be:

$$J(\tau,\mu,\phi)=J_{ext}(\tau,\mu,\phi)+\frac{\omega(\tau)}{4\pi}\int_0^{2\pi}d\phi'\int_0^1 d\mu' P(\tau,\mu,\phi;\mu',\phi')I(\tau,\mu',\phi'). \tag{2.6}$$

Here $J_{ext}=J_{beam}+J_{thermal}$ is the sum of the beam and atmospheric thermal emission source terms, $\omega(\tau)$ is the single-scatter albedo, and $P(\tau,\mu,\phi;\mu',\phi')$ the phase function; the last term in Equation (2.6) represents the multiple scatter contribution.

The source term J_{beam} corresponds to scattering of a parallel beam of incident flux $\mu_0 F_\odot$ in direction $\{-\mu_0, \phi_0\}$; $J_{thermal}$ represents thermal emission (assumed isotropic) as determined by a Planck function $B(T)$ at temperature T (which is regarded as a function of τ). Specifically:

$$J_{beam}(\tau,\mu,\phi) = \frac{F_\odot}{4\pi}\omega(\tau)P(\tau,\mu,\phi;-\mu_0,\phi_0)e^{-\tau/\mu_0}, \tag{2.7}$$

$$J_{thermal}(\tau,\mu,\phi) = (1-\omega(\tau))\,B(T). \tag{2.8}$$

Next, we expand the intensity as a Fourier cosine series in the relative azimuth $\phi_0 - \phi$, and the phase function as a series of Legendre polynomials in the cosine of the scatter angle Θ between directions $\{\mu,\phi\}$ and $\{\mu',\phi'\}$:

$$I(\tau,\mu,\phi) = \sum_{m=0}^{2N-1} I^m(\tau,\mu)\cos m(\phi_0-\phi), \tag{2.9}$$

$$P(\cos\Theta) = \sum_{l=0}^{2N-1} \beta_l P_l(\cos\Theta), \tag{2.10}$$

where β_l are the phase function moments of the Legendre expansion, and

$$\cos\Theta = -\mu\mu' + \sqrt{(1-\mu^2)\left(1-\mu'^2\right)}\cos\left(\phi-\phi'\right). \tag{2.11}$$

This development yields a separate equation for each of the $2N$ Fourier components:

$$\mu\frac{dI^m(\tau,\mu)}{d\tau} = I^m(\tau,\mu) - \int_{-1}^{1} D^m(\tau,\mu,\mu')I^m(\tau,\mu')d\mu' - J^m_{ext}(\tau,\mu), \tag{2.12}$$

where $m = 0, 1, \ldots 2N-1$. The external source term may be written

$$J^m_{ext}(\tau,\mu) = \delta_{0m}\,(1-\omega(\tau))\sum_{s=0}^{S} b_s\tau^s + \frac{F_\odot}{2\pi}e^{-\tau/\mu_0}\,(2-\delta_{m0})\,D^m(\tau,\mu,\mu_0). \tag{2.13}$$

The auxiliary quantities $D^m(\tau,\mu,\nu)$ are defined by

$$D^m(\tau,\mu,\nu) = \frac{\omega(\tau)}{2}\sum_{l=m}^{2N-1} \beta_l(\tau)P^m_l(\mu)P^m_l(\nu). \tag{2.14}$$

The $P^m_l(\mu)$ are associated Legendre polynomials. The addition theorem for Legendre polynomials has been used in the Fourier decomposition. For the thermal source term, the Planck function $B(T)$ has been expressed as a power series in optical depth [52], where the b_s are the expansion coefficients.

In the N^{th} discrete ordinate approximation, the multiple scatter source term integral is replaced by a quadrature sum defined by the set $\{\mu_i, a_i\}, i = (\pm 1, \cdots \pm N)$ of Gauss-Legendre quadrature abscissae and weights. In order to obtain RTE solutions, the atmosphere is assumed to consist of a number of homogeneous layers, with ω and β_l constant for a given layer. In the rest of this section we confine our attention to one such layer (the superposition of layers will be addressed in Section 2.2.3). The solution for Fourier component m is then determined by solving the set of $2N$ linear first-order differential equations for $I^m(\mu_i)$, the intensities at the computational (quadrature) stream angles:

$$\mu_i\frac{dI^m(\tau,\mu_i)}{d\tau} = I^m(\tau,\mu_i) - \sum_j a_j D^m(\tau,\mu_i,\mu_j)I^m(\tau,\mu_j) - J^m_{ext}(\tau,\mu_i). \tag{2.15}$$

Here, $j = (\pm 1, \cdots \pm N)$ is the quadrature sum. In this equation, $J^m_{ext}(\tau, \mu_i)$ and $D^m(\tau, \mu_i, \mu_j)$ are given by Equations (2.13) and (2.14) evaluated at the quadrature cosines.

Two kinds of quadrature regimes are usual – a full-range ("single") scheme over the interval $(-1, 1)$, and a "double" scheme with quadratures defined separately for $\mu \in (0, 1)$ and $\mu \in (-1, 0)$. In both cases $\mu_{-j} = \mu_j$ and $a_{-j} = a_j$, for $j = 1, \ldots N$. For the single scheme, the abscissae are just the $2N$ zeros of $P_{2N-1}(\mu)$ in the interval $(-1, 1)$. The single scheme was used by Chandrasekhar in his original development of an analytic discrete ordinate solution to Equation (2.15) (see Appendix 2.6.4); this solution depends on the orthonormality of the Legendre polynomial set $\{P_l(\mu), l = 0, 1, \ldots 2N-1\}$.

The double quadrature scheme reflects in a natural way the upward and downward stream separation of the intensity field, and the symmetrical distribution of abscissae about $\mu = \pm 0.5$ ensures a more representative spread of points around $\mu = 0$ and $|\mu| = 1$ than that achieved with the single scheme. With the advent of an eigenvalue approach to the solution of Equation (2.15), the double scheme has now become standard in DISORT (see [34] and references therein for a discussion of quadratures). The double scheme is adopted as the default in the present work, though the option to use the single scheme and the analytic solution developed in Appendix 2.6.4 has been retained in the numerical model.

Surface boundary condition

The lower surface of the atmosphere is assumed to have a general bi-directional reflecting property. The bi-directional surface reflection function $\rho(\mu, \phi; \mu', \phi')$ is expanded as a Fourier series in cosine azimuth:

$$\rho(\mu, \phi; \mu', \phi') = \rho_0(\mu, \mu') + 2 \sum_{m=1}^{2N-1} \rho_m(\mu, \mu') \cos m \left(\phi - \phi'\right). \tag{2.16}$$

In the discrete ordinate approximation, the reflection condition for the m^{th} Fourier component of the diffuse intensity at the lower boundary is then

$$I^m(+\mu_i) = (1 + \delta_{m0}) \sum_{j=1}^{N} \mu_j a_j I^m(-\mu_j) \rho_m(\mu_i, -\mu_j), \quad \text{where} \quad i = 1, \ldots N. \tag{2.17}$$

In the present work, a normalized form of the bi-directional reflection is used:

$$\rho_m(\mu_i, -\mu_j) = R \rho^*_m(\mu_i, -\mu_j), \quad \text{where} \quad R = \frac{1}{4} \int_0^1 \int_0^1 \mu \mu' \rho_0(\mu, \mu') d\mu d\mu'. \tag{2.18}$$

R is the surface albedo. For the Lambertian case, $\rho^*_0(\mu_i, \mu_j) = 1$ for all streams and $\rho^*_m = 0$ for $m > 0$. Expressions for ρ_m may be derived from invariance principles [46], and these functions have been investigated in a number of applications ranging from planetary atmospheres [63] to the treatment of terrestrial clouds as bi-directional reflecting surfaces [64].

The upwelling radiation at the lower boundary $\tau = \tau_g$ also has a contribution from the reflection of the direct beam; this has the form:

$$I^m_{direct}(\mu_i, \tau_g) = \frac{F_\odot \mu_0}{\pi} e^{-\tau_g/\mu_0} R \rho^*_m(\mu_i, -\mu_0). \tag{2.19}$$

Furthermore, for the azimuth-independent component, a surface emission term may be included:

$$I_{emission}(\mu_i) = \delta_{m0}\kappa(\mu_i)B(T_g), \tag{2.20}$$

where the black-body function $B(T_g)$ depends on surface temperature T_g. The directional surface emissivity $\kappa(\mu)$ is determined from Kirchhoff's law:

$$\kappa(\mu) = 1 - 2R\int_0^1 \mu'\rho_0^*(\mu,\mu')d\mu'. \tag{2.21}$$

2.2.2. Solutions of the basic equations

Homogeneous solution

We summarize the main results from the eigenvalue approach to the homogeneous RTE developed by Stamnes and co-workers [58, 52, 56]. The treatment is the same for each Fourier component, ,and we henceforth drop the index m except where necessary (for example in the Legendre sum in Equation (2.23) below). Homogeneous solutions of (2.15) may be found with the ansatz $I_j \propto X_j \exp(-k\tau)$ for $j = \pm 1, \cdots \pm N$. Because of the quadrature symmetry, it can be shown that the values of k^2 are real numbers satisfying the following reduced eigenvalue equation of order N:

$$\left(\Gamma - k^2E\right)\varsigma = 0, \quad \text{where} \quad \Gamma = (\zeta - \eta)(\zeta + \eta). \tag{2.22}$$

With indices $i, j = 1, \ldots N$, the matrices ζ and η are given by

$$\zeta_{ij} = \left(D^+_{ij}a_j - \delta_{ij}\right)/\mu_i \quad \text{and} \quad \eta_{ij} = D^-_{ij}a_j/\mu_i, \quad \text{with} \quad D^{\pm}_{ij} = \frac{\omega}{2}\sum_{l=m}^{2N-1}\beta_l P^m_l(\mu_i)P^m_l(\pm\mu_j). \tag{2.23}$$

In the above, E is the unit matrix. Values of k occur in pairs $\pm k_\alpha, \alpha = 1, \ldots N$. The corresponding solution vectors are $X^{\pm}_{j\alpha}$, and these are related to the eigenvectors ς of Equation (2.22) by means of the relation $\varsigma_{j\alpha} = X^+_{j\alpha} + X^-_{j\alpha}$. The difference vector defined by $\vartheta_{j\alpha} = X^+_{j\alpha} - X^-_{j\alpha}$ satisfies the following auxiliary equation linking it to the eigenvector ς:

$$k_\alpha\vartheta_{i\alpha} = \sum_{j=1}^{N}\left(\zeta_{ij} + \eta_{ij}\right)\varsigma_{j\alpha}. \tag{2.24}$$

Details of these derivations may be found in [52] and [58]. For components of $X^{\pm}_{j\alpha}$ at negative stream angles, we use the symmetry relations

$$X^+_{-j\alpha} = X^-_{j\alpha} \quad \text{and} \quad X^-_{-j\alpha} = X^+_{j\alpha}. \tag{2.25}$$

The eigenproblem in Equation (2.22) can be solved reliably using standard numerical packages such as those in LAPACK [65]. A suitable LAPACK driver would be module DGEEV (double precision) for a general non-symmetric eigenmatrix such as Γ in (2.22). However, DGEEV looks for real and imaginary components, and it is quicker to use a dedicated routine solving for real eigenvalues only. The module ASMYTX as used in DISORT is convenient for this purpose. Both modules are implemented in the code; DGEEV and ASYMTX give identical results in all cases, but the latter is faster. A normalization condition will be imposed on the eigenvectors (this will be important in the perturbation analysis):

$$\left\|\varsigma_\alpha^2\right\| \equiv \sum_{j=1}^{N} \varsigma_{j\alpha}^2 = 1, \quad \text{for} \quad \alpha = 1, \ldots N. \tag{2.26}$$

Eigenvectors from module ASYMTX are unnormalized; those from DGEEV already satisfy (2.26).

Particular solutions

For the particular solution of (2.15) appropriate to the plane-parallel beam source term, an ansatz of the form $I_j \sim W_j \exp(-\tau/\mu_0)$ yields the following (see [52] for details):

$$\sum_{j=-N}^{N} A_{ij}^{(beam)} W_j = B_i^{(beam)}, \tag{2.27}$$

where

$$A_{ij}^{(beam)} = \left(1 + \frac{\mu_i}{\mu_0}\right) \delta_{ij} - a_j D_{ij} \quad \text{and} \quad B_i^{(beam)} = \frac{F_\odot}{2\pi} \left(2 - \delta_{m0}\right) D(\mu_i, -\mu_0). \tag{2.28}$$

D_{ij} is defined as in (2.23), but with indices $i, j = \pm 1 \cdots \pm N$ for all stream angles. $D(\mu_i, -\mu_0)$ is defined similarly for the cosine of the beam solution zenith angle. Equation (2.27) may be solved as a standard linear matrix algebra problem for the component values W_j. In the model, this is done using the LAPACK combination DGETRF for an LU-factorization of the matrix $A^{(beam)}$, followed by DGETRS for the solution by back-substitution. Note that it is possible to use the intrinsic symmetry of the discrete ordinate equations to halve the order of the system (2.27); one then requires an auxiliary equation and sum and difference vectors defined in a similar way to those used for the homogeneous solution (see for example [66]).

The particular solution of Equation (2.15) corresponding to the thermal emission source term may be found with the power-series substitution $I_j = \delta_{m0} \sum_{s=0}^{S} T_{j,s} \tau^s$. Successive powers of optical depth τ in the resulting polynomial are equated to zero, generating the following recurrence relation for the coefficients $T_{j,s}$:

$$\sum_j A_{ij}^{(thermal)} T_{j,s} = \begin{cases} (1-\omega)\, b_s e_i & \text{for} \quad s = S, \\ (1-\omega)\, b_s e_i + (s+1)\mu_i T_{i,s+1} & \text{for} \quad s < S, \end{cases} \tag{2.29}$$

where $A_{ij}^{(thermal)} = \delta_{ij} - a_j D_{ij}$ and e_i is a $2N$-vector with unit entries. The linear algebra system (2.29) can again be solved using LAPACK modules DGETRF for the LU decomposition of $A^{(thermal)}$, followed by repeated application of DGETRS for the recurrence coefficients $T_{j,s}$.

2.2.3. Boundary conditions and the complete solution

We assume there are K homogeneous layers in the atmosphere, with $K+1$ layer boundaries. We use indices p, q and r for labeling layers. Combining the discrete ordinate homogeneous solutions

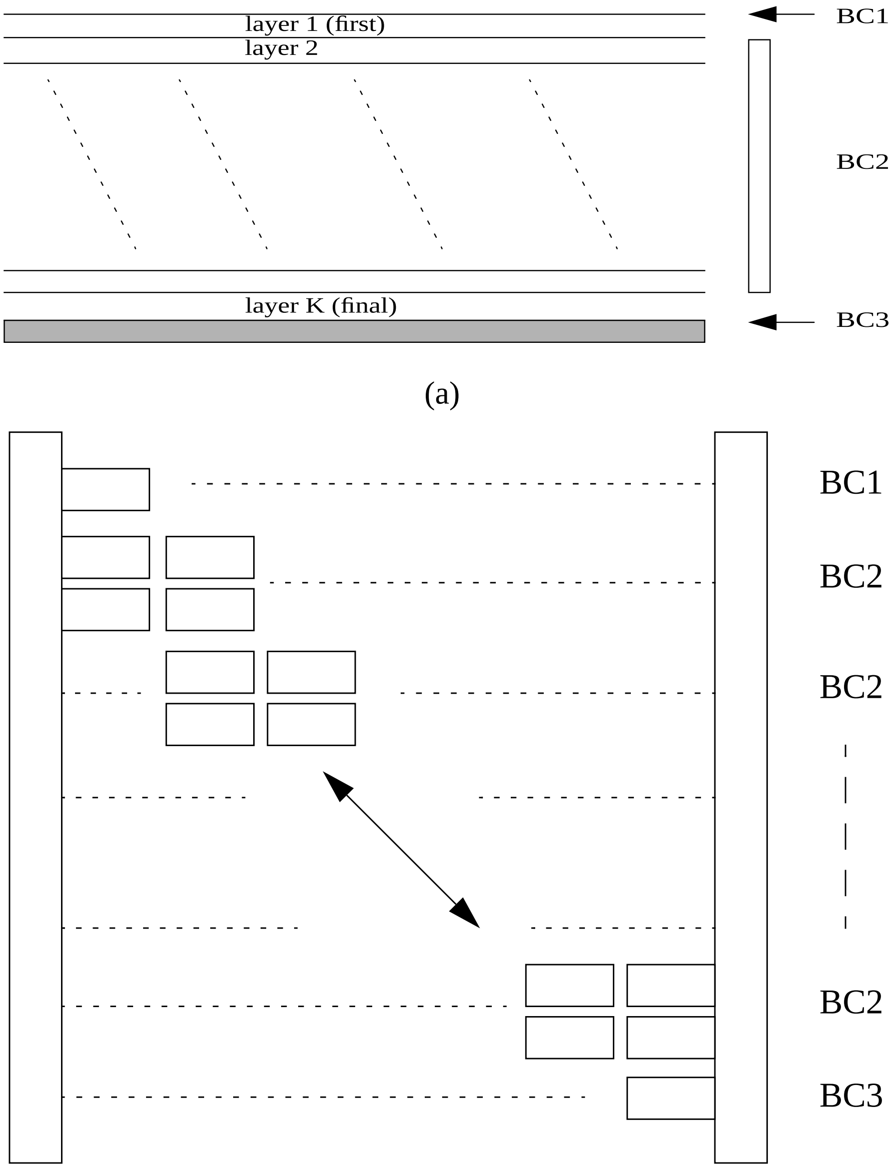

(a)

(b)

Figure 2.1: (a) Boundary conditions for the discrete ordinate solution in a multi-layer atmosphere; (b) schematic matrix structure for the boundary value problem. There are N discrete ordinates in the half-space and K layers in total. In (b), each small block has N rows and $2N$ columns; the complete matrix has $2NK$ columns and $2NK$ rows, with $3N-1$ sub-diagonals and $3N-1$ super-diagonals. All other entries are zero.

and the particular integrals, the *quadrature* components of the diffuse intensity in layer p are given by:

$$I_{jp} = \sum_{\alpha=1}^{N} L_{p\alpha} X^{+}_{jp\alpha} e^{-k_{p\alpha}\left(\tau-\tau_{p-1}\right)} + M_{p\alpha} X^{-}_{jp\alpha} e^{-k_{p\alpha}\left(\tau_{p}-\tau\right)} + J_{jp}, \tag{2.30}$$

where

$$J_{jp} = W_{jp} \exp(-\tau/\mu_0) + \delta_{m0} \sum_{s=0}^{S} T_{jp,s} \tau^{s}. \tag{2.31}$$

Suitable boundary conditions will enable the integration constants $L_{p\alpha}$ and $M_{p\alpha}$ to be determined. Here we have used the scaling transformation suggested by Stamnes and Conklin [56] and used in DISORT [58] to ensure that the exponential factors remain bounded and the discrete ordinate solution numerically stable. The boundary conditions are (see Figure 2.1a):

(BC1) no downward diffuse radiation at the top of atmosphere;
(BC2) continuity of the intensity field at all intermediate levels;
(BC3) a surface reflection condition at the lowest level.

In terms of the discrete ordinate solutions (2.30), these conditions may be written respectively as

$$I_{-jp}(\tau_0) = 0, \text{ for } j = 1, \ldots N \text{ and } p = 1, \tag{2.32a}$$

$$I_{jr}(\tau_r) = I_{jp}(\tau_r), \text{ for } j = \pm 1, \ldots \pm N \text{ and } 1 < p \leqslant K, r = p-1, \tag{2.32b}$$

$$I_{jK}(\tau_K) = (1+\delta_{m0})\, R \sum_{i=1}^{N} a_i \mu_i \rho^{*}_{m}(\mu_j, -\mu_i) I_{-iK}(\tau_K) + I^{*}(\mu_j), \text{ for } j = 1, \ldots N. \tag{2.32c}$$

Here, $I^{*}(\mu_j)$ in (2.32c) comprises a surface emission term and a reflection of the direct beam:

$$I^{*}(\mu_j) = \delta_{m0} \kappa(\mu_j) B(T_g) + \frac{F_{\odot}\mu_0}{\pi} e^{-\tau_K/\mu_0} R \rho^{*}_{m}(\mu_j, -\mu_0). \tag{2.33}$$

Setting transmittances $\Theta_{p\alpha} = \exp\left(-k_{p\alpha}\Delta_p\right)$, for $p = 1, \ldots K, \alpha = 1, \ldots N$, where $\Delta_p = \left(\tau_p - \tau_{p-1}\right)$ is the optical thickness of layer p, we substitute the discrete ordinate solutions (2.30) into the boundary conditions (2.32a)-(2.32c) to arrive at the following set of equations which define the linear algebra system for the solution of the boundary value problem:

$$\sum_{\alpha=1}^{N} \left\{ L_{p\alpha} X^{+}_{-jp\alpha} + M_{p\alpha} \Theta_{p\alpha} X^{-}_{-jp\alpha} \right\} = -J_{-jp}\big|_{\tau_0}; \tag{2.34a}$$

$$\sum_{\alpha=1}^{N} \left[\left\{ L_{r\alpha} \Theta_{r\alpha} X^{+}_{jr\alpha} + M_{r\alpha} X^{-}_{jr\alpha} \right\} - \left\{ L_{p\alpha} X^{+}_{jp\alpha} + M_{p\alpha} \Theta_{p\alpha} X^{-}_{jp\alpha} \right\} \right] = \left(J_{jp} - J_{jr}\right)\big|_{\tau_r}; \tag{2.34b}$$

$$\sum_{\alpha=1}^{N} \left\{ L_{p\alpha} \Theta_{p\alpha} \Phi^{+}_{j\alpha} + M_{p\alpha} \Phi^{-}_{j\alpha} \right\} = I^{*}(\mu_j) - \Psi_j\big|_{\tau_K}. \tag{2.34c}$$

Equation (2.34a) is BC1 for $p = 1$ and $j = 1, \ldots N$; (2.34b) is BC2 for $p = 2, \ldots N$, $r = p-1$ and $j = \pm 1, \ldots \pm N$; and (2.34c) is BC3 for $p = K$ and $j = 1, \ldots N$. J_{jp} are the particular integrals evaluated at the optical depths indicated. We have the following two auxiliary equations for the BC3 condition:

$$\Phi^{\pm}_{j\alpha} = X^{\pm}_{jK\alpha} - (1+\delta_{m0})\, R \sum_{i=1}^{N} a_i \mu_i \rho^*_m(\mu_j, -\mu_i) X^{\pm}_{-iK\alpha}; \tag{2.35a}$$

$$\Psi_j = J_{jK}\big|_{\tau_K} - (1+\delta_{m0})\, R \sum_{i=1}^{N} a_i \mu_i \rho^*_m(\mu_j, -\mu_i)\; J_{-iK}\big|_{\tau_K}. \tag{2.35b}$$

Equations (2.34a)–(2.34c) may be written in the matrix form $AX = B$, and solved simultaneously for the vector X of unknowns. The structure of the matrix A is shown in Figure 2.1b; the order of this linear system is $2NK$. The matrix A has $3N-1$ sub- and super-diagonals; once it is compressed into band-storage form, a standard LU-decomposition linear matrix algebra package can be used to find the solution efficiently. To this end, the double precision driver modules DGBTRF and DGBTRS from LAPACK [65] were used. DBGTRF executes the LU-factorization of A and is called once. DGBTRS finds the solution X by back-substitution and can be called repeatedly for different vectors B. In particular, it will be seen in Section 2.3 that the weighting funtion problem reduces in essence to the creation of a series of vectors B_c which depend on the parameter c being varied; the matrix A is unchanged.

The above procedure gives the intensity field at the *quadrature* streams for *any* optical depth in the atmosphere, and for a single Fourier component. For the satellite application, the upwelling TOA intensity field may be found by substituting $\tau = 0$ for $p = 1$ and $j = 1, \ldots N$ in (2.30).

For the intensity at arbitrary μ, we use the source function integration technique (also known as “post-processing”) which was first developed by Chandrasekhar [46], and is now standard practice in discrete ordinate theory. It has been shown (see for example [34]) that in addition to preserving continuity at off-quadrature stream cosines, this method is superior to numerical interpolation over the quadrature solutions. Here we confine our attention to upwelling TOA intensity.

The procedure relies on the formal integration of Equation (2.5). In an inhomogeneous atmosphere, source terms must be integrated on a layer by layer basis. We adopt the recurrence relation

$$I_{p-1}(\mu) = I_p(\mu)\gamma_p(\mu) + \Lambda_p(\mu) \tag{2.36}$$

for the upwelling intensity $I_{p-1}(\mu)$ at the top of layer p. The layer transmittance factor is defined to be $\gamma_p(\mu) = \exp(-\Delta_p/\mu)$ where $\Delta_p = \tau_p - \tau_{p-1}$, and the *integrated layer source term* Λ_p is defined by

$$\Lambda_p(\mu) = \int_{\tau_{p-1}}^{\tau_p} \frac{d\tau}{\mu} J_p(\tau,\mu) e^{-\left(\tau-\tau_{p-1}\right)/\mu}. \tag{2.37}$$

The recurrence is valid for $p = K$ to $p = 1$. The starting value is the bottom-of-the-atmosphere source term $I_K(\tau_K, \mu)$, and the desired TOA result is $I_0(\mu)$. In (2.37), the term $J_p(\tau, \mu)$ in the integrand is approximated by its discrete ordinate form:

$$J_p(\tau,\mu) \simeq \frac{F_\odot}{2\pi}(2-\delta_{m0})\, D(\mu,-\mu_0)\; e^{-\tau/\mu} + \sum_j a_j D(\mu,\mu_j) I_p(\tau,\mu_j), \tag{2.38}$$

where the $D(\mu, \mu_j)$ and $D(\mu, -\mu_0)$ terms are defined as before, but with the arbitrary stream cosine μ replacing the quadrature values μ_i. One can then perform the optical depth integrations explicitly and write down closed-form expressions for the layer source terms and the recursion starter $I_K(\tau_K, \mu)$. For the details of these calculations, refer to Appendix 2.6.3.

This completes the solution for a single Fourier component; to generate the intensity field at arbitrary azimuth angles, we sum these components according to Equation (2.9). Although it is possible to compute all Fourier terms ($2N-1$ harmonics require at least N half-space quadratures), it is usual to terminate the azimuth series when the addition of an extra harmonic does not alter the overall intensity by more than a pre-specified relative amount υ (a typical value is $\upsilon = 0.005$). This convergence test must be satisfied for each output stream. Furthermore, it makes sense to apply this convergence test to at least two successive azimuth contributions to avoid accidental omissions (the Rayleigh scatter intensity contribution for $m = 2$ is greater than that for $m = 1$ for example). This procedure is adopted in the present work, in line with the policy of DISORT [58] and GOMETRAN [40] regarding series convergence.

2.3. Perturbation analysis of the discrete ordinate solution

2.3.1. Rules for the layer perturbation analysis

For a multi-layer atmosphere, we wish to determine the sensitivity of the discrete ordinate solution to a variation in a single atmospheric variable x_q defined in layer q. A perturbation in x_q will induce changes in the main optical inputs for the layer, namely the single-scatter albedo ω_q and the layer optical thickness Δ_q. We suppose that x_q changes by a relative amount ε, and that to first order in ε, this induces a *relative* change of $u_q\varepsilon$ in ω_q, and an *absolute* change of $v_q\varepsilon$ in Δ_q. The variation x_q in layer q does not affect single-scatter albedos in other layers. However, the optical depth value at the bottom of the layer q has increased by v_q; for all layers below q, the optical depth values are increased by the same amount. The quantities u_q and v_q depend on the constitution and physical properties of the atmosphere. Since the discrete ordinate method is a generic *scattering formalism*, it is not necessary to know this dependence in the perturbation analysis that follows. Using primes to denote first-order perturbed values, we write:

$$x'_q = x_q(1+\varepsilon); \tag{2.39a}$$

$$\omega'_p = \begin{cases} \omega_q\left(1+u_q\varepsilon\right), & \text{for } p = q, \\ \omega_p, & \text{otherwise}; \end{cases} \tag{2.39b}$$

$$\tau'_p = \begin{cases} \tau_p + v_q\varepsilon, & \text{for } p \geqslant q, \\ \tau_p, & \text{for } p < q. \end{cases} \tag{2.39c}$$

To include sensitivity to the thermal emission source term, we suppose that the variable x_q induces an absolute change h_{qs} in each of the Planck function coefficients b_{qs} in Equation (2.13); coefficients for layers other than q are not affected. Thus

$$b'_{ps} = \begin{cases} b_{ps} + \varepsilon h_{ps}, & \text{for } p = q,\ s = 0, \ldots S; \\ b_{ps}, & \text{otherwise}. \end{cases} \tag{2.39d}$$

These are the *perturbation analysis rules*. The variational quantities u_q, v_q and h_{qs} are inputs to the model; the examples in Section 2.4 will illustrate the construction of these inputs for two test-case atmospheres. It should be noted that the above rules apply only to plane-parallel atmospheres; for a curved-atmosphere treatment of the direct beam attenuation (the "pseudo-spherical" model), the rules governing the optical depth variation v_q are quite different (R. Spurr, paper in preparation).

2.3.2. Perturbation analysis of the discrete ordinate component solutions

Now we examine the discrete ordinate solution given by (2.30) and (2.31). For layer q, the beam source particular solution vector W_{jq} and the eigenvalues $k_{q\alpha}$ and solution vectors $X_{jq\alpha}$ of the homogeneous equation depend only on the single-scatter albedo ω_q for that layer. In fact, all three of these quantities are directly proportional to ω_q, and it follows from (2.39b) that changes in these quantities are directly proportional to $u_q\varepsilon$. The first-order perturbed values of k, X and W are thus defined as:

$$k'_{q\alpha} = k_{q\alpha} + u_q\varepsilon f_{q\alpha}; \tag{2.40a}$$

$$X'_{jq\alpha} = X_{jq\alpha} + u_q\varepsilon Y_{jq\alpha}; \tag{2.40b}$$

$$W'_{q\alpha} = W_{q\alpha} + u_q\varepsilon Z_{q\alpha}. \tag{2.40c}$$

The thermal emission particular solution vector T_{jqs} depends both on ω_q and on the expansion coefficients b_{qs}. For this term the first order perturbed value is defined to be:

$$T'_{jqs} = T_{jqs} + \varepsilon V_{jqs}. \tag{2.40d}$$

In these definitions, $j = \pm 1, \ldots \pm N$ labels the quadrature streams, $\alpha = 1, \ldots N$ labels the eigensolutions, and $s = 0, \ldots S$ labels the thermal expansion coefficients. These definitions apply only to the RTE solutions in layer q; for other layers, unperturbed values of the homogeneous solution and particular integrals may be used.

The first task of the perturbation analysis is to establish the quantities f, Y, Z and V defined in Equations (2.40a)–(2.40d). To derive f and Y, it is necessary to construct a perturbed form of the eigenproblem (2.22) based on the single-scatter albedo variation u_q; the normalization condition (2.26) provides an additional constraint. First-order theory reduces the calculation to a linear algebra system of order $N+1$. The details of this calculation can be found in Appendix 2.6.1. Perturbation analysis for the particular integral factors Z and V is more straightforward, since the *original* (unperturbed) solution vectors W and T were determined through linear matrix algebra; the details are also given in Appendix 2.6.1.

Assuming these component factors have been determined, we move on to the second stage of the analysis.

2.3.3. Perturbation analysis of the boundary value problem

This is the most important step of the analysis. We require perturbed values of the constants of integration, which we define as follows:

$$L'_{p\alpha} = L_{p\alpha} + \varepsilon N_{p\alpha}, \tag{2.41a}$$

$$M'_{p\alpha} = M_{p\alpha} + \varepsilon P_{p\alpha}. \tag{2.41b}$$

These definitions are valid for all layers $p = 1, \ldots K$ and for $\alpha = 1, \ldots N$. The task of this section is to determine the factors $N_{p\alpha}$ and $P_{p\alpha}$.

We can write down expressions for the perturbed intensity field I'_{jp}, making a distinction between layer q in which varying atmospheric property x_q induces changes in both single-scatter albedo and optical depth, layers $p < q$ for which there is no change in optical depth, and layers $p > q$, for which only the optical depths are altered. Specifically:

$$I'_{jp} = W'_{jp} e^{-\tau/\mu_0} + \sum_{\alpha=1}^{N} L'_{p\alpha} X'^{+}_{jp\alpha} e^{-k'_{p\alpha}(\tau-\tau_r)} + M'_{p\alpha} X'^{-}_{jp\alpha} e^{-k'_{p\alpha}\left(\tau'_p-\tau\right)}, \text{for } p = q, \tag{2.42a}$$

$$I'_{jp} = W_{jp} e^{-\tau/\mu_0} + \sum_{\alpha=1}^{N} L'_{p\alpha} X^{+}_{jp\alpha} e^{-k_{p\alpha}(\tau-\tau_r)} + M'_{p\alpha} X^{-}_{jp\alpha} e^{-k_{p\alpha}\left(\tau_p-\tau\right)}, \text{for } p < q, \tag{2.42b}$$

$$I'_{jp} = W_{jp} e^{-\tau/\mu_0} + \sum_{\alpha=1}^{N} L'_{p\alpha} X^{+}_{jp\alpha} e^{-k_{p\alpha}(\tau-\tau'_r)} + M'_{p\alpha} X^{-}_{jp\alpha} e^{-k'_{p\alpha}\left(\tau'_p-\tau\right)}, \text{for } p > q. \tag{2.42c}$$

Only the beam source term has been included in the above (this is purely for convenience of exposition). In these definitions, $\tau'_p = \tau_p + \varepsilon v_q$ for $p \geqslant q$, $r = p - 1$, and the argument τ is regarded as a dummy variable.

The key point is that the *same boundary conditions hold for the perturbed field* as those applied to the original field. There are three cases to be distinguished and eight separate conditions; these are illustrated in Figure 2.2, and summarized below with reference to the set of equations (2.42a)–(2.42c). The general situation involves variation in a layer q that is somewhere in the middle of the atmosphere (Case 1, BCL1 to BCL6). For $q = 1$, we have Case 2 with modified TOA condition BCL3M followed by BCL4 to BCL6. For Case 3, $q = K$ (bottom layer), and we require BCL1 to BCL3 followed by a modified lower boundary condition BCL4M. The eight conditions are:

(BCL1) No downward diffuse radiation for $p = 1$ at $\tau = \tau_0$;
$\Longrightarrow$ Set Equation (2.42b) to zero for downwelling streams;

(BCL2) Continuity at level $\tau = \tau_{p-1}$, for $1 < p < q$.
$\Longrightarrow$ Equate two expressions of type (2.42b) at this level, for all streams;

(BCL3) Continuity at upper boundary $\tau = \tau_{q-1}$ of layer q.
$\Longrightarrow$ Equate (2.42a) and (2.42b) at this level, for all streams;

(BCL4) Continuity at lower boundary $\tau = \tau_q$ of layer q.
$\Longrightarrow$ Equate (2.42a) and (2.42c) at this level, for all streams;

(BCL5) Continuity at level $\tau = \tau_p$, for $q < p < K$.
$\Longrightarrow$ Equate two expressions of type (2.42c) at this level, for all streams;

(BCL6) Surface boundary condition for $p = K$ at $\tau = \tau_K$.
$\Longrightarrow$ Construct condition from expressions of type (2.42c) at this level;

(BCL3M) No downward diffuse radiation for $q = 1$ at $\tau = \tau_0$.
$\Longrightarrow$ Set Equation (2.42a) to zero for downwelling streams;

(BCL4M) Surface boundary condition for $q = K$ at $\tau = \tau_K$.
$\Longrightarrow$ Construct condition from expressions of type (2.42a) at this level.

Explicit analytic expressions for these eight boundary conditions can be found in Appendix 2.6.2. It is seen that the boundary value solution for $N_{p\alpha}$ and $P_{p\alpha}$ has the *same form* as that used in Section 2.2.3 for constants $L_{p\alpha}$ and $M_{p\alpha}$. Recalling the linear system $AX = B$ defined by conditions BC1, BC2 and BC3 for the original field, we now have a similar system $AX^* = B^*$ for the perturbed boundary conditions. Here, the column vector B^* depends uniquely through u_q and v_q on the atmospheric parameter x_q that is being varied, and of course on the layer q in which the variation occurs. Since the matrix A has been established and its LU-decomposition already performed for the unperturbed boundary value

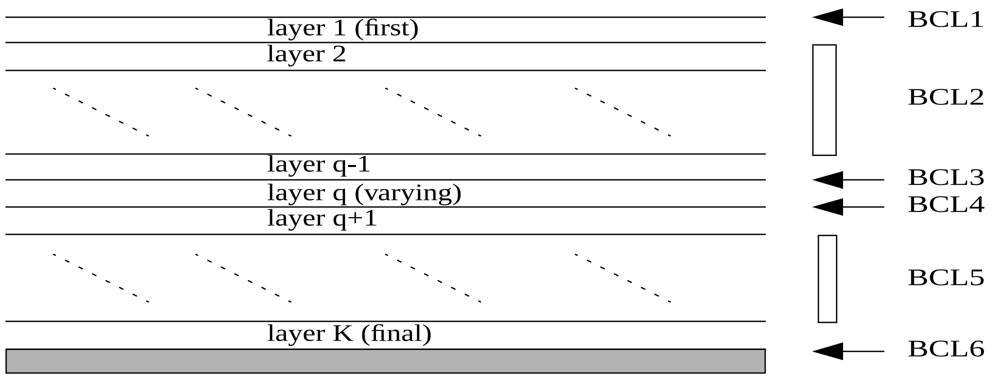

Case 1: 1 < q < K (v arying layer in middle of atmosphere)

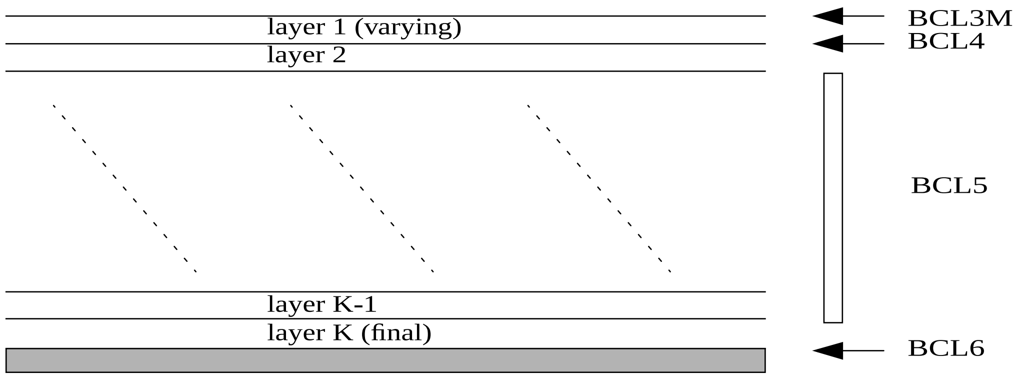

Case 2: q = 1 (v arying layer at top of atmosphere)

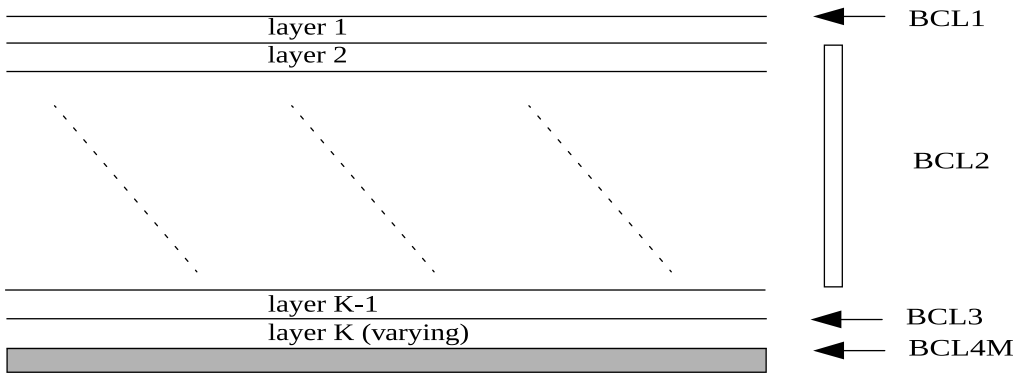

Case 3: q = K (v arying layer at bottom of atmosphere)

Figure 2.2: Boundary conditions for the perturbed discrete ordinate solution in a multilayer atmosphere.

problem, it follows that solutions X^* may be found by straightforward back-substitution using the LU-factorized form of A. Thus the determination of the perturbed integration constants is equivalent to the construction of a series of column vectors B^* for each parameter to be varied. These column vectors may be constructed from the detailed expressions listed in Appendix 2.6.2.

2.3.4. Layer weighting function computation

We now have all the ingredients in place for an explicit derivation of the complete discrete ordinate solution for the perturbed field corresponding to a variation x_q in layer q. The *normalized weighting function components* for the quadrature streams μ_j are found by relaxing the first-order perturbation:

$$K_{jp}(x_q) = x_q \frac{\partial I_{jp}}{\partial x_q} = \lim_{\varepsilon \to 0} \frac{I'_{jp} - I_{jp}}{\varepsilon}. \tag{2.43}$$

This definition is quite general and weighting functions for the quadrature streams can be computed at any optical depth. For the TOA upwelling values, set $p = 1$ and $\tau = 0$. To determine the perturbed field (and hence the weighting functions) at TOA for arbitrary zenith angles μ, we must carry out a post-processing evaluation of the perturbed field. We may write down a perturbed version of the recursion relation (2.36)

$$I'_{p-1}(\mu) = I'_p(\mu)\gamma'_p(\mu) + \Lambda'_p(\mu). \tag{2.44}$$

Note that $\gamma'_q(\mu) = \gamma_q(\mu)\left(1 - v_q\varepsilon/\mu\right)$, and $\gamma'_p(\mu) = \gamma_p$ since only layer q contributes to the variation of optical thickness Δ_q. To determine $\Lambda'_p(\mu)$, we go back to the original expressions derived in Appendix 2.6.3 using the source function integration method, and apply the perturbations explicitly using the quantities derived in sections 2.3.2 and 2.3.3 for the perturbed discrete ordinate solution. This is a relatively involved exercise, and care must be taken to distinguish between the layer q containing the varying parameter x_q and all other layers. We also require the perturbed bottom-of-the-atmosphere source term $I'_K(\mu)$ that starts the recursion (2.44). Details of these calculations may be found in Appendix 2.6.3. As in (2.43) above, the TOA weighting function is determined by relaxing the perturbation ε.

The perturbation analysis described above applies to a single Fourier component (harmonic) of the intensity. The azimuth cosine expansion Equation (2.9) applies equally to the weighting functions defined in (2.43) and (2.44), namely:

$$K_{jp}\left(x, \phi_0 - \phi\right) = \sum_{m=0}^{2N-1} K^m_{jp}(x)\cos m\left(\phi_0 - \phi\right), \tag{2.45}$$

where x is the parameter undergoing variation. In this work, a separate convergence test is not applied to the series in Equation (2.45); we continue to rely on the convergence criterion applied to the unperturbed intensity field.

2.3.5. Albedo weighting functions

To derive an albedo weighting function, a relative perturbation is applied to the albedo: $R' = R(1+\varepsilon)$. This perturbation does not affect layer optical depths and single-scatter albedos so we can use the original homogeneous solutions and particular integrals in all layers. We then have only to solve for the perturbed integration constants $N_{p\alpha}(R)$ and $P_{p\alpha}(R)$ relevant to this problem. The surface boundary condition will require special consideration for an albedo variation (call this condition BCL6R), but for the other levels BCL1 and BCL2 as described in section 2.3.3 will apply. Once again, the determination of the perturbed-field integration constants will emerge from the solution of the linear system $AX^* = B^*$, where the column vector $B^*(R)$ now depends uniquely on the albedo perturbation. The derivation of BCL6R and the associated vector $B^*(R)$ are given in Appendix 2.6.2.

The TOA albedo weighting function is given at the quadrature streams by

$$K_{jp}(R) = R\frac{\partial I_{jp}}{\partial R} = \lim_{\varepsilon\to 0}\frac{I'_{jp} - I_{jp}}{\varepsilon}, \text{ for } p = 1 \text{ and } \tau = 0. \tag{2.46}$$

The post-processed albedo weighting function is easy to establish. Since there is no layer variation, we can use the recursion relation (2.36) and the source function terms (2.37) for the original solution, together with a new bottom of the atmosphere source function which reflects the albedo variation. Details can be found in Appendix 2.6.3.

Surface emission plays no part in the perturbation analysis for weighting functions with respect to layer parameters that may vary. However, since the surface emissivity depends on the albedo R, its variation must be included when dealing with albedo weighting functions. This consideration applies only to the fundamental Fourier harmonic $m = 0$. If $R' = R(1+\varepsilon)$ is the albedo perturbation, then from the definition in Equation (2.21), the perturbed emissivity is found to be

$$\kappa'(\mu) = \kappa(\mu) + (\kappa(\mu) - 1)\,\varepsilon. \tag{2.47}$$

This is true for all values of μ, not just the quadrature streams. Equation (2.47) is required in the determination of the perturbed boundary condition BCL6R in the presence of surface emission.

2.4. The LIDORT model; two weighting function examples

Before discussing the two examples of LIDORT results in sections 2.4.4 and 2.4.5, we summarize the LIDORT package and remark on two practical aspects, the first regarding atmospheric inputs for more than one scatterer, and the second the issue of weighting function verification.

2.4.1. Implementation of the LIDORT package

The numerical model LIDORT aversion 1.1 is based on the theory of the previous two sections. Intensity and weighting function output is determined for the positive (upwelling) direction at TOA ($\tau = 0$), for arbitrary angular direction (μ,ϕ). and for a plane-parallel medium. The number of terms in the Fourier series required for convergence depends on the azimuth angle and the degree of the discrete ordinate approximation. Double precision arithmetic is used throughout LIDORT; the code is written in FORTRAN 77. For the numerical tools, we used module ASYMTX for the homogeneous solution eigenproblem (extracted from DISORT), and LAPACK modules [65] for all linear matrix algebra systems. The model contains a standardized error handling procedure in addition to a number of auxiliary routines for both the reading of input data from files, and the generation of result data to file.

LIDORT has been designed as a generic tool to be used in a wide variety of retrieval applications. It is a pure scattering formalism; the detailed physics required to set up the optical inputs for any given application must be supplied by the user. The “atmospheric preparation” interface for LIDORT is one of the most important aspects, and we discuss this in detail for the two examples below. There are no databases or climatologies of atmospheric and optical properties in the model. The LIDORT package is called as a subroutine within a user-defined environment; the usage is similar to that for DISORT citestammes:88.

In order to make the model portable and robust, it is necessary to develop a clearly-interfaced and well-documented software package that will help the user to find the right application. The LIDORT User's Guide has a description of the complete package, with detailed notes on the input variables required to run the model, a discussion with examples on the construction of a typical environment for the model and an interface to set up the appropriate geophysical inputs. The User's Guide also contains instructions on installation and execution. A test data set has been prepared for release; this is based closely on the example described in detail in Section 2.4.5. The LIDORT source code and User's Guide may be downloaded from the SAO web site (http://cfa-www.harvard.edu/lidort/).

2.4.2. Treatment with several types of scatterers

In most practical applications, there are often two or more scatterers present (for example in terrestrial atmospheres). Although the theory of Sections 2.2 and 2.3 was presented for a single scatterer, it is straightforward to extend the equations to deal with two or more particulates. For an intensity-only calculation, we can define a *combined* single-scatter albedo ω_q and phase function moments β_{lq} for layer q:

$$\omega_q = \sum_d \omega_{qd} \quad \text{and} \quad \beta_{lq} = \sum_d \frac{\beta_{lqd}\omega_{qd}}{\omega_q}. \tag{2.48}$$

where d is an index for the scatterers and l for the phase function moment. One can then apply the discrete ordinate formalism using the quantities defined in (2.48); the combination $\omega_q\beta_{lq}$ appears in the Legendre polynomial sums (2.14). (DISORT [58] also uses this kind of input). For the weighting functions, we suppose that atmospheric parameter x_q is varying in layer q, inducing variational changes u_{qxd} in the individual single-scatter albedos ω_{qd}. Using the above combination, we can define a perturbed form $(\omega_q\beta_{lq})' = \omega_q\beta_{lq}\left(1+u_{qlx}\varepsilon\right)$. The combined variational input u_{qlx} is then given by

$$u_{qlx} = \frac{1}{\omega_q\beta_{lq}} \sum_d \beta_{lqd}\omega_{qd}u_{qxd}. \tag{2.49}$$

One can then proceed with the perturbation theory as described in Section 2.3. These considerations do not apply to the optical depth variation. In the examples below, we will illustrate the generation of input quantities ω_{qd} and u_{qxd}.

2.4.3. Weighting function verification

All weighting function output may be checked against finite-difference equivalents calculated using independent intensity-only calls to the model for externally perturbed atmospheric conditions. To obtain a "finite-difference" weighting function $K_{FD}(x_q)$ with respect to atmospheric parameter x_q in layer q, we apply small relative *external* perturbations $\pm\varepsilon_{FD}$ to x_q. The layer input to the model is reconfigured by using $x_q^+ = x_q(1+\varepsilon_{FD})$ instead of x_q in layer q, and leaving all other inputs unchanged. The perturbation will change the single-scatter albedo in layer q and the optical depth grid for all levels below and including q. The resulting TOA intensity is denoted $I(x_q^+)$. The simulation is repeated with $x_q^- = x_q(1-\varepsilon_{FD})$ for the perturbed variable, with the result $I(x_q^-)$. The finite difference approximation to the weighting function is

$$K_{FD}(x_q) \simeq \frac{I(x_q^+) - I(x_q^-)}{2\varepsilon_{FD}}. \tag{2.50}$$

Although the double quadrature scheme is usual, some extra runs were also carried out using the single scheme over the interval $(1,-1)$. For this latter scheme, we have the additional closed-form expressions for the homogeneous and particular solutions developed in the original work by Chandrasekhar; as noted in Appendix 2.6.4, these require an initial determination of the roots of the characteristic equation. It is also shown in this appendix that closed-form expressions for the perturbed values of these component solutions can be derived. These alternative expressions allow us to make an independent check on weighting function solutions derived using the usual "eigenproblem-and-linear-algebra" approach to the RTE solution. (The characteristic equation was solved using standard eigenvalue modules from Numerical Recipes [67]; this involves considerably less work than solving the complete eigenproblem).

2.4.4. LIDORT test for a 5-layer medium with two types of scatterers

The first example described here is for a 5-layer atmosphere (5 layers is sufficient to test all eight of the perturbed boundary conditions in Section 2.3.3). This example will illustrate the generation of variational inputs u_q and v_q controlling weighting function output. This scenario also provides a shakedown test for the model.

First consider a single homogeneous layer with absorption and scattering coefficients α and σ (per unit depth), and altitude thickness z. The single-scatter albedo is $\omega = \sigma/(\alpha+\sigma)$, and the optical depth is $\tau = z(\alpha+\sigma)$. If we perturb the absorption coefficient α by a relative amount ε, then $\alpha' = \alpha(1+\varepsilon)$,

$$\omega' = \omega\left(1+u_a\varepsilon\right), \text{ where } u_a = -\alpha/(\alpha+\sigma), \quad \text{and} \tag{2.51a}$$

$$\tau' = \tau + v_a\varepsilon, \qquad \text{where } v_a = \alpha z. \tag{2.51b}$$

Similarly if the scattering coefficient σ is perturbed by a relative amount ε, so that $\sigma' = \sigma(1+\varepsilon)$, then

$$\omega' = \omega\left(1+u_s\varepsilon\right), \text{ where } u_s = \alpha/(\alpha+\sigma), \quad \text{and} \tag{2.52a}$$

$$\tau' = \tau + v_s\varepsilon, \qquad \text{where } v_s = \sigma z. \tag{2.52b}$$

Thus for a single layer specified solely by absorption and scattering coefficients, the parameter variations $\{u_a, v_a\}$ and $\{u_s, v_s\}$ must be input to LIDORT in order to obtain weighting functions with respect to these coefficients.

We now extend these arguments to a 5-layer atmosphere with two particulates. Let the absorption and scattering coefficients be α_{qd} and σ_{qd}, with $q = 1,\ldots 5$, indexing the layers, and $d = 1,2$ indexing particulates, along with altitude thickness values z_q. The layer optical thickness values are $\delta_q = e_q z_q$, where the layer extinction is $e_q = \alpha_{q1} + \sigma_{q1} + \alpha_{q2} + \sigma_{q2}$. Single scatter albedos are $\omega_{qd} = \sigma_{qd}/e_q$. The two particulates have layer phase function moments β_{lq1} and β_{lq2}, where $l = 0,\ldots 2N-1$. Phase function moments for this test case can be generated by assuming the Henyey-Greenstein phase envelope (see for example [68]), for which the moments are powers of the asymmetry parameters g_{qd}, that is, $\beta_{lqd} = (g_{qd})^l$. Table 2.1 summarizes all the optical properties used in this example.

In a given layer q, there are four possibilities for the parameter x_q, namely the absorption coefficient of particulate 1, the scattering coefficient of particulate 1, the absorption coefficient of particulate

2, or the scattering coefficient of particulate 2. (In Equation (2.53) below, we keep this ordering). Now let u_{qdx} be the perturbations induced in ω_{qd} by x_q, that is, $\omega'_{qd} = \omega_{qd}(1+\varepsilon u_{qdx})$. Let v_{qx} be the corresponding changes induced in optical thickness values τ_q. By the reasoning used to derive Equations (2.51a,b) and (2.52a,b), we have for this scenario:

$$u_{q1x} = \begin{bmatrix} -\alpha_{q1}/e_q \\ 1-\sigma_{q1}/e_q \\ -\alpha_{q2}/e_q \\ -\sigma_{q2}/e_q \end{bmatrix}, u_{q2x} = \begin{bmatrix} -\alpha_{q1}/e_q \\ -\sigma_{q1}/e_q \\ -\alpha_{q2}/e_q \\ 1-\sigma_{q2}/e_q \end{bmatrix}, \text{ and } v_{qx} = \begin{bmatrix} \alpha_{q1}z_q \\ \sigma_{q1}z_q \\ \alpha_{q2}z_q \\ \sigma_{q2}z_q \end{bmatrix}. \tag{2.53}$$

For each layer, the quantities in (2.53) constitute the required input to the LIDORT model to obtain the desired weighting function output.

Property/Layer	1	2	3	4	5
Absorption coefficient, scatterer 1	0.05	0.17	0.32	0.50	0.35
Absorption coefficient, scatterer 2	0.04	0.18	0.36	0.56	0.37
Scattering coefficient, scatterer 1	0.25	0.25	0.25	0.25	0.25
Scattering coefficient, scatterer 2	0.25	0.26	0.27	0.28	0.29
Layer thickness	0.05	0.05	0.05	0.05	0.05
Cumulative optical depth	0.0295	0.0725	0.1325	0.2120	0.2750
Single scatter albedo, 1	0.42373	0.29070	0.28033	0.15733	0.19841
Single scatter albedo, 2	0.42373	0.30233	0.22500	0.17610	0.23016
Asymmetry parameter, scatterer 1	0.63	0.71	0.69	0.69	0.69
Asymmetry parameter, scatterer 2	0.65	0.70	0.60	0.65	0.65
Thermal emission coefficient b_0	0.2813	0.5684	0.5820	0.5692	-0.7276
Thermal emission coefficient b_1	19.128	9.3951	9.2080	9.3048	15.422

Table 2.1: Setup for 5-layer test of LIDORT

The solar zenith angle cosine μ_0 is taken to be 0.75 and the relative azimuth angle 0°. The surface is assumed Lambertian with albedo $R = 0.3$. Thermal emission is omitted from the first set of results. The RTE is solved using eight discrete ordinate streams in the hemisphere. With four possible parameter variations for each of the five layers, there are 20 layer weighting functions in all. LIDORT will generate the TOA intensity and all 20 weighting functions with a single call from a master module. Generation of this set of weighting functions using the external finite-difference approximation (2.50) would require 40 separate calls to an intensity-only model. In addition to the eight quadrature values, intensity and weighting function output is given at seven user-defined zenith angles, several of which are deliberately chosen close to quadrature values in order to test the accuracy of the post-processing function. With a Fourier azimuth series accuracy criterion of 0.001, seven Fourier terms are required for convergence. All the results in Table 2.2 are direct-beam normalized (that is, the flux factor $F_\odot$ in Equation (2.7) is set to 1).

In this table, DISORT intensity output for the same scenario is presented for comparison; the agreement with the LIDORT values is excellent, with small differences in the last decimal places probably due to the single-precision arithmetic used in DISORT. The last two columns are normalized weighting functions for a variation in layer 3 of the scattering coefficient for particulate 1, calculated first with LIDORT in weighting function mode, and secondly with LIDORT in intensity-only mode calculating finite difference approximations to the weighting functions based on a 2% external perturbation of the scattering coefficient. The results are close, because of the near-linear dependence

Stream angle in °	LIDORT Intensity	DISORT Intensity	σ_{31} Weighting Function	σ_{31} WF by 2% Finite Diff.
88.86231∗	0.105562	0.105592	-1.623333E-03	-1.623342E-03
84.16484∗	0.0661006	0.0661281	-4.062011E-03	-4.062021E-03
76.27667∗	0.0516912	0.0516913	-3.317248E-03	-3.317252E-03
65.90300∗	0.0491804	0.0491682	-2.687362E-03	-2.687364E-03
53.72103∗	0.0490656	0.0490606	-2.313743E-03	-2.313744E-03
40.29133∗	0.0498576	0.0498572	-2.107697E-03	-2.107698E-03
26.06016∗	0.0501983	0.0501983	-1.989064E-03	-1.989065E-03
11.43654∗	0.0504737	0.0504737	-1.932222E-03	-1.932223E-03
88.85	0.105363	0.105393	-1.637481E-03	-1.637491E-03
80.0	0.0557402	0.0557520	-3.682994E-03	-3.683000E-03
76.27	0.0516864	0.0516865	-3.316667E-03	-3.316671E-03
45.0	0.0495563	0.0495551	-2.164834E-03	-2.164835E-03
30.00	0.0500726	0.0500726	-2.013753E-03	-2.013753E-03
11.44	0.0504737	0.0504737	-1.932232E-03	-1.932232E-03
0.0	0.0504358	0.0504359	-1.917111E-03	-1.917111E-03

Table 2.2: LIDORT output for relative azimuth 0°. Quadrature angles are marked with an asterisk.

of the solution on the input optical parameters. Figure 2.3 (top) shows the intensity output (stream angles are marked with an asterisk) from Table 2.2. Note the smooth interpolation to user-defined zenith angles. Figure 2.3 (bottom) are the TOA weighting functions with respect to the absorption and scattering coefficients in layer 3.

Some further runs with this scenario were carried out to test the inclusion of thermal emission source terms. Two thermal expansion coefficients b_{0q} and b_{1q} were computed off-line using the Planck function module in DISORT, for a temperature of 550K (TOA), and 600K, 620K, 640K, 660K, and 680K at the lower boundaries of the succeeding five layers, and for spectral range of 5000 to 5100 wavenumbers. The coefficients b_{0q} and b_{1q} are shown in Table 2.1 in the last two rows (up to a factor of 4π, DISORT takes the same numbers in its computation of the intensity). Using these coefficients enables us to check intensity values against DISORT output. To test the effect of changes in intensity due to thermal emission variations, we assume that any of the optical properties of the atmosphere will induce an identical change in the thermal expansion coefficients. That is, if $\zeta'_q = \zeta_q(1+\varepsilon)$ for property ζ_q, then $b'_{sq} = b_{sq}(1+\varepsilon)$ for each of the thermal expansion coefficients. This means that the perturbation input values defined in Equation (2.39d) are $h_{sq} = b_{sq}$ for $s = 0$ and $s = 1$. This is obviously not a physical situation, but it serves to check that weighting functions with respect to the Plank function coefficients are being correctly calculated. A similar selection of results for this scenario is shown in Figure 2.4.

2.4.5. Ozone VMR and temperature profile weighting functions in a terrestrial atmosphere

For this example, the atmosphere has height 60 km, with a vertical resolution throughout of 1 km. Molecular (Rayleigh) scattering and aerosol scattering are present in all layers. We take O_3 volume mixing ratio (VMR) temperatures and pressures for a "tropical" standard atmosphere [69],

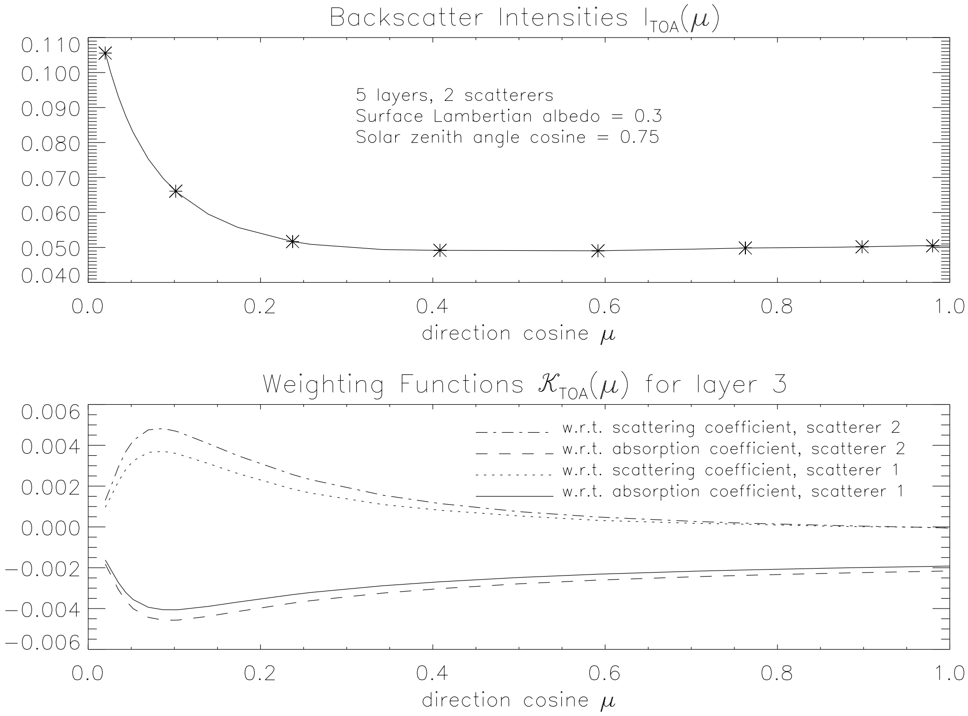

Figure 2.3: Intensity and weighting function output for a 5-layer atmosphere, relative azimuth 0°: (top) intensity (quadrature values marked by asterisk); (bottom) weighting functions for layer 3.

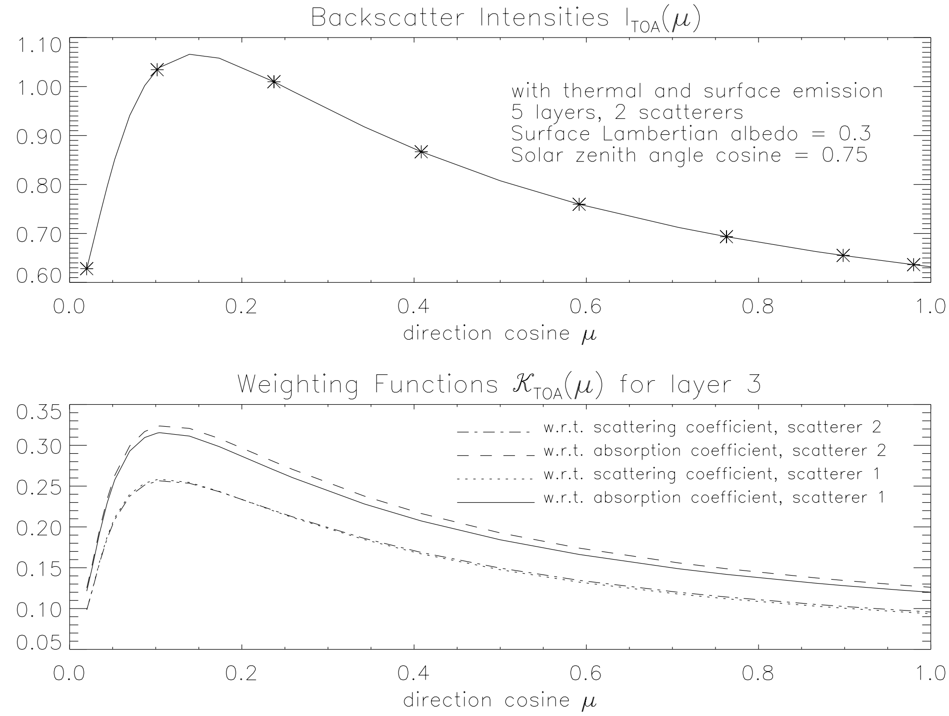

Figure 2.4: Intensity and weighting function output for 5-layer atmosphere, relative azimuth 0°, including thermal and surface emission: (top) intensity (quadrature values marked by asterisk); (bottom) weighting functions for layer 3.

interpolated to the mid-points of each layer. The temperature and ozone VMR profiles are shown in Figure 2.5.

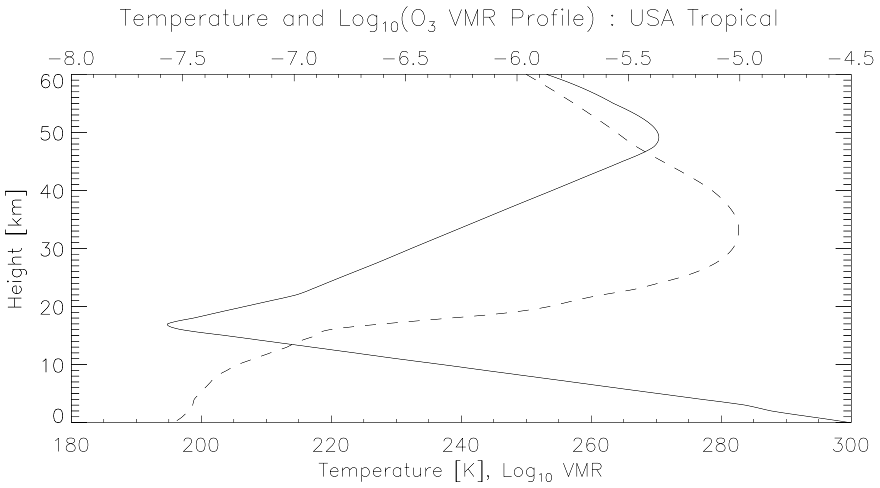

Figure 2.5: Temperature and O_3 volume mixing ratio profiles for 0–60 km; “tropical” atmosphere.

For the first runs, we take a single wavelength of $\lambda = 324.8863$ nm at one of the peaks of the O_3 Huggins absorption bands; cross section values are obtained from a standard data set [70]. These cross sections ξ are temperature-dependent so they must be evaluated for each layer temperature T_q using the quadratic parameterization [70]:

$$\xi_\lambda(T_q) = \xi_{\lambda 0}\left\{1 + \left(T_q - T_0\right)\xi_{\lambda 1} + \left(T_q - T_0\right)^2 \xi_{\lambda 2}\right\}. \tag{2.54}$$

Here, the first coefficient $\xi_{\lambda 0}$ is the value at reference temperature T_0. If the O_3 VMR in layer q is C_q, and the cross-section is $\xi_\lambda(T_q)$, then the molecular absorption coefficient α_{q1} (in [km^{-1}]) is $\alpha_{q1} = C_q \xi_\lambda(T_q)\rho_q$, with the air density ρ_q in [mol cm^{-2} km^{-1}] given by $\rho_q = \left(T_0 P_q / P_0 T_q\right)\rho_0$, where the zero suffix denotes values at standard temperature and pressure (STP).

The Rayleigh scattering cross section at STP is given by:

$$Q_{Ray}(T_0) = \frac{32\pi^3(n-1)^2}{3L^2\lambda^4} \times \frac{6+3\Delta}{6-7\Delta}, \tag{2.55}$$

where Δ is the depolarization ratio, L is Loschmidt’s number, and n is the refractive index of air. Values of Q_{Ray} may be calculated from an empirical formula [18]. Q_{Ray} needs to be multiplied by the layer air density ρ_q to obtain the required scattering coefficient σ_{q1} [km^{-1}]. For the aerosol loading and optical properties, a LOWTRAN model [71] is selected, with maritime-type boundary layer aerosol and background stratospheric and tropospheric optical properties; values from the database are linearly interpolated to wavelength λ. The resulting optical coefficients (in [km^{-1}]) are α_{q2} and σ_{q2}.

The Rayleigh scattering envelope has an $a + b\cos^2\theta$ dependence with respect to scatter angle θ; there are only three terms in the phase function Legendre expansion. The Rayleigh phase function Legendre moments are $\beta_0 = 1$, $\beta_1 = 0$ and $\beta_2 = (1-\Delta)/(2+\Delta)$. The depolarization ratio Δ is wavelength-dependent and may be computed from another empirical formula [18]. For the aerosols we assume Henyey-Greenstein phase functions with asymmetry parameters taken from the appropriate choice of LOWTRAN aerosol loading and interpolated to the wavelength of interest. The solar zenith cosine μ_0 is taken to be 0.75, the relative azimuth 60° and the Lambertian surface albedo 0.75. A 10-stream approximation is used in the RTE solution, with accuracy criterion 0.001. All output is normalized to the incident intensity of the direct beam. There is no thermal or surface emission.

We are interested in weighting functions with respect to the O$_3$ VMR profile distribution C_q. Writing $C'_q = C_q(1+\varepsilon)$ for the perturbation, we find that

$$u_{q1}(C_q) = u_{q2}(C_q) = -\alpha_{q1}/e_q, \tag{2.56a}$$
$$v_{q1}(C_q) = \alpha_{q1} z_q. \tag{2.56b}$$

Here, α_{q1} is the O$_3$ absorption coefficient as defined in (2.54) *et.seq.*, and e_q and z_q the total extinction and height thickness for layer q.

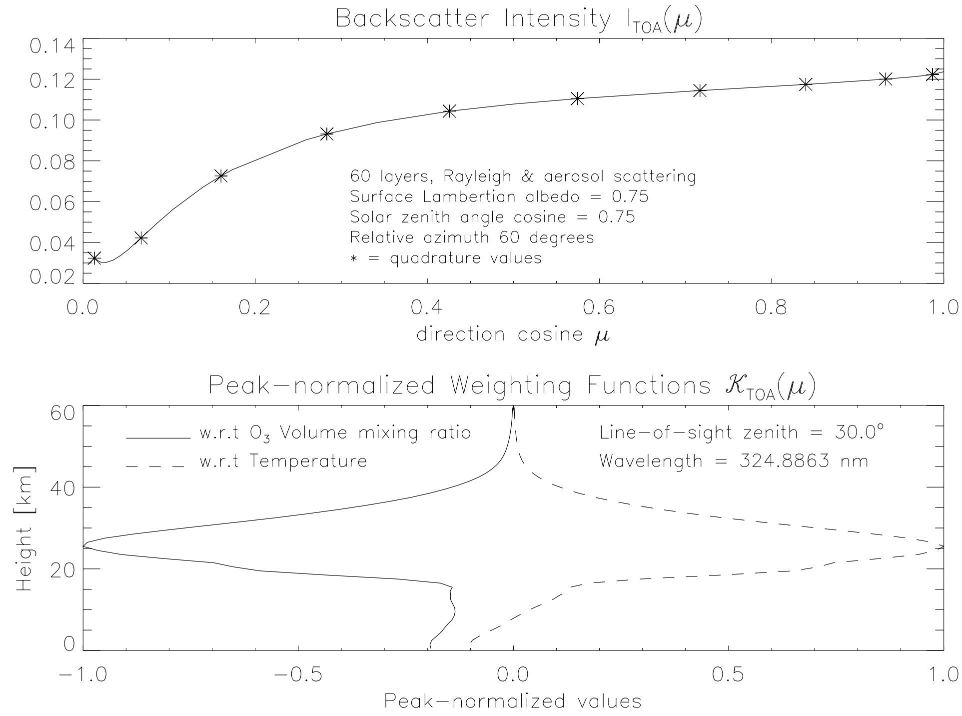

Figure 2.6: LIDORT results for a 60-layer atmosphere for wavelength 324.8863 nm, albedo 0.75, relative azimuth 60°, $\mu_0 = 0.75$; (top) sun-normalized TOA intensity at various zenith angles (quadrature streams marked by an asterisk); (bottom) Peak-normalized weighting functions for O$_3$ VMR and temperature profiles, at zenith angle 30°.

For temperature weighting functions, the functional dependence of the optical properties on temperature is more complex. If the relative variation in temperature T_q in layer q is ε, so that $T'_q = T_q(1+\varepsilon)$, then it follows that $\rho'_q = \rho_q(1-\varepsilon)$ for the air density, and from Equation (2.54) the variation in O$_3$ cross-section is

$$\xi'_\lambda(T_q) \equiv \xi_q + \varepsilon\eta_q = \xi_\lambda(T_q) + \varepsilon T_q \xi_{\lambda 0}\left\{\xi_{\lambda 1} + 2\left(T_q - T_0\right)\xi_{\lambda 2}\right\}. \tag{2.57}$$

Since $Q_{Ray}(T_q) = \rho_q Q_{Ray}(T_0)$, and the STP value $Q_{Ray}(T_0)$ has no dependence on T_q, then the variations for the absorption and scattering coefficients are

$$\alpha'_{q1} = \alpha_{q1}\left[1 - \varepsilon\left(1 - \eta_q/\xi_q\right)\right], \tag{2.58a}$$
$$\sigma'_{q1} = \sigma_{q1}(1-\varepsilon). \tag{2.58b}$$

These in turn lead to the following variational inputs for the layer single-scatter albedos and optical depth required by LIDORT.

$$u_{q1}(T_q) = -\left(1+\psi_q/e_q\right), \quad u_{q2}(T_q) = -\psi_q/e_q, \quad \text{and} \quad v_q(T_q) = z_q\psi_q, \tag{2.59}$$

where

$$\psi_q = \alpha_{q1}\left(\eta_q/\xi_q - 1\right) - \sigma_{q1}. \tag{2.60}$$

Note in particular that the aerosol single-scatter albedo has the non-zero variation $u_{q2}(T_q)$, even though the aerosol coefficients themselves are unaffected by the perturbations.

Figure 2.6 (top) shows the intensity output for this scenario at $\lambda = 324.8863$ nm. Quadrature values are marked by an asterisk to illustrate the smoothness of the post-processing function for user-defined zenith angles. Figure 2.6 (bottom) shows results for a line-of-sight zenith angle of 30° for the O_3 VMR and temperature weighting functions plotted against altitude; values are normalized to the peak values in each case. The sensitivity of both functions around the peak O_3 concentration level is evident.

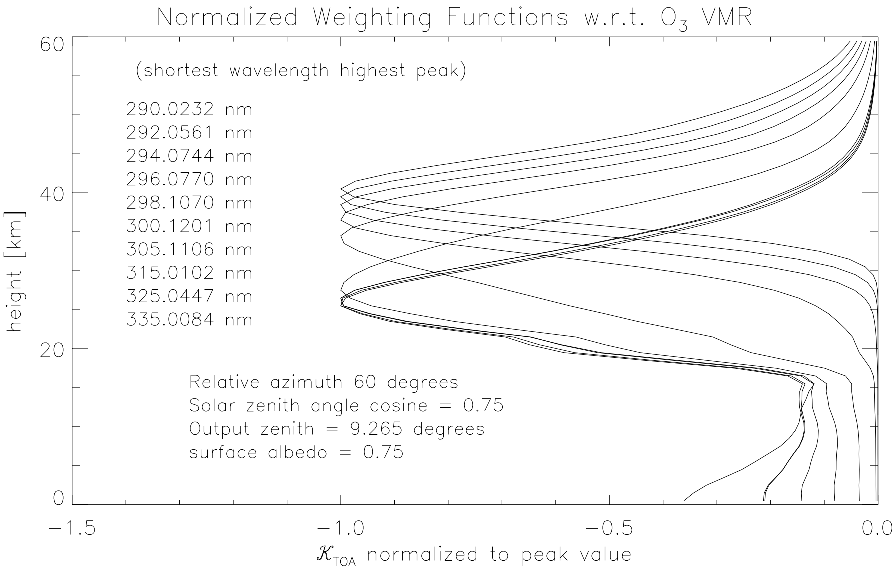

Figure 2.7: LIDORT weighting functions for O_3 VMR for a 60-layer atmosphere for a number of wavelengths in the UV, for zenith angle 9.265°.

In Figure 2.7, O_3 VMR weighting functions are presented for a number of wavelengths in the UV from 290 nm to 335 nm as indicated (these wavelengths are used as found in the data set [70]; their use obviates the need for interpolation of cross section values). Below 300 nm, peak values occur at heights that increase with lower wavelengths. It is this well-known differential scattering height behavior that underpins the BUV technique for O_3 profile retrieval [11, 13]. Note also the increasing tropospheric sensitivity for the longer wavelengths.

Finally a comparison is made with results from the GOMETRAN [43] model computed at $\lambda = 324.8863$ nm for the same atmosphere. GOMETRAN input profiles are given at 61 levels from 0 to 60 km. O_3 cross-sections are given by Equation (2.54) for temperatures at the layer boundaries. Figure 2.8 gives the comparison for O_3 VMR weighting functions at stream angle 9.265° (one of the quadrature values). The agreement between these two independently-calculated results is excellent, with differences of 1% or less at virtually all levels away from the shoulder near 17 km. Here the

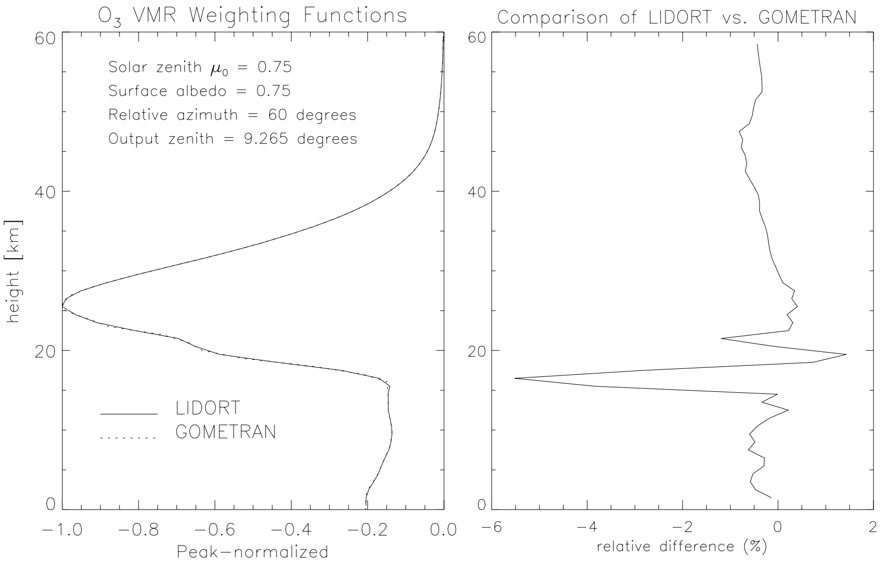

Figure 2.8: LIDORT and GOMETRAN weighting functions for O_3 VMR for a 60-layer (61-level) atmosphere for wavelength 324.8863 nm and for zenith angle 9.265°.

O_3 concentration gradient changes sharply, and the 1 km height resolution of the models is not fine enough to ensure "layer-versus-level" interpolation errors are kept to a minimum.

2.5. Summary and future developments

In this paper we have developed an extension of the discrete ordinate solution of the radiative transfer equation in a plane-parallel, multiply scattering, anisotropic, multilayer atmosphere with beam and thermal emission sources. The extension is essentially an internal perturbation analysis of the discrete ordinate solution, and along with standard intensity output, it allows for the simultaneous calculation of analytically accurate weighting function fields with respect to a wide variety of atmospheric parameters. This extension avoids the time-consuming procedure of using external perturbation calculations to approximate the weighting functions. A numerical model (LIDORT) has been constructed and tested for two scenarios, one of which is a representative terrestrial atmosphere with ozone absorption and molecular and aerosol scattering. The model is generic in character, requiring as the main input the single-scatter albedos and grid optical depths, plus variations induced on these inputs by the set of parameters for which the weighting functions are to be computed. These application-specific inputs are defined by the user, and they depend on the physics of the atmosphere under consideration.

The model described here has recently been extended to cover a much wider range of scenarios; intensity and weighting function output is now available for upwelling and downwelling directions, at arbitrary optical depth and stream angle. A "pseudo-spherical" treatment of the direct beam attenuation has also been implemented in the new version of LIDORT. This gives the model the power to accommodate solar zenith angles up to 90° (c.f. [35]). There is also the option to treat sharply-peaked phase functions using the delta-M scaling approximation [36]. LIDORT Version 2.1 is now available from the SAO website; the new version will be described in a companion paper to the present work (Chapter 3 of this thesis).

The implementation of a vectorized radiative transfer code to give a full Stokes-vector treatment of the perturbed discrete ordinate solution is also under consideration. The intensity-only problem has been analyzed, and there now exists a robust vectorized DISORT [72, 73].

Acknowledgments

This work was supported in part by a contract from the Deutsches Forschunszentrum für Luft und Raumfahrt, contract number 332/60570480 (SCIAMACHY Data Processor Development), and in part with internal funding from the Smithsonian Astrophysical Observatory. Special thanks are due to Knut Stamnes for helpful suggestions regarding the manuscript.

2.6. Appendices

2.6.1. Perturbation analysis for the discrete ordinate component solutions

In this appendix the perturbation factors defined in Equations (2.40a)–d are established. We consider a single layer and Fourier component, omitting the respective indices for the sake of clarity.

Homogeneous solution

Consider first the eigenvalue problem Equation (2.22) and associated definitions in Equation (2.23). The perturbation rule $\omega' = \omega(1+u\varepsilon)$ applies to the single-scatter albedo, and since the eigenmatrix and its eigensolutions are proportional to ω, then they will also perturb in a similar fashion. Define the first-order perturbation for the eigenmatrix Γ in Equation (2.22) as follows:

$$\Gamma'_{ij} = \Gamma_{ij} + u\varepsilon\xi_{ij} = \sum_{l=1}^{N} \left(\zeta'_{il} - \eta'_{il}\right) \left(\zeta'_{lj} + \eta'_{lj}\right). \tag{2.61}$$

Since the $D^{\pm}_{ij}$ in Equation (2.23) depend linearly on ω, their first-order perturbed values are given by $D^{\pm'}_{ij} = D^{\pm}_{ij}(1+u\varepsilon)$. From the definitions of matrices ζ_{ij} and η_{ij}, we obtain

$$\zeta'_{ij} = \zeta_{ij} + u\varepsilon a_j D^{+}_{ij}\mu_i^{-1} \quad \text{and} \quad \eta'_{ij} = \eta_{ij} + u\varepsilon a_j D^{-}_{ij}\mu_i^{-1}. \tag{2.62}$$

Substituting Equations (2.62) in Equation (2.61), we get the following determination of ξ_{ij}:

$$\xi_{ij} = \sum_{l=1}^{N} \left\{ \frac{a_l C^{-}_{il}}{\mu_i} \left(\zeta_{lj} + \eta_{lj}\right) + \left(\zeta_{il} - \eta_{il}\right) \frac{a_j C^{+}_{lj}}{\mu_l} \right\}, \tag{2.63}$$

where $C^{\pm}_{ij} = D^{+}_{ij} \pm D^{-}_{ij}$.

Next, we have the perturbed version of the eigenproblem of Equation (2.22):

$$\sum_{j=1}^{N} \Gamma'_{ij}\varsigma'_{j\alpha} = k'^{2}_{\alpha}\varsigma'_{i\alpha}, \quad \text{for } i = 1,\ldots N,\ \alpha = 1,\ldots N. \tag{2.64}$$

The eigenvalues perturb as $k'_{\alpha} = k_{\alpha} + u\varepsilon f_{\alpha}$. For the eigenvector perturbation, we define $\varsigma'_{j\alpha} = \varsigma_{j\alpha} + u\varepsilon\Upsilon_{j\alpha}$. In order to find scalar f_{α} and vector $\Upsilon_{j\alpha}$ for each α, we use the result of Equation (2.63) in (2.64) and remove the zero-order term using the original eigenvalue (2.22). This gives the following N equations satisfied by the first-order term:

$$\sum_{j=1}^{N}\left(\Gamma_{ij}\Upsilon_{j\alpha}+\xi_{ij}\varsigma_{j\alpha}\right)=k_{\alpha}^{2}\Upsilon_{i\alpha}+2k_{\alpha}f_{\alpha}\varsigma_{i\alpha}, \quad \text{for } i=1,\dots N. \tag{2.65}$$

Since there are $N+1$ unknowns $\{f_\alpha,\Upsilon_{i\alpha}\}$ for each α, an additional condition is required in order to find the solution. This comes from the normalization condition (2.26). If the perturbed vector also has unit normalization, then $\left\|\varsigma_{\alpha}^{\prime 2}\right\|=1$; from the definition of this vector, we get the following for the first-order term:

$$\sum_{j=1}^{N}\Upsilon_{j\alpha}\varsigma_{j\alpha}=0. \tag{2.66}$$

Equations (2.65) and (2.66) are now combined in a linear system of order $N+1$. Define vectors Q_α and B_α and matrix A_α as follows:

$$Q_{\alpha}=\begin{bmatrix} f_{\alpha} \\ \Upsilon_{1\alpha} \\ \Upsilon_{2\alpha} \\ \vdots \\ \Upsilon_{N\alpha} \end{bmatrix}, B_{\alpha}=\begin{bmatrix} \sum_{j}\xi_{1j}\varsigma_{j\alpha} \\ \sum_{j}\xi_{2j}\varsigma_{j\alpha} \\ \vdots \\ \sum_{j}\xi_{Nj}\varsigma_{j\alpha} \\ 0 \end{bmatrix}, A_{\alpha}=\begin{bmatrix} 2k_{\alpha}\varsigma_{1\alpha} & k_{\alpha}^{2}-\Gamma_{11} & -\Gamma_{12} & \cdots & -\Gamma_{1N} \\ 2k_{\alpha}\varsigma_{2\alpha} & -\Gamma_{21} & k_{\alpha}^{2}-\Gamma_{22} & \cdots & -\Gamma_{2N} \\ \vdots & \vdots & \vdots & \ddots & \vdots \\ 2k_{\alpha}\varsigma_{N\alpha} & -\Gamma_{N1} & -\Gamma_{N2} & \cdots & k_{\alpha}^{2}-\Gamma_{NN} \\ 0 & \varsigma_{1\alpha} & \varsigma_{2\alpha} & \cdots & \varsigma_{N\alpha} \end{bmatrix}. \tag{2.67}$$

Then for each α, the linear algebra system $A_\alpha Q_\alpha = B_\alpha$ is solved to obtain the vector Q_α of desired perturbation values. (In the model, LAPACK linear algebra routines DGETRF and DGETRS were used for the numerical solution of this system). This completes the perturbation analysis of the eigenproblem.

The perturbed version of the auxiliary relation (2.24) is

$$k_{\alpha}^{\prime}\vartheta_{i\alpha}^{\prime}=\sum_{j=1}^{N}\left(\zeta_{ij}^{\prime}+\eta_{ij}^{\prime}\right)\varsigma_{j\alpha}^{\prime}. \tag{2.68}$$

We now make the definition $\vartheta_{i\alpha}^{\prime}=\vartheta_{i\alpha}+u\varepsilon\chi_{i\alpha}$ for the perturbation of the difference vector ϑ. Using the results obtained so far for f_α and $\Upsilon_{j\alpha}$, together with (2.62), and concentrating on the first-order term in (2.68), we find after some manipulation that vectors χ_α have components

$$\chi_{i\alpha}=\frac{1}{k_{\alpha}}\left\{\sum_{j=1}^{N}\left[\frac{a_{j}C_{ij}^{+}}{\mu_{i}}\varsigma_{j\alpha}+\left(\zeta_{ij}+\eta_{ij}\right)\Upsilon_{j\alpha}\right]-f_{\alpha}\vartheta_{i\alpha}\right\}, \text{ for } i=1,\dots N. \tag{2.69}$$

Having completed the perturbation analysis for the sum and difference vectors ς_α and ϑ_α, perturbation factors $Y_{i\alpha}^{\pm}$ for the actual homogeneous solution vectors follow from the relations

$$\chi_{i\alpha}=Y_{i\alpha}^{+}-Y_{i\alpha}^{-} \quad \text{and} \quad \Upsilon_{i\alpha}=Y_{i\alpha}^{+}+Y_{i\alpha}^{-}. \tag{2.70}$$

Application of the symmetry relations $Y_{-i\alpha}^{+}=Y_{i\alpha}^{-}$ and $Y_{-i\alpha}^{-}=Y_{i\alpha}^{+}$ (cf. (2.25)) completes the perturbation analysis of the homogeneous solution.

Particular solutions

The particular solution for the beam source is determined from Equation (2.27). The perturbed version of this equation is

$$\sum_{j=-N}^{N} A_{ij}^{(beam)'} W_j' = B_i^{(beam)'}. \tag{2.71}$$

The definitions of $A^{(beam)}$ and $B^{(beam)}$ in (2.28) indicate that they are linearly dependent on the single-scatter albedo ω. Hence the first-order perturbed values are

$$A_{ij}^{'(beam)} = A_{ij}^{(beam)} - u\varepsilon a_j D_{ij} \quad \text{and} \quad B_i^{'(beam)} = B_i^{(beam)}(1+u\varepsilon). \tag{2.72}$$

Since $W_i' = W_i + u\varepsilon Z_i$ for the perturbed solution, then application of (2.72) in (2.71) yields

$$\sum_j A_{ij}^{(beam)} Z_j = B_i^{(beam)} - \sum_j a_j D_{ij} W_j. \tag{2.73}$$

Since the LU-decomposition of the matrix $A^{(beam)}$ has been found already in the course of determining the original beam solution, the solution for Z follows immediately by back-substitution using the right hand side of (2.73).

The situation for the thermal emission source term is similar. The recurrence relations in (2.29) for the expansion coefficients $T_{j,s}$ may be written in the perturbed form

$$\sum_j A_{ij}^{'(thermal)} T_{j,s}' = \begin{cases} (1-\omega')\, b_s' e_i & \text{for} \quad s = S, \\ (1-\omega')\, b_s' e_i + (s+1)\mu_i T_{i,s+1}' & \text{for} \quad s < S. \end{cases} \tag{2.74}$$

The definition of the matrix $A^{(thermal)}$ implies that $A_{ij}^{'(thermal)} = A_{ij}^{(thermal)} - u\varepsilon a_j D_{ij}$. From the definitions $b_s' = b_s + \varepsilon h_s$, $T_{j,s}' = T_{j,s} + \varepsilon V_{j,s}$ and using (2.74), the following recurrence relations for the first-order perturbation factors $V_{j,s}$ are found:

$$\sum_j A_{ij}^{(thermal)} V_{j,s} = \begin{cases} [(1-\omega)\, h_s - u b_s \omega]\, e_i + u \sum_j a_j D_{ij} T_{j,s} & \text{for} \quad s = S, \\ [(1-\omega)\, h_s - u b_s \omega]\, e_i + u \sum_j a_j D_{ij} T_{j,s} + (s+1)\mu_i V_{i,s+1} & \text{for} \quad s < S. \end{cases} \tag{2.75}$$

The LU-decomposition of the matrix $A^{(thermal)}$ is known already from the original determination of vector T, and thus the solution for the coefficients V follows by back-substitution in (2.75). This completes the perturbation analysis of the RTE particular solutions.

2.6.2. Boundary conditions for the perturbed field

We will establish here the eight boundary conditions summarized in Section 2.3.3 and indicated in Figure 2.2 for the atmospheric layer weighting functions. Only the beam particular integral terms will be included in the full boundary condition equations that follow; however, we indicate the additional contributions needed for atmospheric thermal emission. The calculation of TOA weighting functions is also described. Finally, we determine the special boundary condition BCL6R required for the albedo perturbation problem.

BCL1 (Cases 1 and 3)

At the top of the atmosphere, the perturbed downwelling intensity is zero, that is, $I'_{-jp} = 0$ for $\tau = 0$, $p = 1$ and $j = 1, \ldots N$. There is no variation in this layer, so $k'_{p\alpha} = k_{p\alpha}$, $X'_{jp\alpha} = X_{jp\alpha}$, and $W'_{jp} = W_{jp}$ for the homogeneous and particular solutions; we have only to consider perturbations of the integration constants as defined in (2.41a,b). The first-order perturbed intensity for this layer is then

$$I'_{-jp} = I_{-jp} + \varepsilon \sum_{\alpha=1}^{N} \left\{ N_{p\alpha} e^{-k_{p\alpha}\left(\tau - \tau_{p-1}\right)} X^{+}_{-jp\alpha} + P_{p\alpha} e^{-k_{p\alpha}\left(\tau_p - \tau\right)} X^{-}_{-jp\alpha} \right\}. \tag{2.76}$$

Since $I_{-jp}(\tau_0) = 0$ for the original (unperturbed) boundary condition BC1, BCL1 for $p = 1$ may be written

$$\sum_{\alpha=1}^{N} \left[N_{p\alpha} X^{+}_{-jp\alpha} + P_{p\alpha} \Theta_{p\alpha} X^{-}_{-jp\alpha} \right] = U_j^{(1)}, \quad \text{[BCL1]} \tag{2.77}$$

where $U_j^{(1)} = 0$. As before, the transmittance factor is given by $\Theta_{p\alpha} = \exp\left(-k_{p\alpha}\Delta_p\right)$, with $\Delta_p = \tau_p - \tau_{p-1}$ the layer optical thickness. where $U_j^{(1)} = 0$. Note the similarity to BC1 in (2.34a).

BCL2 (Cases 1 and 3)

This applies to all layers p such that $1 < p < q$ (q is the varying layer). As with BCL1, the RTE solutions remain unperturbed in these layers, and Equation (2.76) applies for both positive and negative stream angles. At the boundary between layer $r = p - 1$ and layer p, the optical depth is τ_r and continuity across this boundary yields BCL2 for $j = \pm 1, \ldots \pm N$:

$$\sum_{\alpha=1}^{N} \left\{ N_{r\alpha} \Theta_{r\alpha} X^{+}_{jr\alpha} + P_{r\alpha} X^{-}_{jr\alpha} \right\} - \sum_{\alpha=1}^{N} \left\{ N_{p\alpha} X^{+}_{jp\alpha} + P_{p\alpha} \Theta_{p\alpha} X^{-}_{jp\alpha} \right\} = U_{jp}^{(2)}, \quad \text{[BCL2]} \tag{2.78}$$

where $U_{jp}^{(2)} = 0$. Again the similarity to BC2 in Equation (2.34b) is clear.

BCL3 (Cases 1 and 3)

This is the upper boundary of the layer q that is varying ($q > 1$ for this condition). If $p = q - 1$, the boundary condition is $I'_{jp} = I'_{jq}$ at $\tau = \tau_p$. In layer p, there is no variation of the RTE solutions, so we can use an expression like Equation (2.76) for the perturbed field. For layer q, we must use the expression in Equation (2.42a) together with the perturbed RTE solution variables $k'_{q\alpha}$, $X'_{jq\alpha}$ and W'_{jq}, with perturbation factors $f_{q\alpha}$, $Y_{jq\alpha}$ and Z_{jq} as derived from Section 2.3.2 and Appendix A. Since $\tau'_q = \tau_q + v_q\varepsilon$ and $\tau'_p = \tau_p$, we can expand the exponential factors in (2.42a) to first order in ε:

$$e^{-k'_{q\alpha}\tau'_p} = e^{-k_{q\alpha}\tau_p}\left(1 - \varepsilon u_q f_{q\alpha}\tau_p\right), \tag{2.79a}$$

and

$$e^{-k'_{q\alpha}\tau'_q} = e^{-k_{q\alpha}\tau_q}\left(1 - \varepsilon u_q f_{q\alpha}\tau_q - \varepsilon v_q k_{q\alpha}\right). \tag{2.79b}$$

In the perturbed boundary condition, the zero-order term is eliminated by using the original unperturbed boundary condition BC2. Collecting all terms of order ε, and using (2.79a,b), the condition BCL3 for $j = \pm 1, \dots \pm N$ is written

$$\sum_{\alpha=1}^{N} \left\{ N_{p\alpha}\Theta_{p\alpha}X^{+}_{jp\alpha} + P_{p\alpha}X^{-}_{jp\alpha} \right\} - \sum_{\alpha=1}^{N} \left\{ N_{q\alpha}X^{+}_{jq\alpha} + P_{q\alpha}\Theta_{q\alpha}X^{-}_{jq\alpha} \right\} = U^{(3)}_{jq}. \quad \text{[BCL3]} \tag{2.80}$$

Here, we have the auxiliary vector

$$U^{(3)}_{jq} = u_q Z_{jq} e^{-\tau_p/\mu_0} + \sum_{\alpha=1}^{N} \left\{ L_{q\alpha}u_q Y^{+}_{jq\alpha} + M_{q\alpha}\Theta_{q\alpha}\left(u_q Y^{-}_{jq\alpha} - \varpi_{q\alpha}X^{-}_{jq\alpha} \right) \right\}, \tag{2.81}$$

where

$$\varpi_{q\alpha} = u_q f_{q\alpha}\Delta_q + v_q k_{q\alpha}. \tag{2.82}$$

BCL4 (Cases 1 and 2)

This is the lower boundary of the layer q that is varying ($q < K$ for this condition). If now $p = q+1$ the boundary condition is $I'_{jq} = I'_{jp}$ at $\tau = \tau'_q$. In layer p, there is no variation of the RTE solutions so an expression of type (2.42c) applies for the perturbed field, whereas for layer q, (2.42a) is appropriate. In addition to the expressions (2.79a,b), there is the following first-order expansion for the beam solution exponential term:

$$e^{-\tau'_q/\mu_0} = e^{-\tau_q/\mu_0}\left[1 - \varepsilon\frac{v_q}{\mu_0} \right]. \tag{2.83}$$

The zero-order term is again removed by using the original BC2 boundary condition, and with the help of (2.79a,b) and (2.83), BCL4 for $j = \pm 1, \dots \pm N$ may be written:

$$\sum_{\alpha=1}^{N} \left\{ N_{q\alpha}\Theta_{q\alpha}X^{+}_{jq\alpha} + P_{q\alpha}X^{-}_{jq\alpha} \right\} - \sum_{\alpha=1}^{N} \left\{ N_{p\alpha}X^{+}_{jp\alpha} + P_{p\alpha}\Theta_{p\alpha}X^{-}_{jp\alpha} \right\} = U^{(4)}_{jq}, \quad \text{[BCL4]} \tag{2.84}$$

where

$$U^{(4)}_{jq} = \left(-E_{jq} - \frac{v_q W_{jp}}{\mu_0} \right) e^{-\tau_q/\mu_0} - \sum_{\alpha=1}^{N} \left\{ L_{q\alpha}\Theta_{q\alpha}\left(u_q Y^{+}_{jq\alpha} - \varpi_{q\alpha}X^{+}_{jq\alpha} \right) + M_{q\alpha}u_q Y^{-}_{jq\alpha} \right\}. \tag{2.85}$$

$\varpi_{q\alpha}$ is defined in (2.82) and

$$E_{jq} = u_q Z_{jq} - \frac{v_q W_{jq}}{\mu_0}. \tag{2.86}$$

BCL5 (Cases 1 and 2)

In this case, the boundary lies between layers p and $r = p-1$, where $r > q$ and $q < K$. The only perturbation is with the optical depth boundary value $\tau'_r = \tau_r + v_q\varepsilon$, and perturbed fields of type (2.42c) apply to both layers. Again using the original BC2 condition to remove the zero-order term, the first-order term is written as BCL5 for $j = \pm 1, \ldots \pm N$:

$$\sum_{\alpha=1}^{N} \left\{ N_{r\alpha}\Theta_{r\alpha}X^{+}_{jr\alpha} + P_{r\alpha}X^{-}_{jr\alpha} \right\} - \sum_{\alpha=1}^{N} \left\{ N_{p\alpha}X^{+}_{jp\alpha} + P_{p\alpha}\Theta_{p\alpha}X^{-}_{jp\alpha} \right\} = U^{(5)}_{jp}, \quad \text{[BCL5]} \tag{2.87}$$

where

$$U^{(5)}_{jp} = \frac{v_q}{\mu_0} e^{-\tau_r/\mu_0} \left(W_{jr} - W_{jp} \right). \tag{2.88}$$

BCL6 (Cases 1 and 2)

Here $p = K$, the final layer, and the boundary is the bottom surface, with the diffuse radiation satisfying the reflection condition. The optical depth variation is $\tau'_p = \tau_p + v_q\varepsilon$; the single-scatter albedo has no variation. We require the diffusely reflected intensities (these appeared in BC3 in Section 2.2). We will require also the quantities $\Phi^{\pm}_{j\alpha}$ in (2.35a) and Ψ_j in (2.35b). The reflection condition includes the surface source term I^*_j defined in (2.33). Leaving aside the surface emission contribution, perturbations of I^*_j are generated by the change in optical depth at the lower boundary. Thus

$$I^{*'}_j = I^*_j \left(1 - \frac{v_q\varepsilon}{\mu_0} \right). \tag{2.89}$$

to first order. Bringing together the relevant terms, and using BC3 to eliminate the zero-order terms, the boundary condition BCL6 for $j = 1, \ldots N$ is:

$$\sum_{\alpha=1}^{N} \left[N_{p\alpha}\Theta_{p\alpha}\Phi^{+}_{j\alpha} + P_{p\alpha}\Phi^{-}_{j\alpha} \right] = U^{(6)}_{j}, \quad \text{[BCL6]} \tag{2.90}$$

where

$$U^{(6)}_{j} = \frac{v_q}{\mu_0} \left[\Psi_j e^{-\tau_p/\mu_0} - I^*_j \right]. \tag{2.91}$$

Once again, we note the similarity in the left hand side of BCL6 to that in BC3 (2.34c).

BCL3M (Case 2 only)

This is really a combination of BCL1 and BCL3, wherein the upper boundary of the layer that is varying happens to be the top of the atmosphere. Since $q = 1$ for this case, the boundary condition is $I'_{-jq} = 0$ at $\tau_{q-1} = 0$. We take the BCL3 result above, ignore the term in the left hand side involving layer $p = q - 1$ (which does not exist at TOA), and set $\tau_p = 0$ in (2.81). The result is BCL3M for $j = 1, \ldots N$:

$$\sum_{\alpha=1}^{N} \left\{ N_{q\alpha}X^{+}_{-jq\alpha} + P_{q\alpha}\Theta_{q\alpha}X^{-}_{-jq\alpha} \right\} = U^{(3M)}_{j}, \quad \text{[BCL3M]} \tag{2.92}$$

where

$$U^{(3M)}_{j} = -u_q Z_{-jq} - \sum_{\alpha=1}^{N} \left\{ L_{q\alpha}u_q Y^{+}_{-jq\alpha} + M_{q\alpha}\Theta_{q\alpha} \left(u_q Y^{-}_{-jq\alpha} - \varpi_{q\alpha}X^{-}_{-jq\alpha} \right) \right\}. \tag{2.93}$$

BCL4M (Case 3 only)

This is a combination of the conditions BCL4 and BCL6 with $q = K$. At the bottom boundary, the optical depth variation is $\tau'_q = \tau_q + v_q\varepsilon$. All of the exponential variations in (2.79a,b) and (2.83) are now required, since both the homogeneous solutions and the particular integral are perturbed in this layer. Both the original and the perturbed diffuse intensities must now satisfy the reflection condition. Thus in addition to the quantities Φ and Ψ in (2.35a,b) defined for unperturbed solutions $X_{jq\alpha}$ and W_{jq}, we must define similar quantities for the perturbation terms $Y_{jq\alpha}$ and E_{jq} (the latter is defined in (2.86)). Let

$$\Xi^{\pm}_{j\alpha} = Y^{\pm}_{jq\alpha} - (1+\delta_{m0})\, R \sum_{i=1}^{N} a_i \mu_i \rho^*_m(\mu_j, -\mu_i) Y^{\pm}_{-iq\alpha}, \tag{2.94}$$

and

$$F_j = E_{jq} - (1+\delta_{m0})\, R \sum_{i=1}^{N} a_i \mu_i \rho^*_m(\mu_j, -\mu_i) E_{-iq}. \tag{2.95}$$

Combining all the variations for this case, and including the variation of the direct beam from (2.89), BCL4M for $j = 1,\ldots N$ is

$$\sum_{\alpha=1}^{N} \left\{ N_{q\alpha}\Theta_{q\alpha}\Phi^{+}_{j\alpha} + P_{q\alpha}\Phi^{-}_{j\alpha} \right\} = U^{(4M)}_j, \quad \text{[BCL4M]} \tag{2.96}$$

where

$$U^{(4M)}_j = -F_j e^{-\tau_q/\mu_0} - \frac{v_q}{\mu_0} I^*_j - \sum_{\alpha=1}^{N} \left\{ L_{q\alpha}\Theta_{q\alpha} \left(u_q \Xi^{+}_{j\alpha} - \varpi_{q\alpha}\Phi^{+}_{j\alpha} \right) + M_{q\alpha} u_q \Xi^{-}_{j\alpha} \right\}. \tag{2.97}$$

An examination of the left hand sides of all these eight conditions shows that the boundary value problem for $N_{p\alpha}$ and $P_{p\alpha}$ has the same form as that for the original integration constants $L_{p\alpha}$ and $M_{p\alpha}$. Thus, as indicated in Section 2.3.3, the solution has the form $X^* = A^{-1}B^*$, where the matrix A is the same as that used in the unperturbed boundary value problem, and the column vector B^* is constructed from the appropriate combination of vectors $U^{(1)}$, $U^{(2)}_q$, $U^{(3)}_q$, $U^{(4)}_q$, $U^{(5)}_q$, $U^{(6)}$, $U^{(3M)}$ and $U^{(4M)}$, the exact choice depending on the layer q containing the variation in parameter x_q.

TOA weighting function output

Assuming now that the perturbed boundary problem has been solved for $N_{p\alpha}$ and $P_{p\alpha}$, we use definition (2.43) to calculate the weighting functions at positive computational angles at the top of the atmosphere. We distinguish between Cases 1 and 3 ($q > 1$), where the variation is with respect to parameter x_q in a layer below the first one, and Case 2 ($q = 1$), where the variation is actually in the top layer. For Cases 1 and 3:

$$K_{jp}(x_q) = \lim_{\varepsilon\to 0} \frac{I'_{jp} - I_{jp}}{\varepsilon} = \sum_{\alpha=1}^{N} \left\{ N_{p\alpha} X^{+}_{jp\alpha} + P_{p\alpha}\Theta_{p\alpha} X^{-}_{jp\alpha} \right\}, \tag{2.98}$$

where $j = 1,\dots N$ and $p = 1$. For Case 2 ($q = 1$):

$$K_{jq}(x_q) = \sum_{\alpha=1}^{N} \left\{ N_{q\alpha} X^{+}_{jq\alpha} + P_{q\alpha}\Theta_{q\alpha} X^{-}_{jq\alpha} \right\} + Q^{(3M)}_{j}, \tag{2.99}$$

where

$$Q^{(3M)}_{j} = u_q Z_{jq} + \sum_{\alpha=1}^{N} \left\{ L_{q\alpha} u_q Y^{+}_{jq\alpha} + M_{q\alpha}\Theta_{q\alpha} \left(u_q Y^{-}_{jq\alpha} - \varpi_{q\alpha} X^{-}_{jq\alpha} \right) \right\}. \tag{2.100}$$

Inclusion of atmospheric thermal emission terms in the perturbed boundary conditions

The coefficients $T_{jq,s}$ in the thermal emission particular integral (derived by solving (2.29)) have first-order perturbations V_{jqs} defined in (2.40d) only for the layer q that is varying. The solution for $V_{jq,s}$ is given in (2.75). Since the thermal emission term includes powers of optical depth, we must also account for changes εv_q in optical depths in and below the layer q. Defining

$$I'^{(te)}_{jp} = I^{(te)}_{jp} + \varepsilon J^{(te)}_{jp}, \tag{2.101}$$

for the perturbed thermal emission particular integral, the following additional contributions are required in the 8 boundary conditions of Section 2.3.3:

$$J^{(te)}_{jq} = \sum_{s=0}^{S} V_{jp,s}\tau^{s}_{q-1}, \qquad \text{for layer } q, \text{ upper boundary;} \tag{2.102a}$$

$$J^{(te)}_{jq} = \sum_{s=0}^{S} V_{jp,s}\tau^{s}_{q} + v_q \sum_{s=0}^{S} sT_{jq,s}\tau^{s-1}_{q}, \text{ for layer } q, \text{ lower boundary;} \tag{2.102b}$$

$$J^{(te)}_{jp} = v_q \sum_{s=0}^{S} sT_{jp,s}\tau^{s-1}_{p}, \qquad \text{for layers } p > q, \text{ lower boundaries.} \tag{2.102c}$$

Equation (2.102a) is required for BCL3, (2.102b) and (2.102c) for BCL4, and (2.102c) for BCL5 and BCL6. For BCL4M, (2.102b) is relevant for the thermal emission contribution to the positive (upwelling) quadrature-angle intensity components, but the downwelling stream components of the thermal emission contributions in (2.102b) must be integrated over the half space and included in the surface reflection boundary condition.

Boundary condition BCL6R for albedo weighting functions

Layer homogeneous and particular solutions are unaffected by variations of the surface albedo, so we may use their unperturbed forms. Only the boundary value constants of integration will change, and we denote their first-order perturbations by $N^{(R)}_{q\alpha}$ and $P^{(R)}_{q\alpha}$ to indicate the dependence on albedo. The perturbed intensity in all layers will have the form expressed in (2.42b), with boundary condition BCL1 applying to the TOA level and BCL2 to all intermediate levels. To express the surface boundary condition for the perturbed field, we first rewrite the *unperturbed* reflecting boundary condition in order to define $Q^{(R)}_{j}$ as follows (omitting the surface emission term):

$$I_{jK} \equiv RQ^{(R)}_{j} = R\left\{ \frac{F_{\odot}\mu_0}{\pi}\rho^{*}(\mu_j,-\mu_0)e^{-\tau_K/\mu_0} + (1+\delta_{m0})\sum_{i=1}^{N} a_i\mu_i\rho^{*}(\mu_j,-\mu_i)I_{-iK} \right\}. \tag{2.103}$$

For a variation $R' = R(1+\varepsilon)$, the perturbed version of (2.103) is

$$I'_{jK} = R(1+\varepsilon)\left\{\frac{F_\odot\mu_0}{\pi}\rho^*(\mu_j,-\mu_0)e^{-\tau_K/\mu_0} + (1+\delta_{m0})\sum_{i=1}^{N} a_i\mu_i\rho^*(\mu_j,-\mu_i)I'_{-iK}\right\}, \tag{2.104}$$

where the perturbed downwelling quadrature-stream intensity at the surface is given by

$$I'_{-iK} = I_{-iK} + \varepsilon\sum_{\alpha=1}^{N}\left\{N^{(R)}_{K\alpha}\Theta_{K\alpha}X^{+}_{-iK\alpha} + P^{(R)}_{K\alpha}X^{-}_{-iK\alpha}\right\}. \tag{2.105}$$

Using BC3 to remove the zero-order terms, the special albedo boundary condition (BCL6R) for $j = 1,\ldots N$ then becomes

$$\sum_{\alpha=1}^{N}\left[N^{(R)}_{K\alpha}\Theta_{K\alpha}\Phi^{+}_{j\alpha} + P^{(R)}_{K\alpha}\Phi^{-}_{j\alpha}\right] = U^{(6R)}_{j}, \quad \text{[BCL6R]} \tag{2.106}$$

where $U^{(6R)}_j = RQ^{(R)}_j$, and $\Phi^{\pm}_{j\alpha}$ have been defined in (2.35a). The solution for $N^{(R)}_{q\alpha}$ and $P^{(R)}_{q\alpha}$ again follows from the back-substitution $X^{(R)} = A^{-1}B^{(R)}$, where $B^{(R)}$ is now constructed from a combination of vectors $U^{(1)}$, $U^{(2)}_q$ and $U^{(6R)}$.

2.6.3. Post-processing (source function integration)

Source function integration for the original (unperturbed) field

Referring to the recurrence relation for the upwelling post-processed solution in Section 2.2.3, we substitute the values of $J_p(\tau,\mu)$ as given in (2.38) in the source function integration (2.37). Omitting the thermal emission term for now, the optical depth integrations may be carried out explicitly. The result for Λ_p is:

$$\Lambda_p(\mu) = H_p(\mu)F_p(\mu) + \sum_{\alpha=1}^{N}\left[L_{p\alpha}G^{+}_{p\alpha}E^{+}_{p\alpha}(\mu) + M_{p\alpha}G^{-}_{p\alpha}E^{-}_{p\alpha}(\mu)\right], \tag{2.107}$$

where

$$E^{+}_{p\alpha}(\mu) = \left[1-\Theta_{p\alpha}\gamma_p(\mu)\right]/\left(1+\mu k_{p\alpha}\right); \tag{2.108a}$$
$$E^{-}_{p\alpha}(\mu) = \left[\Theta_{p\alpha}-\gamma_p(\mu)\right]/\left(1-\mu k_{p\alpha}\right); \tag{2.108b}$$
$$F_p(\mu) = e^{-\tau_{p-1}/\mu_0}\left[1-e^{-\Delta_p/\mu_0}\gamma_p(\mu)\right]/\left(1+\mu/\mu_0\right), \tag{2.108c}$$

and transmittance factors $\Theta_{p\alpha}$ and $\gamma_p(\mu)$ have been defined previously. In addition, Eq. (2.107) requires the following double quadrature sums over discrete ordinate variables:

$$G^{\pm}_{p\alpha}(\mu) = \sum_j a_j D_p(\mu,\mu_j)X^{\pm}_{jp\alpha}, \tag{2.109a}$$

$$H_p(\mu) = \frac{F_\odot}{2\pi}\left(2-\delta_{m0}\right)D_p(\mu,-\mu_0) + \sum_j a_j D_p(\mu,\mu_j)W_{jp}. \tag{2.109b}$$

Here D_p are the usual Legendre polynomial sums for the streams indicated, with single-scatter albedo and phase function moments defined for layer p. The quantities in (2.108a–c) and (2.109a–b) will be needed again when we carry out a perturbation analysis of (2.107).

For the inclusion of atmospheric thermal emission terms, there is an additional contribution $\Lambda_p^{(te)}(\mu)$ to the integrated layer source function in a given layer p. This is only present for Fourier component $m = 0$. In the source function integration, we must include the thermal emission particular integral given by the last term in (2.31). By analogy to (2.107) we define

$$\Lambda_p^{(te)}(\mu) = \sum_{s=0}^{S} U_{ps}(\mu) A_{ps}(\mu), \tag{2.110}$$

where the $A_{ps}(\mu)$ term arises from the optical depth integration, and the $U_{ps}(\mu)$ is a quadrature sum over discrete ordinate variables. It may be shown readily that:

$$A_{ps}(\mu,\tau) = \begin{cases} 1-\gamma_p(\mu), & \text{if } s = 0, \\ \tau_p^s - \tau_{p-1}^s \gamma_p(\mu) + s\mu A_{p,s-1}(\mu), & \text{if } s > 0, \end{cases} \tag{2.111a}$$

and

$$U_{ps}(\mu) = (1-\omega_p) b_s + \sum_j a_j D_p(\mu,\mu_j) T_{jp,s}. \tag{2.111b}$$

The Legendre sum for layer D_p is defined in the usual way, using Fourier component $m = 0$.

It remains to find the boundary source term $I_K(\tau_K,\mu)$ which is the upwelling radiation at the lower boundary for direction μ. The discrete ordinate approximation is used again to write the reflection condition for direction μ in a similar manner to that given in (2.32c) and (2.33):

$$I_K(\tau_K,\mu) = (1+\delta_{m0})\, R \sum_{i=1}^{N} a_i \mu_i \rho_m^*(\mu,-\mu_i) I_{-iK}(\tau_K) + \frac{\mu_0 F_\odot}{\pi} e^{-\tau_K/\mu_0} R \rho_m^*(\mu,-\mu_0). \tag{2.112}$$

This is easy to evaluate since the components $I_{-iK}(\tau_K)$ are known from the discrete ordinate solution for the lowest layer K. It is necessary however to specify the bi-directional reflection functions $\rho_m^*(\mu,-\mu_i)$ and $\rho_m^*(\mu,-\mu_0)$ for the (user-defined) directions μ. (With surface thermal emission present, we add the factor $\delta_{m0}\kappa(\mu)B(T_g)$ to the right hand side of (2.112), where the emissivity $\kappa(\mu)$ follows from (2.21)).

Source function integration for the perturbed field

In this section the same technique is applied to the perturbed intensity field. First we look at the source function integrations required for weighting functions with respect to layer variations, before dealing with the albedo weighting function source terms at the end.

For the layer variations, we require the perturbed form of (2.44) for the source function recurrence relation, and we now consider the analysis for the perturbed source term $\Lambda'_p(\mu)$. Leaving aside the layer thermal emission terms for now (we return to them later in this section), we define perturbations of the quantities defined in (2.108a–c) and (2.109a,b):

$$E'^{\pm}_{p\alpha}(\mu) = E^{\pm}_{p\alpha}(\mu) + \varepsilon E^{\pm}_{p\alpha}(\mu), \tag{2.113a}$$

$$F'_p(\mu) = F_p(\mu) + \varepsilon F_p(\mu), \tag{2.113b}$$

$$G'^{\pm}_{q\alpha}(\mu) = G^{\pm}_{q\alpha}(\mu) + \varepsilon G^{\pm}_{q\alpha}(\mu), \tag{2.113c}$$

$$H'_q(\mu) = H_q(\mu) + \varepsilon H_q(\mu). \tag{2.113d}$$

For layer q, perturbations in (2.113a,b) will depend both on terms εv_q induced in the optical depth boundary value τ_q, and on terms εu_q which will be manifested in the perturbed eigenvalues $k'_{q\alpha}$. For layers $p > q$, only variations v_q induced in the optical depth boundary values τ_p will be required. The results for E are

$$E^{+}_{q\alpha} = \frac{\Theta_{q\alpha}\gamma_q(\mu)\left[\mu^{-1}v_q + \varpi_{q\alpha}\right] - \mu u_q f_{q\alpha} E^{+}_{q\alpha}(\mu)}{1+\mu k_{q\alpha}}, \tag{2.114a}$$

$$E^{-}_{q\alpha} = \frac{-\Theta_{q\alpha}\varpi_{q\alpha} + \mu^{-1}v_q\gamma_q(\mu) + \mu u_q f_{q\alpha} E^{-}_{q\alpha}(\mu)}{1-\mu k_{q\alpha}}, \tag{2.114b}$$

$$E^{\pm}_{p\alpha} = 0, \text{ for } p \neq q. \tag{2.114c}$$

In these equations, we use the following perturbation results on transmittance factors $\Theta_{q\alpha}$ and $\gamma_q(\mu)$:

$$\Theta'_{q\alpha} = \Theta_{q\alpha}\left(1 - \varpi_{q\alpha}\varepsilon\right); \tag{2.115a}$$

$$\gamma'_q(\mu) = \gamma_q(\mu)\left(1 - \varepsilon v_q/\mu\right), \tag{2.115b}$$

where $\varpi_{q\alpha}$ is given by (2.82). Similarly for F_p we have

$$F_p = \begin{cases} v_q\mu^{-1}e^{-\tau_q/\mu_0}\gamma_q(\mu), & \text{for } p = q, \\ -v_q\mu_0^{-1}F_p, & \text{for } p > q, \\ 0, & \text{for } p < q. \end{cases} \tag{2.116}$$

Now consider the perturbation analysis for quantities G and H in (2.109a,b), using the definitions in (2.113c,d). As before, the quantities D_q perturb to first order with factor $(1+\varepsilon u_q)$, since they are both directly proportional to ω_q. Using perturbations of the homogeneous solution vectors $X_{q\alpha}$ and the particular integral vectors W_q, we obtain:

$$G^{\pm}_{q\alpha}(\mu) = u_q\left[\sum_j a_j D_q(\mu,\mu_j)\left(X^{\pm}_{jq\alpha} + Y^{\pm}_{jq\alpha}\right)\right], \tag{2.117a}$$

$$H_q(\mu) = u_q\left[\frac{F_\odot}{2\pi}(2-\delta_{m0})D_q(\mu,-\mu_0) + \sum_j a_j D_q(\mu,\mu_j)\left(W_{jq} + Z_{jq}\right)\right]. \tag{2.117b}$$

It is clear that $G^{\pm}_{p\alpha}(\mu)$ and $H_p(\mu)$ are both zero for $p \neq q$.

We return now to the complete source function term in (2.107). This contains the integration constants $L_{p\alpha}$ and $M_{p\alpha}$. We must include their perturbations $N_{p\alpha}$ and $P_{p\alpha}$ in the analysis. We combine the results in (2.116) and (2.117a,b) and proceed by using the chain rule. The final result for the first-order layer source term perturbation is

$$\Lambda'_p(\mu) = \Lambda_p(\mu) + \varepsilon\Omega_p(\mu), \tag{2.118}$$

where (simplifying the notation by dropping the dependence on μ):

$$\Omega_p = \begin{cases} \sum\limits_{\alpha=1}^{N} \Omega^{(1)}_{p\alpha}, & \text{for } p < q, \\ \sum\limits_{\alpha=1}^{N} \left[\Omega^{(1)}_{p\alpha} + \Omega^{(2)}_{p\alpha}\right] + H_pF_p + H_pF_p, & \text{for } p = q, \\ \sum\limits_{\alpha=1}^{N} \Omega^{(1)}_{p\alpha} + H_pF_p, & \text{for } p > q. \end{cases} \tag{2.119}$$

The following definitions are required:

$$\begin{aligned} \Omega^{(1)}_{p\alpha} &= N_{p\alpha}G^+_{p\alpha}E^+_{p\alpha} + P_{p\alpha}G^-_{p\alpha}E^-_{p\alpha}, \\ \Omega^{(2)}_{p\alpha} &= L_{p\alpha}\left[G^+_{p\alpha}E^+_{p\alpha} + G^+_{p\alpha}E^+_{p\alpha}\right] + M_{p\alpha}\left[G^-_{p\alpha}E^-_{p\alpha} + G^-_{p\alpha}E^-_{p\alpha}\right]. \end{aligned} \tag{2.120}$$

We now consider perturbations of the thermal emission layer source terms defined in (2.110). These contributions will be added to the above expressions for Ω_p when there is a thermal emission source present in the atmosphere. First, we note that the solution coefficients U_{ps} contain no dependence on optical depth, so they experience perturbation only for the layer q that contains the atmospheric parameter x_q causing the variation. Defining

$$U'_{qs}(\mu) = U_{qs}(\mu) + \varepsilon U_{qs}(\mu), \tag{2.121}$$

we find from the definitions in (2.111b) that

$$U_{qs}(\mu) = \left[(1-\omega_q)h_{qs} - u_q\omega_q b_{qs}\right] + \sum_j a_j D_q(\mu,\mu_j)\left(u_q T_{jq,s} + V_{jq,s}\right), \tag{2.122}$$

where h_{qs} are the perturbations of b_{qs}. The recurrence factors A_{ps} in (2.111a) are perturbed as follows:

$$A'_{ps}(\mu) = A_{ps}(\mu) + \varepsilon B_{ps}(\mu). \tag{2.123}$$

We must again distinguish between the layer q containing the parameter x_q, and layers below q. Values of B_{ps} are found to obey similar recurrence relationships to those for A_{ps}. The result is

$$B_{ps}(\mu) = \begin{cases} 0, & \text{for } p < q, \quad s = 0,\ldots S, \\ \dfrac{v_q}{\mu}\gamma_q(\mu), & \text{for } p = q, \quad s = 0, \\ v_q\tau_q^s\gamma_q(\mu)\left(\dfrac{1}{\mu} + \dfrac{s}{\tau_q}\right) + s\mu B_{q,s-1}(\mu), & \text{for } p = q, \quad s = 1,\ldots S, \\ 0, & \text{for } p > q, \quad s = 0, \\ sv_q\left(\tau_p^{s-1} - \tau_{p-1}^{s-1}\gamma_p(\mu)\right) + s\mu B_{p,s-1}(\mu), & \text{for } p > q, \quad s = 1,\ldots S. \end{cases} \tag{2.124}$$

For the perturbation of the thermal emission contribution to the source integral term, we write

$$\Lambda'^{(te)}_p(\mu) = \Lambda^{(te)}_p(\mu) + \varepsilon\Omega^{(te)}_p(\mu), \tag{2.125}$$

and use the above results in (2.122) and (2.124) to produce:

$$\Omega^{(te)}_p(\mu) = \begin{cases} \sum\limits_{s=0}^{S}\left[U_{ps}(\mu)B_{ps}(\mu) + U_{ps}(\mu)A_{ps}(\mu)\right], & \text{for } p = q, \\ \sum\limits_{s=0}^{S} U_{ps}(\mu)B_{ps}(\mu), & \text{for } p > q, \end{cases} \tag{2.126}$$

with $\Omega_p^{(te)}(\mu) = 0$ for $p < q$. These contributions should be added to those in (2.118) so that thermal emission terms can be included in the TOA weighting functions at arbitrary μ.

Now we examine the perturbation of the upwelling lower boundary source term $I_K(\tau_K, \mu)$ in (2.112). We use the definition

$$I'_K(\tau_K, \mu) = I_K(\tau_K, \mu) + \varepsilon J_K(\tau_K, \mu), \tag{2.127}$$

and our task is to determine $J_K(\tau_K, \mu)$. Since the perturbed field obeys the surface boundary condition, we can remove the zero-order terms (boundary condition BC3) and write the following for the first-order contribution:

$$J_K(\tau_K, \mu) = (1 + \delta_{m0})\, R \sum_{i=1}^{N} a_i \mu_i \rho_m^*(\mu, -\mu_i) J_K(\tau_K, -\mu_i) - \frac{v_q}{\mu_0} I^*(\mu), \tag{2.128}$$

where the last term is the variation of the direct-beam term $I^*(\mu)$ as given by Equation (2.33) minus the surface emission, and $J_K(\tau_K, -\mu_j)$ is the first-order perturbation for the downwelling radiation at the *quadrature* values. In other words, $I'_K(\tau_K, -\mu_j) = I_K(\tau_K, -\mu_j) + \varepsilon J_K(\tau_K, -\mu_j)$. Expressions for $J_K(\tau_K, -\mu_j)$ can be written down immediately, since the results are available from the boundary problem perturbation analysis. There are two cases: BCL6, for which $q < K$, and BCL4M, for which $q = K$:

$$J(\tau_K, -\mu_j) = \begin{cases} -\dfrac{v_q W_{-jK}}{\mu_0} e^{-\tau_K/\mu} + \sum\limits_{\alpha=1}^{N} \left[N_{K\alpha} \Theta_{K\alpha} X^+_{-jK\alpha} + P_{K\alpha} X^-_{-jK\alpha} \right], & \text{BCL6}\,, \\ \left(u_q Z_{-jq} - \dfrac{v_q W_{-jq}}{\mu_0} \right) e^{-\tau_q/\mu} + \sum\limits_{\alpha=1}^{N} \left\{ P_{q\alpha} X^-_{-jq\alpha} + M_{q\alpha} u_q Y^-_{-jq\alpha} \right\} & \\ \quad + \sum\limits_{\alpha=1}^{N} \Theta_{q\alpha} \left\{ N_{j\alpha} X^+_{-jq\alpha} + L_{q\alpha} \left[u_q Y^+_{-jq\alpha} - X^+_{-jq\alpha} \varpi_{q\alpha} \right] \right\} & ,\quad \text{BCL4M}\,. \end{cases} \tag{2.129}$$

Albedo weighting functions at arbitrary μ

We complete this appendix by examining the perturbed field at arbitrary μ for an albedo variation. Homogeneous and particular solutions remain unchanged, and only the constants of integration in the boundary value problem will be perturbed. We proceed using the definition (2.107), writing $\Omega_p^{(R)}(\mu)$ for the source function perturbation, where the superscript (R) is used to indicate quantities derived with respect to an albedo variation $R' = R(1 + \varepsilon)$. We find

$$\Omega_p^{(R)}(\mu) = \sum_{\alpha=1}^{N} \left[N_{p\alpha}^{(R)} G^+_{p\alpha} E^+_{p\alpha} + P_{p\alpha}^{(R)} G^-_{p\alpha} E^-_{p\alpha} \right] \quad \text{for all} p, \tag{2.130}$$

where all other quantities occur in the original unperturbed solution.

To start the source function recurrence, we need the perturbed upwelling intensity at the lower boundary. To first order, we define $I'_K(\tau_K, \mu) = I_K(\tau_K, \mu) + \varepsilon J_K^{(R)}(\tau_K, \mu)$. Ignoring the surface emission term, we apply the surface boundary condition to $I'_K(\tau_K, \mu)$ and obtain:

$$J_K^{(R)}(\tau_K, \mu) = (1 + \delta_{m0})\, R \sum_{i=1}^{N} a_i \mu_i \rho_m^*(\mu, -\mu_i) \left[I_K(\tau_K, -\mu_i) + J_K^{(R)}(\tau_K, -\mu_i) \right] + I^*(\mu), \tag{2.131}$$

where $I^*(\mu)$ has already been defined in (2.33). From the solution of the perturbed albedo boundary value problem, we have already the quadrature terms:

$$J_K^{(R)}(\tau_K, -\mu_j) = \sum_{\alpha=1}^{N} \left[N_{K\alpha}^{(R)} \Theta_{K\alpha} X_{-jK\alpha}^{+} + P_{K\alpha}^{(R)} X_{-jK\alpha}^{-} \right]. \tag{2.132}$$

2.6.4. Chandrasekhar's solution and associated perturbation analysis

We first derive Chandrasekhar's solution to the unperturbed RTE. The notation follows that in [46]; in particular the Legendre polynomials in this Appendix are un-normalized. The Fourier index m is retained throughout. Quadrature over the interval $\mu \in (-1,1)$ is assumed. The treatment of thermal emission is omitted.

For the homogeneous part, Chandrasekhar developed solutions of the form:

$$I^m(\mu_i) \sim \sum_{l=m}^{2N-1} \frac{\xi_l^m(k_\alpha^m)\varphi_l^m P_l^m(\mu_i)}{1+\mu_i k_\alpha^m} e^{-k_\alpha^m \tau}, \tag{2.133}$$

where μ_i are the quadrature cosines, k_α^m are the roots of the characteristic equation (see below), and factors ξ_l^m are to be determined (their dependence on k_α^m is indicated). Here, $\varphi_l^m = \beta_l(l-m)!/(l+m)!$ denotes the phase moment factorial term. Substitution of Equation (2.133) in the RTE (2.15) without the external source terms gives the following set of conditions for $\xi_l^m(k)$:

$$\xi_l^m(k) = \sum_{\lambda=m}^{2N-1} \xi_\lambda^m(k)\varphi_\lambda^m D_{l\lambda}^m(k), \tag{2.134}$$

where

$$D_{l\lambda}^m(k) = \frac{1}{2}\sum_j \frac{a_j P_\lambda^m(\mu_j)P_l^m(\mu_j)}{1+\mu_j k}. \tag{2.135}$$

Using the orthonormality of the Legendre polynomials over the interval $(-1,1)$, one can develop a recurrence relation for the D-polynomials in (2.135), and use that to generate further recurrence relations for ξ_l^m ([46], p. 153):

$$\xi_{l+1}^m(k) = \frac{-(2l+1)+\omega\beta_l}{k(l-m+1)}\xi_l^m(k) - \frac{l+m}{l-m+1}\xi_{l-1}^m(k), \text{ for } m+1<l<2N-2; \tag{2.136a}$$

$$\xi_{m+1}^m(k) = \frac{-(2m+1)+\omega\beta_m}{k}. \tag{2.136b}$$

The indeterminacy in (2.134) allows the recursion initialization condition to be set at will. Letting $\xi_m^m = 1$ gives the characteristic equation

$$1 = \frac{\omega}{2}\sum_j \frac{a_j}{1+\mu_j k}\sum_{\lambda=m}^{2N-1}\xi_\lambda^m(k)\varphi_\lambda^m P_\lambda^m(\mu_j)P_m^m(\mu_j). \tag{2.137}$$

The roots of (2.137) occur in pairs $\pm k_\alpha, \alpha = 1,\dots N$. It is no surprise that these roots are precisely the eigenvalues from the equivalent formulation in Equation (2.22). We again use the index α to label the roots (eigenvalues). It is also clear that (up to constants of proportionality) the solutions developed in Section 2.2 are given by the following:

$$X_{j\alpha}^{m+} = \sum_{l=m}^{2N-1} \frac{\xi_l^m(k_\alpha^m)\varphi_l^m P_l^m(\mu_j)}{1+\mu_j k_\alpha^m}, \tag{2.138a}$$

$$X_{j\alpha}^{m-} = \sum_{l=m}^{2N-1} \frac{\xi_l^m(-k_\alpha^m)\varphi_l^m P_l^m(\mu_j)}{1-\mu_j k_\alpha^m}. \tag{2.138b}$$

For the particular integral (beam source), a solution of the form

$$J^m(\mu_i) = (2-\delta_{m0})\, W_i^m e^{-\tau/\mu_0} \tag{2.139}$$

is used, where

$$W_i^m = \omega \sum_{l=m}^{2N-1} \frac{\gamma_l^m \varphi_l^m P_l^m(\mu_i)}{1+\mu_i/\mu_0}. \tag{2.140}$$

Substitution in the RTE yields the following equation for the constants γ_l^m in terms of the recurrence factors defined above:

$$\gamma_l^m = \gamma_m^m(\mu_0)\xi_l^m\left(\mu_0^{-1}\right), \text{ for } l > m, \tag{2.141a}$$

$$\gamma_m^m(\mu_0) = \frac{P_m^m(\mu_0)}{1 - \sum\limits_{\lambda=m}^{2N-1} \xi_\lambda^m\left(\mu_0^{-1}\right)\varphi_\lambda^m D_{m\lambda}^m\left(\mu_0^{-1}\right)}, \tag{2.141b}$$

where ξ_l^m are again given by the recurrence relation Equations (2.136a,b) but with argument μ_0^{-1} instead of k. Symmetry relationships are the same as for the solutions in Section 2.2.2.

This formulation is equivalent to the solution of the RTE given in Section 2.2.2, assuming the “single” quadrature scheme (numerical results agree to high accuracy). This analytic formalism is not valid for the “double” quadrature scheme. Clearly, all quantities can be computed explicitly once the roots of the characteristic equation are found. Attempts to evaluate these roots by polynomial root-finding algorithms [74] have now been supplanted by the eigenvalue approach.

Perturbation of the solution

We are interested only in the perturbation of the RTE homogeneous solutions and particular integrals. (The boundary condition analysis of Section 2.3.3 is independent of the method of obtaining RTE solutions). The definitions of Equations (2.40a–c) hold, but we suppress the layer index p and add the Fourier harmonic index m as a subscript:

$$k_\alpha^{'m} = k_\alpha^m + u\varepsilon f_\alpha^m, \quad X_{j\alpha}^{'m} = X_{j\alpha}^m + u\varepsilon Y_{j\alpha}^m, \quad \text{and } W_j^{'m} = W_j^m + u\varepsilon Z_j^m. \tag{2.142}$$

As in Section 2.3, the single-scatter albedo will be perturbed according to $\omega' = \omega(1+u\varepsilon)$. We perturb the recurrence relation (2.136a,b) first. We write $\xi_{l,\alpha}^m = \xi_l^m(k_\alpha^m)$ for the quantity ξ corresponding to root k_α^m, and for the first-order perturbation, we define

$$\xi_{l,\alpha}^{'m} = \xi_{l,\alpha}^m + u\varepsilon\left(\zeta_{l,\alpha}^m + \eta_{l,\alpha}^m f_\alpha^m\right). \tag{2.143}$$

Using the perturbation rules for ω and k_α^m, and equating terms in u and $u f_\alpha^m$, we find that $\zeta_{l,\alpha}^m$ and $\eta_{l,\alpha}^m$ satisfy recurrence relationships similar to Equations (2.136a,b), but with additional terms:

$$\zeta_{l+1,\alpha}^m = \frac{\omega\beta_l}{k_\alpha^m(l-m+1)}\xi_{l,\alpha}^m + \frac{-(2l+1)+\omega\beta_l}{k_\alpha^m(l-m+1)}\zeta_{l,\alpha}^m - \frac{l+m}{l-m+1}\zeta_{l-1,\alpha}^m, \tag{2.144a}$$

$$\eta_{l+1,\alpha}^m = \frac{(2l+1)-\omega\beta_l}{(k_\alpha^m)^2(l-m+1)}\xi_{l,\alpha}^m + \frac{-(2l+1)+\omega\beta_l}{k_\alpha^m(l-m+1)}\eta_{l,\alpha}^m - \frac{l+m}{l-m+1}\eta_{l-1,\alpha}^m, \tag{2.144b}$$

$$\zeta_{m+1,\alpha}^m = \frac{\omega\beta_m}{k_\alpha^m}, \tag{2.144c}$$

$$\eta_{m+1,\alpha}^m = \frac{(2l+1)-\omega\beta_m}{(k_\alpha^m)^2}. \tag{2.144d}$$

Equations (2.144a,b) are valid for $m+1 < l < 2N-2$. The starting points for these recurrences are $\xi_{m,\alpha}^m = 0$ and $\eta_{m,\alpha}^m = 0$. We now substitute (2.143), (2.144a–d) and the definitions (2.142) into the perturbed version of the characteristic equation (2.137) to obtain variations for k_α^m:

$$f_\alpha^m = \frac{\Psi_\alpha^m + 2/\omega}{\Lambda_\alpha^m - \Phi_\alpha^m}, \tag{2.145}$$

where

$$\Psi_\alpha^m = \sum_j \frac{a_j}{\left(1+\mu_j k_\alpha^m\right)^2} \left\{ \sum_{\lambda=m}^{2N-1} \zeta_{\lambda,\alpha}^m \varphi_\lambda^m P_\lambda^m(\mu_j) P_m^m(\mu_j) \right\}, \tag{2.146a}$$

$$\Lambda_\alpha^m = \sum_j \frac{\mu_j a_j}{\left(1+\mu_j k_\alpha^m\right)^2} \left\{ \sum_{\lambda=m}^{2N-1} \xi_{\lambda,\alpha}^m \varphi_\lambda^m P_\lambda^m(\mu_j) P_m^m(\mu_j) \right\}, \tag{2.146b}$$

and

$$\Phi_\alpha^m = \sum_j \frac{a_j}{\left(1+\mu_j k_\alpha^m\right)^2} \left\{ \sum_{\lambda=m}^{2N-1} \eta_{\lambda,\alpha}^m \varphi_\lambda^m P_\lambda^m(\mu_j) P_m^m(\mu_j) \right\}. \tag{2.146c}$$

Equation (2.145) may be compared directly to the results obtained for quantity f_α in Appendix 2.6.1. To find the perturbed solution vector $X_\alpha'^{m+}$, we define a perturbed form of (2.138a):

$$X_{j\alpha}'^{m+} = X_{j\alpha}^{m+} + \varepsilon u Y_{j\alpha}^{m+} = \sum_{l=m}^{2N-1} \frac{\xi_l'^m(k_\alpha'^m)\varphi_l^m P_l^m(\mu_j)}{1+\mu_j k_\alpha'^m}. \tag{2.147}$$

Using the definitions in Eq. (2.142) and the results in Eqs. (2.144a–d), (2.145) and (2.146a–c), we find after some manipulation that the perturbation factor $Y_{j\alpha}^{m+}$ is given by:

$$Y_{j\alpha}^{m+} = \sum_{l=m}^{2N-1} \frac{\omega\varphi_l^m P_l^m(\mu_j)}{1+\mu_j k_\alpha^m} \left\{ \left(\xi_{l,\alpha}^m + \zeta_{l,\alpha}^m\right) + f_\alpha^m \left(\eta_{l,\alpha}^m - \frac{\xi_{l,\alpha}^m \mu_j}{1+\mu_j k_\alpha^m} \right) \right\}. \tag{2.148}$$

Perturbations for the negative solution (2.138b) can be determined in a similar fashion.

For the particular integral (beam source), look first at the perturbation:

$$\xi_{l,\alpha}'^m\left(\mu_0^{-1}\right) = \xi_{l,\alpha}^m\left(\mu_0^{-1}\right) + u\varepsilon\zeta_{l,\alpha}^m\left(\mu_0^{-1}\right). \tag{2.149}$$

This time only the variation in ω is required, and since ξ satisfies the recurrence relations (2.136a,b) with μ_0^{-1} instead of k, then ζ in (2.149) will satisfy a similar recurrence with additional terms:

$$\zeta_{l+1}^m = \frac{\omega\beta_l}{l-m+1}\mu_0\xi_l^m + \frac{-(2l+1)+\omega\beta_l}{l-m+1}\mu_0\zeta_l^m - \frac{l+m}{l-m+1}\zeta_{l-1}^m, \text{ for } m+1<l<2N-2; \tag{2.150a}$$

$$\zeta_{m+1}^m = \mu_0\omega\beta_m. \tag{2.150b}$$

The recurrence (2.150a,b) starts with $\zeta_m^m = 0$. This result is now used in the perturbation of the γ_l^m constants in (2.141a,b). Defining

$$W_i'^m = W_i^m + \varepsilon u Z_i^m = \omega' \sum_{l=m}^{2N-1} \frac{\gamma_l'^m \varphi_l^m P_l^m(\mu_i)}{1+\mu_i/\mu_0}, \tag{2.151}$$

where

$$\gamma_l'^m = \gamma_l^m \left(1+\varepsilon u \Gamma_l^m\right), \tag{2.152}$$

then we find after manipulation that

$$Z_i^m = \omega \sum_{l=m}^{2N-1} \frac{\gamma_l^m \varphi_l^m \left(1+\Gamma_l^m\right) P_l^m(\mu_i)}{1+\mu_i/\mu_0}, \tag{2.153}$$

where

$$\Gamma_l^m = \frac{\zeta_l^m}{\xi_l^m} - \frac{\omega \sum_{\lambda=m}^{2N-1} \left(\xi_\lambda^m + \zeta_\lambda^m\right) \varphi_\lambda^m D_{m\lambda}^m}{1 - \sum_{\lambda=m}^{2N-1} \xi_\lambda^m \varphi_\lambda^m D_{m\lambda}^m}. \tag{2.154}$$

This completes the analytic perturbation for the beam solution.

Chapter 3

Simultaneous derivation of intensities and weighting functions in a general pseudo-spherical radiative transfer treatment

This chapter has been accepted for publication in the Journal of Quantitative Spectroscopy and Radiative Transfer (14 March 2001).

Abstract

The retrieval of atmospheric constituents from measurements of backscattered light requires a radiative transfer forward model that can simulate both intensities and weighting functions (partial derivatives of intensity with respect to atmospheric parameters being retrieved). The radiative transfer equation is solved in a multi-layer multiply-scattering atmosphere using the discrete ordinate method. In an earlier paper dealing with the upwelling top-of-the-atmosphere radiation field, it was shown that a full internal perturbation analysis of the plane-parallel discrete ordinate solution leads in a natural way to the simultaneous generation of analytically-derived weighting functions with respect to a wide range of atmospheric variables. In the present paper, a more direct approach is used to evaluate explicitly all partial derivatives of the intensity field. A generalization of the post-processing function is developed for the derivation of weighting functions at arbitrary optical depth and stream angles for both upwelling and downwelling directions. Further, a complete treatment is given for the pseudo-spherical approximation of the direct beam attenuation; this is an important extension to the range of viewing geometries encountered in practical radiative transfer applications. The numerical model LIDORT developed for this work is able to generate intensities and weighting functions for a wide range of retrieval scenarios, in addition to the passive remote sensing application from space. We present a number of examples in an atmosphere with O_3 absorption in the UV, for satellite (upwelling radiation) and ground-based (downwelling radiation) applications. In particular, we examine the effect of various pseudo-spherical parameterizations on backscatter intensities and weighting functions with respect to O_3 volume mixing ratio. In addition, the use of layer-integrated multiple scatter output from the model is shown to be important for satellite instruments with wide-angle off-nadir viewing geometries.

3.1. Introduction

3.1.1. Background and rationale

Measuring the Earth's atmosphere is an essential requirement for the understanding of physical and chemical processes that determine radiative balance. This is particularly important in the light of possible climate change induced by man's activities on this planet. A key ingredient in atmospheric monitoring is the retrieval of surface properties and atmospheric constituent distributions from measurements of earthshine radiation. This applies not only to in-situ measurements from ground-based instruments and local measurements from aircraft and balloons, but also to the global coverage provided by passive remote sensing satellite instruments.

Given a state vector $\mathbf{X}$ of atmospheric constituents, we may generate a vector $\mathbf{Y}$ of synthetic radiance measurements at different wavelengths or geometries through the symbolic relation $\mathbf{Y} = F(\mathbf{X})$, where F is the *forward model* describing the attenuation and scattering of light in the atmosphere. Retrieval involves the solution of the inverse problem $\mathbf{X} = F^{-1}(\mathbf{Y})$. This is commonly done by iteration based on a series of linear inversion steps. The *linearization* of the forward model is given by $\mathbf{Y} - \mathbf{Y}_n = \mathbf{K}(\mathbf{X} - \mathbf{X}_n)$, where the matrix $\mathbf{K}$ is the set of *weighting functions* (intensity partial derivatives with respect to atmospheric parameters to be retrieved), and $\mathbf{Y}_n = F(\mathbf{X}_n)$ is the synthetic measurement vector corresponding to state vector estimate $\mathbf{X}_n$ at iteration step n. The inversion is carried out using cost-function minimization techniques such as non-linear least squares fitting [2], the widely-used optimal estimation method [4], or other methods such as Phillips-Tikhonov regularization [3]. All such iterative fitting methods require a radiative transfer model that will simultaneously generate both intensities and weighting functions.

The main purpose behind this paper and the previous work (Spurr, Kurosu and Chance [75], hereafter denoted by SKC) is to develop a general radiative transfer tool LIDORT with the capability to generate simultaneous and accurate intensity and weighting function fields. The discrete ordinate method is used to solve the radiative transfer equation (RTE). In SKC, the intensity model and its weighting function linearization were developed for the upwelling radiation fields at top-of-atmosphere (TOA) radiation fields in plane-parallel geometry. The aim of the present paper is to extend and generalize the LIDORT model, and to develop new tools for dealing with a wider range of atmospheric scenarios.

In the discrete ordinate formalism [46, 58], the intensity calculation depends only on knowledge of optical depths, single scattering albedos and phase function moments. Preparation of these quantities depends on the application and is carried out beforehand. The discrete ordinate method is a *generic* scattering formalism; it is not necessary to know the composition and detailed physics of the medium in question in order to solve the radiative transfer problem. The DISORT package [58] was developed with this philosophy in mind, and it is the most flexible and widely-used plane-parallel radiative transfer tool available to the atmospheric community. We adopt the same strategy for LIDORT, that is, to maintain the generic nature of the scattering formalism, but to develop extensions to generate weighting functions as well as intensities, for both plane-parallel and pseudo-spherical geometries.

In this work, the evaluation of weighting functions is based on an explicit analytic determination of partial derivatives of all components of the discrete ordinate solution for intensity. In line with the above remark on linearizing the forward model, we use the term *linearization analysis* to indicate the process of obtaining the set of partial derivatives that constitute the matrix of weighting functions. [A different emphasis was used in SKC, where weighting functions were determined through a complete first-order perturbation analysis of the discrete ordinate solution]. All weighting functions are determined analytically to the same accuracy as the intensity field. LIDORT can compute weighting functions with respect to a wide range of atmospheric variables; as with DISORT, the tool is not application-specific. In addition to the above-mentioned optical properties required as input to the intensity calculation, LIDORT requires as input for the weighting function calculations the derivatives of layer single scattering albedos and extinction coefficients with respect to the set of atmospheric parameters for which weighting functions are required.

For an intensity-only RT model without the linearization capability, weighting functions must be estimated using finite-difference methods; in a multi-parameter retrieval, this involves many separate calls to the model. With LIDORT, a single call will generate the set of intensities and weighting functions at one wavelength required for an iteration step in a typical multi-parameter atmospheric retrieval; this represents a very substantial saving of computer effort. Furthermore, the analytically accurate derivation of LIDORT weighting functions avoids concerns over the accuracy of finite-difference estimates based on *ad hoc* choices of the external perturbations. We note that at the present time, to our knowledge, only the GOMETRAN RT model [40] [43] has the capability to generate simultaneous fields of intensity and analytically accurate weighting functions.

Weighting functions with respect to ozone volume mixing ratio are important for the retrieval of ozone profiles from nadir-viewing remote sensing instruments measuring in the UV and visible. A full multiple-scatter RT treatment is a necessary requirement in this part of the spectrum. This retrieval problem has been discussed in the context of the GOME [5] instrument in a number of studies [13, 15, 14, 16]. In the present work, we will give examples of LIDORT output for a terrestrial atmosphere scenario relevant to the ozone profile retrieval context, not only for GOME but also for future instruments such as SCIAMACHY [76], GOME-2 [6] and OMI [8]. A fast 4-stream version of LIDORT has recently been developed for use in near-real-time ozone profile retrieval algorithms for these instruments [77].

Many atmospheric RT problems can be treated using the assumption of a plane-parallel medium. However, this assumption breaks down for solar zenith angles and/or line-of-sight viewing angles approaching 90°, and it then becomes necessary to make some allowance for the sphericity of the atmosphere. This is particularly important for polar-orbiting satellite instruments such as GOME, for which large solar zenith angles are frequently encountered. In a stratified spherical-shell medium, the intensity field changes with angular variables (solar and line of sight zenith angles, relative azimuth angle between planes containing the line of sight and solar directions) in addition to the zenith variation with optical depth.

The *pseudo-spherical* assumption ignores these angular derivatives; only the variation of intensity with the vertical coordinate is present in the RTE. The attenuation of the direct beam to the point of scatter is treated for a curved spherical-shell atmosphere (see Figure 3.1); apart from the transmittance calculation for single scatter, all higher-order scattering events are treated as locally plane-parallel. In a pseudo-spherical RT model, scattering takes place along the local vertical AC in Figure 3.1. It has been shown [35] [78] that the pseudo-spherical approximation provides a useful and sufficiently accurate RT intensity simulation for solar zenith angles up to 90°, provided that the line-of-sight is reasonably close to the nadir. A pseudo-spherical model is adequate for simulating backscatter intensities and weighting functions for the GOME and SCIAMACHY instruments in their normal nadir scanning modes (where the off-nadir scan angle does not exceed 31° at the satellite). The great advantage of this approach is that it utilizes the power, speed and flexibility of the plane-parallel discrete scattering formalism, and avoids the greatly more complex and computationally intensive full-spherical RT treatment.

It is possible to extend such a model to deal with wide off-nadir satellite viewing conditions (angle

θ_B in Figure 3.1 up to 70°); such geometry will be encountered routinely with the GOME-2 and OMI instruments. We consider scattering events along line AB instead of the vertical AC assumed for the regular pseudo-spherical computation. The basic idea behind the extension for wide-angle nadir satellite geometry is to make precise calculations of the single scatter contributions along AB (with both solar and line-of-sight transmittances for a curved atmosphere), but to approximate the *multiple-scatter* contributions using regular pseudo-spherical output for points along AB. In a detailed study for the TOMS project [78], it was shown that the major source of error in the regular pseudo-spherical model arises from an incorrect computation of the single scatter terms. We shall call this extension the *enhanced pseudo-spherical model*. Given the LIDORT capability to generate both intensities and weighting functions, it is then possible to use the enhanced model in profile retrieval algorithms in wide-angle viewing scenarios.

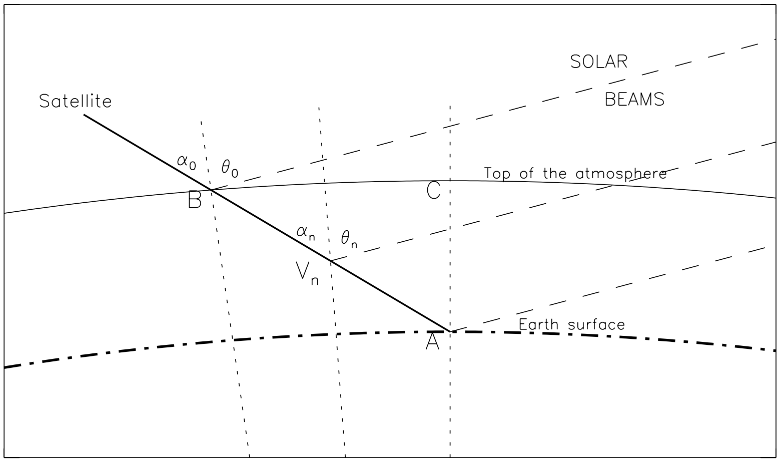

Figure 3.1: Satellite viewing geometry in a curved spherical-shell atmosphere.

The accuracy of the pseudo-spherical approximation depends on the parameterization used to describe the direct beam attenuation. For most cases, the *average secant* parameterization is sufficient: in a multi-layer atmosphere, slant path transmittances are taken to be exact at layer boundaries, with a simple exponential in optical thickness to approximate the attenuation across layers. The main LIDORT development is based on this assumption. However, we will examine more accurate parameterizations of direct beam transmittance in situations with optically thick layers. In any case, the *particular* solution to the discrete ordinate RTE must be modified to deal with the solar beam attenuation in a curved atmosphere (the *homogeneous* solutions are unchanged). In this work, we will examine two different approaches to the particular integral solution for the direct solar beam: the classical substitution method first used by Chandrasekhar [46] and standard in DISORT, and secondly, the more recent Green's function technique developed by Siewert and co-workers ([66] and references therein). Particular solutions for atmospheric thermal emission source terms will not be considered here; a derivation of TOA intensity and weighting functions for thermal emission sources in a plane-parallel atmosphere was given in SKC [75]. As in SKC, we shall consider only the solution to the scalar RTE; polarization will not be considered.

The generalization to arbitrary optical depth and stream angle involves the further development and extension of the *post-processing function*, in which the discrete ordinate solution is used to interpolate both the intensity and the weighting functions to arbitrary polar viewing angles. The approach adopted here is the standard source function integration technique [46, 34]. Output options for standard angle-integrated quantities (azimuthally-independent fluxes and mean intensities and associated weighting functions) have been incorporated in the model. The delta-M scaling transformation [36] is also a standard feature in the new version. LIDORT will also generate layer-integrated multiple scatter source terms and their weighting functions; as noted above, this output is an essential part of the enhanced pseudo-spherical model for RT simulation in wide-angle off-nadir satellite viewing geometries.

3.1.2. Organization of the paper

Section 3.2 is a brief recapitulation of the discrete ordinate solution to the RTE in a multi-layer atmosphere with a pseudo-spherical parameterization of the beam source attenuation. We summarize solutions for the homogeneous RTE equation, the boundary-value determination of integration constants from the boundary conditions, and the post-processing function. Determination of the particular solutions is deferred to the following section. In Section 3.3.1, we introduce three parameterizations for the attenuation of the direct beam in a curved atmosphere; these are the *average secant*, the *exponential-sine* and the *exponential-polynomial* parameterizations. In Sections 3.3.2 and 3.3.3 we determine respectively the classical and Green's function solutions for the particular integral using the average secant parameterization. In addition, in Section 3.3.3, the Green's function technique is used to derive more accurate solutions based on the other parameterizations of the direct beam attenuation.

In Section 3.4, we look at the linearization analysis. For a set of atmospheric parameters in a given layer for which we desire weighting functions, we require the derivatives of the extinction coefficient and single scattering albedo in that layer with respect to these parameters; these derivatives then determine the rules for the linearization analysis (Section 3.4.1). Once the latter are specified, the evaluation of intensity partial derivatives follows the same sequence of steps required for the complete intensity solution. In Sections 3.4.2 and 3.4.3 we apply the linearization analysis to the homogeneous and particular solutions, followed by the linearized boundary value problem (Section 3.4.4) and the post-processing function for generalized weighting function output in Section 3.4.5. The particular solution linearization in this section is restricted to the average secant parameterization.

Section 3.5 gives a brief description of the LIDORT software package based on the theory of the preceding sections. We give some comparisons with DISORT and SDISORT [79] output, and discuss the issue of weighting function validation. Section 3.6 contains some examples. The main emphasis here is on the satellite application for the retrieval of ozone profiles from nadir UV backscatter measurements. We concentrate on ozone absorption in the Hartley-Huggins bands (290-335 nm), and consider weighting functions with respect to ozone volume mixing ratio. Intensities and weighting functions are compared in the pseudo-spherical and plane-parallel approximations. Examples of output appropriate for ground-based instruments are also presented. In Section 3.6.3, we illustrate the use of the enhanced pseudo-spherical LIDORT model to improve intensity and weighting function simulations for the GOME, GOME-2, SCIAMACHY and OMI instruments at wide-angle viewing geometries.

3.2. Discrete ordinate theory: pseudo-spherical source function

3.2.1. The radiative transfer equation (RTE)

We consider the solution of the RTE in the pseudo-spherical approximation. Scattering will be non-conservative. We summarize the homogeneous solutions to the discrete ordinate equations, the boundary value problem and the post-processing function. Derivations of the particular solutions are deferred until Section 3.3; however, the role played by the particular solution will be outlined here. Although the theory summarized here may be found in various places (see for example [34] and references therein), it is important to have each stage of the discrete ordinate intensity solution clearly laid out in order to facilitate the linearization analysis in Section 3.4.

The RTE for the *diffuse* intensity $I(\tau,\mu,\phi)$ is:

$$\mu\frac{dI(\tau,\mu,\phi)}{d\tau} = I(\tau,\mu,\phi) - \frac{\omega(\tau)}{4\pi}\int_0^{2\pi} d\phi' \int_{-1}^{1} d\mu' P(\tau,\mu,\phi;\mu',\phi')I(\tau,\mu',\phi') - S_\odot(\tau,\mu,\phi). \tag{3.1}$$

Here, τ is the optical depth of the medium, μ is the absolute value of the cosine of the polar angle cosine (measured with respect to the zenith), and ϕ is the azimuth angle measured with respect to a suitable axis perpendicular to the zenith. $\omega(\tau)$ is the single scattering albedo, and $P(\tau,\mu,\phi;\mu',\phi')$ the phase function. For a parallel beam of net incident flux $\mu_0\pi F_\odot$ and direction $\{-\mu_0,\phi_0\}$ at the top of the atmosphere ($\tau = 0$), the single scattering source term is:

$$S_\odot(\tau,\mu,\phi) = \frac{F_\odot}{4}\omega(\tau)P(\tau,\mu,\phi;-\mu_0,\phi_0)e^{-\tau_{spher}(\tau)}. \tag{3.2}$$

The solar beam transmittance is expressed in terms of a slant path optical depth $\tau_{spher}(\tau)$ which is a function of τ. For now, we will not deal with this term explicitly, referring to the next section for particular integral derivations using explicit parameterizations of this transmittance. We note that the *total* intensity is actually the sum of the diffuse field $I(\tau,\mu,\phi)$ in (3.1) and an unscattered sunlight term $I_{sun}(\tau,\mu,\phi)$ given by:

$$I_{sun}(\tau,\mu,\phi) = \pi F_\odot e^{-\tau_{spher}(\tau)}\delta(\mu-\mu_0)\delta(\phi-\phi_0). \tag{3.3}$$

We assume the atmosphere is divided into a number of homogeneous layers, each layer having uniform optical properties. We first consider the solutions for a single layer, with single scattering albedo and phase functions regarded as independent of τ. The intensity is expanded as a Fourier cosine series in the relative azimuth $\phi-\phi_0$:

$$I(\tau,\mu,\phi) = \sum_{m=0}^{2N-1} I^m(\tau,\mu)\cos m(\phi-\phi_0). \tag{3.4}$$

Using the expansion of the phase function in terms of Legendre polynomials in the cosine of the scatter angle, plus the addition theorem for Legendre functions, the azimuthal dependence of P can also be expressed as a cosine series in relative azimuth. The azimuth separation follows immediately, and we obtain the following for each Fourier component m:

$$\mu\frac{dI^m(\tau,\mu)}{d\tau} = I^m(\tau,\mu) - S^m(\tau,\mu), \tag{3.5}$$

$$S^m(\tau,\mu) = \int_{-1}^{1} \Pi^m(\mu,\mu')I^m(\tau,\mu')d\mu' - \frac{F_\odot}{2}(2-\delta_{m0})\Pi^m(\mu,-\mu_0)e^{-\tau_{spher}(\tau)}, \tag{3.6}$$

where $m = 0,1,\ldots,2N-1$, and δ_{m0} is 1 for $m = 0$ and vanishes for $m \neq 0$. The auxiliary quantities Π^m are defined in terms of *normalized* Legendre polynomials $P_l^m(\mu)$ and phase function moment coefficients β_l (the actual Legendre expansion moments are $\beta_l/(2l+1)$) through

$$\Pi^m(\mu,\mu') = \frac{\omega}{2}\sum_{l=m}^{2N-1}\beta_l P_l^m(\mu)P_l^m(\mu'). \tag{3.7}$$

To obtain discrete ordinate solutions, we replace the multiple-scatter integral in (3.6) with a summation using two Gauss-Legendre quadratures defined separately in each polar angle half-space. Each quadrature has N points, with abscissae and weights $\{\mu_i, w_i\}, i = 1, \ldots, N$ in the positive half-space, and $\{-\mu_i, w_i\}, i = 1, \ldots, N$ for the negative half-space. The advantages of the double quadrature scheme have been discussed in the literature (see for example [34]). Equations (3.5) and (3.6) are then replaced by the discrete ordinate form:

$$\mu_i \frac{dI^m(\tau,\mu_i)}{d\tau} = I^m(\tau,\mu_i) - \sum_{j=\pm1}^{j=\pm N} w_j \Pi^m(\mu_i,\mu_j) I^m(\tau,\mu_j) - Q^m(\mu_i) e^{-\tau_{spher}(\tau)}, \tag{3.8}$$

$$Q^m(\mu_i) = \frac{F_\odot}{2} \left(2 - \delta_{m0}\right) \Pi^m(\mu_i, -\mu_0). \tag{3.9}$$

3.2.2. Homogeneous solutions

To get solutions of the homogeneous version of (3.8), we substitute $I_j \propto X_j e^{-k\tau}$ for $j = \pm1, \ldots, \pm N$. By using the sum and difference vectors $\varsigma_j = X_j + X_{-j}$ and $\vartheta_j = X_j - X_{-j}$ for $j = 1, \ldots, N$, (3.8) can be reduced to an N-rank eigenproblem with eigenvalues k_α^2 and eigenvectors $\boldsymbol{\varsigma}_\alpha$:

$$\left(\boldsymbol{\Gamma} - k^2 \hat{\mathbf{E}}\right) \boldsymbol{\varsigma} = 0, \quad \text{where} \quad \boldsymbol{\Gamma} = (\boldsymbol{\zeta} - \boldsymbol{\eta})(\boldsymbol{\zeta} + \boldsymbol{\eta}); \tag{3.10}$$

$$\zeta_{ij} = \left(\Pi^{+}_{ij} w_j - \delta_{ij}\right) / \mu_i \quad \text{and} \quad \eta_{ij} = \Pi^{-}_{ij} w_j / \mu_i. \tag{3.11}$$

Separation constants $\pm k_\alpha$ occur in pairs. In the above equations, $\alpha = 1, \ldots, N$, $\hat{\mathbf{E}}$ is the unit matrix and the elements $\Pi^{\pm}_{ij} = \Pi^{\pm}(\mu_i, \pm\mu_j)$ are given by (3.7) evaluated at quadrature polar angle cosines. The difference vector $\boldsymbol{\vartheta}_\alpha$ satisfies the following auxiliary equation linking it to the eigenvector $\boldsymbol{\varsigma}_\alpha$:

$$k_\alpha \vartheta_{i\alpha} = \sum_{j=1}^{N} \left(\zeta_{ij} + \eta_{ij}\right) \varsigma_{j\alpha}. \tag{3.12}$$

Equations (3.10) and (3.12) are sufficient to determine the solution of the homogeneous equations. The eigenproblem in (3.10) can be solved reliably using standard numerical routines. We assume that the eigenvectors $\boldsymbol{\varsigma}_\alpha$ have unit length. If we define $2N$-vectors $\mathbf{X}_\alpha^{(P)}$ and $\mathbf{X}_\alpha^{(N)}$ such that

$$X_{j\alpha}^{(P)} = \frac{\varsigma_{j\alpha} + \vartheta_{j\alpha}}{2} \quad \text{and} \quad X_{-j\alpha}^{(P)} = \frac{\varsigma_{j\alpha} - \vartheta_{j\alpha}}{2}; \tag{3.13}$$

$$X_{j\alpha}^{(N)} = X_{-j\alpha}^{(P)} \quad \text{and} \quad X_{-j\alpha}^{(N)} = X_{j\alpha}^{(P)}, \tag{3.14}$$

where $j = 1, \ldots, N$, then the complete *homogeneous* solution is

$$I_j(x) = \sum_{\alpha=1}^{N} \left\{ \tilde{L}_\alpha X_{j\alpha}^{(P)} e^{-k_\alpha \tau} + \tilde{M}_\alpha X_{j\alpha}^{(N)} e^{+k_\alpha \tau} \right\}, \tag{3.15}$$

where $\tilde{L}_\alpha$ and $\tilde{M}_\alpha$ are integration constants.

3.2.3. The boundary value problem

We assume that a particular solution $G(\tau, \mu_j)$ corresponding to the source term $Q^m(\mu_j) e^{-\tau_{spher}(\tau)}$ in (3.8) has been found. Consider first a single layer p with upper and lower optical depths given by τ_{p-1} and τ_p respectively, and optical thickness $\Delta_p = \tau_p - \tau_{p-1}$. Rather than use the cumulative optical depth τ as the vertical coordinate, we express the homogeneous and particular solutions in terms of the partial layer optical thickness $x = \tau - \tau_{p-1}$. The complete solution for the discrete ordinate components of the intensity field in the layer is:

$$I_{jp}(x) = \sum_{\alpha=1}^{N} \left\{ L_{p\alpha} X_{jp\alpha}^{(P)} e^{-k_{p\alpha}x} + M_{p\alpha} X_{jp\alpha}^{(N)} e^{-k_{p\alpha}\left(\Delta_p - x\right)} \right\} + G_p(x, \mu_j), \tag{3.16}$$

This is valid for upwelling and downwelling streams, $j = \pm 1, \ldots \pm N$. The integration constants $L_{p\alpha}$ and $M_{p\alpha}$ will be determined from the boundary value problem. The definition with x and $\Delta - x$ is equivalent to the scaling transformation suggested by Stamnes and Conklin [56] to express homogeneous transmission factors as negative exponentials; this ensures the stability of the numerical solution.

In a multi-layer atmosphere with K homogeneous layers and $K+1$ layer boundaries, the boundary conditions are:

(BC1) no downward diffuse radiation at the top of atmosphere;
(BC2) continuity of the intensity field at all intermediate levels;
(BC3) a surface reflection condition at the lowest level.

For the reflectance of the lower boundary, we use an expansion of the bi-directional surface reflection function $\rho(\mu, \phi; \mu', \phi')$ in terms of a Fourier series in the cosine of the relative azimuth. The condition for the m^{th} Fourier component of the reflected intensity (diffuse and direct) at the lower boundary is then

$$I^m(\tau_K, +\mu_i) = (1 + \delta_{m0}) \sum_{j=1}^{N} \mu_j w_j I^m(-\mu_j) \rho_m(\mu_i, -\mu_j) + \mu_0 F_\odot e^{-\tau_{spher}(\tau_K)} \rho_m(\mu_i, -\mu_0), \tag{3.17}$$

where $i = 1, \ldots, N$, $\tau_{spher}(\tau_K)$ is the slant optical depth of the whole atmosphere (total vertical optical depth τ_K), and ρ_m are the bi-directional Fourier coefficients with polar angles as indicated. As in SKC, we use a normalized form ρ^* of the bi-directional reflection function:

$$\rho_m(\mu_i, -\mu_j) = R \rho_m^*(\mu_i, -\mu_j); \quad \text{with} \quad R = \frac{1}{4} \int_0^1 \int_0^1 \mu\mu' \rho_0(\mu, -\mu') d\mu d\mu', \tag{3.18}$$

where R is the spherical albedo. For a Lambertian surface, $\rho_0^*(\mu_i, -\mu_j) = 1$ and $\rho_m^*(\mu_i, -\mu_j) = 0$ for $m > 0$, where $i, j = 1, \ldots, N$.

We can now write down expressions for the boundary conditions. We introduce the indices p, q, and r to label layers. BC1 is

$$\sum_{\alpha=1}^{N} \left\{ L_{1\alpha} X_{-j1\alpha}^{(P)} + M_{1\alpha} \Theta_{1\alpha} X_{-j1\alpha}^{(N)} \right\} = -G_{-j1}\big|_{\tau=0}, \tag{3.19}$$

where $G_{jp} = G(\tau, \mu_j)$ for τ in layer p. In (3.19), $j = 1, \ldots N$, and $-j$ denotes the downwelling stream directions. On the right hand side, the particular integral is evaluated at the optical depth indicated. The transmittance factors $\Theta_{p\alpha}$ are defined by

$$\Theta_{p\alpha} = \exp\left(-k_{p\alpha}\Delta_p\right), \tag{3.20}$$

where $\alpha = 1,\ldots N$, and $\Delta_p = (\tau_p - \tau_{p-1})$ is the optical thickness of layer p. BC2 is

$$\sum_{\alpha=1}^{N} \left[\left\{ L_{r\alpha}\Theta_{r\alpha}X^{(P)}_{jr\alpha} + M_{r\alpha}X^{(N)}_{jr\alpha} \right\} - \left\{ L_{p\alpha}X^{(P)}_{jp\alpha} + M_{p\alpha}\Theta_{p\alpha}X^{(N)}_{jp\alpha} \right\} \right] = \left(G_{jp} - G_{jr} \right)\big|_{\tau_r}, \tag{3.21}$$

where $r = p-1$. This is valid for both upwelling and downwelling directions $j = \pm 1,\ldots,\pm N$, and for $p = 2,\ldots,K$. BC3 at the lower boundary $\tau = \tau_K$ ($p = K$) is

$$\sum_{\alpha=1}^{N} \left\{ L_{K\alpha}\Theta_{K\alpha}\Phi^{(P)}_{j\alpha} + M_{K\alpha}\Phi^{(N)}_{j\alpha} \right\} = R\mu_0 F_{\odot}\rho^*_m(\mu_j,-\mu_0)e^{-\tau_{spher}(\tau_K)} - \Psi_j, \tag{3.22}$$

where

$$\Phi^{(P)}_{j\alpha} = X^{(P)}_{jK\alpha} - (1+\delta_{m0})\,R\sum_{i=1}^{N} w_i\mu_j\rho^*_m(\mu_j,-\mu_i)X^{(P)}_{-iK\alpha}, \qquad \text{and similarly for } \Phi^{(N)}_{j\alpha}; \tag{3.23a}$$

$$\Psi_j = G_{jK}\big|_{\tau_K} - (1+\delta_{m0})\,R\sum_{i=1}^{N} w_i\mu_i\rho^*_m(\mu_j,-\mu_i)\; G_{-iK}\big|_{\tau_K}. \tag{3.23b}$$

The normalized bi-directional reflectance coefficients have been used in BC3, and $e^{-\tau_{spher}(\tau_K)}$ is the whole atmosphere solar beam transmittance. (3.22) is valid for $j = 1,\ldots,N$. It is possible to write down a surface boundary to include surface blackbody thermal emission in BC3 [34].

BC1, BC2 and BC3 together constitute a linear algebra system $\boldsymbol{AX} = \boldsymbol{B}$ of order $2NK$. The vector $\boldsymbol{X}$ consists of the unknown integration constants $L_{p\alpha}$ and $M_{p\alpha}$. Matrix $\boldsymbol{A}$ has $3N-1$ sub- and super-diagonals; it may be compressed into band-storage form and then inverted using standard methods (the LAPACK [65] modules DGBTRF for the LU-decomposition and DGBTRS for the back-substitution were used in the numerical model).

3.2.4. The post-processing function and the complete solution

Finding the intensity for arbitrary direction μ and optical depth τ is known as "post-processing" of the RTE solution. We use the source function integration technique, which relies on the formal integration of (3.5); it has a clear physical interpretation, and is convenient to use numerically. It is essentially a form of interpolation for the intensity [34]. For a single layer with upper and lower boundary optical depths τ_U and τ_B, the upwelling and downwelling intensities at any intermediate layer optical thickness $x = \tau - \tau_U$ are given by

$$I^+(x,\mu) = I^+_B(\mu)e^{-(\Delta-x)/\mu} + \Lambda^+(x,\mu); \tag{3.24a}$$

$$I^-(x,\mu) = I^-_U(\mu)e^{-x/\mu} + \Lambda^-(x,\mu), \tag{3.24b}$$

where $\Delta = \tau_B - \tau_U$ and the *integrated* source terms are

$$\Lambda^+(x,\mu) = e^{x/\mu}\int_x^{\Delta} J^+(y,\mu)e^{-y/\mu}\frac{dy}{\mu}, \tag{3.25a}$$

$$\Lambda^-(x,\mu) = e^{-x/\mu}\int_0^{x} J^-(y,\mu)e^{y/\mu}\frac{dy}{\mu}. \tag{3.25b}$$

Here $J^{\pm}(y,\mu)$ is a sum of the multiply-scattered source term intensity at optical thickness y in direction μ and the term due to single scattering of the direct beam into this direction. The first of these terms is evaluated by approximating the multiple-scatter integral by its discrete-ordinate quadrature, using the discrete-ordinate solutions already obtained in (3.16). Without going into details of the derivation, we can write:

$$\Lambda^{\pm}(x,\mu) = H^{\pm}(x,\mu) + D^{\pm}(x,\mu) + E^{\pm}(x,\mu), \tag{3.26}$$

where the three terms represent contributions from the integrated homogeneous solutions, the integrated particular solution and the integrated single scatter term respectively. The single scatter contribution $E^{\pm}(x,\mu)$ and the particular solution contribution $D^{\pm}(x,\mu)$ both depend on the beam attenuation parameterization and the latter depends also on the method used to determine the particular solution. The homogeneous solution term $H^{\pm}(x,\mu)$ is independent of these aspects. Expressions for $H^{\pm}(x,\mu)$ may be found in [34] and are noted in Appendix 3.8.2. For now we defer discussion of the single scatter term $E^{\pm}(x,\mu)$ to the appropriate place in Section 3.3.1, while the particular solution contributions $D^{\pm}(x,\mu)$ will be treated later on when we consider the form taken by the particular solution (Sections 3.3.2, 3.3.3).

In an inhomogeneous atmosphere, source terms must be integrated on a layer-by-layer basis. Denoting $I^{\pm}_{p-1}(\mu)$ and $I^{\pm}_{p}(\mu)$ for the upwelling and downwelling intensities at the upper and lower boundaries of layer p respectively, we have from (3.24a) and (3.24b):

$$I^{+}_{p-1}(\mu) = I^{+}_{p}(\mu)e^{-\Delta/\mu} + \Lambda^{+}(0,\mu); \quad I^{-}_{p}(\mu) = I^{-}_{p-1}(\mu)e^{-\Delta/\mu} + \Lambda^{-}(\Delta,\mu), \tag{3.27}$$

where $\Lambda^{+}(0,\mu)$ is expression (3.25a) evaluated at $x=0$ and $\Lambda^{-}(\Delta,\mu)$ is (3.25b) evaluated at $x=\Delta$. These two relations are applied on a recursive basis to get the upwelling and downwelling intensities at layer boundaries. The downwelling recursion starts at TOA, where the downwelling diffuse intensity is zero ($I^{-}_{0}(\mu)=0$).

The starting value for the upwelling recursion is the bottom-of-the-atmosphere (BOA) source term $I^{+}_{K}(\mu)$, which may be determined from the surface reflection condition. For a general bi-directionally reflecting surface with albedo R and normalized reflection coefficients $\rho^{*}_{m}(\mu,-\mu_j)$ defined for upwelling directions μ, this is:

$$I^{+}_{K}(\mu) = (1+\delta_{m0})\, R \sum_{j=1}^{N} w_j \mu_j \rho^{*}_{m}(\mu,-\mu_j) I_{-jK}(\tau_K) + R\mu_0 F_{\odot} \rho^{*}_{m}(\mu,-\mu_0) e^{-\tau_{spher}(\tau_K)}. \tag{3.28}$$

This is easy to evaluate since the components $I_{-jK}(\tau_K)$ are known from the discrete ordinate solution for the lowest layer $p=K$. This BOA source term is only present for the $m=0$ Fourier term in the Lambertian case. This result can easily be extended to include surface thermal emission (see SKC for details). Thus to find the upwelling intensity at arbitrary stream angle μ and to arbitrary optical depth τ (assumed to lie within layer q), we start with (3.28), then use (3.27) recursively until the lower boundary of layer q is reached. We then apply (3.24a) once to get the required intensity at τ.

To complete the discrete ordinate solution, we sum the Fourier series (3.4). It is usual to terminate the azimuth series when the addition of an extra harmonic does not alter the overall intensity by more than a pre-specified relative quantity (the accuracy criterion). This convergence test should be applied to all intensities for which output is desired. Furthermore, it makes sense to apply this test to at least two successive azimuth contributions to avoid accidental omission. This procedure is standard in DISORT [58] and GOMETRAN [40] regarding series convergence.

The *layer-integrated* multiple scatter source term output may be obtained by simply dropping the single scatter contribution from (3.26):

$$\Lambda_q^{(MS)\pm}(\Delta_q,\mu) = H_q^{\pm}(\Delta_q,\mu) + D_q^{\pm}(\Delta_q,\mu) \tag{3.29}$$

in terms of layer optical thickness Δ_q.

For mean-value (angle-integrated) output, it is only necessary to compute the azimuth-independent term of the Fourier series ($m = 0$). Mean value output does not require the above post-processing analysis. The half-space angular integrations are performed using the discrete ordinate quadrature values. Upwelling and downwelling fluxes $\langle F\rangle$ and mean intensities $\langle J\rangle$ at optical depth τ inside the layer p are given by

$$\left\langle F^{+}(\tau)\right\rangle = 2\pi\sum_{j=1}^{N} w_j\mu_j I_{jp}^{+}(\tau) \quad \text{and} \quad \left\langle F^{-}(\tau)\right\rangle = 2\pi\sum_{j=1}^{N} w_j\mu_j I_{jp}^{-}(\tau) + F_{\odot}\mu_0 e^{-\tau_{spher}(\tau)}; \tag{3.30}$$

$$\left\langle J^{+}(\tau)\right\rangle = \frac{1}{2}\sum_{j=1}^{N} w_j I_{jp}^{+}(\tau) \quad \text{and} \quad \left\langle J^{-}(\tau)\right\rangle = \frac{1}{2}\sum_{j=1}^{N} w_j I_{jp}^{-}(\tau) + \frac{F_{\odot}\mu_0}{4\pi} e^{-\tau_{spher}(\tau)}, \tag{3.31}$$

where $I_{jp}^{\pm}(\tau)$ are the discrete ordinate solutions in layer p. Additional direct beam contributions are present in the downwelling case.

3.3. The pseudo-spherical particular integral

3.3.1. Direct-beam attenuation in a curved atmosphere

We first discuss the parameterization of the pseudo-spherical source term. In a multi-layer atmosphere, we may write

$$\kappa_q = \sum_{p=1}^{q} \kappa_{qp} = \sum_{p=1}^{q} s_{qp} e_p \tag{3.32}$$

for the cumulative slant optical depth κ_q to the bottom boundary of layer q in terms of layer path lengths s_{qp}, layer extinctions e_p and slant optical thickness values κ_{qp} for layers p above and equal to q. In a plane-parallel atmosphere, $\kappa_{qp} = \Delta_p/\mu_0$. For straight line paths (shell geometry only) the distances s_{qp} may be expressed easily in terms of vertical altitudes. In a non-refracting atmosphere, κ_q is expressed as the Chapman function [35]. In a refractive atmosphere, s_{qp} can be calculated with repeated application of Snell's law. The zenith solar angle cosine is always $-\mu_0$ for a non-refractive atmosphere. With refractive geometry, one must compute an average value $-\overline{\mu}_{0p}$ for each layer p. In the rest of this paper, we will continue to work with a non-refractive atmosphere, but the analysis is equally valid for the refractive case, provided the above points are noted. To characterize the pseudo-spherical input, we need to specify an input grid of slant path optical depths κ_{qp}, and (for a refractive atmosphere) a local grid of solar zenith cosines $-\overline{\mu}_{0p}$. $\left\{\kappa_{qp}, -\overline{\mu}_{0p}\right\}$ are additional inputs to the RT model; in keeping with the philosophy to maintain the generic nature of the discrete ordinate formalism, we do not include ray tracing as part of the model (this should be application-specific).

In a plane-parallel atmosphere, the direct beam attenuation is given by $\exp[-\tau/\mu_0]$. In a curved spherical-shell atmosphere this is replaced by $\exp[-\kappa(\tau)]$. We wish to find a parameterization of this transmittance. The simplest assumption uses an expression which is exact at layer boundaries:

$$e^{-\kappa(\tau)} \simeq T_q(x) = \hat{T}_q e^{-x\lambda_q}, \quad \text{where} \quad \hat{T}_q = e^{-\kappa_{q-1}} \quad \text{and} \quad \lambda_q = \frac{\kappa_q - \kappa_{q-1}}{\Delta_q}. \tag{3.33}$$

Here, $x = \tau - \tau_{q-1}$ is the partial layer optical thickness. Clearly λ_q is an *average secant factor* which replaces μ_0^{-1} in layer q. Note that this definition is slightly different to that used in [35], where λ_q is defined in terms of the slant path optical depth at the center of the layer. The definition here has the advantage that the attenuation is a continuous function of τ.

This approximation is equivalent to assuming an average attenuation across the layer, and takes no account of variations in optical depth through the layer. Some accuracy is lost for optically thick layers, or for geometrically extensive layers where there is considerable curvature. An improved parameterization may be obtained with the following exponential-sine and exponential-polynomial expressions:

$$e^{-\kappa(\tau)} \simeq \hat{T}_q e^{-x\lambda_q} \left[1 + \sum_{n=1}^{N_q^*} c_{qn} sin(\frac{nx\pi}{\Delta_q}) \right]; \tag{3.34a}$$

$$e^{-\kappa(\tau)} \simeq \hat{T}_q e^{-x\lambda_q} \left[1 + x\left(\Delta_q - x\right) \sum_{n=1}^{N_q^*} c_{qn} x^{n-1} \right], \tag{3.34b}$$

where x, $\hat{T}_q$ and λ_q are defined in (3.33). In both cases, correct slant path attenuations obtain at the layer boundaries, and the coefficients c_{qn} may be found by linear fitting, assuming that a suitable number of fine-level attenuation values are available. The number of coefficients N_q^* depends both on the layer optical and geometrical thickness values and on the degree of accuracy desired for the parameaterization. In practice, we use a single accuracy measure to ensure that the parameterization is consistently accurate for all layers.

In order to get an idea of the accuracy of these parameterizations, consider a single uniform atmospheric layer L above the ground (lower height level of 0 km), and with varying optical and geometrical thicknesses. We assume that this layer is bounded above by another homogeneous layer of fixed optical thickness 0.25, and extending up to a fixed upper level of 50 km. A non-refractive atmosphere is assumed; the earth radius is 6371 km. We make exact calculations of the attenuation for a large number of subdivisions of L and use these results to find the factors λ_q and T_q and the fitted coefficients c_{qn} in (3.33). A maximum of 4 coefficients was found to be sufficient in the fitting. Figure 3.2 shows the results of these computations for a number of different solar zenith angles (indicated as contours) ranging from 77° to 89.5°. An accuracy criterion of 5% was set for the average secant approximation, and 2% for the other parameterizations. Thus for example in Figure 3.2 (center), for all combinations of the ground layer optical and geometric thickness values lying above and to the right of the contour labeled 87°, the exponential-polynomial parameterization will reproduce the solar beam attenuation to better than 2% for a solar zenith angle of 87°. From Figure 3.2 (top), a 5% accuracy level for solar zenith angles up to 87° implies that for the average secant approximation, the ground layer optical thickness values should be below $\simeq$0.6, and corresponding geometrical thickness values should be less than $\simeq$0.6 km. In practical applications in a multi-layer atmosphere, a sufficient number of layers is used to ensure that inaccuracies in the average secant parameterization due to geometric effects are minimized. However, it is clear that there are limitations on the accuracy of the average secant approximation in the presence of optically thick layers. In Section 3.5, we give an example of the effect of a more accurate pseudo-spherical parameterization on backscatter intensities at high solar zenith angle.

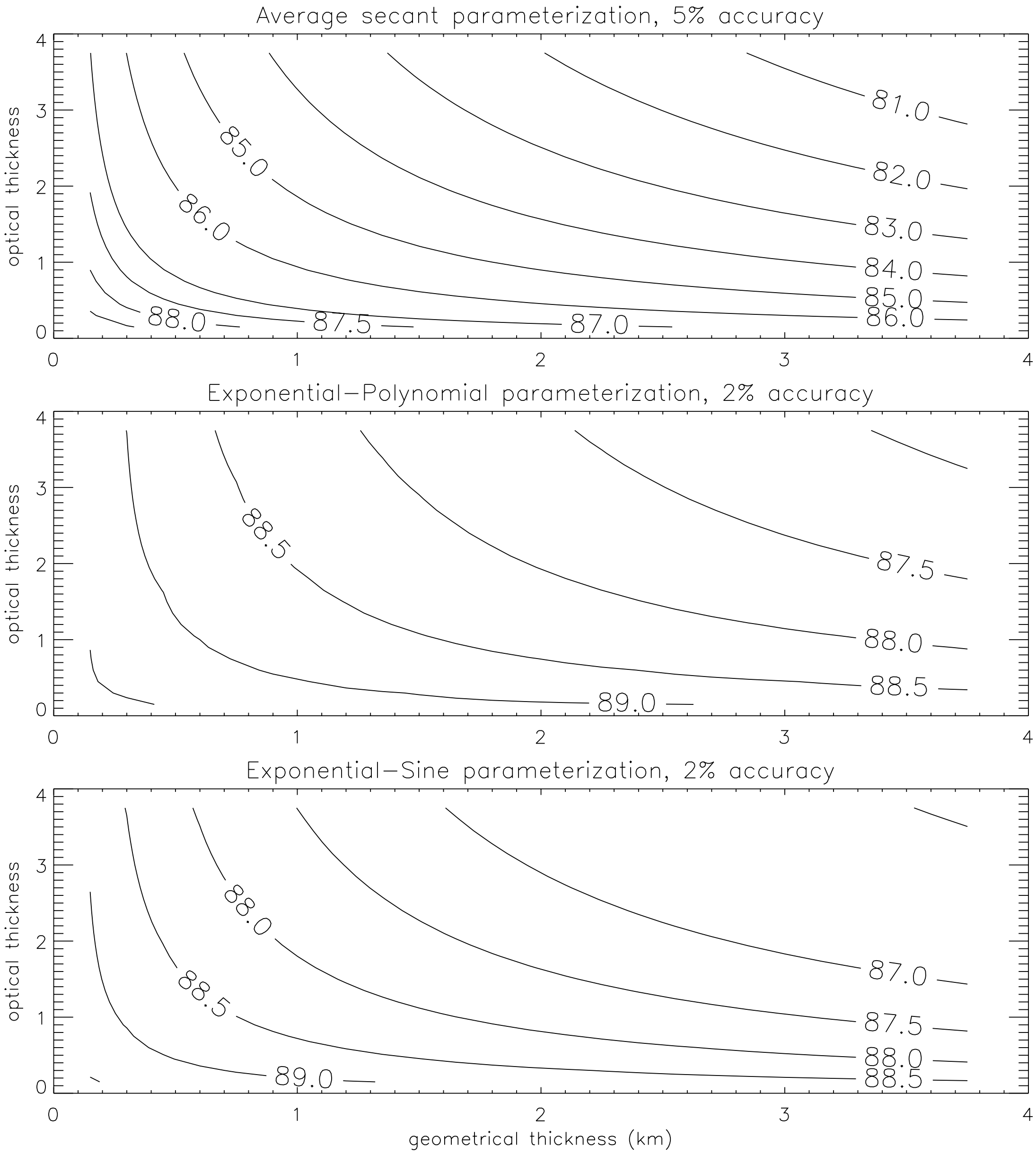

Figure 3.2: Direct beam attenuation accuracy; contours label solar zenith angles in (°), so that all geometrical and optical conditions above and right of a given contour indicate that the parameterization is accurate to the specified level for the corresponding solar zenith angle: (top) 5% accuracy levels in the average secant parameterization; (center) 2% accuracy level for the exponential-polynomial parameterization; (bottom) 2% accuracy levels for the exponential-sine parameterization.

Finally, we determine the single scatter contributions $E^{\pm}(x,\mu)$ which appeared in the integrated layer source terms (3.26). The source term to be integrated in this case is $Q^{m}(\mu)\hat{T}e^{-x\lambda}$ for the average secant pseudo-spherical approximation, where $Q^{m}(\mu)$ is given by (3.9) evaluated at zenith cosine μ. Source term integration over optical depth along the lines of (3.25a) is straightforward. Details are given in Appendix 3.8.2 for all three parameterizations of the direct beam transmittance noted in this section.

3.3.2. The classical (Chandrasekhar) particular solution

We find the particular solution for the average secant approximation. We use a notation similar to that in Section 3.2.1. For a double-Gauss discrete ordinate scheme with N quadrature abscissae and weights $\left\{\mu_j, w_j\right\}$ in the half space, we require the particular solution of the following $2N$ coupled linear differential equations (we drop the layer index q temporarily):

$$\frac{dI_i^{+}}{dx} = -\sum_{j=1}^{N}\left\{\zeta_{ij}I_j^{+} + \eta_{ij}I_j^{-}\right\} - Q_i^{+}\mu_i^{-1}\hat{T}e^{-x\lambda} \tag{3.35a}$$

$$\frac{dI_i^{-}}{dx} = +\sum_{j=1}^{N}\left\{\eta_{ij}I_j^{+} + \zeta_{ij}I_j^{-}\right\} + Q_i^{-}\mu_i^{-1}\hat{T}e^{-x\lambda}. \tag{3.35b}$$

where

$$Q_i^{\pm} = (2-\delta_{m0})\frac{F_{\odot}}{2\pi}\Pi^{m}(-\mu_0, \pm\mu_i). \tag{3.36}$$

These expressions are obtained by substituting the average secant form (3.33) in the general discrete ordinate equation (3.9), and using the definitions of matrices $\boldsymbol{\zeta}$ and $\boldsymbol{\eta}$ in (3.11). For the plane-parallel case, $\lambda = \mu_0^{-1}$ and $\hat{T} = \exp\left[-\tau_U/\mu_0\right]$ (τ_U is the upper boundary vertical optical depth). The particular solution $G_j^{\pm}$ is found by substituting $I_j^{\pm} \sim F_j^{\pm}\hat{T}\exp(-x\lambda)$ in (3.35a) and (3.35b). This eliminates the optical depth dependence and we are left with a linear system of order $2N$:

$$\lambda F_i^{+} = \sum_{j=1}^{N}\left\{\zeta_{ij}F_j^{+} + \eta_{ij}F_j^{-}\right\} - Q_i^{+}\mu_i^{-1}, \tag{3.37a}$$

$$\lambda F_i^{-} = -\sum_{j=1}^{N}\left\{\eta_{ij}F_j^{+} - \zeta_{ij}F_j^{-}\right\} - Q_i^{-}\mu_i^{-1}. \tag{3.37b}$$

If we define sum and difference vectors $\mathbf{H} = \mathbf{F}^{+} + \mathbf{F}^{-}$, $\mathbf{J} = \mathbf{F}^{+} - \mathbf{F}^{-}$, $\mathbf{S} = \mathbf{Q}^{+} + \mathbf{Q}^{-}$ and $\mathbf{D} = \mathbf{Q}^{+} - \mathbf{Q}^{-}$, we can eliminate $\mathbf{J}$ in favor of $\mathbf{H}$, thereby reducing the order of the system from $2N$ to N. The result is

$$\left(\boldsymbol{\Gamma} - \hat{\mathbf{E}}\lambda^{2}\right)\mathbf{H} = -\left(\boldsymbol{\zeta} - \boldsymbol{\eta}\right)\mathbf{S} - \lambda\mathbf{D} \tag{3.38}$$

for the sum vector $\mathbf{H}$. $\boldsymbol{\Gamma}$ is the eigenmatrix in (3.10) and $\hat{\mathbf{E}}$ is again the unit matrix. This system is solved numerically by standard means. The difference vector $\mathbf{J}$ is found from the auxiliary equation

$$\lambda\mathbf{J} = \left(\boldsymbol{\zeta} + \boldsymbol{\eta}\right)\mathbf{H} + \mathbf{S} \tag{3.39}$$

Equations (3.38) and (3.39) are sufficient to complete the solution. The derivation here (in particular, the reduction in order) follows closely that found in [66].

A similar approach applies to the exponential-polynomial parameterization given in (3.34b) above. Solutions of the form

$$I_j^{\pm} \sim \hat{T} e^{-x\lambda} \textstyle\sum_n F_{jn}^{\pm} x^n \tag{3.40}$$

may be substituted in the discrete ordinate equation (3.8). Successive powers of x are then equated, and this yields a series of linked linear equations for the components $F_{jn}^{\pm}$ which are solved recursively starting with the highest power of x. A solution for the particular integral in a plane-parallel atmosphere has been developed for an exponential-linear form [79]. For the exponential-sine parameterization (3.34a), the ansatz $I_j^{\pm} \sim \hat{T}\exp(-x\lambda)\sum_n F_{jn}^{\pm}\sin(nx\pi/\Delta)$ can be used. We will not go into details for the determination of classical solutions for these two parameterizations, as the procedures are somewhat cumbersome. In the next section we will see that the Green's function technique allows particular solution to be evaluated in a convenient analytic fashion, without the need for solving linear systems numerically.

For integrated particular solution source functions with the classical method, we refer again to the definition in (3.26), where we now require the particular solution contribution $D_{class}^{\pm}$. This derivation is given in Appendix 3.8.2. In line with our preference for using the Green's function technique, we do not consider similar expressions for the exponential-sine and exponential-polynomial parameterizations (these will however be derived below in section 3.3.3 for the Green's function particular integral contributions).

3.3.3. The Green's function particular solution

The Green's function method is based on expansions for the upwelling and downwelling particular solution in terms of solution vectors $\mathbf{X}_\alpha^{(P)}$ and $\mathbf{X}_\alpha^{(N)}$ and separation constants $\pm k_\alpha$ for the homogeneous problem. A rigorous derivation of this result is outside the scope of the present paper, but the reader is referred to the explicit formulation of the infinite-medium Green's function found in [50]. The particular form used in the present work assumes that the eigenproblem separation constants occur in pairs, but this is not a necessary requirement. In this section, we summarize the results given in [66]. We write

$$G_j^{+}(\tau) = \sum_{\alpha=1}^{N} \left\{ A_\alpha(\tau) X_{j\alpha}^{(P)} + B_\alpha(\tau) X_{j\alpha}^{(N)} \right\}; \quad G_j^{-}(\tau) = \sum_{\alpha=1}^{N} \left\{ A_\alpha(\tau) X_{j\alpha}^{(N)} + B_\alpha(\tau) X_{j\alpha}^{(P)} \right\}, \tag{3.41}$$

for the upwelling $(+)$ and downwelling $(-)$ particular integral solutions $G_j^{\pm}(x)$ of (3.8), where the multipliers A and B are given by

$$A_\alpha(\tau) = a_\alpha C_\alpha^{-}(\tau) \quad \text{and} \quad B_\alpha(\tau) = b_\alpha C_\alpha^{+}(\tau). \tag{3.42}$$

In (3.42), the terms independent of optical depth are given by

$$a_\alpha = \frac{1}{N_\alpha} \sum_{j=1}^{N} w_j \left[P_j^{-} X_{j\alpha}^{(N)} + P_j^{+} X_{j\alpha}^{(P)} \right]; \quad b_\alpha = \frac{1}{N_\alpha} \sum_{j=1}^{N} w_j \left[P_j^{+} X_{j\alpha}^{(N)} + P_j^{-} X_{j\alpha}^{(P)} \right], \tag{3.43}$$

where the normalization factor N_α is given by

$$N_\alpha = \sum_{j=1}^{N} \mu_j w_j \left[X_{j\alpha}^{(N)} X_{j\alpha}^{(N)} - X_{j\alpha}^{(P)} X_{j\alpha}^{(P)} \right], \tag{3.44}$$

and $P_j^{\pm} = (2-\delta_{m0})\,\Pi^m(\pm\mu_j, -\mu_0)$ (the Π function was defined in (3.7)). If the layer upper and lower optical depths are τ_U and τ_L respectively, then the *optical depth multipliers* in (3.42) are given by

$$C_\alpha^-(\tau) = \int_{\tau_U}^{\tau} e^{-k_\alpha(\tau-y)} e^{-\tau_{spher}(y)} dy, \quad \text{and} \quad C_\alpha^+(\tau) = \int_{\tau}^{\tau_L} e^{-k_\alpha(y-\tau)} e^{-\tau_{spher}(y)} dy. \tag{3.45}$$

These results may be verified by substituting (3.41) in the discrete ordinate RTE (3.8) and using (3.42) and (3.43) together with the properties of the eigensolutions to separate the optical depth dependence and construct the multipliers in (3.45). The most important property of these eigensolutions is their full-range orthogonality. We note that the particular integral is written in analytic form, requiring only the evaluation of the optical depth integrals (3.45). Results for $C_\alpha^{\pm}(\tau)$ in a plane-parallel medium have been noted several times in the literature (see for example [50] or [66]). Since the average secant parameterization is in fact a local plane-parallel formulation with $e^{-\tau_{spher}(y)} \simeq \hat{T} e^{-(y-\tau_U)\lambda}$, the integrals in (3.45) are straightforward:

$$C_\alpha^-(x) = \hat{T}\frac{e^{-xk_\alpha} - e^{-x\lambda}}{\lambda - k_\alpha}, \quad \text{and} \quad C_\alpha^+(x) = \hat{T}\frac{e^{-x\lambda} - e^{-\Delta\lambda} e^{-(\Delta-x)k_\alpha}}{\lambda + k_\alpha}, \tag{3.46}$$

where again, $x = \tau - \tau_U$ and $\Delta = \tau_L - \tau_U$. In Appendix 3.8.1 we calculate optical depth multipliers for the exponential-polynomial and exponential-sine parameterizations.

For the post-processing function, we again refer to (3.26) and write $D_{Green}^{\pm}(x,\mu)$ for the integrated particular solution contribution to the partial-layer source terms. In Appendix 3.8.2, we present derivations of $D_{Green}^{\pm}$ for all three parameterizations of the direct beam transmittance considered in this paper.

The Green's function method offers a more systematic way of dealing with parameterizations of the direct beam. In general, the classical method (which relies on substitution) is limited to source terms with straightforward and separable dependence on optical depth; the Green's function formalism is more powerful and offers greater scope for dealing with a wider variety of source terms.

3.4. Linearization of the pseudo-spherical discrete ordinate solution

3.4.1. Preamble: linearization rules

In the previous work (SKC), a perturbation analysis of the intensity field in a plane-parallel multilayer multiply scattering atmosphere was carried out in order to establish analytical weighting functions. In this paper, we adopt a slightly different emphasis, instead working directly with the partial derivatives of the discrete ordinate solution components. Since the discrete ordinate RTE comprises a set of coupled *linear* first-order differential equations, this is equivalent to the perturbation analysis. We also extend the analysis in two directions: (1) the derivation of weighting functions for the pseudo-spherical model, and (2) the generalization to upwelling and downwelling output at arbitrary stream angles and optical depth. Together this enables weighting functions to be calculated for any atmospheric application, in addition to extending the range of viewing geometries to include large solar zenith angle scenarios.

In order to generate weighting functions with respect to any given atmospheric parameter, we require the corresponding variational derivatives of the basic optical property inputs to the RTE. We consider variations only of layer single-scatter albedo and extinction coefficient, though it is possible to consider variations of the phase function moments. Consider an atmospheric parameter ξ_q in layer q; the relative (parameter-normalized) weighting function definition is:

$$K_{\xi_q}(\tau,\mu,\phi_0-\phi)=\sum_{m=0}^{2N-1}K^m_{\xi_q}(\tau,\mu)\cos m(\phi_0-\phi); \tag{3.47}$$

$$K^m_{\xi_q}(\tau,\mu)=L_{\xi_q}[I^m(\tau,\mu)]=\xi_q\frac{\partial I^m(\tau,\mu)}{\partial\xi_q}. \tag{3.48}$$

Equation (3.48) defines the *linearization operator* $L_\xi=\xi\partial/\partial\xi$, and we will continue to use this notation in the weighting function analysis.

The input variational quantities that determine the weighting functions may be expressed as

$$\{u_q,v_q\}=\left\{\frac{L_q[\omega_q]}{\omega_q},\frac{L_q[e_q]}{e_q}\right\}=\left\{\frac{\xi_q}{\omega_q}\frac{\partial\omega_q}{\partial\xi_q},\frac{\xi_q}{e_q}\frac{\partial e_q}{\partial\xi_q}\right\}. \tag{3.49}$$

Here, u_q can be thought of as the *relative change* in single scattering albedo ω_q induced by a relative change in property ξ_q, and v_q as the *relative change* in extinction coefficient e_q induced by a relative change in ξ_q. The pairs $\{u_q,v_q\}$ are fundamental to the weighting function derivation, and they will be established beforehand and entered as additional inputs to LIDORT.

A simple example will illustrate the construction of the optical properties and their derivatives. Consider a single homogeneous layer of depth h with Rayleigh (molecular) scattering and absorption by one trace gas species g. The single scattering albedo is $\omega=\sigma_{Ray}/\sigma_{total}$, where $\sigma_{total}=\sigma_{Ray}+X_g\sigma_g$, σ_{Ray} is the Rayleigh cross section, σ_g the trace gas absorption cross section, and X_g the trace gas volume mixing ratio. The layer extinction coefficient is $e=\sigma_{total}\rho_{air}$, and the vertical optical thickness is $\Delta=eh$, where ρ_{air} is the air number density (assumed constant). If $\xi=X_g$ is the property undergoing variation, it can be shown readily that

$$u_\xi=-\frac{X_g\sigma_g}{\sigma_{Ray}+X_g\sigma_g},\quad\text{and}\quad v_\xi=+\frac{X_g\sigma_g}{\sigma_{Ray}+X_g\sigma_g}. \tag{3.50}$$

In the Earth's atmosphere, there are normally at least two scatterers (molecules and aerosols, where the latter may include clouds). For each particulate s in layer q, we have single scattering albedos ω_{qs} and phase function moment coefficients β_{lqs}. Each single scattering albedo is normalized to the total extinction coefficient. Then we have $\omega_q=\sum_s\omega_{qs}$, and the combination $\omega_q\beta_{lq}$ which appears in the equations in Sections 3.2 and 3.3 is defined by the sum $\sum_s\omega_{qs}\beta_{lqs}$ over particulates. β_{lq} is a weighted mean value of the separate moment coefficients β_{lqs}. For the linearization, we also have relative derivatives u_{qs} defined for each scatterer s. Continuing to use these definitions of ω_q and β_{lq}, it is necessary to define weighted mean values u_{lq} such that $\omega_q\beta_{lq}u_{lq}=\sum_s\beta_{lqs}\omega_{qs}u_{qs}$. This is the combination that appears in the linearization analysis.

In a multi-layer atmosphere, it is important to note that variations in parameter ξ_q in layer q will affect all *cumulative* vertical optical depths τ in and below that layer. For layers below q, the variation in τ is $\Delta_q v_q$, since the optical thickness of layer q will undergo variation by this amount, but optical thicknesses for all layers below q are not affected. This observation applies equally to slant path optical depth values, since layer slant optical thicknesses are also proportional to extinction coefficients.

Summarizing, we may write down the rules for the linearization analysis:

$$L_q[\tau] = \begin{cases} xv_q, & \text{for } \tau_{q-1} < \tau < \tau_q, \\ 0, & \text{for } \tau \leqslant \tau_{q-1}, \\ \Delta_q v_q, & \text{for } \tau \geqslant \tau_q; \end{cases} \tag{3.51a}$$

$$L_q[\omega_p] = \begin{cases} u_q\omega_q, & \text{for } q = p, \\ 0, & \text{for } q \neq p. \end{cases} \tag{3.51b}$$

for $x = \tau - \tau_{q-1}$ and $\Delta_q = \tau_q - tau_{q-1}$.

Now we examine the linearization of the direct beam attenuation. From (3.32), it follows that $L_q[\kappa_p] = v_q\kappa_{pq}$, and from the definition (3.33) of the average secant parameterization, we obtain:

$$L_q\left[\hat{T}_p\right] = -v_q\kappa_{p-1,q}\hat{T}_p, \quad \text{for} \quad q < p; \quad L_q\left[\hat{T}_p\right] = 0 \quad \text{for} \quad q \geqslant p, \tag{3.52}$$

with

$$\Delta_p L_q[\lambda_p] = \begin{cases} -v_q\left(\kappa_{pq} - \kappa_{p-1,q}\right), & \text{for} \quad q < p \quad \text{and} \quad p > 1, \\ -v_q\left(\kappa_{pq} - \Delta_p\lambda_p\right), & \text{for} \quad q = p, \\ 0, & \text{for} \quad q > p. \end{cases} \tag{3.53}$$

Bringing these results together, we find

$$\Delta_p L_q[T_p(x)] = \begin{cases} -v_q\left[\kappa_{pq}(\Delta_p - x) - \kappa_{p-1,q}x\right]T_p(x), & \text{for} \quad q < p \quad \text{and} \quad p > 1, \\ -v_q\kappa_{pq}xT_p(x), & \text{for} \quad q = p, \\ 0, & \text{for} \quad q > p. \end{cases} \tag{3.54}$$

These results are vital for the linearization analysis of the particular integral, and we will need them later. For the plane-parallel (pp) case, we have $\lambda_p = \mu_0^{-1}$ and $\kappa_{pq} = \Delta_p\mu_0^{-1}$, and hence

$$\mu_0 L_q\left[T_p^{(pp)}(x)\right] = \begin{cases} -v_q\Delta_q T_p^{(pp)}(x), & \text{for} \quad q < p \\ -v_q x T_p^{(pp)}(x), & \text{for} \quad q = p \\ 0, & \text{for} \quad q > p. \end{cases} \tag{3.55}$$

The plane-parallel result was derived in a different form in SKC; the average secant result is new.

In Section 3.4.2 we go through the linearization process for the discrete ordinate homogeneous solutions; this mirrors the treatment in SKC. Sections 3.4.3 and 3.4.4 deal with the linearization of the classical and Green's function particular integrals, with particular emphasis paid to the effects of the pseudo-spherical assumption. The analysis for the particular solutions is restricted to the average secant parameterization. The linearization of the boundary value problem follows in Section 3.4.5; the treatment is more general than the plane-parallel analysis presented in SKC. In Section 3.4.6 we examine the post-processing function in order to establish linearizations (and hence weighting functions) at arbitrary optical depth and stream angle, again paying particular attention to the pseudo-spherical treatment.

Note also that one can define an albedo weighting function: $K_R(\tau,\mu) = R\partial I(\tau,\mu)/\partial R$. For a Lambertian surface, this weighting function is only nonzero for the azimuth-independent Fourier term. Layer homogeneous and particular solutions do not depend on the albedo, so their partial derivatives with respect to R vanish. The albedo only appears explicitly in the surface boundary condition BC3, so the corresponding linearization operator L_R need only be applied to this result. We note this development in section 3.4.5, and mention the post-processing function for albedo weighting functions in 3.4.6. The notion of an albedo weighting function can easily be extended to a more general surface reflectance condition, if we assume no sensitivity to the shape of the bi-directional reflectance function.

The analysis presented here is restricted to a solar beam source; we do not consider weighting functions with respect to sources of atmospheric thermal emission. However, the latter was done in SKC, where thermal emission was assumed isotropic, and the results established in that work can easily be incorporated in the present analysis.

3.4.2. Linearization analysis for the homogeneous solutions

We assume that derivatives $\left\{u_q, v_q\right\}$ have been defined with respect to property ξ varying in layer q. We drop the index q for now, since derivatives with respect to ξ vanish for homogeneous solutions in layers other than q. If x is the optical thickness measured from the top boundary of the layer, and Δ the thickness for the whole layer, then as noted above, $L\left[x\right] = xv$ and $L\left[\Delta\right] = \Delta v$. The homogeneous solutions are $\mathbf{X}^{(P)}_{\alpha} e^{-k_\alpha x}$ and $\mathbf{X}^{(N)}_{\alpha} e^{-k_\alpha(\Delta - x)}$. Applying the linearization operation and using the chain rule gives us:

$$L\left[\mathbf{X}^{(P)}_{\alpha} e^{-k_\alpha x}\right] = e^{-k_\alpha x}\left\{L\left[\mathbf{X}^{(P)}_{\alpha}\right] - \left(L\left[k_\alpha\right] + v k_\alpha\right) x \mathbf{X}^{(P)}_{\alpha}\right\}, \tag{3.56}$$

$$L\left[\mathbf{X}^{(N)}_{\alpha} e^{-k_\alpha(\Delta - x)}\right] = e^{-k_\alpha(\Delta - x)}\left\{L\left[\mathbf{X}^{(N)}_{\alpha}\right] - \left(L\left[k_\alpha\right] + v k_\alpha\right)\left(\Delta - x\right) \mathbf{X}^{(N)}_{\alpha}\right\}. \tag{3.57}$$

To determine $L\left[k_\alpha\right]$ and $L\left[\mathbf{X}_\alpha\right]$, we apply the linearization operator to the eigenvalue problem (3.10). We note first that the elements Π_{ij} in the definitions of $\boldsymbol{\zeta}$ and $\boldsymbol{\eta}$ in (3.11) are proportional to ω, so that $L\left[\Pi_{ij}\right] = u\Pi_{ij}$. It follows that:

$$L\left[\Gamma_{ij}\right] = u\sum_{l=1}^{N}\left\{\frac{w_l C^{-}_{il}}{\mu_i}\left(\zeta_{lj} + \eta_{lj}\right) + \left(\zeta_{il} - \eta_{il}\right)\frac{w_j C^{+}_{lj}}{\mu_l}\right\}, \quad \text{where} \quad C^{\pm}_{ij} = \Pi^{+}_{ij} \pm \Pi^{-}_{ij}. \tag{3.58}$$

The linearization of (3.10) gives:

$$\sum_{j=1}^{N}\left(\Gamma_{ij} - \delta_{ij}k^2_\alpha\right) L\left[\varsigma_{j\alpha}\right] = 2k_\alpha L\left[k_\alpha\right]\varsigma_{i\alpha} + \sum_{l=1}^{N} L\left[\Gamma_{ij}\right]\varsigma_{j\alpha}. \tag{3.59}$$

Since for each α there are $N+1$ unknowns $L\left[k_\alpha\right]$ and $L\left[\varsigma_{i\alpha}\right]$, $i = 1, \ldots, N$, an additional condition is required in order to find the solution. This comes from the unit normalization condition imposed on the eigenvectors. Since $\boldsymbol{\varsigma}_\alpha \cdot \boldsymbol{\varsigma}_\alpha = 1$ (vector product), then it follows that $L\left[\boldsymbol{\varsigma}_\alpha\right] \cdot \boldsymbol{\varsigma}_\alpha = 0$. Together with (3.59), we get the combined linear system $\boldsymbol{M}_\alpha \boldsymbol{\Xi}_\alpha = \boldsymbol{B}_\alpha$, where vectors $\boldsymbol{\Xi}_\alpha$ and $\boldsymbol{B}_\alpha$ and matrix $\boldsymbol{M}_\alpha$

are given by:

$$\boldsymbol{\Xi}_\alpha = \begin{bmatrix} L\left[k_\alpha\right] \\ L\left[\varsigma_{1\alpha}\right] \\ L\left[\varsigma_{2\alpha}\right] \\ \vdots \\ L\left[\varsigma_{N\alpha}\right] \end{bmatrix}, \boldsymbol{B}_\alpha = \begin{bmatrix} \sum_j \xi_{1j}\varsigma_{j\alpha} \\ \sum_j \xi_{2j}\varsigma_{j\alpha} \\ \vdots \\ \sum_j \xi_{Nj}\varsigma_{j\alpha} \\ 0 \end{bmatrix},$$

$$\boldsymbol{M}_\alpha = \begin{bmatrix} 2k_\alpha\varsigma_{1\alpha} & k_\alpha^2 - \Gamma_{11} & -\Gamma_{12} & \cdots & -\Gamma_{1N} \\ 2k_\alpha\varsigma_{2\alpha} & -\Gamma_{21} & k_\alpha^2 - \Gamma_{22} & \cdots & -\Gamma_{2N} \\ \vdots & \vdots & \vdots & \ddots & \vdots \\ 2k_\alpha\varsigma_{N\alpha} & -\Gamma_{N1} & -\Gamma_{N2} & \cdots & k_\alpha^2 - \Gamma_{NN} \\ 0 & \varsigma_{1\alpha} & \varsigma_{2\alpha} & \cdots & \varsigma_{N\alpha} \end{bmatrix}. \tag{3.60}$$

Solving this system gives us $L\left[k_\alpha\right]$ and $L\left[\boldsymbol{\varsigma}_\alpha\right]$. We now linearize the auxiliary equation (3.12) to find $L\left[\boldsymbol{\vartheta}_\alpha\right]$. From these results, the linearizations $L\left[\mathbf{X}_\alpha^{(P)}\right]$ and $L\left[\mathbf{X}_\alpha^{(N)}\right]$ may be obtained; these have the same symmetry properties (3.14) as the original solution vectors. Re-introducing layer indices, we note that for $q \neq p$, $L_q\left[k_{p\alpha}\right] = 0$, $L_q\left[\mathbf{X}_{p\alpha}^{(P)}\right] = 0$ and $L_q\left[\mathbf{X}_{p\alpha}^{(P)}\right] = 0$. These results were derived in SKC using perturbation methods.

3.4.3. Linearization analysis for the classical particular solution

In this section, we retain the layer indices. We derive the linearization only for the average secant parameterization of the direct beam transmittance. The original particular solution in a given layer q was determined from the linear system (3.38), so that application of the linearization operator L_q will result in the same linear system with a different source vector. From the previous section, we know the linearizations $L_q\left[\boldsymbol{\Gamma}_q\right]$, $L_q\left[\boldsymbol{\zeta}_q\right]$ and $L_q\left[\boldsymbol{\eta}_q\right]$; all these matrices are linearly proportional to ω_q, so their linearizations depend only on u_q. Further, $L_q\left[\boldsymbol{\Gamma}_p\right] = 0$ for $q \neq p$, and similarly for $\boldsymbol{\zeta}_p$ and $\boldsymbol{\eta}_p$. Secondly, we have $L_q\left[\mathbf{S}_q\right] = u_q\mathbf{S}_q$ and $L_q\left[\mathbf{D}_q\right] = u_q\mathbf{D}_q$, since $\mathbf{S}_q = \mathbf{Q}_q^+ + \mathbf{Q}_q^-$, $\mathbf{D}_q = \mathbf{Q}_q^+ - \mathbf{Q}_q^-$ and $\mathbf{Q}_q^\pm$ as defined in (3.36) varies with ω_q. Again there is no variation of these quantities for $q \neq p$. With these considerations in mind, we can now apply the linearization operator directly to (3.38). The result for the pseudo-spherical case is:

$$\left(\boldsymbol{\Gamma}_p - \hat{\mathbf{E}}\lambda_p^2\right) L_q\left[\mathbf{H}_p\right] = \delta_{pq}\mathbf{Z}_q + \left(2\lambda_p\mathbf{H}_p - \mathbf{D}_p\right) L_q\left[\lambda_p\right] \tag{3.61}$$

where

$$\mathbf{Z}_q = -L_q\left[\boldsymbol{\zeta}_q - \boldsymbol{\eta}_q\right]\mathbf{S}_q - \left(\boldsymbol{\zeta}_q - \boldsymbol{\eta}_q\right) L_q\left[\mathbf{S}_q\right] - \lambda_q L_q\left[\mathbf{D}_q\right] - L_q\left[\boldsymbol{\Gamma}_q\right]\mathbf{H}_q \tag{3.62}$$

This result is valid for $p \geqslant q$. [The plane-parallel result is considerably simpler: only the term $\delta_{pq}\mathbf{Z}_q$ is present, since $L_q\left[\lambda_p\right] = 0$ for $\lambda_p = \mu_0^{-1}$ a constant; it follows that $L_q\left[\mathbf{H}_p\right] = 0$ for $p \neq q$ in this case]. It is clear from (3.61) that the solutions $L_q\left[\mathbf{H}_p\right]$ are determined using the same matrices $\boldsymbol{\Gamma}_p - \hat{\mathbf{E}}\lambda_p^2$ that were used in the original system (3.38). Since we have already inverted these matrices while solving for the original vectors $\mathbf{H}_p$, the linearizations follow by straightforward back-substitution.

In a similar vein, we can linearize the auxiliary equation (3.39) to find $L_q\left[\mathbf{J}_p\right]$:

$$\lambda_p L_q\left[\mathbf{J}_p\right] = -\mathbf{J}_p L_q\left[\lambda_p\right] + \left(\boldsymbol{\zeta}_p + \boldsymbol{\eta}_p\right) L_q\left[\mathbf{H}_p\right] + \delta_{pq}\mathbf{Z}_q, \tag{3.63}$$

where this time the auxiliary vector $\mathbf{Z}_q$ is given by

$$\mathbf{Z}_q = L_q\left[\boldsymbol{\zeta}_q + \boldsymbol{\eta}_q\right]\mathbf{H}_q. \tag{3.64}$$

This result is valid for $p \geqslant q$ in the pseudo-spherical case. [In the plane-parallel case, $L_q[\mathbf{J}_p] = 0$ for $p \neq q$]. Equations (3.61)-(3.64) are sufficient to determine the linearizations $L_q\left[\mathbf{F}_p^{\pm}\right]$ in the definition of the particular solution. Since the particular solutions themselves are given by $\mathbf{G}_p^{\pm}(x) = \mathbf{F}_p^{\pm}T_p(x)$, where $T_p(x) = \hat{T}_p e^{-x\lambda_p}$, we can now write down the complete result for the linearization of $\mathbf{G}_p^{\pm}$:

$$L_q\left[\mathbf{G}_p^{\pm}(x)\right] = L_q\left[\mathbf{F}_p^{\pm}\right]T_q(x) + \mathbf{F}_p^{\pm}L_q\left[T_p(x)\right], \quad \text{for} \quad p \geqslant q, \tag{3.65}$$

where $L_q[T_p(x)]$ is given by (3.54).

3.4.4. Linearization analysis for the Green's function particular solution

In this section we carry out a linearization analysis on the Green's function solution. We retain layer indices throughout. In (3.43), $a_{p\alpha}$ is independent of optical depth, so that $L_q[a_{p\alpha}] = 0$ for $p \neq q$, and similarly for the other terms defined in (3.43) and (3.44). We proceed by applying the linearization operator to (3.41) and using the chain rule:

$$L_q\left[G_{jp}^{+}(x)\right] = \sum_{\alpha=1}^{N}\left\{L_q[A_{p\alpha}(\tau)]X_{jp\alpha}^{(P)} + L_q[B_{p\alpha}(\tau)]X_{jp\alpha}^{(N)}\right\} + \delta_{pq}Z_{jq} \tag{3.66}$$

where now

$$Z_{jq} = \sum_{\alpha=1}^{N}\left\{A_{q\alpha}(\tau)L_q\left[X_{jp\alpha}^{(P)}\right] + B_{q\alpha}(\tau)L_q\left[X_{jp\alpha}^{(N)}\right]\right\}, \tag{3.67}$$

with a similar result for $L_q\left[G_{jp}^{-}(x)\right]$. The linearizations of $\mathbf{X}_{p\alpha}^{(P)}$ and $\mathbf{X}_{p\alpha}^{(N)}$ are known from Section 3.4.2. Further, we have from (3.42)

$$L_q[A_{p\alpha}(\tau)] = \delta_{pq}L_q[a_{p\alpha}]C_{p\alpha}^{+}(\tau) + a_{p\alpha}L_q\left[C_{p\alpha}^{+}(\tau)\right], \tag{3.68}$$

and similarly for $L_q[B_{p\alpha}(\tau)]$. From the definition (3.43) for $a_{p\alpha}$, we find

$$L_q\left[a_{q\alpha}\right] = \frac{a_{q\alpha}}{N_{q\alpha}}\left\{u_q N_{q\alpha} - L_q\left[N_{q\alpha}\right]\right\} + \frac{1}{N_{q\alpha}}\sum_{j=1}^{N} w_j\left\{Q_{jq}^{-}L_q\left[X_{jq\alpha}^{(N)}\right] + Q_{jq}^{+}L_q\left[X_{jq\alpha}^{(P)}\right]\right\}, \tag{3.69}$$

and similarly for $L_q\left[b_{q\alpha}\right]$. In deriving this result we used the fact that $L_q\left[Q_{jq}^{\pm}\right] = u_q Q_{jq}^{\pm}$. For the linearization of the normalization factor $N_{q\alpha}$ in (3.44), we obtain

$$L_q\left[N_{q\alpha}\right] = 2\sum_{j=1}^{N}\mu_j w_j\left\{X_{j\alpha}^{(N)}L_q\left[X_{jq\alpha}^{(N)}\right] - X_{j\alpha}^{(P)}L_q\left[X_{jq\alpha}^{(P)}\right]\right\}. \tag{3.70}$$

In dealing with the linearizations of the optical depth multipliers in (3.46), we must distinguish between those multipliers in the layer q in which the variation in parameter ξ_q is taking place, and multipliers in layers $p > q$ which will be affected by the variation in layer q. Using the fact that $L_q[\Delta_p] = \Delta_q v_q \delta_{pq}$ and $L_q[x] = x v_q \delta_{pq}$ for x in q, and the result already established in Section 3.4.2 for $L_q\left[k_{q\alpha}\right]$, we find

$$L_q\left[C^+_{p\alpha}(x)\right] = \frac{\hat{T}_p}{\lambda_p - k_{p\alpha}}\left\{-e^{-x\lambda_p} x\chi_{pq} + e^{-\Delta_p\lambda_p} e^{-(\Delta_p - x)k_{p\alpha}}\psi_{pq\alpha}\right\} + \varpi^+_{pq\alpha} C^+_{p\alpha}(x), \tag{3.71}$$

$$L_q\left[C^-_{p\alpha}(x)\right] = \frac{\hat{T}_p}{\lambda_p + k_{p\alpha}}\left\{-e^{-xk_{p\alpha}}\delta_{pq} x\gamma_{q\alpha} + e^{-x\lambda_p} x\chi_{pq}\right\} + \varpi^-_{pq\alpha} C^-_{p\alpha}(x), \tag{3.72}$$

where

$$\gamma_{q\alpha} = L_q\left[k_{q\alpha}\right] + v_q k_{q\alpha}, \tag{3.73}$$

$$\chi_{pq} = \delta_{pq} v_q \lambda_p + L_q\left[\lambda_p\right], \tag{3.74}$$

$$\varpi^\pm_{pq\alpha} = \frac{L_q\left[\hat{T}_p\right]}{\hat{T}_p} \mp \frac{L_q\left[\lambda_p\right] \mp \delta_{pq} L_q\left[k_{q\alpha}\right]}{\lambda_p \mp k_{p\alpha}}, \quad \text{and} \tag{3.75}$$

$$\psi_{pq\alpha} = \Delta_p \varpi^+_{pq\alpha} + \delta_{pq}(\Delta_p - x)\gamma_{q\alpha}. \tag{3.76}$$

Again this is valid for $p \geqslant q$. This completes the linearization of the Green's function solution.

3.4.5. Linearization analysis of the boundary value problem

This is one of the most important aspects of the weighting function analysis. Applying the linearization operator to the boundary conditions will determine the linearizations $L_q\left[L_{p\alpha}\right]$ and $L_q\left[M_{p\alpha}\right]$ for the integration constants $L_{p\alpha}$ and $M_{p\alpha}$ in (3.16) in terms of the linearizations worked out in the previous three sub-sections for the component homogeneous and particular solutions. We first apply the chain rule to (3.16) in layer p:

$$L_q\left[I_{jp}\right] = \sum_{\alpha=1}^{N}\left\{L_q\left[L_{p\alpha}\right] X^{(P)}_{jp\alpha} e^{-k_{p\alpha}x} + L_q\left[M_{p\alpha}\right] X^{(N)}_{jp\alpha} e^{-k_{p\alpha}\left(\Delta_p - x\right)}\right\} + L_q\left[G_{jp}\right] + \delta_{pq} L_q\left[Z_{jq}\right], \tag{3.77}$$

where some of the dependence on x has been suppressed for convenience. The last term is only present when $p = q$ and is given by

$$L_q\left[Z_{jq}\right] = \sum_{\alpha=1}^{N}\left\{L_{q\alpha} L_q\left[X^{(P)}_{jq\alpha} e^{-k_{q\alpha}x}\right] + M_{q\alpha} L_q\left[X^{(N)}_{jq\alpha} e^{-k_{q\alpha}\left(\Delta_q - x\right)}\right]\right\}. \tag{3.78}$$

We can now apply the linearization operator to the three boundary conditions BC1, BC2 and BC3 as written down in Section 3.2.3. Clearly the linearization $L_q\left[I_{jp}\right]$ must also satisfy these conditions (in terms of the perturbation analysis in SKC, the perturbed field also obeys the same conditions). Using the notation developed earlier for the boundary conditions for the intensity problem, we can write down explicit equations for these boundary conditions, noting that x takes values only at the layer boundaries (that is, $x = 0$ or $x = \Delta_p$ for layer p). We use indices p and r to label layers, while q is reserved for the layer that contains a varying parameter. By analogy with (3.19), (3.21) and (3.22), we have

$$\sum_{\alpha=1}^{N}\left\{L_q\left[L_{p\alpha}\right]X^{(P)}_{-jp\alpha}+L_q\left[M_{p\alpha}\right]\Theta_{p\alpha}X^{(N)}_{-jp\alpha}\right\}=B^{(1)}_{jp}, \tag{3.79a}$$

$$\sum_{\alpha=1}^{N}\left[\left\{L_q\left[L_{r\alpha}\right]\Theta_{r\alpha}X^{(P)}_{jr\alpha}+L_q\left[M_{r\alpha}\right]X^{(N)}_{jr\alpha}\right\}-\left\{L_q\left[L_{p\alpha}\right]X^{(P)}_{jp\alpha}+L_q\left[M_{p\alpha}\right]\Theta_{p\alpha}X^{(N)}_{jp\alpha}\right\}\right]=B^{(2)}_{jp}, \tag{3.79b}$$

$$\sum_{\alpha=1}^{N}\left\{L_q\left[L_{p\alpha}\right]\Theta_{p\alpha}\Phi^{(P)}_{j\alpha}+L_q\left[M_{p\alpha}\right]\Phi^{(N)}_{j\alpha}\right\}=B^{(3)}_{jp}. \tag{3.79c}$$

The right hand side vectors are

$$B^{(1)}_{jp}=-\left\{L_q\left[G_{-jp}\right]+\delta_{pq}L_q\left[Z_{-jp}\right]\right\}\big|_{\tau_0}, \tag{3.80a}$$

$$B^{(2)}_{jp}=\left\{\left(L_q\left[G_{jp}\right]-L_q\left[G_{jr}\right]\right)+\left(\delta_{pq}L_q\left[Z_{jp}\right]-\delta_{rq}L_q\left[Z_{jr}\right]\right)\right\}\big|_{\tau_r}, \tag{3.80b}$$

$$B^{(3)}_{jp}=R\mu_0F_{\odot}L_q\left[\hat{T}_pe^{-\Delta_p\lambda_p}\right]-L_q\left[\Psi_j\right]-\delta_{pq}L_q\left[Y_{jp}\right]. \tag{3.80c}$$

In (3.79a) and (3.79c), $j=1,\dots N$, and $-j$ denotes the downwelling stream directions. In (3.79b), $j=\pm1,\dots,\pm N$. On the right hand sides, the vectors B are evaluated at the optical depths indicated; $p=1$ in (3.79a), $r=p-1$ in (3.79b) and $p=K$ in (3.79c). The transmittance factors $\Theta_{p\alpha}$ have been defined in (3.20), vectors $\mathbf{\Phi}^{(P)}$ and $\mathbf{\Phi}^{(N)}$ in (3.23a), and $\mathbf{\Psi}$ in (3.23b). The BC3 condition was written down for a Lambertian surface in (3.80c), but the generalization to a bi-directional surface is straightforward. There is one additional definition in (3.80c), namely

$$L_q\left[Y_{jq}\right]=\sum_{\alpha=1}^{N}\left\{L_{q\alpha}L_q\left[\Phi^{(P)}_{j\alpha}\Theta_{p\alpha}\right]+M_{q\alpha}L_q\left[\Phi^{(N)}_{jq\alpha}\right]\right\}. \tag{3.81}$$

It is seen immediately that these conditions provide a linear system similar to that used to solve the original boundary value problem. Indeed the solution matrix A in section is the same as before, so we can write $AL_q[X]=L_q[B]$, where the vector $L_q[X]$ consists of the set of unknown linearized integration constants $L_q[L_{p\alpha}]$ and $L_q[M_{p\alpha}]$, and the solution vector $L_q[B]$ is constructed from the expressions (3.80a), (3.80b) and (3.80c). Since we have already found the inverse of A while solving the original boundary value problem, it is straightforward to determine the vector $L_q[X]$ by back-substitution. No additional matrix inversion is required, and the results are analytic, depending only on the accuracy with which the original intensity was calculated. The formulation presented here is slightly different from that in SKC, where a more explicit breakdown of the boundary conditions was presented in a plane-parallel multilayer atmosphere.

For the albedo weighting function, the discrete ordinate homogeneous and particular solutions have no partial derivatives, and we need only find $L_R[L_{p\alpha}]$ and $L_R[M_{p\alpha}]$. For a Lambertian surface, the corresponding linearization of BC1, BC2 and BC3 for the Fourier $m = 0$ component gives:

$$\sum_{\alpha=1}^{N}\left\{L_R\left[L_{p\alpha}\right]X^{(P)}_{-jp\alpha}+L_R\left[M_{p\alpha}\right]\Theta_{p\alpha}X^{(N)}_{-jp\alpha}\right\}=B^{(R1)}_{jp},\tag{3.82}$$

$$\sum_{\alpha=1}^{N}\left[\left\{L_R\left[L_{r\alpha}\right]\Theta_{r\alpha}X^{(P)}_{jr\alpha}+L_R\left[M_{r\alpha}\right]X^{(N)}_{jr\alpha}\right\}-\left\{L_R\left[L_{p\alpha}\right]X^{(P)}_{jp\alpha}+L_R\left[M_{p\alpha}\right]\Theta_{p\alpha}X^{(N)}_{jp\alpha}\right\}\right]=B^{(R2)}_{jp},\tag{3.83}$$

$$\sum_{\alpha=1}^{N}\left\{L_R\left[L_{p\alpha}\right]\Theta_{p\alpha}\Phi^{(P)}_{j\alpha}+L_R\left[M_{p\alpha}\right]\Phi^{(N)}_{j\alpha}\right\}=B^{(R3)}_{jp},\tag{3.84}$$

where $B^{(R1)}_{jp} = 0$ for $p = 1$ and $j = 1,\ldots,N$; $B^{(R2)}_{jp} =$ for all $p > K$ and $j = 1 \pm 1,\ldots,\pm N$, and

$$B^{(R3)}_{jK} = R\mu_0 F_{\odot} e^{-\tau_{spher}(\tau_K)} - 2R\sum_{i=1}^{N} w_i\mu_i\, G_{-iK}\big|_{\tau_K}.\tag{3.85}$$

We have used (3.23a) and (3.23b) to establish $B^{(R3)}_{jp}$ for $p = K$ and $j = 1,\ldots,N$. Again, we have the same linear system, this time with a new source vector constructed from the right-hand entries. The solution for $L_R\left[L_{p\alpha}\right]$ and $L_R\left[M_{p\alpha}\right]$ follows once again by back-substitution.

Once the linearizations of the integration constants have been found, it is possible to write the linearization of the discrete-ordinate solution anywhere in the atmosphere, and hence we have determined weighting functions at quadrature values and at arbitrary optical depth. In order to complete the weighting function solution for arbitrary stream angles, we now look at the linearization analysis of the post-processing function.

3.4.6. Linearization analysis of the post-processing function

We return to expressions (3.24a) and (3.24b) for the partial layer intensities derived using the source function integration technique. Since $L_q\left[\Delta_q\right] = \Delta_q v_q$ and $L_q\left[x\right] = x v_q$ for x in layer q, we have

$$L_q\left[I^{+}(x,\mu)\right]=\left\{L_q\left[I^{+}_{p}(\mu)\right]-\delta_{pq}v_q\left(\Delta_p-x\right)\mu^{-1}I^{+}_{p}(\mu)\right\}e^{-\left(\Delta_p-x\right)/\mu}+\varepsilon_{pq}L_q\left[\Lambda^{+}_{p}(x,\mu)\right],\tag{3.86a}$$

$$L_q\left[I^{-}(x,\mu)\right]=\left\{L_q\left[I^{-}_{p-1}(\mu)\right]-\delta_{pq}v_q x\mu^{-1}I^{-}_{p-1}(\mu)\right\}e^{-x/\mu}+\varepsilon_{pq}L_q\left[\Lambda^{-}_{p}(x,\mu)\right],\tag{3.86b}$$

where $\delta_{pq} = 1$ for $p = q$ and $\delta_{pq} = 0$ otherwise, and $\varepsilon_{pq} = 1$ for $p \geqslant q$ and $\varepsilon_{pq} = 0$ for $p < q$. The latter condition arises from the fact that the source terms $\Lambda^{\pm}_{p}(x,\mu)$ have no linearization for $p < q$. Expressions for whole layers can be obtained by setting $x = 0$ in (3.86a) and $x = \Delta_p$ in (3.86b).

Recalling the expression (3.26) for the source function terms, we write

$$L_q\left[\Lambda^{\pm}_{p}(x,\mu)\right]=L_q\left[H^{\pm}_{p}(x,\mu)\right]\delta_{pq}+L_q\left[D^{\pm}_{p}(x,\mu)\right]+L_q\left[E^{\pm}_{p}(x,\mu)\right].\tag{3.87}$$

This is valid for variations in layers $p \leqslant q$. Note that the homogeneous solution contribution $H^{\pm}_{p}(x,\mu)$ has no variation outside layer q. Finding the linearizations of the three quantities on the right hand side of this equation is a straightforward but lengthy exercise; one proceeds using already-established results from the linearization of the discrete ordinate solution, along with repeated applications of the chain rule. The mathematical details are given in Appendices 3.8.3, 3.8.3 and 3.8.3 for the three right hand side terms in (3.87) respectively.

As with the intensity calculation, the above results can be used recursively to generate weighting functions at arbitrary optical depth and direction. For whole layer terms we simply set $x = \Delta_p$ or $x = 0$ for layer p. For the upwelling values at point x in layer p, we start with the bottom-of-the atmosphere linearization $L_q[I^+(\tau_K, \mu)]$ and use the whole-layer expressions repeatedly for layers below p, followed by a single partial-layer application of (3.86a) in layer p to finish. Care should be taken to distinguish the cases $p = q$, $p < q$ and $p > q$.

3.5. The LIDORT package

Based on the theory presented in this paper and the preceding one (SKC), the numerical model LIDORT (LInearized Discrete Ordinate Radiative Transfer) has been developed as a general tool for use in forward model studies connected with atmospheric retrieval. The model can be used in an intensity-only mode (without the linearization options) or additionally to generate simultaneous fields of weighting functions. The first version based on SKC dealt with the satellite application in a plane-parallel atmosphere. The second version has two important extensions to cover the pseudo-spherical treatment of the direct beam attenuation and to generate output for any atmospheric application. The LIDORT V2 package has the following attributes:

1. Multiple scatter treatment of the radiative transfer equation in an inhomogeneous atmosphere, with any number of scatterers. A general treatment for a bi-directionally reflecting surface is available;
2. Generation of upwelling and/or downwelling intensity and weighting function fields for arbitrary viewing geometry and optical depth;
3. Option to perform a plane-parallel calculation or a pseudo-spherical calculation using the average secant approximation. Both methods of particular integral solution (classical and Green's function) are implemented;
4. Weighting functions may be generated with regard to any atmospheric parameter that causes variation in layer extinction coefficient and single-scatter albedo. Options to output weighting functions with respect to albedo and surface blackbody temperature are implemented;
5. Additional output includes mean-value quantities (flux, mean intensity) and their weighting functions, and layer-integrated multiple scatter source terms and associated weighting functions;
6. The delta-M scaling transformation has been incorporated both in the intensity calculation and in the weighting function analysis.

Double precision arithmetic is used throughout LIDORT; the code is written in FORTRAN 77. For the numerical tools, the module ASYMTX from DISORT was used for the homogeneous solution eigenproblem, and LAPACK modules [65] were employed for all linear matrix algebra systems. LIDORT contains a standardized error handling procedure in addition to a number of auxiliary routines for both the reading of input data from files, and the generation of result data to file. As noted already, LIDORT is a pure scattering formalism; there are no databases or climatologies of atmospheric and optical properties in the model. The LIDORT package is called as a subroutine within a user-defined environment; the usage is similar to that for DISORT [58]. The software has been quality controlled and is portable and robust; it can be installed on PCs under the Linux operating system. Memory requirements are modest.

For the average secant parameterization, both methods of particular integral solution (Green's function and substitution) are implemented in the software. Intensity results for the two methods were found to be identical to 9 places of decimals. Computation speeds are similar: the Green's function method is faster for the determination of the discrete ordinate solution, but a little slower for the post-processing step. An off-line intensity-only version of LIDORT has been written to deal with the exponential-sine and exponential-polynomial parameterizations of the direct beam transmittance.

All plane-parallel intensity output was verified using the DISORT model; pseudo-spherical results were validated against the SDISORT code [79]. Table 3.1 gives a sample of these validations for the test atmosphere described in Section 3.6.1. Results are for upwelling intensities at TOA for line-of-sight viewing zenith angles as indicated. DISORT comparisons were done for a solar zenith angle of 15°, SDISORT validations with solar angle 82°; in both cases the relative azimuth angle was 60°. The figures apply to a 60-layer atmosphere with 10 discrete ordinate streams in the half-space for the DISORT validation, and 8 streams for the SDISORT comparison.

Angle (°)	DISORT	LIDORT PP	SDISORT	LIDORT PS
0.0	8.83804E-02	8.838043E-02	1.74379E-02	1.743787E-02
1.0	8.82865E-02	8.828647E-02	1.74259E-02	1.742588E-02
2.0	8.81990E-02	8.819904E-02	1.74194E-02	1.741939E-02
5.0	8.79799E-02	8.797986E-02	1.74333E-02	1.743328E-02
10.0	8.77839E-02	8.778397E-02	1.75709E-02	1.757091E-02
15.0	8.78271E-02	8.782700E-02	1.78613E-02	1.786122E-02
20.0	8.81004E-02	8.810022E-02	1.83187E-02	1.831864E-02
25.0	8.86090E-02	8.860901E-02	1.89573E-02	1.895727E-02

Table 3.1: TOA upwelling intensity comparisons: LIDORT plane-parallel (PP) and DISORT, LIDORT pseudo-spherical (PS) and SDISORT.

All weighting function output may be verified against finite-difference estimates

$$K_{FD}(\xi_q) \simeq \left(I(\xi_q^+) - I(\xi_q^-)\right) / (2\varepsilon_{FD}), \tag{3.88}$$

where $I(\xi_q^\pm)$ are the intensities calculated using perturbed values $\xi_q^\pm = \xi_q(1 \pm \varepsilon_{FD})$ of parameter ξ_q in layer q for an external perturbation ε_{FD}. For parameters such as volume mixing ratio for which the optical thickness dependence is linear, agreement between analytically-derived results $K_{LIDORT}(\xi_q)$ and the finite-difference equivalents $K_{FD}(\xi_q)$ can be made very close for small enough ε_{FD}. For other parameters such as temperature, where the optical property dependence is usually non-linear, the finite-difference result is at best an approximation.

The delta-M scaling transformation [36] is a useful adjunct to any radiative transfer model dealing with multiple scattering. It provides a convenient way of dealing with phase functions which are sharply peaked in the forward scattering direction; the original phase function is replaced by a delta-function forward peak plus a smoother residual which requires a limited number of Legendre phase function moments for its description. The delta-M process essentially involves an initial scaling of the optical depth inputs (single scattering albedo and vertical optical depth) before the RTE is solved. (Slant path optical thickness inputs must also be scaled when the pseudo-spherical treatment is required in the RTE solution). In a model with a simultaneous weighting function capability, it is also necessary to scale the variational inputs $\{u_q, v_q\}$ before the RTE is linearized. Details of the delta-M scaling transformations for LIDORT are presented in Appendix 3.8.4.

Creating the right inputs for the model is very important, and we will examine this in more detail in the next section when we consider examples in a real atmospheric situation. We enumerate here the main *geophysical* inputs:

1. Layer single scattering albedos ω_{qs} for any number of scatterers, each such albedo normalized to the total layer extinction coefficient. A vertical optical depth grid τ_q, plus layer slant path optical thicknesses κ_{qp} for each layer p traversed by the direct beam in its path to a scatter point at vertical optical depth τ_q.
2. Surface albedo R and an albedo-normalized bi-directional reflection function specified at all stream angles (ordinates and off-quadrature) for sufficient Fourier terms.
3. Layer phase function moment coefficients β_{lqs} for layer q, scatterer s in this layer, and for sufficient Legendre moments l to ensure valid application of the delta-M scaling.
4. Variational input $u_{q\xi s}$ which is the relative differential variation of layer single scattering albedo ω_{qs} with respect to atmospheric parameter ξ. Variational input $v_{q\xi}$ which is the relative differential variation of layer extinction coefficient e_q with respect to atmospheric parameter ξ.

The LIDORT User's Guide has a description of the complete package, and a discussion with examples on the construction of a typical environment for the model and an interface to set up the appropriate optical property inputs. The User's Guide also contains instructions on installation and execution. A test data set has been prepared for release; this is based in part on the example described in detail in below. The LIDORT source code and User's Guide may be downloaded from the SAO web site (http://cfa-www.harvard.edu/pub/lidort/v2).

3.6. Nadir and zenith examples with the LIDORT model

3.6.1. Construction of LIDORT inputs for a terrestrial scenario

For the applications considered below in Sections 3.6.2 and 3.6.3, we take a terrestrial atmosphere with height 60 km, a vertical height resolution of 1 km, with O_3 volume mixing ratios (VMRs) X_q, temperatures T_q and pressures P_q for a "tropical" standard atmosphere [69], interpolated to the mid-points of each layer. We choose a range of wavelengths in the UV covering the O_3 Hartley-Huggins absorption bands. We take O_3 cross sections σ_q^{O3} [cm^2] for layers q to possess quadratic temperature-dependency. Thus $\sigma_q^{O3} = \sigma_0 + T_q\sigma_1 + T_q^2\sigma_2$, where T_q is in °C. Coefficients $\sigma_0, \sigma_1, \sigma_2$ are taken from a standard data set [70].

Molecular (Rayleigh) scattering and aerosol scattering are present in all layers. For the wavelength dependence of the Rayleigh scattering cross section σ^{Ray} [cm^2] and the depolarization ratio δ_{Ray}, we use empirical formulae [18] based on data from Bates [80]. The only non-zero phase function moment coefficients are $\beta_0^{Ray} = 1$ and $\beta_2^{Ray} = (1 - \delta_{Ray})/(2 + \delta_{Ray})$. For the aerosol properties, a LOWTRAN model [71] is selected, with maritime-type boundary layer aerosol (visibility 23 km, relative humidity 70%) and background stratospheric and tropospheric optical properties. Aerosol scattering coefficients σ_q^{Aer} and extinction coefficients e_q^{Aer} (in [cm^{-1}]) are linearly interpolated to wavelength. For the aerosols we assume Henyey-Greenstein phase functions with asymmetry parameters g taken from the appropriate selection of LOWTRAN aerosol types and interpolated linearly with wavelength (phase function moment coefficients are $\beta_0^{Aer} = 1$, and $\beta_l^{Aer} = g^l$ for $l > 0$). The clear sky total optical thickness for this atmosphere is 1.256 at wavelength 335.4579 nm, with corresponding total Rayleigh scattering optical thickness 0.759, and total ozone absorption optical thickness 0.00707.

We illustrate the construction of LIDORT inputs for this atmosphere. Writing ρ_q for the average air number density [cm^{-3}], e_q for the layer total extinction coefficient, Δ_q the layer optical thickness, and ω_q^{Ray} and ω_q^{Aer} for the layer single scattering albedos, we get:

$$e_q = \rho_q \left[X_q \sigma_q^{O3} + \sigma^{Ray}\right] + e_q^{Aer}, \quad \text{with} \quad \Delta_q = e_q h_q, \tag{3.89a}$$

$$\omega_q^{Ray} = \rho_q \sigma^{Ray} / e_q, \quad \text{and} \quad \omega_q^{Aer} = \sigma^{Aer} / e_q, \tag{3.89b}$$

where h_q is the layer geometrical thickness [cm]. Together with β_l^{Ray} and β_l^{Aer}, these results define the LIDORT model input for the plane-parallel atmosphere in an intensity-only mode. For the pseudo-spherical approximation, we need the slant optical depths κ_{pq} as defined in (3.32); since the extinctions are known, these layer optical depths can be specified once the slant path distances s_{pq} in (3.32) have been worked out from a suitable ray-tracing program.

The second step concerns inputs $\{u_q, v_q\}$ for the weighting functions. The definitions are $L_q\left[\omega_q\right] = \xi_q \partial\omega_q / \partial\xi_q = u_q \omega_q$ and $L_q\left[e_q\right] = \xi_q \partial e_q / \partial\xi_q = v_q e_q$. We consider two atmospheric parameters ξ: the volume mixing ratio X_q and the temperature T_q. For $\xi = X_q$, the dependence on X_q is straightforward and we can write

$$u_{\xi q}^{Ray} = -\rho_q X_q \sigma_q^{O3} / e_q; \quad u_{\xi q}^{Aer} = -\rho_q X_q \sigma_q^{O3} / e_q; \quad \text{and} \quad v_{\xi q} = +\rho_q X_q \sigma_q^{O3} / e_q. \tag{3.90}$$

For $\xi = T_q$ the dependence is more complex. From the temperature dependence of the cross-sections, we find $\partial\sigma_q^{O3} / \partial T_q = \sigma_1 + 2T_q\sigma_2$. Also we have $\partial\rho_q / \partial T_q = -\rho_q / T_q$, since $\rho_q = \rho_S(P_q T_S)/(P_S T_q)$ (the S suffix indicates values for a standard atmosphere). Using this information in the definitions gives us

$$u_{\xi q}^{Ray} = -T_q^{-1} - e_q^{-1} \partial e_q / \partial T_q; \quad u_{\xi q}^{Aer} = -e_q^{-1} \partial e_q / \partial T_q; \quad \text{and} \quad v_{\xi q} = +e_q^{-1} \partial e_q / \partial T_q, \tag{3.91}$$

where

$$\partial e_q / \partial T_q = -\rho_q T_q^{-1} \left(X_q \sigma_q^{O3} + \sigma_q^{Ray}\right) + \rho_q X_q \left(\sigma_1 + 2T_q \sigma_2\right). \tag{3.92}$$

3.6.2. Intensity and O_3 VMR weighting functions from LIDORT

We look at two nadir viewing situations: (1) the upwelling radiation field at TOA as seen by a nadir-viewing satellite such as GOME, GOME-2 or SCIAMACHY; and (2) the downwelling radiation at the surface as seen by a ground-based instrument measuring sky radiances. In both cases, we assume a Lambertian surface and no surface or atmospheric thermal emission. We show results for a wide range of solar zenith angles, concentrating in particular on the higher values from 65° to 89.5° in order to examine the effect of the pseudo-spherical approximation. Line-of-sight zenith angles will range from 0° to 35°, with azimuth angles as noted. A 10-stream discrete ordinate solution was used in LIDORT, with an accuracy criterion of 0.001 on the convergence of the Fourier azimuth series (this model control is sufficient for a UV scenario with a large Rayleigh scattering component). The examples that follow are indications of the output that the model can generate.

First we compare pseudo-spherical intensities against comparable plane-parallel results. Figure 3.3 (left panel) shows the differences between the TOA upwelling intensities calculated using the plane-parallel mode and average secant parameterization to the pseudo-spherical mode. The limitation on the validity of the plane-parallel assumption is clear. A similar picture emerges for downwelling intensities at the bottom of the atmosphere (BOA) (right panel). These intensities were calculated at a single wavelength (335.4579 nm) for a number of solar zenith angles as indicated, for a range of line-of-sight angles up to 25° and for a relative azimuth of 60°.

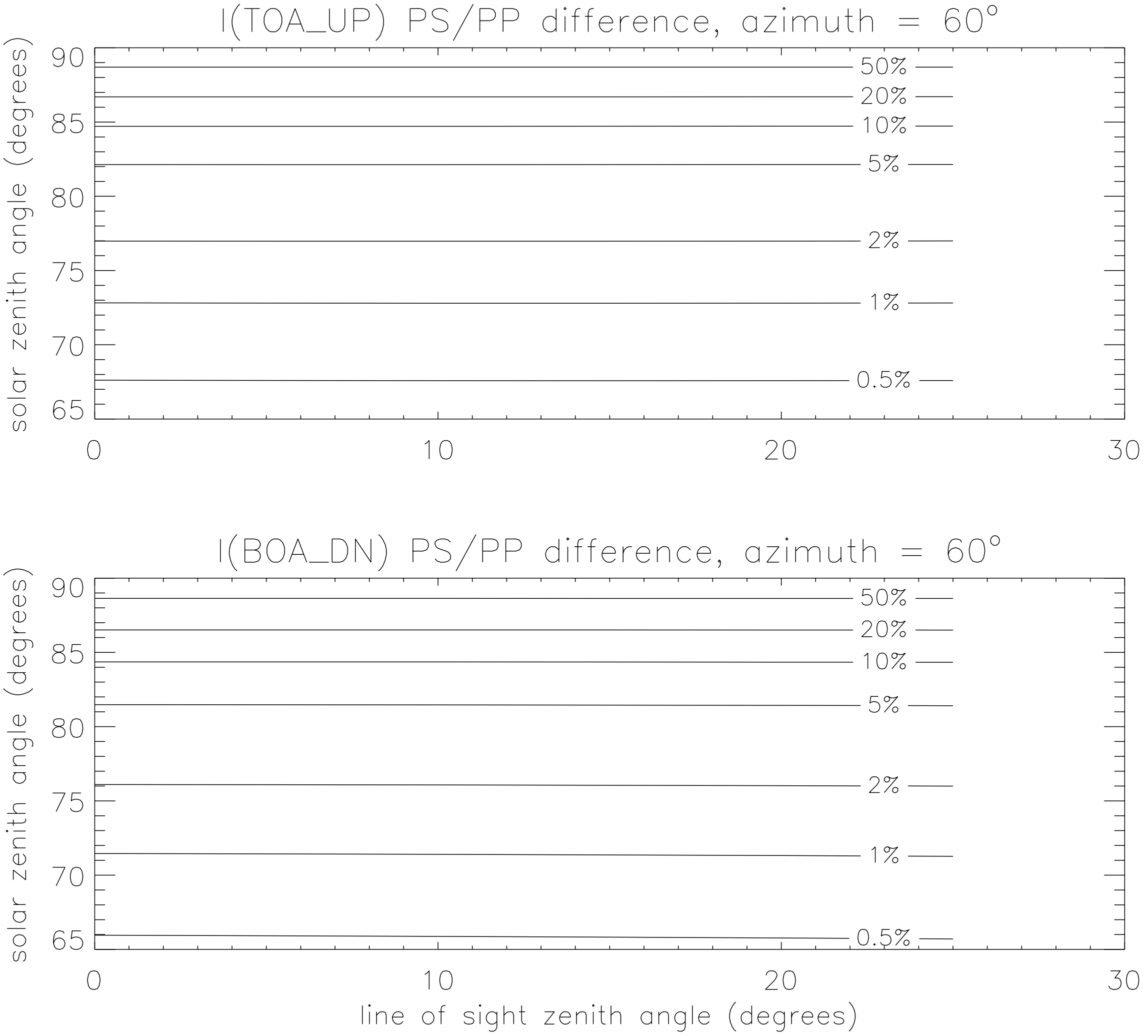

Figure 3.3: (top) TOA upwelling intensities: % difference between pseudo-spherical (average secant) and plane-parallel results for the geometries indicated, albedo 0.3, wavelength 335.4579 nm; (bottom) the same comparison for downwelling intensity at the lower boundary.

Next we look at the pseudo-spherical approximation in a little more detail. In Figure 3.4, we show the effect of neglecting refraction using the average secant parameterization. As noted before, the inclusion of refraction is really a question of providing properly ray-traced optical depth inputs; the execution of LIDORT itself is not affected by this input choice. All computations were done for the azimuth-independent term (nadir/zenith viewing) and for a number of heights (optical depths) through the atmosphere. The top panel (for the upwelling field) indicates the spread of differences through the atmosphere; the peak around 18 km is clear. The difference is less noticeable for downwelling intensities (lower panel), where the largest effect is close to the surface for the highest solar zenith angles.

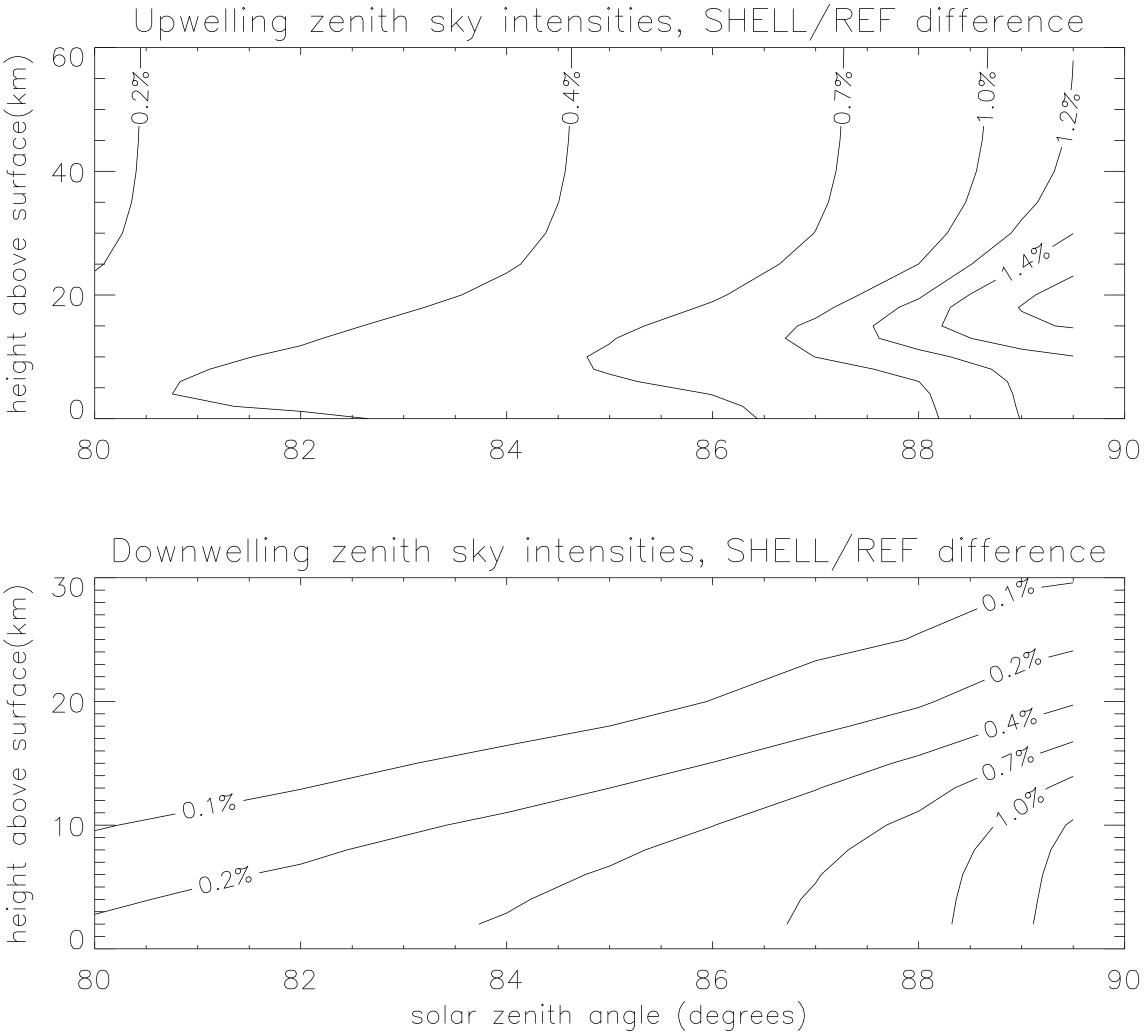

Figure 3.4: (top) Zenith upwelling intensities in the whole atmosphere: a comparison with and without refraction using the pseudo-spherical average secant parameterization. Albedo and wavelength as in Figure 3.3; (bottom) similar comparison for zenith downwelling intensities in the lower atmosphere.

The average secant pseudo-spherical parameterization is adequate for clear sky scenarios with a number of optically thin layers. We now examine a scenario where a more accurate parameterization of the direct beam is useful. To the atmosphere described in Section 3.6.1, we add a highly scattering optically thick particulate in one layer. We take a hypothetical polar stratospheric cloud (PSC) scenario, with a cloud layer of optical thickness 1.0 and single scattering albedo 0.996 between 24 and 25 km. The solar zenith angle is 88°; at this sort of incidence, layers beneath the cloud will be opaque to direct beam illumination and the light is multiply scattered in this part of the atmosphere. Figure 3.5 shows upwelling intensity LIDORT results for 3 line-of-sight viewing angles at a relative azimuth of 60°, calculated with the average secant and exponential-polynomial parameterizations of the direct beam attenuation. The latter parameterization required 3 fitted coefficients to ensure an accuracy of 1% in the beam attenuation through the cloud layer. For the viewing geometries considered, errors in the intensity due to the average secant approximation are in the range 2.5 to 4%. It is clear that for atmospheres with cloud layers, an improved direct beam parameterization will result in significantly better intensity accuracy.

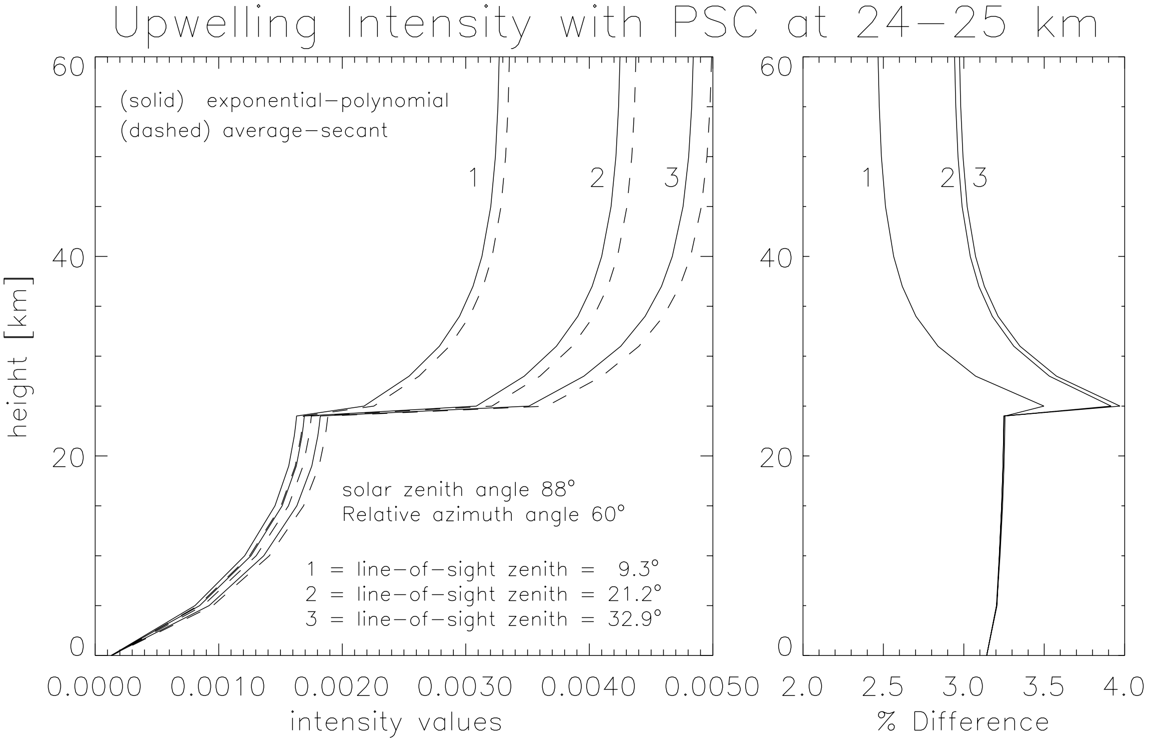

Figure 3.5: Upwelling intensities in the atmosphere using the average secant and exponential-polynomial pseudo-spherical parameterizations: a comparison. Albedo and wavelength as in Figure 3.3; geometries as indicated.

We now look at some weighting function output. Figure 3.6 shows the weighting functions with respect to O_3 volume mixing ratio for all levels in the atmosphere, and for a number (10) of wavelengths in the Hartley-Huggins range of ozone absorption. Results have been normalized to the peak values; a pseudo-spherical calculation was performed for albedo 0.3, for two solar zenith angles 35° and 82°, line of sight 15° and relative azimuth 0°. Below 300 nm, peak values occur at heights that increase with lower wavelengths. It is this well-known differential scattering height behavior that underpins the BUV technique for O_3 profile retrieval in the stratosphere [11]. Note also the increasing tropospheric sensitivity for the longer wavelengths; this sensitivity tends to disappear with increasing solar zenith angle.

Figure 3.7 shows nadir-view O_3 VMR weighting functions at one wavelength (335.4579 nm), calculated in the average secant pseudo-spherical and plane-parallel approximations for a number of solar zenith angles. The top panel shows results for the satellite application (TOA upwelling) at four selected solar zenith angles. There is a significant loss of tropospheric sensitivity for higher solar zenith angles. Note also the spurious upward drift of the peak sensitivity for the plane-parallel results. The lower panel illustrates in more detail the differences in these results.

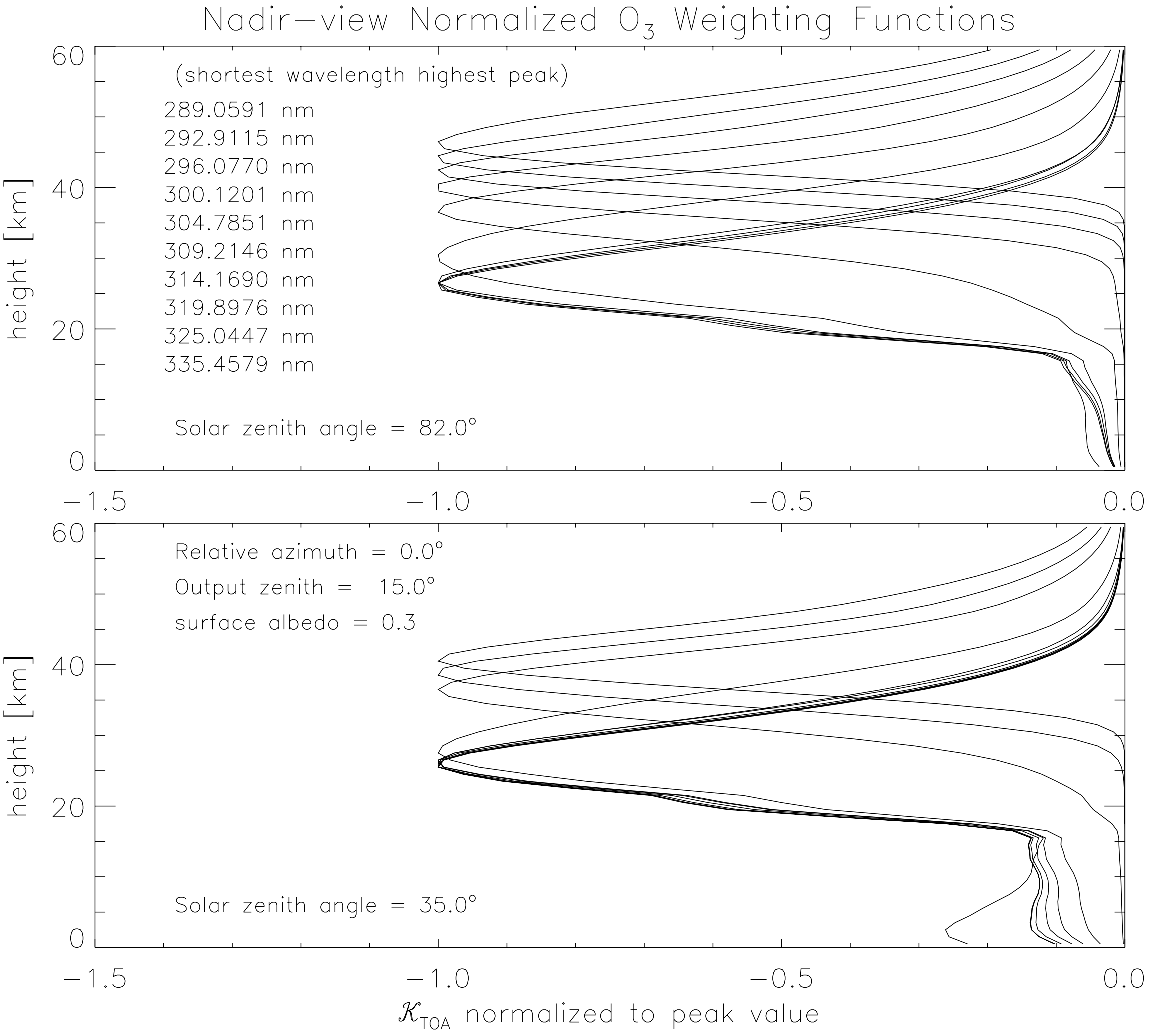

Figure 3.6: TOA upwelling O_3 VMR weighting functions for a number of wavelengths as indicated. Output is normalized to the peak values.

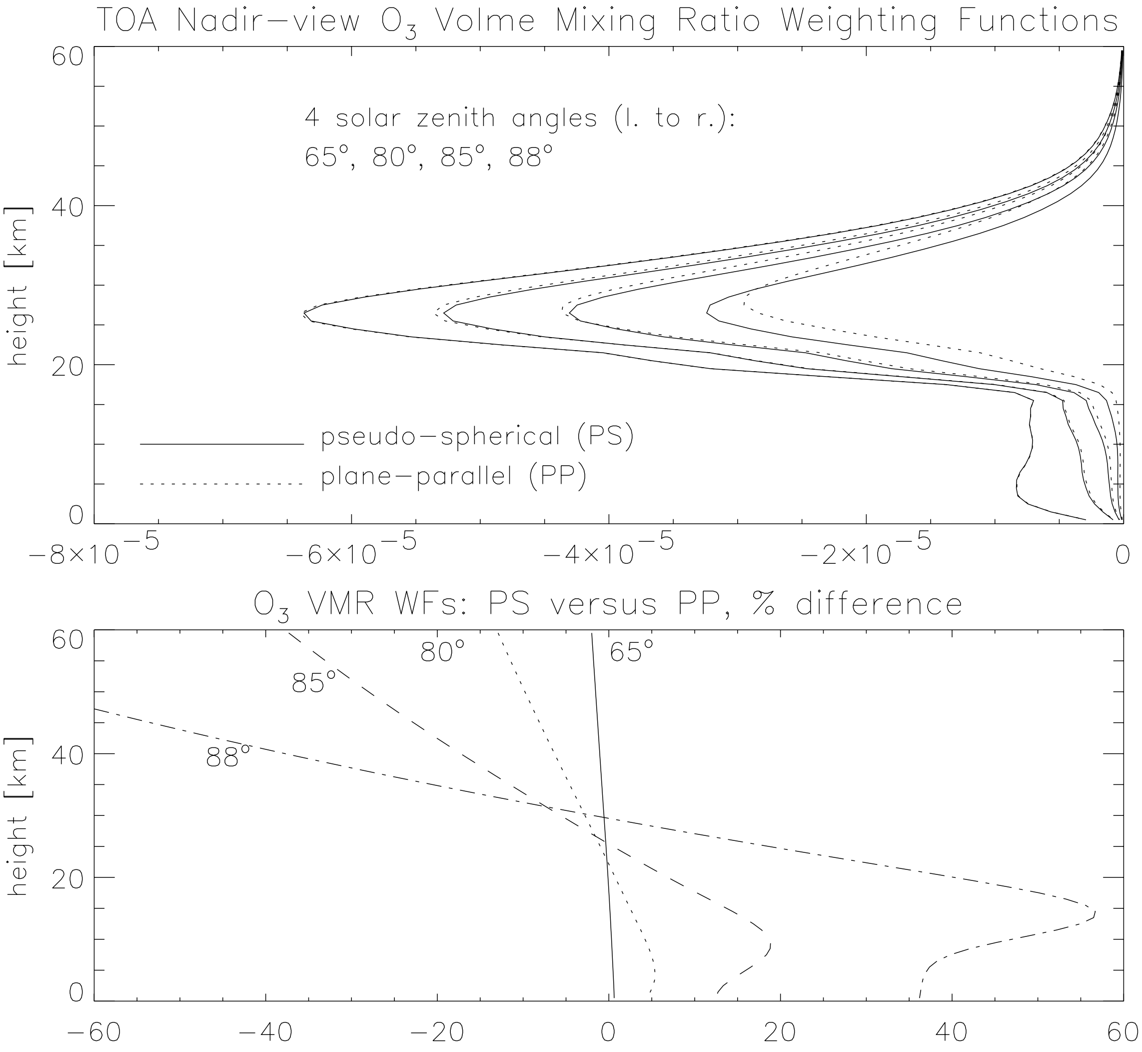
TOA Nadir–view O_3 Volme Mixing Ratio Weighting Functions

O_3 VMR WFs: PS versus PP, % difference

Figure 3.7: (top panel) TOA upwelling O_3 weighting functions in the nadir direction for 4 solar zenith angles, wavelength 335.4579 nm, albedo 0.3; (lower panel) corresponding percentage differences.

3.6.3. LIDORT model simulations for wide off-nadir satellite viewing

Under normal viewing conditions, GOME-2 has a swath width of 1920 km; at the extremes, the line-of-sight at the satellite is $\simeq 48^\circ$ from the nadir (this translates to a zenith angle of $\simeq 55.3^\circ$ at the top of an atmosphere of height 100 km). The swath for the OMI instrument is even larger ($\simeq$2600 km), the off-nadir line-of-sight angle at the satellite being 57° at the swath ends. Wide-angle views are also a feature of the GOME and SCIAMACHY instruments operating in special polar-viewing modes [5]. As noted in the Introduction, the regular pseudo-spherical model treats all scatter events along the zenith AC in Figure 3.1 (the solar zenith angle is always θ_A); the solar path to the point of scatter is attenuated in a curved atmosphere. In the enhanced pseudo-spherical approach, we consider precise calculations of the single scatter at all points P_n along AB, treating both solar beam and line-of-sight attenuation for the curved atmosphere. All multiple scatter contributions to the upwelling intensity I_B are computed from regular LIDORT computations done for points along AB. We adopt the source function integration method to compute I_B.

Referring to Figure 3.1, consider points P_n and P_{n-1} at the lower boundaries of layers n and $n-1$ respectively. Using an integration of the RTE along the segment $\mathrm{P}_n\mathrm{P}_{n-1}$, we can write:

$$I_{n-1} = I_n\Theta_n + \Lambda_n^{(SS)} + \Lambda_n^{(MS)+}, \tag{3.93}$$

where Θ_n is the line-of-sight transmittance along the segment, $\Lambda_n^{(SS)}$ is the layer-integrated single scatter contribution to the upwelling radiance, and $\Lambda_n^{(MS)}$ is the layer-integrated upwelling multiple scatter contribution. For a curved atmosphere with appropriate viewing geometry along the segment, Θ_n and $\Lambda_n^{(SS)}$ are evaluated accurately in a separate calculation for the single scatter. $\Lambda_n^{(MS)+}$ is simply replaced by the upwelling whole layer multiple scatter contribution derived in equation (3.29) from the LIDORT model. Since viewing geometries vary along AB, separate LIDORT calculations should be done for each geometry $\{\theta_n, \gamma_n, \phi_n\}$ at P_n (where ϕ_n is the relative azimuth angle).

The recursion (3.93) starts with the upwelling intensity I_A at the lower boundary at position A, and finishes with I_B, the upwelling intensity at B. I_A is returned from a LIDORT calculation with the appropriate geometry at A. Between A and B, one can reduce the number of intermediate multiple scatter calculations by calling LIDORT for a small subset of points along AB (to include the first and last points P_1 and A), and then interpolating the multiple scatter source term output against the cosine of the solar zenith angle along AB. (Remember that a single LIDORT call can return layer-integrated multiple scatter terms for *all* layers in the atmosphere). Any error induced by this interpolation will be very much smaller that the basic enhancement itself. Note also that the corrected single scatter computation uses the phase function directly without the truncation implicit in the discrete ordinate treatment. A similar approach using multiple-scatter source terms has been developed for the pseudo-spherical GOMETRAN finite-difference model [44].

In a non-refractive atmosphere, the scattering angle is a constant for all points on the path AB. Figure 3.1 illustrates the forward scatter situation; for the backward (antisolar) scenario, the scatter angle will be quite different. We can thus expect some additional asymmetry between the forward and backward scatter cases. Also, in the forward scatter scenario the solar zenith angle at A is less than the value at B; for the backward scatter case, the reverse is true (the difference is about $\mp 1.5^\circ$ for a TOA line-of-sight zenith of 60° for the solar/antisolar positions). This variation in solar zenith angle is an additional source of asymmetry, both in the single scatter calculation and in the multiple scatter source terms.

Figure 3.8 shows the differences between regular pseudo-spherical LIDORT output and improved estimates of intensity using the multiple-scatter layer-integrated source term output from LIDORT and the corrected single scatter calculation. Intensity results were performed for 0° (solar) and 180° (antisolar) azimuth angles, for a solar zenith angle of 85° and for line-of-sight angles from 0 to 70°. The results were performed at five different wavelengths in the UV for the atmosphere outlined in Section 3.6.1 but without aerosols (Rayleigh scattering alone) and with a surface albedo of 0.1. The results mirror closely those found in [44]. In general the absolute magnitude of the correction is greater for the antisolar scenarios. It is immediately clear that this correction is essential for the wide-angle viewing geometries of GOME-2 and OMI; differences for viewing zenith angles in excess of 50° vary from 3 to 8%.

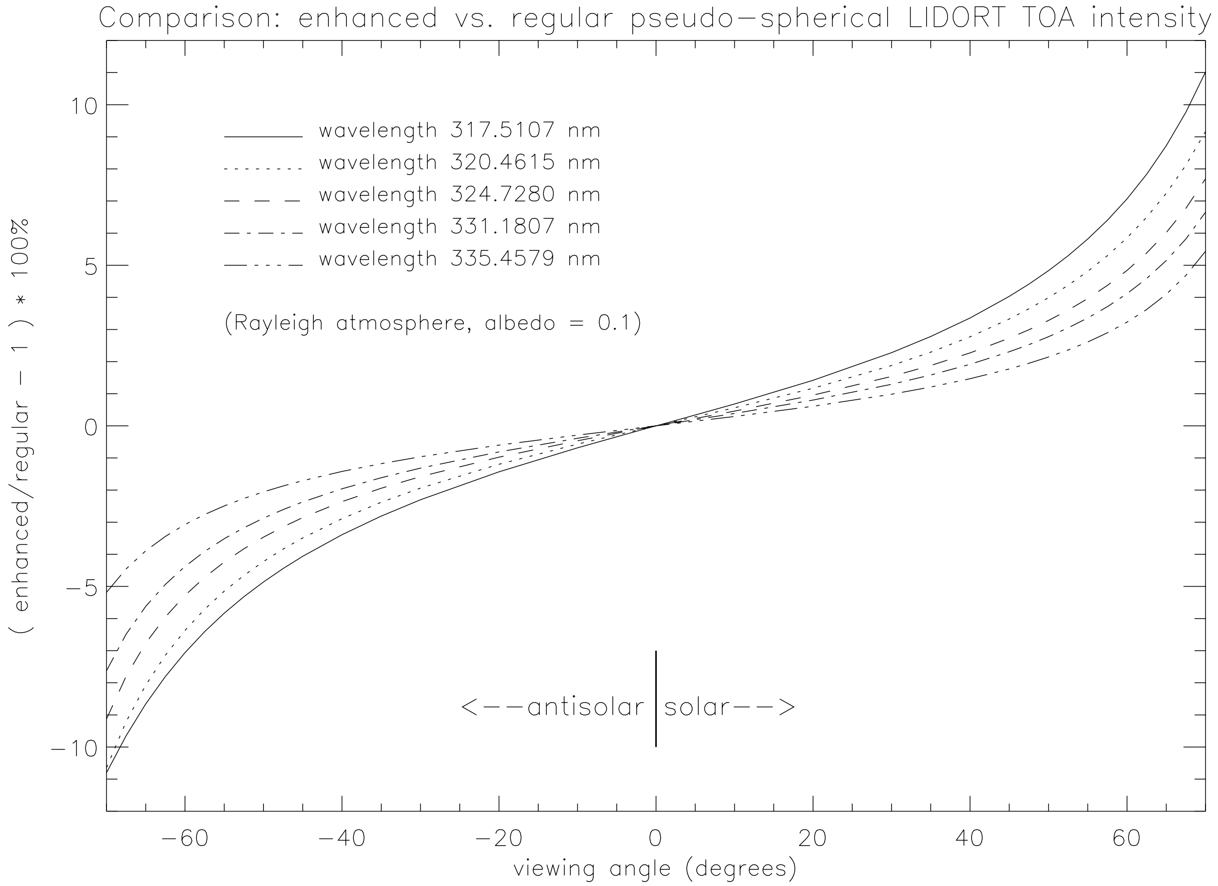

Figure 3.8: Comparison of TOA upwelling intensities from regular and enhanced pseudo-spherical model output, for 0° (solar) and 180° (antisolar) azimuth angles, solar zenith angle 85°. Rayleigh atmosphere, albedo 0.1. 5 wavelengths as indicated.

The situation for weighting functions is also straightforward. With respect to an atmospheric parameter ξ_q in layer q, we may apply the linearization operator L_q to the recursion (3.93):

$$L_q[I_{n-1}] = L_q[I_n]\Theta_n + I_n\delta_{qn}L_n[\Theta_n] + L_q\left[\Lambda_n^{(SS)}\right] + L_q\left[\Lambda_n^{(MS)+}\right]. \tag{3.94}$$

Again, $L_n[\Theta_n]$ and $L_q\left[\Lambda_n^{(SS)}\right]$ may be evaluated directly for a curved atmosphere in a dedicated single scatter calculation. Assuming $\Lambda_n^{(MS)+}$ to be approximated by the pseudo-spherical LIDORT value, then its linearization $L_q\left[\Lambda_n^{(MS)+}\right]$ can also be taken straight from LIDORT output. The linearized recursion starts with $L_q\,[I_A]$ which is returned from the LIDORT calculation at A, and finishes with the weighting function at the top of the atmosphere B.

Figure 3.9 shows differences in ozone VMR weighting functions for a solar zenith angle of 85°, a viewing zenith angle of 55° (this is a typical value for GOME-2 at the swath limits), and for the solar and anti-solar positions. Calculations were done for the same atmosphere and wavelengths as used in Figure 3.8. The asymmetry between forward and backward scatter weighting function differences is more marked, with a broad bias apparent for the lowest wavelength (greatest sensitivity). It is again clear that the correction will be essential for retrievals of ozone profiles from GOME-2 and OMI.

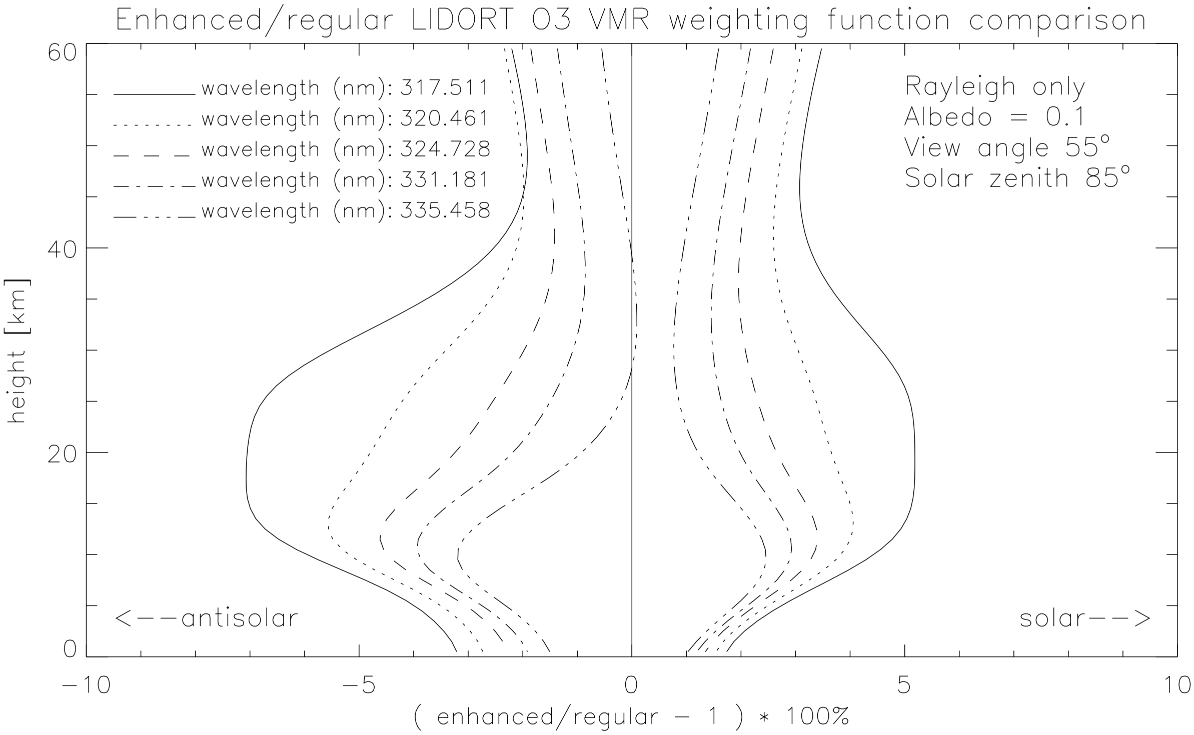

Figure 3.9: Comparison of TOA upwelling ozone VMR weighting functions from regular and enhanced pseudo-spherical model output for solar zenith angle 85°, viewing zenith angle 55° and for the solar and anti-solar positions. Atmosphere and wavelengths as in Figure 3.8.

3.7. Concluding remarks

In this paper we have described an extension of the discrete ordinate solution of the radiative transfer equation in a multiply scattering multi-layer atmosphere to the simultaneous calculation of analytically accurate weighting function fields. A pseudo-spherical treatment of the direct beam transmittance enables the backscatter fields to be obtained for a range of solar zenith angles up to 90°. Examples of intensity and weighting function output using the numerical model LIDORT were presented for a number of nadir and zenith viewing earthshine backscatter applications in the UV part of the spectrum.

The GOME, SCIAMACHY and GOME-2 instruments have the ability to measure earthshine spectra in two directions of polarization; intensity measurements are polarization-corrected before use in retrieval algorithms. Vector radiative transfer studies in and around the O_2 *A* band have shown that the polarization correction is critically important for certain GOME retrievals [81]. Comparisons between scalar (intensity) and polarized vector RT models indicate that the scalar assumption can lead to significant sources of error in the simulation of backscatter intensity [48]. Feasibility studies have shown the value of polarization measurements for the retrieval of aerosol properties (see for example [82]). Polarized light measurements from the POLDER instrument have been used to separate aerosol and surface contributions to earthshine reflectance [83]. This instrument was flown in space on ADEOS-1 (1996-1997) and a second POLDER device will be on board ADEOS-2 scheduled for launch in 2001.

Although there are a number of vector RT models in existence, they all calculate the Stokes vector alone; weighting functions must be estimated by finite differencing. Most retrieval studies using vector RT models have used phase-space diagrams and look-up tables. Vectorized discrete ordinate models have been written for a plane-parallel medium [73, 84], but the pseudo-spherical treatment has not been included. A third version of LIDORT will address these issues, namely the development of a linearization analysis of a vectorized model for the generation of weighting functions, and the use of a consistent pseudo-spherical vector RT treatment.

Acknowledgments

This work was supported in part by a contract from the Deutsches Forschungszentrum für Luft und Raumfahrt, contract number 332/60570480 (SCIAMACHY Data Processor Development), in part from an Ozone SAF Visiting Scientist Grant (P-4799-2-00) at KNMI (Royal Dutch Meteorological Institute), and in part with internal funding from the Smithsonian Astrophysical Observatory. The author would like to thank Piet Stammes for valuable feedback on the manuscript, Hennie Kelder for advice and support, and especially Roeland van Oss for many fruitful discussions regarding this work. Contributions from Thomas Kurosu, Werner Thomas and Knut Stamnes are also gratefully acknowledged.

3.8. Appendices

3.8.1. Green's function optical depth multipliers

We derive Green's function optical depth multipliers (3.45) for the exponential-sine and exponential-polynomial pseudo-spherical parameterizations. We can define

$$C^{\pm}_{\alpha}(x) = \hat{T}\sum_{n=0}^{N^*} c_n K^{\pm}_{n\alpha}(x) \tag{3.95}$$

by analogy with the coefficient expansions (3.34a) and (3.34b), with c_0 = 1 for both parameterizations, and $\hat{T}K^{\pm}_{0\alpha}(x)$ the average secant results already noted in (3.46).

For the exponential-sine parameterization, the functions $K^{\pm}_{n\alpha}(x)$ for $n > 0$ are:

$$K^{-}_{n\alpha}(x) = e^{-xk_\alpha} S_n(f^{-}_{\alpha}, x), \tag{3.96a}$$

$$K^{+}_{n\alpha}(x) = e^{+xk_\alpha}\left[S_n(f^{+}_{\alpha}, \Delta) - S_n(f^{+}_{\alpha}, x)\right], \tag{3.96b}$$

with the definition

$$S_n(\beta, x) \equiv \int_0^x e^{-y\beta} \sin(\phi_n y)\,dy = \frac{\phi_n\left(1 - e^{-x\beta}\cos(\phi_n x)\right) - \beta e^{-x\beta}\sin(\phi_n x)}{\beta^2 + \phi_n^2}. \tag{3.97}$$

Here, $f^{\pm}_{\alpha} = \lambda \pm k_{\alpha}$ and $\phi_n = \pi n/\Delta$.

For the exponential-polynomial parameterization, the functions $K^{\pm}_{n\alpha}(x)$ for $n > 0$ are:

$$K^{-}_{n\alpha}(x) = e^{-xk_{\alpha}}\left\{\Delta Q_n(f^{-}_{\alpha},x) - Q_{n+1}(f^{-}_{\alpha},x)\right\}, \tag{3.98a}$$

$$K^{+}_{n\alpha}(x) = e^{+xk_{\alpha}}\left\{\left[\Delta Q_n(f^{+}_{\alpha},\Delta) - Q_{n+1}(f^{+}_{\alpha},\Delta)\right] - \left[Q_n(f^{+}_{\alpha},x) - Q_{n+1}(f^{+}_{\alpha},x)\right]\right\}, \tag{3.98b}$$

with definitions

$$Q_n(\beta,x) \equiv \int_0^x e^{-y\beta} y^n dy, \tag{3.99}$$

$$\beta Q_n(\beta,x) = nQ_{n-1}(\beta,x) - x^n e^{-x\beta} \quad \text{for } n > 0, \quad \text{and} \quad Q_0(\beta,x) = \frac{1-e^{-x\beta}}{\beta}. \tag{3.100}$$

3.8.2. Integrated source term contributions in the post-processing function

In this appendix, we establish the integrated source term contributions that appear in (3.26). The appendix is divided into four parts, dealing first with the homogeneous contribution, then the single scatter contribution, followed by the two particular integral contributions evaluated for the classical and Green's function solution methods.

Homogeneous integrated solution source term contribution

We first look at the contribution $H^{\pm}(x,\mu)$ to the source function terms in (3.26). This may be written

$$H^{\pm}(x,\mu) = \sum_{\alpha=1}^{N}\left\{L_{\alpha}X^{(P)}_{\alpha}(\mu)H^{\pm +}_{\alpha}(x,\mu) + M_{\alpha}X^{(N)}_{\alpha}(\mu)H^{\pm -}_{\alpha}(x,\mu)\right\} \tag{3.101}$$

where the two functions

$$X^{(P)}_{\alpha}(\mu) = \frac{\omega}{2}\sum_{l=m}^{2N-1}\beta_l P^l_m(\mu)\sum_{j=1}^{N}P^l_m(-\mu_j)w_j X^{(P)}_{j\alpha}, \tag{3.102}$$

$$X^{(N)}_{\alpha}(\mu) = \frac{\omega}{2}\sum_{l=m}^{2N-1}\beta_l P^l_m(\mu)\sum_{j=1}^{N}P^l_m(+\mu_j)w_j X^{(N)}_{j\alpha}, \tag{3.103}$$

can be thought of as the solution vectors $\mathbf{X}^{(P)}_{\alpha}$ and $\mathbf{X}^{(N)}_{\alpha}$ defined at off-quadrature directions μ. The sum over j indicates that the discrete-ordinate solutions have been used in the source function derivations. The *integrated homogeneous multipliers* $H^{\pm\pm}_{\alpha}(x,\mu)$ arise from the optical depth integrations implicit in the source function derivation. These are straightforward exponential integrals, and the results are

$$H^{++}_{\alpha}(x,\mu) = \frac{e^{-xk_{\alpha}} - e^{-\Delta k_{\alpha}}e^{-(\Delta-x)/\mu}}{1+\mu k_{\alpha}}; \tag{3.104}$$

$$H^{+-}_{\alpha}(x,\mu) = \frac{e^{-(\Delta-x)k_{\alpha}} - e^{-(\Delta-x)/\mu}}{1-\mu k_{\alpha}}, \tag{3.105}$$

for the upwelling source function terms, and

$$H_\alpha^{-+}(x,\mu) = \frac{e^{-xk_\alpha} - e^{-x/\mu}}{1-\mu k_\alpha}; \tag{3.106}$$

$$H_\alpha^{--}(x,\mu) = \frac{e^{-(\Delta-x)k_\alpha} - e^{-\Delta k_\alpha} e^{-x/\mu}}{1+\mu k_\alpha}, \tag{3.107}$$

for the downwelling terms. These results have appeared a number of times in the literature (see for example [66]). To evaluate whole layer source terms we set $x = 0$ in (3.104) and (3.105) for upwelling contributions, and $x = \Delta$ in (3.106) and (3.107) for the downwelling terms. The whole layer multipliers are

$$H_\alpha^{++}(0,\mu) = H_\alpha^{--}(\Delta,\mu) = \frac{1 - e^{-\Delta k_\alpha} e^{-\Delta/\mu}}{1+\mu k_\alpha}, \tag{3.108}$$

$$H_\alpha^{+-}(0,\mu) = H_\alpha^{-+}(\Delta,\mu) = \frac{e^{-\Delta k_\alpha} - e^{-\Delta/\mu}}{1-\mu k_\alpha}. \tag{3.109}$$

Primary scatter integrated source term contribution

Next we look at single scatter contributions to the integrated source terms. These are

$$E^{\pm}(x,\mu) = Q^{\pm}(\mu) E^{\pm}(x,\mu) \tag{3.110}$$

where

$$Q^{\pm}(\mu) = \frac{F_\odot}{2}(2-\delta_{m0})\,\Pi^m(\mu,-\mu_0) \tag{3.111}$$

and the *single scatter multipliers* $E_\alpha^{\pm}(x,\mu)$ are

$$E^{+}(x,\mu) = \frac{e^{x/\mu}}{\mu}\int_x^\Delta T(y)e^{-y/\mu}dy, \quad \text{and} \quad E^{-}(x,\mu) = \frac{e^{-x/\mu}}{\mu}\int_0^x T(y)e^{y/\mu}dy, \tag{3.112}$$

where $T(y)$ is the direct beam transmittance. These results (3.112) are valid for all parameterizations of the direct beam attenuation; furthermore, they are independent of the Fourier index m in (3.111), so only need evaluation once. The integrations are straightforward for the average secant parameterization $T(y) = \hat{T}\exp(-y\lambda)$:

$$E^{+}(x,\mu) = \hat{T}\frac{e^{-x\lambda} - e^{-\Delta\lambda}e^{-(\Delta-x)/\mu}}{1+\mu\lambda}, \tag{3.113}$$

$$E^{-}(x,\mu) = -\hat{T}\frac{e^{-x\lambda} - e^{-x/\mu}}{1-\mu\lambda}. \tag{3.114}$$

The plane-parallel result may be obtained by setting $\lambda = \mu_0^{-1}$. Note also that l'Hopital's rule should be used in (3.114) when λ is close to μ^{-1}; the limiting value is:

$$\lim_{\mu\to\lambda} E^{-}(x,\mu) = -\hat{T}x\lambda e^{-x\lambda}. \tag{3.115}$$

Whole layer source term contributions are obtained by setting $x = 0$ in (3.113) (upwelling), and $x = \Delta$ in (3.114) (downwelling).

For the other pseudo-spherical parameterizations we have some additional terms corresponding to the series expansions used in these approximations. We may write

$$E^{\pm}(x,\mu) = E^{\pm}_{AS}(x,\mu) + \frac{\hat{T}}{\mu}\sum_{n=1}^{N^*} c_n W_n^{\pm}(x,\mu) \tag{3.116}$$

where $E^{\pm}_{AS}(x,\mu)$ are the average secant multipliers from (3.113) and (3.114), and for $n > 0$,

$$W_n^{+}(x,\mu) = e^{x/\mu}\int_x^{\Delta} e^{-y(\lambda+\mu^{-1})}\sin(\frac{\pi n y}{\Delta})dy; \quad W_n^{-}(x,\mu) = e^{-x/\mu}\int_0^{x} e^{-y(\lambda-\mu^{-1})}\sin(\frac{\pi n y}{\Delta})dy \tag{3.117}$$

for the exponential-sine parameterization, and

$$W_n^{+}(x,\mu) = e^{x/\mu}\int_x^{\Delta} e^{-y(\lambda+\mu^{-1})}y^n(\Delta-y)dy; \quad W_n^{-}(x,\mu) = e^{-x/\mu}\int_0^{x} e^{-y(\lambda-\mu^{-1})}y^n(\Delta-y)dy \tag{3.118}$$

for the exponential-polynomial parameterization. In both cases, the integrals are straightforward and mirror similar calculations in Appendix 3.8.1.

Classical particular solution integral source term contributions

We first look at the contributions $D^{\pm}(x,\mu)$ to the source function terms in (3.26) from the classical form of the particular integral. We do this for the average secant form $G_j(x) = F_j T(x)$, where $T(x) = \hat{T}\exp(-x\lambda)$ and the vector **F** was determined in section 3.3.3. The results are

$$D^{\pm}(x,\mu) = F^{\pm}(\mu)\mathcal{D}^{\pm}(x,\mu) \tag{3.119}$$

where

$$F^{\pm}(\mu) = \frac{\omega}{2}\sum_{l=m}^{2N-1}\beta_l P_m^l(\mu)\sum_{j=1}^{N} P_m^l(\mp\mu_j)w_j F_j^{\pm} \tag{3.120}$$

can be thought of as the particular solution vector **F** defined at off-quadrature streams μ. Since the particular solution has the same optical depth dependence as the single scatter term in the previous section, the *integrated classical solution multipliers* $\mathcal{D}^{\pm}(x,\mu)$ are

$$\mathcal{D}^{\pm}(x,\mu) = E^{\pm}_{AS}(x,\mu) \tag{3.121}$$

as defined by results (3.113) and (3.114) for the average secant approximation. One can also use the results in Eqs. (3.116)-(3.118) for the other parameterizations. This would require additional functions such as (3.120) to be defined for each term in the coefficient expansion beyond the average secant.

Green's function integral source term contributions

Since the Green's function particular integral is also an expansion in terms of homogeneous solution vectors, we would expect the analysis to be similar to that in Appendix 3.8.2. Recalling the particular integral definitions from Section 3.3.3, we may write

$$D^{\pm}(x,\mu) = \sum_{\alpha=1}^{N} \left\{ a_\alpha X_\alpha^{(P)}(\mu) D_\alpha^{\pm +}(x,\mu) + b_\alpha X_\alpha^{(N)}(\mu) D_\alpha^{\pm -}(x,\mu) \right\} \tag{3.122}$$

where $X_\alpha^{(P)}(\mu)$ and $X_\alpha^{(N)}(\mu)$ have been defined in (3.102) and (3.103) respectively, with a_α and b_α given by (3.43).

The *integrated Green's function multipliers* $D^{\pm\pm}(x,\mu)$ again arise from the optical depth integrations implicit in the source function derivation. They are

$$D_\alpha^{+\pm}(x,\mu) = \frac{e^{x/\mu}}{\mu} \int_x^\Delta C_\alpha^{\pm}(y) e^{-y/\mu} dy, \tag{3.123a}$$

$$D_\alpha^{-\pm}(x,\mu) = \frac{e^{-x/\mu}}{\mu} \int_0^x C_\alpha^{\pm}(y) e^{+y/\mu} dy, \tag{3.123b}$$

for the upwelling and downwelling contributions respectively. For the average secant (and by default, the plane-parallel) parameterizations, explicit expressions for $C_\alpha^{\pm}(y)$ were written down in (3.46). Using these results, one can carry out the integrations to give

$$D_\alpha^{+\pm}(x,\mu) = \frac{\hat{T} e^{-\Delta\lambda} H_\alpha^{+\pm}(x,\mu) \pm E^{+}(x,\mu)}{\lambda \pm k_\alpha}, \tag{3.124a}$$

$$D_\alpha^{-\pm}(x,\mu) = \frac{\hat{T} e^{-\Delta\lambda} H_\alpha^{-\pm}(x,\mu) \pm E^{-}(x,\mu)}{\lambda \pm k_\alpha}, \tag{3.124b}$$

for upwelling and downwelling multipliers respectively. Quantities $H_\alpha^{\pm\pm}$ and $E^{\pm}$ have been determined from Appendices 3.8.2 and 3.8.2, the latter determination being made for the average secant case. Expressions (3.124a) and (3.124b) are convenient for computation; it is obviously possible to write out the full results in terms of many transmittance factors.

For the exponential-sine and exponential-polynomial parameterizations, we can substitute the results of Appendix 3.8.1 for $C_\alpha^{\pm}(y)$ in (3.123a) and (3.123b). All integrals are again straightforward and we summarize the results for the exponential-polynomial parameterization. For the upwelling multipliers, the results are:

$$D_\alpha^{+\mp}(x,\mu) = \frac{\hat{T}}{\mu} e^{+x/\mu} \sum_{n=0}^{N^*} c_n K_{n\alpha}^{+\mp}(x,\mu), \tag{3.125}$$

where $c_0 = 1$, and the first term in the series duplicates the average secant result (3.124a). For $n > 0$ the K-functions are:

$$K_{n\alpha}^{+\mp}(x,\mu) = C_{n\alpha}^{\mp}(x,\mu) \mp \Delta R_n(f_\alpha^{\mp}, g_\alpha^{\pm}, x) \pm R_{n+1}(f_\alpha^{\mp}, g_\alpha^{\pm}, x) \tag{3.126}$$

with the function R defined by the recurrence relation

$$\beta R_{n+1}(\beta,\gamma,x) = nR_{n-1}(\beta,\gamma,x) - Q_n(\beta+\gamma,x) \tag{3.127}$$

for general inputs β and γ. The function $Q_n(\beta,x)$ was defined in (3.99). The particular arguments are $f^{\pm}_{\alpha} = \lambda \pm k_{\alpha}$ and $g^{\pm}_{\alpha} = \mu^{-1} \pm k_{\alpha}$. We also have

$$C^{-}_{n\alpha}(x,\mu) = \Delta R_n(f^{-}_{\alpha}, g^{+}_{\alpha}, \Delta) - R_{n+1}(f^{-}_{\alpha}, g^{+}_{\alpha}, \Delta), \tag{3.128}$$

$$C^{+}_{n\alpha}(x,\mu) = J_{n\alpha}(\mu)\left[Q_0(g^{-}_{\alpha},\Delta) - Q_0(g^{-}_{\alpha},x)\right] - \Delta R_n(f^{+}_{\alpha}, g^{-}_{\alpha}, \Delta) + R_{n+1}(f^{+}_{\alpha}, g^{-}_{\alpha}, \Delta), \tag{3.129}$$

$$J_{n\alpha}(f^{+}_{\alpha}) = \Delta Q_n(f^{+}_{\alpha},\Delta) - Q_{n+1}(f^{+}_{\alpha},\Delta), \tag{3.130}$$

For the downwelling multipliers, one finds similar results:

$$D^{-\pm}_{\alpha}(x,\mu) = \frac{\hat{T}}{\mu} e^{-x/\mu} \sum_{n=0}^{N^*} c_n K^{-\pm}_{n\alpha}(x,\mu), \tag{3.131}$$

where $c_0 = 1$, and the first term in the series duplicates the average secant result (3.124b). For $n > 0$ the K-functions are:

$$K^{-\pm}_{n\alpha}(x,\mu) = C^{\pm}_{n\alpha}(x,\mu) \pm \Delta R_n(f^{\mp}_{\alpha}, -g^{\mp}_{\alpha}, x) \mp R_{n+1}(f^{\mp}_{\alpha}, -g^{\mp}_{\alpha}, x) \tag{3.132}$$

with the function R defined in (3.127), and $f^{\pm}_{\alpha}$ and $g^{\pm}_{\alpha}$ as before. We also have

$$C^{-}_{n\alpha}(x,\mu) = 0, \tag{3.133}$$

$$C^{+}_{n\alpha}(x,\mu) = J_{n\alpha}(f^{+}_{\alpha}) Q_0(-g^{+}_{\alpha}, x), \tag{3.134}$$

where $J_{n\alpha}(f^{+}_{\alpha})$ was given in (3.130).

3.8.3. Linearization analysis of the post-processing source terms

We wish to apply the linearization operator L to each of the source term contributions that appear in the post-processing result (3.26). The procedure is based on linearization results already obtained for the discrete ordinate solutions in all layers and the linearizations of the boundary value constants, and application of the chain rule of differentiation. The algebraic manipulations are fairly extensive but quite straightforward, illustrating once again that the determination of partial derivatives of the complete discrete ordinate intensity field can be done in an entirely analytic fashion. We follow the same sequence as in the previous appendix. Linearizations for the particular integrals and the single scatter terms are confined to the average secant parameterization of the pseudo-spherical treatment.

Linearization of the homogeneous source term contributions

We first look at the source function contributions $H^{\pm}(x,\mu)$ from the homogeneous solutions. We apply the chain rule to (3.101), noting that $L_q[L_{p\alpha}]$ and $L_q[M_{p\alpha}]$ are known from the linearization analysis of the boundary value problem. All other quantities in (3.101) have vanishing derivatives for $p \neq q$, so we will drop the index q in the rest of this section. From (3.102) and (3.103), we find

$$L\left[X^{(P)}_{\alpha}(\mu)\right] = \frac{\omega}{2} \sum_{l=m}^{2N-1} \beta_l P^l_m(\mu) \sum_{j=1}^{N} P^l_m(-\mu_j) w_j \left\{ L\left[X^{(P)}_{j\alpha}\right] + uX^{(P)}_{j\alpha} \right\}, \tag{3.135}$$

$$L\left[X^{(N)}_{\alpha}(\mu)\right] = \frac{\omega}{2} \sum_{l=m}^{2N-1} \beta_l P^l_m(\mu) \sum_{j=1}^{N} P^l_m(+\mu_j) w_j \left\{ L\left[X^{(N)}_{j\alpha}\right] + uX^{(N)}_{j\alpha} \right\}, \tag{3.136}$$

where the layer index q is assumed throughout. The terms with $u\mathbf{X}_\alpha$ arise from the linearization $L[\omega] = u\omega$.

Next we look at the linearizations of the homogeneous multipliers defined in (3.104) and (3.105). We proceed by chain rule differentiation, using the known result for $L[k_\alpha]$ from Section 3.4.2 and the linearization rules $L[\Delta] = v\Delta$ and $L[x] = vx$ from Section 3.4.1. The result for H^{++} is:

$$L\left[H_\alpha^{++}(x,\mu)\right] = \frac{-H_\alpha^{++}(x,\mu)\mu f_\alpha - e^{-xk_\alpha}x\gamma_\alpha + e^{-\Delta k_\alpha}e^{-(\Delta-x)/\mu}\left[\Delta\gamma_\alpha + (\Delta - x)\,v\mu^{-1}\right]}{1+\mu k_\alpha}, \tag{3.137}$$

where $f_\alpha = L[k_\alpha]$, and $\gamma_\alpha = vk_\alpha + f_\alpha$. In a similar vein, we find:

$$L\left[H_\alpha^{+-}(x,\mu)\right] = \frac{H_\alpha^{+-}(x,\mu)\mu f_\alpha - e^{-(\Delta-x)k_\alpha}(\Delta-x)\gamma_\alpha + e^{-(\Delta-x)/\mu}\,(\Delta-x)\,v\mu^{-1}}{1-\mu k_\alpha}, \tag{3.138}$$

$$L\left[H_\alpha^{-+}(x,\mu)\right] = \frac{H_\alpha^{-+}(x,\mu)\mu f_\alpha - e^{-xk_\alpha}x\gamma_\alpha + e^{-x/\mu}\,(\Delta-x)\,v\mu^{-1}}{1-\mu k_\alpha}, \tag{3.139}$$

$$L\left[H_\alpha^{--}(x,\mu)\right] = \frac{-H_\alpha^{--}(x,\mu)\mu f_\alpha - e^{-xk_\alpha}(\Delta-x)\gamma_\alpha + e^{-\Delta k_\alpha}e^{-x/\mu}\left[\Delta\gamma_\alpha + xv\mu^{-1}\right]}{1+\mu k_\alpha}. \tag{3.140}$$

As with the original multipliers, values of these linearizations at the layer boundaries can be obtained by setting $x = 0$ in (3.137) and (3.138), and $x = \Delta$ in (3.139) and (3.140). The above results appeared in SKC in a slightly different form.

Linearization of the single scatter source term contributions

We start with the definition of $E_p^{\pm}(x,\mu)$ in (3.110), this time keeping an explicit layer indexing throughout. Applying the linearization operator L_q for a parameter ξ_q varying in layer q, we find

$$L_q\left[E_p^{\pm}(x,\mu)\right] = Q_p^{\pm}(\mu)\left\{\delta_{pq}u_q E_p^{\pm}(x,\mu) + L_q\left[E_p^{\pm}(x,\mu)\right]\right\}. \tag{3.141}$$

$Q_p^{\pm}(\mu)$ as defined in (3.111) is directly proportional to ω_p, so the corresponding linearization is then $\delta_{pq}u_q Q_p^{\pm}(\mu)$. For the second term in (3.141), we apply linearization to the definitions of these multipliers given in (3.112). Using the linearizations established in Section 3.4.1 for $L_q\left[\hat{T}_p\right]$ and $L_q[\lambda_p]$, we get

$$L_q\left[E_p^{+}\right] = \frac{-e^{-x\lambda_p}x\chi_{pq} + e^{-\Delta_q\lambda_p}e^{-(\Delta_q-x)/\mu}\left[\Delta_q\chi_{pq} + (\Delta-x)\,\delta_{pq}v_q\mu^{-1}\right]}{1+\mu\lambda_p} + E_p^{+}\varpi_{pq}^{+}, \tag{3.142a}$$

$$L_q\left[E_p^{-}\right] = \frac{-e^{-x\lambda_p}x\chi_{pq} + e^{-x/\mu}\left[\Delta_q\chi_{pq} + x\delta_{pq}v_q\mu^{-1}\right]}{1-\mu\lambda_p} + E_p^{-}\varpi_{pq}^{-}, \tag{3.142b}$$

where the dependence of $E_p^{\pm}$ on (x,μ) has been assumed, and

$$\varpi_{pq}^{\pm} = \frac{L_q\left[\hat{T}_p\right]}{\hat{T}_p} \mp \frac{\mu L_q[\lambda_p]}{1\pm\mu\lambda_p} \quad \text{and} \quad \chi_{pq} = L_q[\lambda_p] + \delta_{pq}v_q. \tag{3.143}$$

A form of these results were derived for the plane-parallel case in SKC using a perturbation analysis. The above results are a generalization to the average secant pseudo-spherical approximation, and it is clear that there are important contributions to multipliers in layer p from variational derivatives in layer q above p. This illustrates the care that need to be taken in setting up the linearization rules for the pseudo-spherical case.

Linearization of the classical particular solution source term contributions

From the definition (3.119), we find

$$L_q\left[D_p^{\pm}(x,\mu)\right] = L_q\left[F_p^{\pm}(\mu)\right] D_p^{\pm}(x,\mu) + F_p^{\pm}(\mu) L_q\left[D_p^{\pm}(x,\mu)\right]. \tag{3.144}$$

For the first term, we note that

$$L_q\left[F_p^{\pm}(\mu)\right] = \frac{\omega_p}{2} \sum_{l=m}^{2N-1} \beta_l P_m^l(\mu) \sum_{j=1}^{N} P_m^l(-\mu_j) w_j \left\{ L_q\left[F_{jp}^{\pm}\right] + \delta_{pq} u_q F_{jp}^{\pm} \right\}, \tag{3.145}$$

This is similar to the result in (3.135), and follows from the definition in (3.120). Note that the particular solution discrete ordinate vector $\mathbf{F}_p^{\pm}$ has cross-layer derivatives outside layer p; the linearization of this vector was dealt with in section 3.4.3. Finally, since the multipliers $D_p^{\pm}$ are actually equal to $E_p^{\pm}$, then we may use the results already established for $L_q\left[E_p^{\pm}\right]$ in Appendix 3.8.3.

Linearization of the Green's function particular integral source term contributions

Although the Green's function particular integral source term contributions defined in (3.122) have a number of contributions, we may use the results established in Appendices 3.8.2 and 3.8.2 to simplify the analysis considerably. We retain layer indices throughout. In applying chain-rule differentiation to the terms in (3.122), we note that

$$L_q\left[a_{p\alpha} X_{p\alpha}^{(P)}(\mu) D_{p\alpha}^{\pm +}(x,\mu)\right] = \delta_{pq} L_q\left[a_{p\alpha} X_{p\alpha}^{(P)}(\mu)\right] D_{p\alpha}^{\pm +}(x,\mu) + a_{p\alpha} X_{p\alpha}^{(P)}(\mu) L_q\left[D_{p\alpha}^{\pm +}(x,\mu)\right] \tag{3.146}$$

since the terms $a_{p\alpha}$ and $X_{p\alpha}^{(P)}(\mu)$ have no optical depth dependence. Their linearizations are given by (3.69) in section 3.4.4 and (3.135) in appendix 3.8.3 respectively. Similar remarks apply to the combination $b_{p\alpha} X_{p\alpha}^{(N)}(\mu)$ which comprises the second half of (3.122). We are thus left with the task of determining linearizations for the multipliers $D_{p\alpha}^{\pm\pm}$.

We note that the Green's function multipliers defined in (3.124a) and (3.124b) are expressed in terms of multipliers $H_p^{\pm\pm}$ and $E_p^{\pm}$. Since we already have linearizations for these quantities from appendices 3.8.3 and 3.8.3, a straightforward application of the chain rule in terms of known linearizations will yield the desired result. Compacting the notation somewhat by dropping the (x,μ) dependence which is assumed throughout, we find

$$L_q\left[D_{p\alpha}^{+\pm}\right] = \frac{\varphi_p \left\{\delta_{pq} L_q\left[H_{p\alpha}^{+\pm}\right] + \psi_{pq} H_{p\alpha}^{+\pm}\right\} \pm L_q\left[E_p^{+}\right] - D_{p\alpha}^{+\pm} \varpi_{pq\alpha}}{\lambda \pm k_\alpha}, \tag{3.147}$$

$$L_q\left[D_{p\alpha}^{-\pm}\right] = \frac{\varphi_p \left\{\delta_{pq} L_q\left[H_{p\alpha}^{-\pm}\right] + \psi_{pq} H_{p\alpha}^{-\pm}\right\} \pm L_q\left[E_p^{-}\right] - D_{p\alpha}^{-\pm} \varpi_{pq\alpha}}{\lambda \pm k_\alpha}, \tag{3.148}$$

where the following auxiliary quantities are evident:

$$\varphi_p = \hat{T}_p e^{-\Delta_p \lambda_p}, \tag{3.149}$$

$$\psi_{pq} = \frac{L_q[\varphi_p]}{\varphi_p} = \frac{L_q\left[\hat{T}_p\right]}{\hat{T}_p} - \Delta_p\left(\delta_{pq}\lambda_p + L_q[\lambda_p]\right), \tag{3.150}$$

$$\varpi_{pq\alpha}^{\pm} = L_q[\lambda_p] \pm \delta_{pq} L_q[k_{p\alpha}]. \tag{3.151}$$

This completes the linearization of the Green's function particular integral source term contributions.

3.8.4. Delta-M scaling transformations

We restrict the discussion to an atmosphere with one scatterer. For single scattering albedo ω_q, optical thickness Δ_q and phase function moment coefficients β_{lq} in layer q, the delta-M scaling [36] is

$$\overline{\omega}_q = \omega_q \frac{(1-f_q)}{(1-\omega_q f_q)}, \quad \overline{\Delta}_q = \Delta_q(1-\omega_q f_q), \quad \text{with} \quad \overline{\beta}_{lq} = \frac{\beta_{lq} - f_q(2l+1)}{1-f_q}. \tag{3.152}$$

Here, $l = 0, \ldots, 2N-1$ and $f_q = \beta_{Mq}/(2M+1)$ is the *truncation factor* in layer q, with $M = 2N$ indicating that all scaled phase function moment coefficients $\overline{\beta}_{lq}$ for $l \geqslant M$ are zero. As far as the pseudo-spherical approximation is concerned, we note that all spherical optical depths κ_{qp} as defined in (3.32) scale in the same way as Δ_p.

This result is standard in intensity-only radiative transfer models; see [34] for more details. For a model such as LIDORT with additional inputs $\{u_q, v_q\}$ expressing the relative partial derivatives of ω_q and e_q due to some parameter ξ_q varying in layer q, we must also consider the scaling of these inputs. Remembering that $L_q[\omega_q] = u_q\omega_q$ and $L_q[\Delta_q] = v_q\Delta_q$, one can simply apply the linearization operator to the first two results in (3.152) to define scaled values $\{\overline{u}_q, \overline{v}_q\}$. The result is

$$\overline{u}_q = \frac{u_q}{1-\omega_q f_q} \quad \text{and} \quad \overline{v}_q = v_q - \frac{\omega_q f_q u_q}{1-\omega_q f_q}. \tag{3.153}$$

It is straightforward to extend these scaling results to a layer with a number of particulates, bearing in mind the combination forms

$$\omega_q = \sum_s \omega_{qs}; \quad \omega_q\beta_{lq} = \sum_s \omega_{qs}\beta_{lqs} \quad \text{and} \quad \omega_q\beta_{lq}u_{lq} = \sum_s \beta_{lqs}\omega_{qs}u_{qs} \tag{3.154}$$

which are used in the RTE (see Section 3.4.1).

Chapter 4

Fast and accurate 4 and 6 stream linearized discrete ordinate radiative transfer models for ozone profile remote sensing retrieval

This chapter has been accepted for publication in the Journal of Quantitative Spectroscopy and Radiative Transfer, and is co-authored by R.F. van Oss.

Abstract

The global and long-term measurement of ozone vertical and horizontal distributions is one of the most important tasks in the monitoring of the earth's atmosphere. A number of satellite instruments are capable of delivering ozone profile distributions from UV nadir backscatter measurements. Retrieval algorithms should be efficient enough to deliver profiles in real-time without compromising accuracy. Such algorithms require a radiative transfer model that can generate quickly and accurately both simulated radiances and Jacobian matrices of weighting functions. We develop fast and analytic 4 stream and 6 stream linearized discrete ordinate models designed to satisfy performance and accuracy requirements for such an algorithm. The models have the pseudo-spherical treatment of the direct beam attenuation. For anisotropic scattering we use the delta-M scaling method to deal with strong forward scattering peaks. We demonstrate that the accuracy of the models is improved greatly upon application of a single scatter correction based on an exact specification of the phase function. For wide-angle off-nadir viewing, a sphericity correction is developed to deal more precisely with attenuation in a curved atmosphere. Radiances and weighting functions for the 4 and 6 stream models are compared with 20 stream output from the LIDORT model. We show that for the UV range pertinent to ozone profile retrieval from space, the 4 stream model generates backscatter radiances to an accuracy of better than 1.25% for all viewing situations in a clear sky Rayleigh and background aerosol reference atmosphere, and up to 1.75% for a number of special scenarios with optically thick particulate layers. 6 stream radiances are accurate to the 0.25% level for clear sky situations, and 0.65% for the special cases; weighting functions for the 6 stream output are accurate to ±2% in all cases. We discuss the implications of these comparisons regarding the performance and accuracy of the radiative transfer forward model in the ozone profile retrieval context.

4.1. Introduction

Monitoring of the earth's atmosphere is an essential requirement to the understanding of chemical and physical processes that maintain atmospheric balance. This is particularly important in view of perceived changes in the atmosphere's constituent distributions due to anthropogenic activity on the planet. Space-based instruments have the potential to deliver global and long-term measurements of the vertical and horizontal distributions of atmospheric constituents, from the determination of column abundances and profile concentrations of ozone and other trace species, to the evaluation of aerosol and cloud properties and distributions. Ozone is the most important trace species, and in this work we will be concerned with the forward model component of ozone profile retrieval algorithms based on satellite nadir earthshine measurements in the UV part of the spectrum.

The GOME (Global Ozone Monitoring Experiment) nadir viewing spectrometer on board the ESA ERS-2 satellite (launched April 1995) takes earthshine measurements in the UV, visible and near infrared; it has a spectral range of 250 to 800 nm, with a moderate spectral resolution of 0.2 to 0.4 nm [7]. An improved version of the GOME instrument, GOME-2, will fly on the first three METOP satellites [6]. The operational period of these platforms is 15 years, and this offers a unique opportunity to obtain a long-term, global ozone record. Other instruments with similar measurement capabilities to GOME and GOME-2 include SCIAMACHY [76] on the ENVISAT platform (launch summer 2001) and OMI [8] on EOS-AURA (launch 2003). GOME and SCIAMACHY have maximum swaths of 960 and 1000km respectively, with a maximum off-nadir scan angle at the satellite of $\simeq 32^\circ$. OMI (swath 2600 km) and GOME-2 (maximum swath 1920 km) have wide-angle nadir viewing scenarios, and sphericity effects will be important for these instruments.

The first operational ozone profile retrieval algorithm from UV nadir measurements was developed for the BUV, SBUV, SBUV/2 and SSBUV experiments [11]. Ozone profile retrieval algorithms for GOME have been reported in the literature [14, 16, 15, 13]. The potential of GOME-type instruments to deliver ozone profiles (Level 2 data) with the temporal and geographical sampling of the corresponding earthshine measurements (Level 1 data) can only be exploited if the retrieval process is fast enough to keep up with the data rate using the best available computer resources. It is highly desirable to develop algorithms which are as efficient as possible, and to find the right balance between accuracy and speed.

The ozone profile algorithm requires repeated calculations of simulated radiances and Jacobian matrices of radiance derivatives with respect to retrieval parameters (weighting functions). A tremendous saving in time is achieved with a radiative transfer (RT) model that is capable of delivering both these quantities simultaneously, without the need for cumbersome finite-difference approximations to the weighting functions obtained by repeated calls to an radiance-only radiative transfer model. The LIDORT (Linearized Discrete Ordinate Radiative Transfer) model [75, 85] has been designed with this purpose in mind; it is able to generate all weighting functions simultaneously to the same degree of accuracy as that pertaining for the radiance. Furthermore, the derivation of weighting functions is analytic, depending on an explicit differentiation of the complete RT solution.

In the discrete ordinate method, multiple scatter integrals over the polar viewing angle are replaced by quadrature sums defined by a set of Gauss-Legendre abscissae and weights (streams). The accuracy of the radiance at TOA computed with the discrete ordinate model is mainly determined by the number of streams. A high level of accuracy can be achieved for a sufficient number of streams; this is especially true for a strongly anisotropic medium. Taking only four or six streams therefore involves some loss of accuracy. For atmospheres with aerosol scattering, we use the standard delta-M scaling [36] to separate the forward scatter peak as a delta-function and truncate the phase function; this process requires an initial scaling of the single scattering albedos and optical thicknesses before the model is executed. For a low number of streams, the single scatter contributions to the upwelling TOA radiance are not well treated in the delta-M approximation. To remedy this, we use the Nakajima-Tanaka (NT) correction procedure [37], which replaces the single scatter terms with analytical results computed for exact phase functions.

Analytic 4 stream solutions were derived by Liou [51] for the azimuth-independent component of the radiance field (this is sufficient to obtain heating rates and fluxes). In this work we extend the analytic 4 stream solution to cover the azimuth dependence of the radiation field, and we develop corresponding analytic expressions for the 6 stream model. A reduction in order by a factor of two is possible when solving for the homogeneous and particular solutions of the discrete ordinate RTE. These solutions can then be developed analytically for the low-stream cases, thereby avoiding numerical procedures (eigenproblem analysis and linear algebra systems) otherwise required for a higher number of streams. In a multi-layer atmosphere, a set of boundary conditions is required to complete the determination of the radiance; the resulting boundary value problem is a sparse linear algebra system. In solving this system, the time-consuming matrix inversion step is greatly speeded up with 4 and 6 stream approximations (speed varies with the square of the number of streams).

The determination of weighting functions for these models is carried out by explicit analytic differentation of the complete radiance field; this is the method adopted in the general LIDORT treatment [85]. Derivatives of the TOA radiance are taken with respect to the input optical properties that control the radiance calculation (total optical thickness, total single scattering albedo and phase function moments). Weighting functions with respect to *atmospheric* parameters then follow once we establish the dependence of the total optical input variables on these atmospheric parameters. We look at this dependence for parameters such as ozone profile volume mixing ratio, temperature, aerosol optical thickness and single scattering albedo. In addition, we derive weighting functions with respect to parameters such as the asymmetry factor which characterize the angular distribution of the phase function; such quantities are important for retrievals of aerosol optical properties.

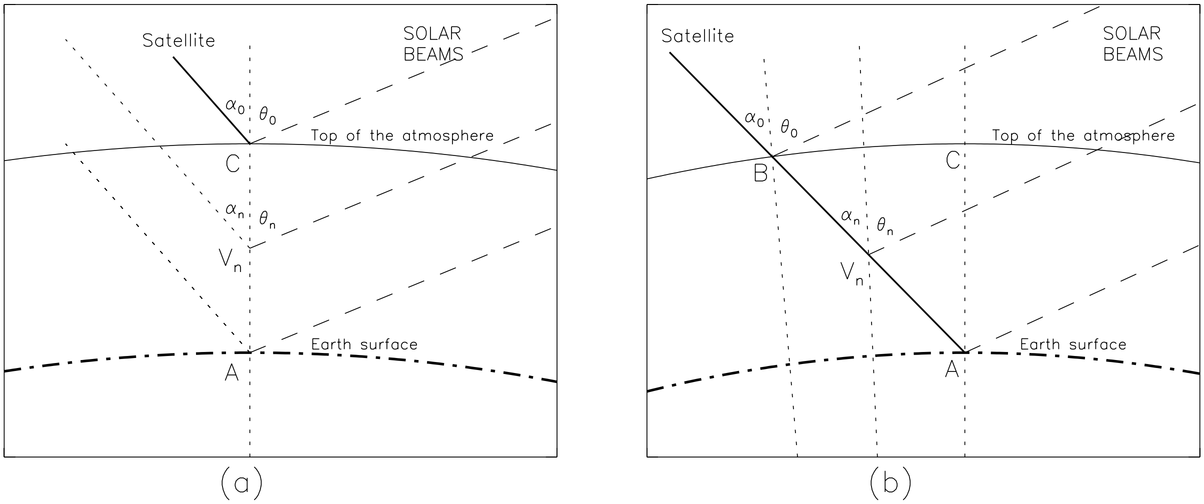

Figure 4.1: (a) Geometry for the regular pseudo-spherical computation of backscatter radiation; (b) geometry for the sphericity correction.

In common with the general LIDORT treatment [85], the 4/6 stream models will use the *pseudo-spherical* approximation, in which the attenuation of the direct solar beam is computed accurately in spherical shell geometry, but all scattered light (with the exception of the NT-corrected single scatter terms) is treated for a plane-parallel atmosphere. The advantage of this approximation is that the power and speed of the plane-parallel scattering formalism can be retained without the need to call a greatly more complex and time-consuming full-spherical radiative transfer model. It has been shown [35, 78] that the PS treatment is adequate for solar zenith angles up to 90° provided the line-of-sight is reasonably close ($\simeq 20 - 25^\circ$ or less) to the nadir. Figure 4.1(a) illustrates the viewing geometry for this case; all scattering takes place along the nadir AC.

For wide-angle off-nadir viewing it is necessary to allow for sphericity effects; the situation is shown in Figure 4.1(b), where scattering takes place along path AB instead of the vertical AC. To determine the upwelling radiation field at B, we obtain accurate single scatter contributions at points V_n along AB, taking curved geometry into account for all solar paths as well as path AB itself. Multiple scatter contributions at points V_n are determined from the pseudo-spherical models with the appropriate geometry for these points; the complete solution at B is found by using a layer-by-layer integrated source function method. Single scatter contributions will be NT-corrected. The multiple scatter contributions vary smoothly with the small changes in viewing geometry from A to B, and we demonstrate that interpolation based on two or three computations is sufficiently accurate. We use the term *sphericity correction* for the calculation of TOA radiance I^B. The correction was developed for LIDORT in [85], and a similar procedure has been applied to the finite difference GOMETRAN model [44]. Studies have shown that this sort of sphericity correction applied to pseudo-spherical RT models gives a very good approximation to the radiance computed using a full-spherical model [78].

The first three sections of the paper deal with theoretical aspects. In Section 4.2 on discrete ordinate theory, we concentrate in particular on the reduction in order which allows the analytic solutions to be written down in the 4 and 6 stream cases. In section 4.3, we carry out an explicit differentiation of all aspects of the discrete ordinate solution in order to obtain analytically-derived weighting functions, again focusing on the low-stream cases. This differentiation process is the *linearization* of the forward model. In section 4.4 we discuss the various correction procedures used to enhance the model accuracy for a low number of streams (delta-M, NT correction and sphericity correction).

In section 4.5 we examine the accuracy of the 4/6 stream models by carrying out extensive comparisons with 20 stream output from the LIDORT model. We look at a wavelength range of 299-335 nm covering that part of the UV spectrum wherein multiple scattering effects must be included in the RT modeling. ozone is the only absorber. We look at three atmospheric situations: a reference clear sky atmosphere with scattering by molecules and background aerosol distributions; the same atmosphere but containing a tropospheric cloud layer of variable optical thickness; and thirdly, the reference atmosphere with one layer containing an optically thick scattering medium such as desert dust. We consider also the dependence on surface albedo (assumed Lambertian). A wide range of viewing geometries will be considered, appropriate to the nadir viewing conditions encountered by the two GOME instruments, SCIAMACHY and OMI. Section 4.5.2 examines the efficacy of the NT single scatter correction, while section 4.5.3 looks at the effect of the sphericity correction. The main conclusions from this study are summarized in Section 4.6, which also contains a discussion on the consequences regarding performance and accuracy trade-off in an operational ozone profile retrieval context.

4.2. Discrete ordinate theory with analytic 4/6-stream solutions

We derive homogeneous and particular solutions for the general discrete-ordinate model, noting especially the factor of 2 reduction that allows analytic solutions to be written down for the 4/6 stream cases. The equation of radiative transfer is solved for a vertically inhomogeneous atmosphere by assuming a division into a number of optically uniform adjacent sub-layers. The RTE is first solved for each of these layers, and this is followed by the application of boundary conditions to match the radiation field at the layer interfaces. The atmosphere is illuminated by a downward-directed parallel beam of sunlight entering at the top of the atmosphere. The diffuse radiation field (excluding the attenuated direct beam) is determined for the whole atmosphere. Since we are dealing with the UV/Visible part of the spectrum, thermal emission is not taken into account. The effect of the sphericity of the atmosphere on the direct beam attenuation is accounted for using the pseudo-spherical "average secant" approximation [85, 35]. Polarization is not considered.

The input optical parameters for the complete problem are for each layer p, where $p = 1, \dots, P$: $\Delta\tau_p = \tau_p - \tau_{p-1}$, the layer optical thickness and the quantity $\beta^*_{l,p} \equiv \omega_p \beta_{l,p}$, where ω_p is the single scattering albedo (ratio of the *total* scattering and extinction coefficients), and $\beta_{l,p}$ are the phase function Legendre expansion moments (indexed by l). We note that ω_p and $\beta_{l,p}$ only enter the discrete ordinate solution through the product $\beta^*_{l,p}$. The optical depth for extinction τ acts as the vertical co-ordinate, with $\tau = \tau_p$ at the bottom of layer p; τ is zero at the top of the atmosphere. These parameters are computed from:

$$\Delta\tau_p = \sum_{\varsigma} \Delta\tau_{\mathrm{s},p,\varsigma} + \sum_{\alpha} \Delta\tau_{\mathrm{a},p,\alpha} \tag{4.1}$$

$$\beta^*_{l,p} = \frac{1}{\Delta\tau_p} \sum_{\varsigma} \Delta\tau_{\mathrm{s},p,\varsigma} \beta_{l,p,\varsigma}. \tag{4.2}$$

Here $\Delta\tau_{\mathrm{s},p,\varsigma}$ is the contribution of scatterer ς to the layer optical thickness for scattering, $\Delta\tau_{\mathrm{a},p,\alpha}$ is the contribution of absorber α to the layer optical thickness for absorption, and $\Delta\tau_p$ is the total layer optical thickness for extinction. A realistic atmosphere contains air molecules and various kinds of aerosols as the scattering agents. Each scatterer is further specified by its phase function moments $\beta_{l,p,\varsigma}$ in (4.2).

We start with the equation of radiative transfer for layer p:

$$\mu \frac{dI(\tau,\mu,\phi)}{d\tau} = I(\tau,\mu,\phi) - J_p(\tau,\mu,\phi) \tag{4.3}$$

$$J_p(\tau,\mu,\phi) = \frac{\omega}{4\pi} \int_{-1}^{1} d\mu' \int_{0}^{2\pi} d\phi' P_p(\mu,\phi;\mu',\phi') I(\tau,\mu',\phi') + \frac{\omega_p}{4\pi} P_p(\mu,\phi;-\mu_0,\phi_0) F_p \mathrm{e}^{-\lambda_p \tau}. \tag{4.4}$$

Here, $I(\tau,\mu,\phi)$ is the diffuse radiance (excluding the direct solar beam) in direction (μ,ϕ) and at optical depth τ; μ is the cosine of the polar angle, ϕ the azimuthal angle. $P_p(\mu,\phi;\mu',\phi') = P_p(\mu_\mathrm{s})$ is the phase function for scattering, which depends on scattering angle θ_s, with $\mu_\mathrm{s} = \cos\theta_\mathrm{s}$. Primes denote the direction of the outgoing beam. The source function J_p represents the sources of diffuse radiation, namely scattered diffuse light and scattered light from the direct solar beam.

The solar beam enters the top of the atmosphere (TOA) in direction $(-\theta_0,\phi_0)$, $\mu_0 = \cos\theta_0$. For the plane-parallel case F_p equals F_0, the solar irradiance at TOA and $\lambda_p = 1/\mu_0$. In the pseudo-spherical treatment, F_p and λ_p are adjusted to account for the reduced path of the direct beam. In the average secant approximation, their values are determined by the requirement that the exponential dependence of the direct beam attenuation is exact at layer boundaries:

$$\lambda_p = \frac{\tilde{\tau}_p - \tilde{\tau}_{p-1}}{\Delta\tau_p}, \tag{4.5}$$

$$F_p = F_0 \exp(-\tilde{\tau}_p + \lambda_p \tau_p), \tag{4.6}$$

with $\tilde{\tau}_p$ the slant optical depth and τ_p the vertical optical depth from TOA to the bottom of layer p. The slant optical depth has to be calculated by ray-tracing for a refractive atmosphere, which should be used for solar zenith angles larger than 85° [85]. In general we can write the slant optical depth as:

$$\tilde{\tau}_p = \sum_{q=1}^{p} s_{pq} \Delta\tau_q. \tag{4.7}$$

This definition introduces the coefficients s_{pq} which characterize the deviation from plane-parallel geometry. In the latter case, all these coefficients are equal to $1/\mu_0$. Without refraction, straightforward goniometry results in the so-called Chapman function [35]:

$$s_{pq} = \frac{\sqrt{z_{q-1}^2 - z_p^2 \sin^2\theta_0} - \sqrt{z_q^2 - z_p^2 \sin^2\theta_0}}{z_{q-1} - z_q}, \tag{4.8}$$

with z_p the altitude of the bottom of layer p relative to the center of the Earth. More precise parameterizations of the direct beam attenuation have been considered in [85]. Note that $1/\lambda_p$ is merely a parameter that describes the dependence of the attenuation on vertical optical depth; in general for the pseudo-spherical treatment, it is not equal to the cosine of the solar zenith angle. Note also that μ_0 is retained in the phase function in (4.3); this is strictly speaking only correct for an atmosphere without refraction.

To solve (4.3), the radiance field is expanded in a Fourier cosine series in the azimuth angle, and the phase function is expanded in a series of $2N$ ordinary Legendre polynomials P_l:

$$I(\tau,\mu,\phi) = \sum_{m=0}^{2N-1} I^m(\tau,\mu)\cos m(\phi_0 - \phi), \tag{4.9}$$

$$P_p(\mu_s) = \sum_{l=0}^{2N-1} \beta_l P_l(\mu_s) \quad \text{with} \quad \beta_{l,p} = \frac{2l+1}{2}\int_{-1}^{1} P_l(\mu_s) P_p(\mu_s) d\mu_s. \tag{4.10}$$

Using the addition theorem for Legendre polynomials and performing the integration over the azimuth angle, we get $2N$ decoupled equations for each successive Fourier component $m = 0,\ldots,2N-1$:

$$\mu\frac{dI^m}{d\tau} = I^m - \int_{-1}^{1} D_p^m(\mu,\mu')I^m(\tau,\mu')d\mu' - Q_p^m(\mu)F_p \mathrm{e}^{-\lambda_p\tau}, \tag{4.11}$$

where

$$D_p^m(\mu,\mu') = \frac{1}{2}\sum_{l=m}^{2N-1} \omega_p \beta_{l,p} Y_l^m(\mu) Y_l^m(\mu') = \frac{1}{2}\sum_{l=m}^{2N-1} \beta_{l,p}^* Y_l^m(\mu) Y_l^m(\mu'), \tag{4.12}$$

$$Q_p^m(\mu) = \frac{1}{2\pi}(2-\delta_{m0})D_p^m(\mu,-\mu_0). \tag{4.13}$$

Y_l^m are the normalized associated Legendre polynomials. In the interests of clarity, we omit the Fourier superscripts m and the layer index p in the following, re-introducing these indices prior to consideration of the boundary value problem.

In the N^{th}-order discrete-ordinates approximation, the integral in (4.11) is approximated by a summation using Gauss-Legendre quadrature over the two half spaces separately. Each quadrature has N points, with abscissae μ_i and weights a_i for $i = 1,\ldots,N$ in the positive half-space, and corresponding values $\mu_{-i} = -\mu_i$ and $a_{-i} = a_i$ in the other half-space. Defining $M_i^+ = I_i^+ + I_i^-$ and $M_i^- = I_i^+ - I_i^-$, with $I_i^\pm = I(\tau, \pm\mu_i)$, we can write from (4.11):

$$\frac{dM_i^+}{d\tau} = -\sum_{j=1}^{N} (\zeta_{ij} - \eta_{ij}) M_j^- - \frac{1}{\mu_i}(Q_i^+ - Q_i^-) F \mathrm{e}^{-\lambda\tau}, \tag{4.14}$$

$$\frac{dM_i^-}{d\tau} = -\sum_{j=1}^{N} (\zeta_{ij} + \eta_{ij}) M_j^+ - \frac{1}{\mu_i}(Q_i^+ + Q_i^-) F \mathrm{e}^{-\lambda\tau}, \tag{4.15}$$

where $Q_i^\pm = Q(\pm\mu_i)$. The two N × N matrices $\boldsymbol{\zeta}$ and $\boldsymbol{\eta}$ are given by:

$$\zeta_{ij} = \frac{1}{\mu_i}(a_i D_{ij}^+ - \delta_{ij}), \quad \eta_{ij} = \frac{1}{\mu_i} a_i D_{ij}^-, \tag{4.16}$$

with $D_{ij}^\pm = D(\mu_i, \pm\mu_j)$. A single equation for M_i^- can be obtained from (4.14) and (4.15):

$$\frac{d^2 M_i^-}{d\tau^2} = \sum_{j=1}^{N} \Gamma_{ij} M_j^- + d_i F \mathrm{e}^{-\lambda\tau}, \tag{4.17}$$

where

$$\Gamma_{ij} = \sum_{k=1}^{N} (\zeta_{ik} + \eta_{ik})(\zeta_{kj} - \eta_{kj}), \tag{4.18}$$

$$d_i = \frac{1}{\mu_i}\lambda(Q_i^+ + Q_i^-) + \frac{1}{\mu_i}\sum_{j=1}^{N} (\zeta_{ij} + \eta_{ij})(Q_i^+ - Q_i^-). \tag{4.19}$$

The general solution to (4.17) may be written:

$$M_i^- = \tilde{M}_i^- + W_i^- F \mathrm{e}^{-\lambda\tau}, \tag{4.20}$$

with $\tilde{M}_i^-$ the general solution to the homogeneous part of (4.17). The latter admits solutions of the form $\tilde{M}_i^- = Y_i^- \mathrm{e}^{-k\tau}$, and this leads to the eigenproblem:

$$\sum_{j=1}^{N} \Gamma_{ij} Y_j^- = \gamma Y_i^-, \tag{4.21}$$

where $\gamma = k^2$. Denote the N eigenvectors and eigenvalues of this system (4.21) as: $\{Y_{ij}^-, \gamma_j\}$, $j = 1, \ldots, N$. Note that since Γ_{ij} is a Hermitian matrix, all eigenvalues are real. In the general case, we solve the system using a standard package such as module DGEEV from the LAPACK numerical suite [65]. However, analytical solutions can be found for the 4 and 6 stream cases $N = 2$ and $N = 3$ respectively (see panels). The eigenvector normalization may be chosen freely; for the 4 and 6 stream analytical eigensolutions, we have set the diagonal elements of the eigenvector matrix to unity.

4 stream eigensolutions:

$$\gamma_{1,2} = \frac{1}{2}(\Gamma_{11}+\Gamma_{22}) \pm \frac{1}{2}\sqrt{(\Gamma_{11}-\Gamma_{22})^2+4\Gamma_{21}\Gamma_{12}}, \tag{4.22}$$

$$Y^-_{11} = 1, \;\; Y^-_{22}=1, \;\; Y^-_{21} = \frac{\Gamma_{21}}{\gamma_1-\Gamma_{22}}, \;\; Y^-_{12} = \frac{\Gamma_{12}}{\gamma_2-\Gamma_{11}}. \tag{4.23}$$

4 stream particular solutions:

$$W^-_1 = \frac{\Gamma_{12}d_2+(\lambda^2-\Gamma_{22})d_1}{\Psi}, \;\; W^-_2 = \frac{\Gamma_{21}d_1+(\lambda^2-\Gamma_{11})d_2}{\Psi}, \tag{4.24}$$

$$\Psi = \lambda^4-(\Gamma_{11}+\Gamma_{22})\lambda^2+\Gamma_{11}\Gamma_{22}-\Gamma_{12}\Gamma_{21}. \tag{4.25}$$

6 stream eigensolutions:

$$0 = \gamma^3 - A\gamma^2 + B\gamma + C,$$

(eigenvalues γ_j, $j=1,2,3$ are real and positive roots of cubic equation)

$$A = \mathrm{Trace}(\boldsymbol{\Gamma}),$$

$$B = \Gamma_{11}\Gamma_{22}+\Gamma_{11}\Gamma_{33}+\Gamma_{22}\Gamma_{33}-\Gamma_{23}\Gamma_{32}-\Gamma_{13}\Gamma_{31}-\Gamma_{12}\Gamma_{21},$$

$$C = \mathrm{Det}(\boldsymbol{\Gamma}).$$

$$\frac{Y^-_{2j}}{Y^-_{1j}} = \frac{\Gamma_{13}\Gamma_{21}-\Gamma_{23}\left(\Gamma_{11}-\gamma_j\right)}{\Gamma_{23}\Gamma_{12}-\Gamma_{13}\left(\Gamma_{22}-\gamma_j\right)}, \quad \frac{Y^-_{3j}}{Y^-_{1j}} = \frac{\Gamma_{12}\Gamma_{31}-\Gamma_{32}\left(\Gamma_{11}-\gamma_j\right)}{\Gamma_{13}\Gamma_{32}-\Gamma_{12}\left(\Gamma_{33}-\gamma_j\right)},$$

$$Y^-_{jj} = 1 \quad \text{for } j=1,2,3. \quad \text{(Normalization)}$$

6 stream particular solutions:

$$W^-_1 = \frac{\mathrm{Det}(\boldsymbol{M}_{(1)})}{\mathrm{Det}(\boldsymbol{M})}, \quad W^-_2 = \frac{\mathrm{Det}(\boldsymbol{M}_{(2)})}{\mathrm{Det}(\boldsymbol{M})},$$

$$W^-_3 = \frac{-d_1-(\Gamma_{11}-\lambda^2)W^-_1-\Gamma_{12}W^-_2}{\Gamma_{13}},$$

$$M_{ij} = \lambda^2\delta_{ij}-\Gamma_{ij},$$

$$\left\{M_{ij}\right\}_{(k)} = \delta_{jk}d_i+(1-\delta_{jk})M_{ij} \quad \text{(matrix } \boldsymbol{M} \text{ with column } k \text{ replaced by vector } \boldsymbol{d}\text{)}$$

The inhomogeneous or particular part of the solution can be found by substitution of (4.20) into (4.17):

$$\lambda^2 W^-_i = \sum_{j=1}^{N}\Gamma_{ij}W^-_j + d_i \tag{4.26}$$

and solving for W^-_i. For the general N-stream case, this linear system of order N can be solved by standard numerical techniques. For the 4 and 6 stream cases ($N=2$ and $N=3$), analytical solutions are written down in the respective panels.

Bringing the two parts together, the general solution to (4.17) is then:

$$M_i^- = \sum_{j=1}^{N} \left\{ \tilde{L}_j^+ Y_{ij}^- \mathrm{e}^{-k_j \tau} + \tilde{L}_j^- Y_{ij}^- \mathrm{e}^{+k_j \tau} \right\} + W_i^- F \mathrm{e}^{-\lambda\tau}, \tag{4.27}$$

where $\tilde{L}_j^+$ and $\tilde{L}_j^-$ are the $2N$ constants of integration, and $k_j = +\sqrt{\gamma_j}$. From (4.14) we have for M_i^+:

$$M_i^+ = \sum_{j=1}^{N} \left\{ \tilde{L}_j^+ Y_{ij}^+ \mathrm{e}^{-k_j \tau} - \tilde{L}_j^- Y_{ij}^- \mathrm{e}^{+k_j \tau} \right\} + W_i^+ F \mathrm{e}^{-\lambda\tau}, \tag{4.28}$$

with:

$$Y_{ij}^+ = \frac{1}{k_j} \sum_{k=1}^{N} (\zeta_{ik} - \eta_{ik}) Y_{kj}^-, \tag{4.29}$$

$$W_i^+ = \frac{1}{\lambda} \sum_{j=1}^{N} (\zeta_{ij} - \eta_{ij}) W_j^- + \frac{1}{\lambda \mu_i} (Q_i^+ - Q_i^-). \tag{4.30}$$

Retention of the inhomogeneous terms in (4.17) shows clearly that the reduction in dimension applies to the particular solution as well as to the homogeneous solutions. Returning to I^+ and I^- and re-introducing the Fourier and layer indices, we can write down the solution for a Fourier component of the radiance at the Gaussian polar angles for any optical depth in a specific layer p:

$$I_p^m(\tau, \mu_i) = \sum_{j=1}^{N} \left\{ L_{j,p}^+ X_{ij,p}^+ \mathrm{e}^{-k_{j,p}(\tau - \tau_{p-1})} + L_{j,p}^- X_{ij,p}^- \mathrm{e}^{-k_{j,p}(\tau_p - \tau)} \right\} + Z_{i,p} F_p \mathrm{e}^{-\lambda\tau}, \tag{4.31}$$

$\forall i \in \{\pm 1, \ldots, \pm N\}$; $L_{j,p}^+$ and $L_{j,p}^-$ are integration constants. We have defined:

$$X_{ij,p}^+ = \frac{1}{2} \left(Y_{ij,p}^+ + Y_{ij,p}^- \right), \quad X_{-ij,p}^+ = \frac{1}{2} \left(Y_{ij,p}^+ - Y_{ij,p}^- \right), \tag{4.32}$$

$$X_{ij,p}^- = X_{-ij,p}^+, \tag{4.33}$$

$$Z_{i,p} = \frac{1}{2} \left(W_{i,p}^+ + W_{i,p}^- \right), \quad Z_{-i,p} = \frac{1}{2} \left(W_{i,p}^+ - W_{i,p}^- \right), \tag{4.34}$$

Exponential arguments in (4.31) have been written as optical depth differences; this safeguards the numerical stability of the solution [56, 34].

The integration constants follow from a set of three boundary conditions. These are (1) radiance values at the $P-1$ layer interfaces are continuous at the Gaussian angles; (2) at the top of the atmosphere the downwelling diffuse radiance is zero; and (3) at the bottom of the atmosphere, upwelling and downwelling radiances are linked by a suitable reflectance relation. These conditions provide a total of $2N \times P$ linear equations to determine the integration constants. The layer interface boundary conditions read:

$$\sum_{j=1}^{N} \left\{ L_{j,p-1}^+ X_{ij,p-1}^+ \Theta_{j,p-1} + L_{j,p-1}^- X_{ij,p-1}^- - L_{j,p}^+ X_{ij,p}^+ - L_{j,p}^- X_{ij,p}^- \Theta_{j,p} \right\} = (Z_{i,p} - Z_{i,p-1}) F_0 \tilde{T}_p, \tag{4.35}$$

where $i = -N, \ldots, N$ ($i \neq 0$) and $p = 2, \ldots, P$. The following definitions have been used:

$$\Theta_{j,p} = \mathrm{e}^{-k_{j,p}\Delta\tau_p}, \tag{4.36}$$

$$\tilde{T}_p = \mathrm{e}^{-\tilde{\tau_p}}. \tag{4.37}$$

The boundary condition at the top of the atmosphere reads:

$$\sum_{j=1}^{N} \left\{ L^{+}_{j,1} X^{+}_{ij,1} + L^{-}_{j,1} X^{-}_{ij,1} \Theta_{j,1} \right\} = -Z_{i,1} F_0, \tag{4.38}$$

where $i = -N, \ldots, 0$. For the boundary condition at the bottom of the atmosphere (BOA) we limit ourselves to the Lambertian condition, with albedo A. For $m = 0$, we have:

$$\sum_{j=1}^{N} \left\{ L^{+}_{j,P} \hat{X}^{+}_{ij,P} \Theta_{j,P} + L^{-}_{j,P} \hat{X}^{-}_{ij,P} \right\} = -\hat{Z}_{i,P} F_0 \tilde{T}_P + \frac{A}{\pi} \mu_0 F_0 \tilde{T}_P, \tag{4.39}$$

which holds $\forall i \in \{1, \ldots, N\}$. For $m \neq 0$, (4.39) still applies, but now $A = 0$. We have introduced:

$$\hat{X}^{\pm}_{ij,P} = X^{\pm}_{ij,P} - 2A \sum_{k=-N}^{-1} a_k \mu_{-k} X^{\pm}_{kj,P}, \tag{4.40}$$

$$\hat{Z}_{i,P} = Z^{\pm}_{i,P} - 2A \sum_{k=-N}^{-1} a_k \mu_{-k} Z_{k,P}. \tag{4.41}$$

This linear system for $L^{\pm}_{i,p}$ is sparse, in the sense that the matrix only contains non-zero terms in a band along the diagonal. The LIDORT code uses a special LU-decomposition routine from LAPACK [65] that makes use of this sparseness and thereby saves considerably on the number of floating point operations. For the 4/6 stream cases this computation step is the only one where a standard numerical package has to be used. Further discussion on these boundary conditions may be found in [75], where in particular, the surface boundary condition has been generalized to cover a bidirectional reflectance condition, and extended to include surface thermal emission. Although processing time for the overall radiance and weighting function computation is dominated by this numerical step, considerable savings are apparent with a small number of streams. Assuming floating-point operations in this step vary with N^2 for the radiance, the 4 stream algorithm is 25 times faster than a 20 stream calculation.

The discrete-ordinate solution gives radiance at Gaussian angles and at every optical depth in the atmosphere. However, the viewing direction does not usually coincide with one of the Gaussian angles; in this case some kind of interpolation in polar angle is desired. This *post processing* step can be done “smartly” by substituting the discrete ordinate solution at the Gaussian streams in the multiple scatter integrals in the original RTE, and integrating the latter. This procedure is known as source function integration [46, 34]. The formal solution to (4.11) can be written:

$$I^m(0,\mu) = B^m(\mu)\mathrm{e}^{-\tau_P/\mu} + \frac{1}{\mu}\sum_{p=1}^{P}\int_{\tau_p}^{\tau_{p-1}} J^m(\tau',\mu)\mathrm{e}^{-\tau'/\mu} d\tau', \tag{4.42}$$

where $B^m(\mu) \equiv I^m(\tau_P, \mu)$ is the BOA upwelling radiance at the surface, J^m is given by the last two terms on the RHS of (4.11), and μ is the cosine of the desired viewing angle. Replacing the integration over polar angle by a quadrature sum and using the discrete ordinate solutions from (4.31), we get:

$$I^m(0,\mu) = B^m(\mu) T_P(\mu) + \sum_{p=1}^{P} T_{p-1}(\mu) \Lambda^m_p(\mu). \tag{4.43}$$

Transmittance along direction μ is simply $T_p(\mu) = \exp(-\tau_p/\mu)$ and the *layer integrated source terms* $\Lambda^m_p(\mu)$ consist of contributions $\Lambda^m_{p,(ms)}(\mu)$ from multiple scattered light and terms $\Lambda^m_{p,(ss)}(\mu)$ from atmospheric single scattering. We have :

$$\Lambda^m_p(\mu) = \Lambda^m_{p,(ms)}(\mu) + \Lambda^m_{p,(ss)}(\mu), \tag{4.44}$$

where

$$\Lambda^m_{p,(ms)}(\mu) = \sum_{j=1}^{N} \left\{ L^+_{j,p} X^+_{j,p}(\mu) E^+_{j,p}(\mu) + L^-_{j,p} X^-_{j,p}(\mu) E^-_{j,p}(\mu) \right\} + Z_p(\mu) F_0 E^0_p(\mu), \tag{4.45}$$

$$\Lambda^m_{p,(ss)}(\mu) = Q_p(\mu) F_0 E^0_p(\mu), \tag{4.46}$$

with the following set of definitions:

$$X^\pm_{j,p}(\mu) = \frac{1}{2} \sum_{i=-N^\dagger}^{N} a_i D_p(\mu, \mu_i) X^\pm_{ij,p}, \tag{4.47}$$

$$Z_p(\mu) = \frac{1}{2} \sum_{i=-N^\S}^{N} a_i D_p(\mu, \mu_i) Z_{i,p}, \tag{4.48}$$

$$E^+_{j,p}(\mu) = \frac{1 - t_p(\mu)\Theta_{j,p}}{1 + \mu k_{j,p}}, \tag{4.49}$$

$$E^-_{j,p}(\mu) = \frac{\Theta_{j,p} - t_p(\mu)}{1 - \mu k_{j,p}}, \tag{4.50}$$

$$E^0_p(\mu) = \frac{1}{1 + \mu\lambda_p} \left(\tilde{T}_{p-1} - \tilde{T}_p t_p(\mu) \right), \tag{4.51}$$

$$t_p(\mu) = \exp(-\Delta\tau_p/\mu). \tag{4.52}$$

The symbol § indicates exclusion of the $i = 0$ term from the summation. For a plane-parallel atmosphere, we use the appropriate particular solutions $Z_{i,p}$ in (4.48) and replace the average secant λ_p in (4.51) with the value μ_0^{-1}. Assuming a Lambertian surface with albedo A, the BOA upwelling radiance $B^m(\mu)$ in (4.43) may be written (for Fourier component $m = 0$):

$$B^m(\mu) = \frac{A\mu_0 F_0}{\pi} \tilde{T}_P + 2A \sum_{k=-N}^{-1} a_k \mu_{-k} \left[\sum_{j=1}^{N} \left\{ L^+_{j,P} X^+_{kj,P} \Theta_{j,P} + > L^-_{j,P} X^-_{kj,P} \right\} + Z_{k,P} F_0 \tilde{T}_P \right]. \tag{4.53}$$

For $m \neq 0$, $B^m(\mu) \equiv 0$ in the Lambertian case.

4.3. Linearized discrete ordinates: analytic weighting functions

4.3.1. Definitions and input optical parameter derivatives

In general, we define the weighting function from TOA radiance as follows:

$$K_x = \frac{\partial I(0, \mu)}{\partial x_p}, \tag{4.54}$$

where x_p is a parameter denoting some physical property in layer p. This parameter affects the TOA radiance through the optical parameters in layer p that are input for the radiative transport model: the product $\beta^*_{l,p}$ of the phase function moments and the single scattering albedo, and the layer optical thickness $\Delta\tau_p$. For a givenretrieval application, we need to know in detail how these optical parameters depend on x_p. Specifically, the derivatives

$$\frac{\partial\Delta\tau_p}{\partial x_p} \text{ and } \frac{\partial\beta^*_{l,p}}{\partial x_p} \tag{4.55}$$

have to be identified for all $l = 0, \ldots, 2N-1$ (Note that $l = 0$ is included, since $\beta^*_{0,p} = \omega_p$ by definition). Before we determine the derivatives in (4.54) of the discrete ordinate solution outlined in the previous section, we must establish the optical parameter derivatives in (4.55). This is an important first step in deriving weighting functions, and we illustrate this process for number of atmospheric parameters.

Layer column density of gas absorber α

The parameter in this case is defined as

$$x_p = \Delta C_{p,\alpha} \tag{4.56}$$

where $C_{p,\alpha}$ is the column number density of gas α in layer p. The required partial derivatives are:

$$\frac{\partial\beta^*_{l,p}}{\partial x_p} = -\frac{\beta^*_{l,p}}{\Delta\tau_p}\sigma_{p,\alpha}, \tag{4.57}$$

$$\frac{\partial\Delta\tau_p}{\partial x_p} = \sigma_{p,\alpha}, \tag{4.58}$$

where $\sigma_{p,\alpha}$ is the absorption cross section of gas α, and the layer index is retained since trace gas cross-sections may possess temperature and pressure dependence. Note that both derivatives are linear in the cross sections, implying that the corresponding weighting functions are also linear in the cross sections. Hence, once the column density weighting functions have been calculated for gas α_1, corresponding weighting functions for any other gas α_2 may be found by scaling the original results by the cross section ratio $\sigma_{p,\alpha_2}/\sigma_{p,\alpha_1}$.

Temperature

The parameter in this case is temperature ϑ_p, which is assumed constant for the layer p. We take the layer to be specified by pressure levels (and not altitudes) at the upper and lower boundaries. When the layer is in local hydrostatic equilibrium with the acceleration due to gravity G assumed constant over the layer, then the column of air in the layer is simply equal to the pressure drop divided by G, and is independent of temperature. In this case temperature dependence is only manifest in the trace gas cross sections. For trace species α with cross section $\sigma_{p,\alpha}$, we find:

$$\frac{\partial\beta^*_{l,p}}{\partial x_p} = -\frac{\beta^*_{l,p}}{\Delta\tau_p}\Delta C_{p,\alpha}\frac{\partial\sigma_{p,\alpha}}{\partial x_p}, \tag{4.59}$$

$$\frac{\partial\Delta\tau_p}{\partial x_p} = \Delta C_{p,\alpha}\frac{\partial\sigma_{p,\alpha}}{\partial x_p}. \tag{4.60}$$

For O_3 absorption in the Huggins bands, the well-known Bass-Paur quadratic temperature parameterization [70] for the cross sections gives:

$$\sigma_{p,\alpha}(\vartheta_p) = \varsigma_0\left(1 + \vartheta_p\varsigma_1 + \vartheta_p^2\varsigma_2\right), \tag{4.61}$$

$$\frac{\partial\sigma_{p,\alpha}(\vartheta_p)}{\partial x_p} = \varsigma_0\left(\varsigma_1 + 2\vartheta_p\varsigma_2\right), \tag{4.62}$$

for ϑ_p in °C, and parameterization coefficients ς independent of atmospheric conditions. We remark that the weighting functions are now linear in the derivatives of the cross sections. Thus, if we have already calculated column density weighting functions for gas α, temperature weighting functions may be obtained by simply scaling these results with the ratio $(\partial\sigma_{p,\alpha}/\partial\vartheta_p)/\sigma_{p,\alpha}$.

Aerosol layer optical thickness

The parameter in this case is given by:

$$x_p \equiv \Delta\tau_{\mathrm{s},p,\varsigma} + \Delta\tau_{\mathrm{a},p,\varsigma} = \omega_{p,\varsigma}\Delta\tau_{\mathrm{s},p,\varsigma}, \tag{4.63}$$

where index ς labels a specific aerosol among the list of scatterers and absorbers. $\Delta\tau_{p,\varsigma}$ is the optical depth for extinction due to aerosol ς for layer p, and $\omega_{p,\varsigma}$ and $\Delta\tau_{\mathrm{s},p,\varsigma}$ are the single scattering albedo of the aerosol (assumed constant) and the layer optical depth for scattering respectively. The relevant partial derivatives are:

$$\frac{\partial\beta^*_{l,p}}{\partial x_p} = \frac{1}{\Delta\tau_p}\left(\omega^{-1}_{p,\varsigma}\beta_{l,p,\varsigma} - \beta^*_{l,p}\right), \tag{4.64}$$

$$\frac{\partial\Delta\tau_p}{\partial x_p} = 1. \tag{4.65}$$

Aerosol layer single scattering albedo

For layer p, the parameter is now:

$$x \equiv \omega_{p,\varsigma} = \frac{\Delta\tau_{\mathrm{s},p,\varsigma}}{\Delta\tau_{\mathrm{a},p,\varsigma} + \Delta\tau_{\mathrm{s},p,\varsigma}}, \tag{4.66}$$

Taking the layer aerosol optical thickness constant, we have:

$$\frac{\partial\beta^*_{l,p}}{\partial x} = \frac{1}{\Delta\tau_p}(\Delta\tau_{\mathrm{a},p,\varsigma} + \Delta\tau_{\mathrm{s},p,\varsigma})\beta_{l,p,\varsigma}, \tag{4.67}$$

$$\frac{\partial\Delta\tau_p}{\partial x} = 0. \tag{4.68}$$

Aerosol asymmetry parameter

In this case parameter x is the layer asymmetry parameter $g_{p,\varsigma}$, where ς again labels a specific aerosol. In this case we require the variation of the phase function moments $\beta_{l,p,\varsigma}$ with respect to x. In general, this would require an examination of the detailed microphysical scattering properties of the given aerosol. However, for a Henyey-Greenstein phase function, this variation is straightforward. Here, $\beta_{p,l,\varsigma} = (2l+1)g^l_{p,\varsigma}$ for $l = 0,\ldots,2N-1$, and hence

$$\frac{\partial\beta^*_{l,p}}{\partial x} = \frac{1}{\Delta\tau_p}\Delta\tau_{\mathrm{s},p,\varsigma}l(2l+1)g^{l-1}_{p,\varsigma}, \tag{4.69}$$

$$\frac{\partial\Delta\tau_p}{\partial x} = 0. \tag{4.70}$$

The first four examples are limited to variations of the *amount* of molecular and/or particulate constituents; in each case the angular distribution of the scattering is regarded as constant (the phase function moments $\beta_{l,p,\varsigma}$ have zero derivatives). The last example (asymmetry parameter) involved derivatives of the phase function moments, and this would be important for the retrieval of aerosol microphysical properties. In the present work, we are interested chiefly in layer column density weighting functions for the trace gas ozone, as these are essential for any ozone profile retrieval algorithm. However, additional weighting functions with respect to quantities such as aerosol optical thickness are also useful in such an algorithm, as they can be used to assess *process* errors in the ozone retrieval due to uncertainties in the assumed aerosol or temperature distributions [4].

Since TOA radiance is also a function of the surface albedo A, we can define an albedo weighting function $K_A = \partial I(0,\mu)/\partial A$ (in this work, we restrict ourselves to the Lambertian case; a more general bidirectional treatment can be found in [75, 85]). Albedo derivatives are included in the next section.

4.3.2. Derivatives of the discrete ordinate solution with respect to x_p

In this section we present a (somewhat lengthy) exposition of the analytical determination of derivatives of the TOA-radiance with respect to layer parameters x_p and also with respect to albedo A. The procedure involves a term-by-term differentiation of the TOA radiance with repeated applications of the chain-rule of differentiation. The chain-rule differentiation terminates when we encounter an explicit dependency on one of the input parameters. At such a point we use the partial derivatives in (4.55) to finalize the procedure. The corresponding "end-point" equations are marked by a † symbol in the exposition; we will refer to these equations in the discussion on numerical implementation that follows. We start with differentiation of the Fourier sum (4.9):

$$\frac{\partial I(0,\mu,\phi)}{\partial x_p} = \sum_{m=0}^{2N-1} \frac{\partial I^m(0,\mu)}{\partial x_p} \cos m(\phi_0 - \phi), \tag{4.71}$$

$$\frac{\partial I(0,\mu,\phi)}{\partial A} = \sum_{m=0}^{2N-1} \frac{\partial I^m(0,\mu)}{\partial A} \cos m(\phi_0 - \phi). \tag{4.72}$$

The derivatives of the Fourier components can be obtained by differentiation of the post-processed discrete ordinate solution (4.43). We find:

$$\frac{\partial I(0,\mu)}{\partial x_p} = \frac{\partial I^m(\tau_P,\mu)}{\partial x_p} T_P(\mu) + I^m(\tau_P,\mu)\frac{\partial T_P(\mu)}{\partial x_p} + \sum_{q=1}^{P}\left\{\frac{\partial T_{q-1}(\mu)}{\partial x_p}\Lambda_q(\mu) + T_{q-1}(\mu)\frac{\partial \Lambda_q(\mu)}{\partial x_p}\right\}, \tag{4.73}$$

$$\frac{\partial I^m(0,\mu)}{\partial A} = \frac{\partial I^m(\tau_P,\mu)}{\partial A} T_P(\mu) + \sum_{q=1}^{P} T_{q-1}(\mu)\frac{\partial \Lambda_q(\mu)}{\partial A}. \tag{4.74}$$

Note that layer source term $\Lambda_q(\mu)$ for layer q will not only depend on optical parameters from that layer, but also on optical parameters from layers p for $p \neq q$. The transmittance in direction μ from TOA to the bottom of layer p depends only on the optical thickness of layers above and including p:

$$\frac{\partial T_q(\mu)}{\partial \Delta\tau_p} = \begin{cases} -T_q(\mu)/\mu & \text{for} \quad p \leq q; \\ 0 & \text{for} \quad p > q. \end{cases} \tag{4.75}$$

Derivatives of the BOA upwelling radiance $B^m(\mu)$ are determined from the surface boundary condition. For a Lambertian surface, we have for Fourier component $m = 0$ (the index m is assumed):

$$
\begin{aligned}
\frac{\partial B(\mu)}{\partial x_p} &= 2A \sum_{k=-N}^{-1} a_k \mu_{-k} \left[\sum_{j=1}^{N} \left\{ \frac{\partial L^+_{j,P}}{\partial x_p} X^+_{kj,P} \Theta_{j,P} + L^+_{j,P} \frac{\partial X^+_{kj,P}}{\partial x_p} \Theta_{j,P} \delta_{pP} + L^+_{j,P} X^+_{kj,P} \frac{\partial \Theta_{j,P}}{\partial x_p} \delta_{pP} \right.\right. \\
&+ \left.\left. \frac{\partial L^-_{j,P}}{\partial x_p} X^-_{kj,P} + L^-_{j,P} \frac{\partial X^-_{kj,P}}{\partial x_p} \delta_{pP} \right\} - \frac{\partial Z_{k,P}}{\partial x_p} F_0 \tilde{T}_P - Z_{k,P} F_0 \frac{\partial \tilde{T}_P}{\partial x_p} \right] + \frac{A}{\pi} \mu_0 F_0 \frac{\partial \tilde{T}_P}{\partial x_p}, \qquad (4.76) \\
\frac{\partial B(\mu)}{\partial A} &= \frac{B(\mu)}{A} + 2A \sum_{k=-N}^{-1} a_k \mu_{-k} \left[\sum_{j=1}^{N} \left\{ \frac{\partial L^+_{j,P}}{\partial A} X^+_{kj,P} \Theta_{j,P} + \frac{\partial L^-_{j,P}}{\partial A} X^-_{kj,P} \right\} \right]. \qquad (4.77)
\end{aligned}
$$

From the definition of the layer transmittance $\Theta_{j,p}$ in Eq. (4.36) we have:

$$
\frac{\partial \Theta_{j,p}}{\partial x_p} = - \left(k_{j,p} + \Delta\tau_p \frac{\partial k_{j,p}}{\partial x_p} \right) \Theta_{j,p} \frac{\partial \Delta\tau_p}{\partial x_p}. \qquad (4.78)
$$

For all layers $p > q$ the derivative of the the pseudo-spherical transmittance $\tilde{T}_q$ is zero. For layers $p \le q$ this derivative can can be found using results (4.7) and (4.37):

$$
\dagger\, \frac{\partial \tilde{T}_q}{\partial x_p} = \begin{cases} -s_{qp} \tilde{T}_q \frac{\partial \Delta\tau_p}{\partial x_p} & \text{for} \quad p \le q; \\ 0 & \text{for} \quad p > q. \end{cases} \qquad (4.79)
$$

The derivatives of the layer source terms follow from the definition (4.44) and differentiation of (4.45) and (4.46). In the following expressions, we have differentiated total layer source terms, but the separation into multiple scatter and single scattering contributions is straightforward. We find:

$$
\begin{aligned}
\frac{\partial \Lambda^m_q(\mu)}{\partial x_p} &= \sum_{j=1}^{N} \left\{ \frac{\partial L^+_{j,q}}{\partial x_p} X^+_{j,q}(\mu) E^+_{j,q}(\mu) + L^+_{j,q} \frac{\partial X^+_{j,q}(\mu)}{\partial x_q} \delta_{pq} E^+_{j,q}(\mu) + L^+_{j,q} X^+_{j,q}(\mu) \frac{\partial E^+_{j,q}(\mu)}{\partial x_q} \delta_{pq} \right. \\
&\quad + \left. \frac{\partial L^-_{j,q}}{\partial x_p} X^-_{j,q}(\mu) E^-_{j,q}(\mu) + L^-_{j,q} \frac{\partial X^-_{j,q}(\mu)}{\partial x_q} \delta_{pq} E^-_{j,q}(\mu) + L^-_{j,q} X^-_{j,q}(\mu) \frac{\partial E^-_{j,q}(\mu)}{\partial x_q} \delta_{pq} \right\} \\
&\quad + \left[\frac{\partial Z_q(\mu)}{\partial x_p} + \frac{\partial Q_q(\tau,\mu)}{\partial x_q} \delta_{pq} \right] F_0 E^0_q(\mu) + \left[Z_q(\mu) + Q_q(\mu) \right] F_0 \frac{\partial E^0_q(\mu)}{\partial x_p}, \qquad (4.80) \\
\frac{\partial \Lambda^m_q(\mu)}{\partial A} &= \sum_{j=1}^{N} \left\{ \frac{\partial L^+_{j,q}}{\partial A} X^+_{j,q}(\mu) E^+_{j,q}(\mu) + \frac{\partial L^-_{j,q}}{\partial A} X^-_{j,q}(\mu) E^-_{j,q}(\mu) \right\}. \qquad (4.81)
\end{aligned}
$$

Some layer quantities depend only on the optical parameters of the layer in which they are defined; others have cross-layer derivatives. The eigenvalues, eigenvectors and the $E^{\pm}(\mu)$ terms in (4.49) and (4.50) have vanishing cross-layer derivatives. Furthermore, the eigen-quantities have no dependence on optical thickness. The $E^0(\mu)$ term in (4.51) defined for layer p depends on optical thicknesses of layers above p. The dependence of the particular solution in layer q on optical thickness values for layers $p \leqslant q$ is more subtle. This dependence is expressed through the average secant factor λ_q appropriate to the pseudo-spherical treatment of the direct beam source. The integration constants depend on all optical parameters in all layers because of the coupling implicit in the linear system defined by the set of boundary conditions. These dependencies will be clarified below, when we consider expressions for the various terms in (4.80) and (4.81).

Starting with $Q_p(\mu)$ from (4.13), we find:

$$\frac{\partial Q_p(\mu)}{\partial x_p} = \frac{1}{2\pi}(2-\delta_{m0})\frac{\partial D_p(\mu,-\mu_0)}{\partial x_p}, \tag{4.82}$$

We have also the cross-layer derivatives:

$$\frac{\partial\{E_q^0(\mu)\}}{\partial x_p} = -\frac{E_q^0(\mu)}{1+\mu\lambda_q}\mu\frac{\partial\lambda_q}{\partial x_p} + \frac{1}{1+\mu\lambda_q}\left[\frac{\partial\tilde{T}_{q-1}}{\partial x_p} - \frac{\partial\tilde{T}_q}{\partial x_p}t_q(\mu) - \tilde{T}_q\frac{\partial t_q(\mu)}{\partial x_q}\delta_{pq},\right] \tag{4.83}$$

with:

$$\dagger\ \frac{\partial t_p(\mu)}{\partial x_p} = -\frac{1}{\mu}t_p(\mu)\frac{\partial\Delta\tau_p}{\partial x_p}. \tag{4.84}$$

Using (4.5) and (4.7) we can write:

$$\dagger\ \frac{\partial\lambda_q}{\partial x_p} = \begin{cases} \frac{s_{qp}-s_{q-1,p}}{\Delta\tau_q}\frac{\partial\Delta\tau_p}{\partial x_p} & \text{for} \quad p<q \\ \frac{s_{qq}-\lambda_q}{\Delta\tau_q}\frac{\partial\Delta\tau_p}{\partial x_p} & \text{for} \quad p=q \\ 0 & \text{for} \quad p>q \end{cases} \tag{4.85}$$

For a plane-parallel medium, $s_{pq} = \lambda_q = 1/\mu_0$ for all $p,q = 1,\ldots,P$, so that the cross-layer derivatives in (4.85) vanish in this case. Derivatives of the other two exponential functions $E^{\pm}(\mu)$ follow from straightforward differentiation using the definitions. We get:

$$\frac{\partial E^+_{j,p}}{\partial x_p} = -\frac{1}{1+\mu k_{j,p}}\left\{t_p(\mu)\frac{\partial\Theta_{j,p}}{\partial x_p} + \frac{\partial t_p(\mu)}{\partial x_p}\Theta_{j,p} + E^+_{j,p}\mu\frac{\partial k_{j,p}}{\partial x_p}\right\}, \tag{4.86}$$

$$\frac{\partial E^-_{j,p}}{\partial x_p} = \frac{1}{1-\mu k_{j,p}}\left\{\frac{\partial\Theta_{j,p}}{\partial x_p} - \frac{\partial t_p(\mu)}{\partial x_p} + E^-_{j,p}\mu\frac{\partial k_{j,p}}{\partial x_p}\right\}. \tag{4.87}$$

Next we consider the derivatives of the eigenvectors, plus derivatives of the eigensolutions defined for user angles in (4.80):

$$\frac{\partial X^{\pm}_{j,p}(\mu)}{\partial x_p} = \frac{1}{2}\sum_{i=-N^{\S}}^{N}\left\{a_i\frac{\partial D_p(\mu,\mu_i)}{\partial x_p}X^{\pm}_{ij,p} + a_i D_p(\mu,\mu_i)\frac{\partial X^{\pm}_{ij,p}}{\partial x_p}\right\}, \tag{4.88}$$

$$\frac{\partial X^{\pm}_{ij,p}}{\partial x_p} = \frac{1}{2}\left(\frac{\partial Y^+_{ij,p}}{\partial x_p} \pm \frac{\partial Y^-_{ij,p}}{\partial x_p}\right), \tag{4.89}$$

and from (4.29) we find:

$$\frac{\partial Y^+_{ij,p}}{\partial x_p} = -Y^+_{ij,p}\frac{1}{k_{j,p}}\frac{\partial k_{j,p}}{\partial x_p} + \frac{1}{k_{j,p}}\sum_{k=1}^{N}\left\{\left(\frac{\partial\zeta_{ik,p}}{\partial x_p} - \frac{\partial\eta_{ik,p}}{\partial x_p}\right)Y^-_{kj,p} + (\zeta_{ik,p}-\eta_{ik,p})\frac{\partial Y^-_{kj,p}}{\partial x_p}\right\}. \tag{4.90}$$

Using (4.16):

$$\frac{\partial\zeta_{ij,p}}{\partial x_p} = \frac{a_i}{\mu_i}\frac{\partial D_p(\mu_i,\mu_j)}{\partial x_p}, \tag{4.91}$$

$$\frac{\partial\eta_{ij,p}}{\partial x_p} = \frac{a_i}{\mu_i}\frac{\partial D_p(\mu_i,-\mu_j)}{\partial x_p}, \tag{4.92}$$

and from (4.12) we arrive at the following termination point:

$$\dagger \; \frac{\partial D_p(\mu,\nu)}{\partial x_p} = \frac{1}{2}\sum_{l=m}^{2N-1} \frac{\partial \beta^*_{l,p}}{\partial x_p} Y_l^m(\mu) Y_l^m(\nu). \tag{4.93}$$

Note that the derivative in (4.93) also applies to the derivatives $\partial D_p(\mu,\mu_i)/\partial x_p$ as found in expressions (4.82) and (4.88). We must now specify derivatives of the eigenvectors $Y^-_{ij,p}$ and eigenvalues $\gamma_{i,p}$ for layer p. We have:

$$\frac{\partial k_{j,p}}{\partial x_p} = \frac{1}{2\sqrt{\gamma_{j,p}}} \frac{\partial \gamma_{j,p}}{\partial x_p}. \tag{4.94}$$

For the general N-stream case derivatives $\partial\gamma_{j,p}/\partial x_p$ of the eigenvalues and $\partial Y_{j,i,p}/\partial x_p$ for the eigenvectors are determined by explicit differentiation of the eigen-equation together with a constraint provided by the eigenvector normalization. This results in a linear system which can be solved numerically for the required derivatives. The procedure for the general case has been described in [75, 85]. The key to this step is to determine first the derivatives of the coefficients of the eigenmatrix $\mathbf{\Gamma}$; these follow from the definition (4.18). We find:

$$\frac{\partial \Gamma_{ij,p}}{\partial \beta^*_{l,p}} = \sum_{k=1}^{N} \left\{ \left(\frac{\partial \zeta_{ik,p}}{\partial \beta^*_{l,p}} + \frac{\partial \eta_{ik,p}}{\partial \beta^*_{l,p}} \right) (\zeta_{kj,p} - \zeta_{kj,p}) + (\zeta_{ik,p} + \zeta_{ik,p}) \left(\frac{\partial \zeta_{kj,p}}{\partial \beta^*_{l,p}} - \frac{\partial \eta_{kj,p}}{\partial \beta^*_{l,p}} \right) \right\}. \tag{4.95}$$

We may use expressions (4.91), (4.92) and (4.93) in the evaluation of the $\mathbf{\Gamma}$ derivative. For the four-stream case the differentiation can be performed analytically (see panel).

For the particular solutions, derivatives with respect to $\beta^*_{l,p}$ contain no cross-layer terms. We have:

$$\begin{aligned} \frac{\partial Z_q(\mu)}{\partial x_p} &= \frac{1}{2}\sum_{i=-N^\S}^{N} \left\{ a_i \frac{\partial D_q(\mu,\mu_i)}{\partial x_q} \delta_{pq} Z_{i,q} + a_i D_q(\mu,\mu_i) \frac{\partial Z_{i,q}}{\partial x_p} \right\}, & (4.96) \\ \frac{\partial Z_{i,q}}{\partial x_p} &= \frac{1}{2}\left(\frac{\partial W^+_{i,q}}{\partial x_p} + \frac{\partial W^-_{i,q}}{\partial x_p} \right), \quad \frac{\partial Z_{-i,q}}{\partial x_p} = \frac{1}{2}\left(\frac{\partial W^+_{i,q}}{\partial x_p} - \frac{\partial W^-_{i,q}}{\partial x_p} \right). & (4.97) \end{aligned}$$

From the auxilliary equation (4.30) we get:

$$\begin{aligned} \frac{\partial W^+_{i,q}}{\partial x_p} = & - W^+_{i,q}\frac{1}{\lambda_q}\frac{\partial \lambda_q}{\partial x_p} + \frac{1}{\lambda_q}\sum_{j=1}^{N} \left\{ \left(\frac{\partial \zeta_{ij,q}}{\partial x_q} - \frac{\partial \eta_{ij,q}}{\partial x_q} \right) \delta_{pq} W^-_{j,q} + (\zeta_{ij,q} - \eta_{ij,q}) \frac{\partial W^-_{j,q}}{\partial x_p} \right\} \\ & + \frac{1}{\lambda_q \mu_i} \left(\frac{\partial Q^+_{i,q}}{\partial x_q} - \frac{\partial Q^-_{i,q}}{\partial x_q} \right) \delta_{pq}. \end{aligned} \tag{4.98}$$

The derivatives of $Q_i^\pm$ follow from (4.82); the $\boldsymbol{\zeta}$ and $\boldsymbol{\eta}$ derivatives are already noted above in (4.91) and (4.92).

The derivatives with respect to λ_q are already given in (4.85). The other derivatives follow from differentiation of Equation (4.19):

$$\begin{aligned} \frac{\partial d_{i,q}}{\partial x_p} = & \frac{1}{\mu_i}(Q^+_{i,q} + Q^-_{i,q})\lambda_q \frac{\partial \lambda_q}{\partial x_p} + \frac{1}{\mu_i}\lambda_p \left(\frac{\partial Q^+_{i,p}}{\partial x_p} + \frac{\partial Q^-_{i,p}}{\partial x_p} \right) \\ & + \frac{1}{\mu_i}\sum_{j=1}^{N} \left\{ \left(\frac{\partial \zeta_{ij,p}}{\partial x_p} + \frac{\partial \eta_{ij,p}}{\partial x_p} \right) (Q^+_{i,p} - Q^-_{i,p}) + (\zeta_{ij,p} + \eta_{ij,p}) \left(\frac{\partial Q^+_{i,p}}{\partial x_p} - \frac{\partial Q^-_{i,p}}{\partial x_p} \right) \right\} \end{aligned} \tag{4.99}$$

Note that the dependency of λ_q on optical thicknesses is the reason for the existence of non-vanishing cross-layer derivatives of the particular solution. Since λ_q is constant for a plane-parallel medium, the particular solution cross-layer derivatives disappear. In the four-stream case we use the analytic solutions (4.24) to derive the particular solution derivatives in an explicit analytic form (see panel).

4 stream eigensolution derivatives:

$$\begin{aligned}\frac{\partial\gamma_{i,p}}{\partial x_p} &= \frac{1}{2}\frac{\partial\Gamma_{11,p}}{\partial x_p}+\frac{1}{2}\frac{\partial\Gamma_{22,p}}{\partial x_p}\pm \\ &\quad \frac{1}{\Xi_p}\left\{\frac{1}{2}(\Gamma_{11,p}-\Gamma_{22,p})\left(\frac{\partial\Gamma_{11,p}}{\partial x_p}-\frac{\partial\Gamma_{22,p}}{\partial x_p}\right)+\Gamma_{21,p}\frac{\partial\Gamma_{21,p}}{\partial x_p}+\Gamma_{12,p}\frac{\partial\Gamma_{21,p}}{\partial x_p}\right\},\end{aligned}\tag{4.100}$$

$$\Xi_p = \sqrt{(\Gamma_{11,p}-\Gamma_{22,p})^2+4\Gamma_{21,p}\Gamma_{12,p}}.\tag{4.101}$$

In (4.100) the plus sign holds for $i=1$ and the minus sign for $i=2$.

$$\frac{\partial Y^-_{11,p}}{\partial x_p} = \frac{\partial Y^-_{22,p}}{\partial x_p} = 0,\tag{4.102}$$

$$\frac{\partial Y^-_{21,p}}{\partial x_p} = \frac{1}{\gamma_{1,p}-\Gamma_{22,p}}\frac{\partial\Gamma_{21,p}}{\partial x_p}-\frac{\Gamma_{21,p}}{(\gamma_{1,p}-\Gamma_{22,p})^2}\left(\frac{\partial\gamma_{1,p}}{\partial x_p}-\frac{\partial\Gamma_{22,p}}{\partial x_p}\right),\tag{4.103}$$

$$\frac{\partial Y^-_{12,p}}{\partial x_p} = \frac{1}{\gamma_{2,p}-\Gamma_{11,p}}\frac{\partial\Gamma_{12,p}}{\partial x_p}-\frac{\Gamma_{12,p}}{(\gamma_{2,p}-\Gamma_{11,p})^2}\left(\frac{\partial\gamma_{2,p}}{\partial x_p}-\frac{\partial\Gamma_{11,p}}{\partial x_p}\right).\tag{4.104}$$

4 stream particular solution derivatives:

$$\begin{aligned}\frac{\partial W^-_{1,q}}{\partial x_p} &= \frac{1}{\Psi_q}\left\{\Gamma_{12,q}\frac{\partial d_{2,q}}{\partial x_p}+\frac{\partial\Gamma_{12,q}}{\partial x_q}\delta_{pq}d_{2,q}+\left(2\lambda_q\frac{\partial\lambda_q}{\partial x_p}-\frac{\partial\Gamma_{22,q}}{\partial x_q}\delta_{pq}\right)d_{1,q}\right\} \\ &+ \frac{1}{\Psi_q}\left\{(\lambda_q^2-\Gamma_{22,q})\frac{\partial d_{1,q}}{\partial x_p}-W^-_{1,q}\frac{\partial\Psi_q}{\partial x_p}\right\},\end{aligned}\tag{4.105}$$

$$\begin{aligned}\frac{\partial W^-_{2,q}}{\partial x_p} &= \frac{1}{\Psi_q}\left\{\Gamma_{21,q}\frac{\partial d_{1,q}}{\partial x_p}+\frac{\partial\Gamma_{21,q}}{\partial x_q}\delta_{pq}d_{1,q}+\left(2\lambda_q\frac{\partial\lambda_q}{\partial x_p}-\frac{\partial\Gamma_{11,q}}{\partial x_q}\delta_{pq}\right)d_{2,q}\right\} \\ &+ \frac{1}{\Psi_q}\left\{(\lambda_q^2-\Gamma_{11,q})\frac{\partial d_{2,q}}{\partial x_p}-\frac{W^-_{2,q}}{\Psi_q}\frac{\partial\Psi_q}{\partial x_p}\right\},\end{aligned}\tag{4.106}$$

$$\begin{aligned}\frac{\partial\Psi_q}{\partial x_p} = &-\left(\frac{\partial\Gamma_{11,p}}{\partial x_p}+\frac{\partial\Gamma_{22,p}}{\partial x_p}\right)\lambda_p^2+\frac{\partial\Gamma_{11,p}}{\partial x_p}\Gamma_{22,p}+\Gamma_{11,p}\frac{\partial\Gamma_{22,p}}{\partial x_p} \\ &-\frac{\partial\Gamma_{12,p}}{\partial x_p}\Gamma_{21,p}-\Gamma_{12,p}\frac{\partial\Gamma_{21,p}}{\partial x_p}+\left[4\lambda_q^3-2\lambda_q(\Gamma_{11}+\Gamma_{22})\right]\frac{\partial\lambda_q}{\partial x_p}\end{aligned}\tag{4.107}$$

The final task is the evaluation of derivatives of the integration constants $L^{\pm}_{i,q}$ in Eqs. (4.35), (4.38) and (4.38). The way to proceed here is to differentiate the boundary conditions with respect to these optical parameters. Differentiating the layer interface boundary conditions gives:

$$
\begin{aligned}
\sum_{j=1}^{N} \left\{ \frac{\partial L^{+}_{j,q-1}}{\partial x_p} X^{+}_{ij,q-1} \Theta_{j,q-1} + \frac{\partial L^{-}_{j,q-1}}{\partial x_p} X^{-}_{ij,q-1} - \frac{\partial L^{+}_{j,q}}{\partial x_p} X^{+}_{ij,q} - \frac{\partial L^{-}_{j,q}}{\partial x_p} X^{-}_{ij,q} \Theta_{j,q} \right\} = \\
- \sum_{j=1}^{N} \left\{ L^{+}_{j,q-1} \frac{\partial X^{+}_{ij,q-1}}{\partial x_{q-1}} \delta_{p,q-1} \Theta_{j,q-1} + L^{+}_{j,q-1} X^{+}_{ij,q-1} \frac{\partial \Theta_{j,q-1}}{\partial x_{q-1}} \delta_{p,q-1} \right. \\
\left. + L^{-}_{j,q-1} \frac{\partial X^{-}_{ij,q-1}}{\partial x_{q-1}} \delta_{p,q-1} - L^{+}_{j,q} \frac{\partial X^{+}_{ij,q}}{\partial x_q} \delta_{pq} - L^{-}_{j,q} \frac{\partial X^{-}_{ij,q}}{\partial x_q} \delta_{pq} \Theta_{j,q} - L^{-}_{j,q} X^{-}_{ij,q} \frac{\partial \Theta_{j,q}}{\partial x_q} \delta_{pq} \right\} \\
+ \left(\frac{\partial Z_{i,q}}{\partial x_p} - \frac{\partial Z_{i,q-1}}{\partial x_p} \right) F_0 \tilde{T}_{q-1} + (Z_{i,q} - Z_{i,q-1}) F_0 \frac{\partial \tilde{T}_{q-1}}{\partial x_p},
\end{aligned}
\tag{4.108}
$$

with $i = -N, \dots, N$ $(i \neq 0)$ and $q = 2, \dots, P$ and $p = 1, \dots, P$. For the boundary condition at TOA, we find similarly that:

$$
\begin{aligned}
\sum_{j=1}^{N} \left\{ \frac{\partial L^{+}_{j,1}}{\partial x_p} X^{+}_{ij,1} + \frac{\partial L^{-}_{j,1}}{\partial x_p} X^{-}_{ij,1} \Theta_{j,1} \right\} = - \frac{\partial Z_{i,1}}{\partial x_1} \delta_{1p} F_0 \\
- \sum_{j=1}^{N} \left\{ L^{+}_{j,1} \frac{\partial X^{+}_{ij,1}}{\partial x_1} \delta_{1p} + L^{-}_{j,1} \frac{\partial X^{-}_{ij,1}}{\partial x_1} \delta_{1p} \Theta_{j,1} + L^{-}_{j,1} X^{-}_{ij,1} \frac{\partial \Theta_{j,1}}{\partial x_1} \delta_{1p} \right\},
\end{aligned}
\tag{4.109}
$$

with $i = -N, \dots, 0$ and $p = 1, \dots, P$. Note that the RHS is zero for $p \neq 1$. Finally, for the boundary condition at the bottom of the atmosphere:

$$
\begin{aligned}
\sum_{j=1}^{N} \left\{ \frac{\partial L^{+}_{j,P}}{\partial x_p} \hat{X}^{+}_{ij,P} \Theta_{j,P} + \frac{\partial L^{-}_{j,P}}{\partial x_p} \hat{X}^{-}_{ij,P} \right\} = - \frac{\partial \hat{Z}_{i,P}}{\partial x_p} F_0 \tilde{T}_P - \hat{Z}_{i,P} F_0 \frac{\partial \tilde{T}_P}{\partial x_p} + A \mu_0 F_0 \frac{\partial \tilde{T}_P}{\partial x_p} \\
- \sum_{j=1}^{N} \left\{ L^{+}_{j,P} \frac{\partial \hat{X}^{+}_{ij,P}}{\partial x_P} \delta_{pP} \Theta_{j,P} + L^{+}_{j,P} \hat{X}^{+}_{ij,P} \frac{\partial \Theta_{j,P}}{\partial x_P} \delta_{pP} + L^{-}_{j,P} \frac{\partial \hat{X}^{-}_{ij,P}}{\partial x_P} \delta_{pP} \right\},
\end{aligned}
\tag{4.110}
$$

which is valid for $i = 0, \dots, N$ and $p = 1, \dots, P$. In the last expression we have the auxiliary definitions:

$$
\frac{\partial \hat{X}^{\pm}_{ij,P}}{\partial x_P} = \frac{\partial X^{\pm}_{ij,P}}{\partial x_P} - 2A \sum_{k=-N}^{-1} a_k \mu_{-k} \frac{\partial X^{\pm}_{kj,P}}{\partial x_P}, \tag{4.111}
$$

$$
\frac{\partial \hat{Z}_{i,P}}{\partial x_p} = \frac{\partial Z_{i,P}}{\partial x_p} - 2A \sum_{k=-N}^{-1} a_k \mu_{-k} \frac{\partial Z_{k,P}}{\partial x_p}. \tag{4.112}
$$

The derivatives of the integration constants with respect to the albedo A in (4.77) and (4.81) follow from differentiation of the boundary conditions:

$$\sum_{j=1}^{N}\left\{\frac{\partial L^{+}_{j,q-1}}{\partial A}X^{+}_{ij,q-1}\Theta_{j,q-1}+\frac{\partial L^{-}_{j,q-1}}{\partial A}X^{-}_{ij,q-1}-\frac{\partial L^{+}_{j,q}}{\partial A}X^{+}_{ij,q}-\frac{\partial L^{-}_{j,q}}{\partial A}X^{-}_{ij,q}\Theta_{j,q}\right\}=0, \tag{4.113}$$

$$\sum_{j=1}^{N}\left\{\frac{\partial L^{+}_{j,1}}{\partial A}X^{+}_{ij,1}+\frac{\partial L^{-}_{j,1}}{\partial A}X^{-}_{ij,1}\Theta_{j,1}\right\}=0, \tag{4.114}$$

$$\begin{aligned}\sum_{j=1}^{N}\left\{\frac{\partial L^{+}_{j,P}}{\partial A}\hat{X}^{+}_{ij,P}\Theta_{j,P}+\frac{\partial L^{-}_{j,P}}{\partial A}\hat{X}^{-}_{ij,P}\right\} &= \frac{\mu_0F_0}{\pi}\tilde{T}_P-\frac{\partial\hat{Z}_{i,P}}{\partial A}F_0\tilde{T}_P\\ &\quad-\sum_{j=1}^{N}\left\{L^{+}_{j,P}\frac{\partial\hat{X}^{+}_{ij,P}}{\partial A}\delta_{pP}\Theta_{j,P}+L^{-}_{j,P}\frac{\partial\hat{X}^{-}_{ij,P}}{\partial A}\delta_{pP}\right\},\end{aligned} \tag{4.115}$$

with

$$\frac{\partial\hat{X}^{\pm}_{ij,P}}{\partial A}=-2\sum_{k=-N}^{-1}a_k\mu_{-k}\,X^{\pm}_{kj,P}, \quad \text{and} \quad \frac{\partial\hat{Z}_{i,P}}{\partial A}=-2\sum_{k=-N}^{-1}a_k\mu_{-k}Z_{k,P}. \tag{4.116}$$

6 stream eigensolution derivatives:

$$\begin{aligned}\frac{\partial\gamma}{\partial x}&=-\frac{\gamma^2\frac{\partial A}{\partial x}+\gamma\frac{\partial B}{\partial x}+\frac{\partial C}{\partial x}}{3\gamma^2+2A\gamma+B},\\ \frac{1}{Y^{-}_{1j}}\frac{\partial Y^{-}_{2j}}{\partial x}-\frac{Y^{-}_{1j}}{Y^{-2}_{2j}}\frac{\partial Y^{-}_{1j}}{\partial x}&=\frac{\partial}{\partial x}\left\{\frac{\Gamma_{13}\Gamma_{21}-\Gamma_{23}\left(\Gamma_{11}-\gamma_j\right)}{\Gamma_{23}\Gamma_{12}-\Gamma_{13}\left(\Gamma_{22}-\gamma_j\right)}\right\},\\ \frac{1}{Y^{-}_{1j}}\frac{\partial Y^{-}_{3j}}{\partial x}-\frac{Y^{-}_{1j}}{Y^{-2}_{3j}}\frac{\partial Y^{-}_{1j}}{\partial x}&=\frac{\partial}{\partial x}\left\{\frac{\Gamma_{12}\Gamma_{31}-\Gamma_{32}\left(\Gamma_{11}-\gamma_j\right)}{\Gamma_{13}\Gamma_{32}-\Gamma_{12}\left(\Gamma_{33}-\gamma_j\right)}\right\},\\ \frac{\partial Y^{-}_{jj}}{\partial x}&=0 \quad \text{for } j=1,2,3.\end{aligned}$$

6 stream particular solution derivatives:

$$\begin{aligned}\frac{\partial W^{-}_{k,q}}{\partial x_p}&=\frac{\mathrm{Det}(\boldsymbol{M}^{pq}_{(k)})}{\mathrm{Det}(\boldsymbol{M})},\\ \left\{M_{ij}\right\}^{pq}_{(k)}&=\delta_{jk}e^{pq}_{i}+(1-\delta_{jk})M_{ij} \quad \text{for } k=1,2,3\\ e^{pq}_{i}&=\frac{\partial d_{i,q}}{\partial x_p}-\left(2\lambda_q\frac{\partial\lambda_q}{\partial x_p}-\frac{\partial\Gamma_{ij,q}}{\partial x_q}\delta_{pq}\right)W^{-}_{i,q}\end{aligned}$$

Quantities d_i, M_{ij}, A, B and C were defined in the earlier 6-stream panel for the solution only.

4.3.3. Computational strategy

Differentiation of the boundary conditions produces a linear system for each x_p and for albedo A, from which the derivatives $\partial L^{\pm}_{i,q}/\partial x_p$ and $\partial L^{\pm}_{i,q}/\partial A$ can be determined. These linear systems contain the same (sparse) matrix that was used for the original boundary value calculation; only the source terms differ. The integration constant derivatives are then obtained by back-substitution using the previously determined LU-decomposition of the sparse matrix.

The computational strategy to compute simultaneously the radiance and the weighting functions is the exact reversal of the derivation outlined above. First the optical input parameters and their derivatives with respect to x_p are computed for the specific retrieval application. The first step is to evaluate quantities (and their derivatives) that depend explicitly on the input parameters - these components can be found in equations marked with the † symbol, namely: the three types of transmittances in Eqs. (4.75), (4.84) and (4.79) and the function $D_P(\mu,\nu)$ in Eq. (4.93). For the pseudo-spherical model the derivatives of the average secant factors λ_q in Eq. (4.85) are computed at this stage.

The next step is to calculate eigenvalues, eigenvectors and the particular solution values and their derivatives. Then the sparse matrix and the source terms for the integration constants plus additional source terms for the linear systems that give integration constant derivatives are computed. Back-substitution using the LU-decomposed sparse matrix then provides the constants and their derivatives. Next, the post-processing step is executed by calculating integrated source term components and their derivatives. This requires the eigenvectors and particular solutions plus associated derivatives to be computed at user-defined (off-quadrature) directions μ. The last components that need calculating are those that make up the BOA upwelling radiance and its derivative. Using the layer-by-layer source term integration, we then derive Fourier components of the TOA radiance and TOA radiance derivative for user-defined directions. The Fourier summations then complete the calculations.

The important point to note here is that the LU-decomposition of the sparse boundary problem matrix has to be performed just once for the complete calculation of radiances and weighting functions; this represents an enormous saving in computational effort. Back-substitutions will be done once for the radiance and once for each weighting function. For a multi-parameter retrieval algorithm such as the ozone profile problem for GOME and GOME-2, the simultaneous calculation of weighting functions using a linearized model gives a major advantage in terms of computing time. Furthermore, the weighting functions have been derived analytically by explicit differentiation of the RTE solution; there is no need for ad-hoc finite-differencing estimates. A full treatment of boundary condition linearization and weighting function derivation for the general $2N$-stream discrete ordinate model can be found in [75] and [85].

4.4. Corrections to enhance accuracy

4.4.1. The delta-M scaling

The delta-M scaling transformation [36] replaces the original phase function by a delta-function forward peak plus a smoother less anisotropic residual. Photons in the forward peak are treated as unscattered; this results in a scaling (reduction) of the optical depth and other optical properties. Radiative transfer with For single scattering albedo ω_q, optical thickness Δ_q and phase function moment coefficients β_{lq} in layer q, the delta-M scaling is

$$\overline{\omega}_q = \omega_q \frac{(1-f_q)}{(1-g_q)}, \quad \overline{\Delta}_q = \Delta_q(1-g_q), \quad \overline{\beta}_{l,q} = \frac{\beta_{l,q} - (2l+1)\, f_q}{1-f_q}, \tag{4.117}$$

where

$$g_q \equiv \omega_q f_q \quad \text{and} \quad f_q = \frac{\beta_{M,q}}{2M+1}. \tag{4.118}$$

Here, $l = 0, \ldots 2N-1$ and f_q is the *truncation factor* in layer q, with $M = 2N$. All scaled phase function moment coefficients $\overline{\beta}_{l,q}$ for $l \geqslant M$ are zero. In the pseudo-spherical model, scaling for the slant path optical depth inputs $\tilde{\tau}_p$ follows from the definition (4.7). In terms of the product $\beta^*_{l,q}$ which governs the discrete ordinate equations, we have:

$$\overline{\beta}^*_{l,q} = \overline{\omega}_q \overline{\beta}_{l,q} = \frac{\beta^*_{l,q} - (2l+1)g_q}{1-g_q}. \tag{4.119}$$

For the weighting function differentiation with respect to variable x_q in layer q, we also require a scaling of the derivatives $\partial\Delta_q/\partial x_q$ and $\partial\beta^*_{l,q}/\partial x_q$ of the optical input parameters. These may be obtained by straightforward differentiation of the above definitions, and the results are;

$$\frac{\partial\overline{\Delta}_q}{\partial x_q} = \frac{\partial\Delta_q}{\partial x_q}(1-g_q) - \frac{\Delta_q}{2M+1}\frac{\partial\beta^*_{M,q}}{\partial x_q}, \tag{4.120}$$

$$\frac{\partial\overline{\beta}^*_{l,q}}{\partial x_q} = \frac{1}{(1-g_q)^2}\left\{(1-g_q)\frac{\partial\beta^*_{l,q}}{\partial x_q} - \frac{(2l+1) - \beta^*_{l,q}}{2M+1}\frac{\partial\beta^*_{M,q}}{\partial x_q}\right\}. \tag{4.121}$$

In the ozone profile application, we do not consider variations of the phase function moments, so that derivatives in (4.121) are given by $\partial\beta^*_{l,q}/\partial x_q = \beta_{l,q}\partial\omega_q/\partial x_q$. The delta-M scaling is not required for a Rayleigh-only atmosphere, since for $N \geqslant 2$ and $M = 2N$, the Rayleigh phase function moments $\beta^{(Ray)}_{M,q}$ are identically zero.

4.4.2. Single scatter correction: the Nakajima-Tanaka procedure

The upwelling radiance at TOA calculated by our model may be written in terms of a contribution I_{dms} due to multiple scattering and to the attenuated direct reflection of the solar beam from the surface, and a contribution I_{ss} due to upward single scattering of the solar beam at points along the line of sight. Surface-reflected light (apart from the direct beam) is regarded as multiply scattered; in particular this includes photons scattered singly in *downward* directions before undergoing reflection at the surface. The model computation of I_{ss} is likely to be inaccurate with a low number of streams, since a lot of phase function information is lost in the truncation (with or without the delta-M scaling). A single scatter correction replaces I_{ss} with an exact computation $I_{ssexact}$ which retains an accurate description of the phase function. Using definitions (4.43) for the TOA intensity mth Fourier component and (4.44) for the single and multiple scatter layer source terms, we can then perform the Fourier sum over cosine azimuth to get I_{dms} and I_{ss} for a given geometry (μ,ϕ):

$$I_{dms}(0,\mu,\phi) = \sum_{m=0}^{MC}\left\{B^m(\mu)T_P(\mu) + \sum_{p=1}^{P} T_{p-1}(\mu)\Lambda^m_{p,(ms)}(\mu)\right\}\cos m(\phi_0-\phi), \tag{4.122}$$

$$I_{ss}(0,\mu,\phi) \equiv \sum_{p=1}^{P} T_{p-1}(\mu)S^{MC}_p(\mu,\phi) = \sum_{p=1}^{P} T_{p-1}(\mu)\sum_{m=0}^{MC}\Lambda^m_{p,(ss)}\cos m(\phi_0-\phi). \tag{4.123}$$

In the last expression the Fourier-summed single scatter layer source term $S_p^{MC}(\mu,\phi)$ has been defined. In calculating the *total* TOA radiance, it is normal practice to apply an accuracy convergence criterion to the Fourier azimuth series for the total (multiple and single scatter) Fourier components. Convergence testing dictates the number *MC* of terms included in the series; *MC* is not necessarily equal to $2N-1$ (the maximum allowed number of Fourier terms). However, a single scatter correction means that we need only retain $I_{dms}(0,\mu,\phi)$ from our discrete ordinate model; we do not need expression (4.123) since this will be replaced by an exact calculation. Thus our model needs to examine convergence only for the multiple scatter radiance, for which the required number of Fourier components may be different from *MC* which applies to the total radiance. In situations where single scattering tends to predominate (this is true for our application, especially for lower wavelengths in the UV), the multiple scatter Fourier series will in general converge faster than that for the total radiance. This represents a further saving of computer resources. Henceforth in this section, we assume that only multiple scatter output (radiances and weighting functions) has been generated by the discrete ordinate model.

We wish to replace the single scatter contribution $S_p^{MC}(\mu,\phi)$ with quantities $S_p^{exact}(\mu,\phi)$ calculated using a more precise form of the phase function. These corrected single scatter layer source terms may be determined by straightforward integration of the radiative transfer equation in the absence of multiple scatter sources. One can either use the Legendre phase function expansion developed for the discrete ordinate model, taking a sufficient number of phase function moments to ensure an accurate representation of the phase function, or employ an exact expression for the phase function if the latter is available. When the delta-M scaling has been applied, we must implement the single scatter correction using *scaled* optical thickness values, but without scaling the single scatter albedo and by using an exact (unscaled) phase function. In this case a division by $1-g_p$ is necessary because of the scaling on optical thickness (see equation (4.117) above), with $g_p = \beta^*_{2N,p}/(2M+1)$ from (4.118). This calculation is the *first-order Nakajima-Tanaka (NT) correction procedure* [37]. For the pseudo-spherical approximation in a non-refracting atmosphere, the total corrected TOA single scatter radiance computed in this way is:

$$I_{ssexact}(0,\mu,\phi) \equiv \sum_{p=1}^{P} T_{p-1}(\mu) S_p^{exact} = \sum_{p=1}^{P} T_{p-1}(\mu) \frac{F_0 E_p^0(\mu)}{4\pi(1-g_p)} \sum_{l=0}^{MX} \beta^*_{l,p} P_l(\cos\theta_s), \tag{4.124}$$

where multiplier $E_p^0(\mu)$ is defined in (4.51).

We have used expansions for the layer phase functions in terms of Legendre polynomials $P_l(\cos\theta_s)$ in the cosine of the scatter angle θ_s, and the number of moments *MX* is sufficient for an accurate evaluation of the scattering in all layers. θ_s is constant for all layers in a non-refracting atmosphere, and is given by the usual expression:

$$\cos\theta_s = -\mu\mu_0 + \sqrt{(1-\mu^2)(1-\mu_0^2)}\cos(\phi_0-\phi). \tag{4.125}$$

In an unscaled atmosphere, $\beta^*_{2N,p}$ and hence g_p are zero in each layer, and unscaled optical depths are used in the calculations of $T_{p-1}(\mu)$ and $E_p^0(\mu)$. It is straightforward to write down the derivatives of (4.124):

$$\frac{\partial I_{ssexact}(0,\mu,\phi)}{\partial x_p} = \sum_{q=1}^{P} \left\{ \frac{\partial T_{q-1}(\mu)}{\partial x_p} S_q^{exact} + T_{q-1}(\mu) \frac{\partial S_q^{exact}}{\partial x_p} \right\} \tag{4.126}$$

with:

$$
\begin{aligned}
\frac{\partial S_q^{exact}}{\partial x_p} &= \frac{F_0 \delta_{pq} E_q^0(\mu)}{4\pi(1-g_q)^2} \left\{ (1-g_q) \sum_{l=0}^{MX} \frac{\partial \beta^*_{l,q}}{\partial x_q} P_l(\cos\theta_s) + \frac{1}{2M+1} \frac{\partial \beta^*_{2N,q}}{\partial x_q} \sum_{l=0}^{MX} \beta^*_{l,q} P_l(\cos\theta_s) \right\} \\
&\quad + \frac{F_0}{4\pi(1-g_q)} \frac{\partial E_q^0(\mu)}{\partial x_p} \sum_{l=0}^{MX} \beta^*_{l,q} P_l(\cos\theta_s). \qquad (4.127)
\end{aligned}
$$

View angle (degrees)	Stream number	DISORT output	LIDORT output
Original radiance before correction I(original)			
0.0	6	7.83513E-02	7.835137E-02
10.0	6	7.64205E-02	7.642062E-02
20.0	6	7.66746E-02	7.667478E-02
30.0	6	7.92090E-02	7.920910E-02
40.0	6	8.41525E-02	8.415261E-02
Nakajima-Tanaka single scatter term I(ssexact)			
0.0	6	2.36675E-02	2.366747E-02
10.0	6	2.15248E-02	2.152485E-02
20.0	6	2.04918E-02	2.049182E-02
30.0	6	2.08425E-02	2.084254E-02
40.0	6	2.29805E-02	2.298054E-02
Removed single scatter term I(ss)			
0.0	6	2.34218E-02	2.342177E-02
10.0	6	2.12635E-02	2.126346E-02
20.0	6	2.05236E-02	2.052363E-02
30.0	6	2.12063E-02	2.120627E-02
40.0	6	2.33098E-02	2.330982E-02
NT-corrected Radiance I(corrected)			
0.0	6	7.85970E-02	7.859707E-02
10.0	6	7.66818E-02	7.668200E-02
20.0	6	7.66428E-02	7.664297E-02
30.0	6	7.88453E-02	7.884536E-02
40.0	6	8.38232E-02	8.382333E-02

Table 4.1: LIDORT/DISORT comparisons with Nakajima-Tanaka single scatter correction.

The explicit dependence of (4.124) on the products $\beta^*_{l,q}$ allows for a straightforward differentiation with respect to these quantities. However, caution should be exercised with the derivatives of the NT-corrected term with respect to quantities such as the asymmetry parameter which impinge upon the phase function moments; the corresponding weighting functions are sensitive to the additional phase function moments which have been included in the exact single scatter calculation but which are absent from the I_{dms} computation. This problem does not arise for derivatives which only affect only the single scattering albedos ω_q; this will be the case in our ozone profile retrieval application. This completes the Nakajima-Tanaka (NT) single scatter correction for radiances and weighting functions.

The NT correction has been incorporated in the DISORT code (Version 2.0), where it is automatically applied as a post-processing correction to the radiance output. It has been reported [37, 86] that the correction is very effective for all situations away from scattering in the solar aureole region. For this case, Nakajima and Tanaka [37] developed a second-order correction which has also been implemented in DISORT. However, the aureole scenario never pertains in the satellite viewing context, so this refinement will not be necessary in the present application. By way of validation, Table 4.1 gives some comparisons with DISORT Version 2.0 output, for a 60-layer atmosphere with Rayleigh and aerosol scattering and ozone as the trace gas absorber. Calculations were done at one wavelength (335.4579 nm) for a solar zenith angle of 55°, a relative azimuth of 0° and for a number of line-of-sight viewing angles. The albedo was 0.3. In order to achieve consistency with DISORT, our model was run in plane-parallel mode; all $2N-1$ Fourier terms were included in the results (convergence criterion for the azimuth series was switched off). We compare not only the original uncorrected radiances, but also the single scatter computations I_{ss} and $I_{ssexact}$.

4.4.3. Sphericity correction

The treatment in this section is an extension of that given in [85]. As noted in the Introduction, we must consider sphericity effects when dealing with large off-nadir viewing. Referring again to Figure 4.1(b), we consider the atmosphere to consist of a number of horizontally homogeneous layers, and we desire the radiance at B. The line-of-sight is now treated in a curved atmosphere, so that the actual solar and line-of-sight path directions will change from A to B. Thus for each layer n, we must define *local* viewing geometries $G_n = \{\alpha_n, \theta_n, \phi_n\}$ for points V_n at the lower layer boundaries ($n = 1, \ldots, P$, where P is the bottom layer of the atmosphere). Here, α_n is the local line-of-sight zenith angle, θ_n the local solar zenith angle (SZA), and ϕ_n the local value of the relative azimuth between two planes containing these directions. The scenario is defined by TOA angles at B, in other words by the geometry G_0 which is the required input. Straightforward ray tracing in a curved atmosphere (with or without refraction) may be used to determine all G_n given the input G_0.

We can again use source-function integration techniques to derive the TOA radiance at B, but this time noting the local dependence on geometry $G_n, n = 1, \ldots, P$. We write for the multiple scatter and direct-beam radiance at B:

$$I^B_{dms}(0, \alpha_B, \phi_B) = \sum_{m=0}^{MC} \left\{ B^m(\alpha_A) T^{sph}_P(\alpha_p) + \sum_{p=1}^{P} T^{sph}_{p-1}(\alpha_p) \Lambda^{(ms)}_{p,p}(\alpha_p) \right\} \cos m(\phi_0 - \phi_p). \quad (4.128)$$

The BOA source terms $B^m(\alpha_A)$ are evaluated for the geometry G_P at A. The line-of-sight transmittance attenuations $T^{sph}_p(\alpha_p)$ from points V_p to B must now be evaluated for a curved atmosphere. Finally, the multiple scatter *layer* source terms $\Lambda^{(ms)}_{p,p}(\alpha_p)$ for layer p must be computed using geometry G_p. In a similar vein, we have for the single scatter correction:

$$I^B_{ssexact}(0, \alpha_B, \phi_B) = \sum_{p=1}^{P} T^{sph}_{p-1}(\alpha_p) S^{(exact)}_{p,p}(\alpha_p, \phi_p), \quad (4.129)$$

where now the term $S^{(exact)}_{p,p}(\alpha_p, \phi_p)$ for layer p must be evaluated with the appropriate geometry G_p. The final result for radiance I^B is obtained by adding the two contributions in (4.128) and (4.129); the difference between I^B and the regular pseudo-spherical result I^C is the *sphericity correction*.

In particular, we note that solar beam attenuations to points along AB will differ significantly from the attenuations computed for corresponding points along the path AC which is used for the regular pseudo-spherical calculation. Thus it is not surprising that the sphericity correction tends to be dominated by the difference in single scatter computations between paths AB and AC. Computing transmittances and attenuations for points along AB is straightforward in a curved atmosphere; path distances may be evaluated using the Chapman function or by suitable application of Snell's law in a refractive atmosphere. In a non-refractive atmosphere, the scatter angle is a constant for all points along AB. We now describe an interpolation procedure for speeding up the calculation of I^B.

Strictly speaking, we require a series of P calls to the RT model, one for each geometry $G_n, n = 1,\ldots,P$, in order to establish the right multiple scatter layer source terms. However we note that geometries G_n are slowly varying from A to B; an example will illustrate this. We take a non-refractive atmosphere of height 60 km and earth radius 6371 km and TOA input geometry $G_0 = \{65^\circ, 85^\circ, 0^\circ\}$. A simple calculation gives $G_P = \{66.18^\circ, 83.82^\circ, 0^\circ\}$; the change in solar zenith angle is only 1.18°. We expect that the multiple scatter source terms also vary slowly and smoothly with the change in geometry from A to B, and therefore an interpolation procedure using only a few RT model calls will be sufficient. For each geometry G_n, there is a complete set $\Lambda^{(ms)}_{n,p}$ of multiple scatter layer source terms, where $p = 1,\ldots,P$. We thus have a matrix of such results, and it is the diagonal entries $\Lambda^{(ms)}_{n,n}$ in this matrix that are required for the sphericity-corrected radiance I^B. Figure 4.2 plots matrices $\Lambda^{(ms)}_{n,p}$ computed in this manner for a 60-layer mixed Rayleigh/aerosol atmosphere, a TOA geometry $G_0 = \{65^\circ, 85^\circ, 0^\circ\}$, and with optical properties computed at wavelength 329.6 nm. 4 stream, 6 stream and 20 stream LIDORT output is presented. There are 60 lines in total in each graph; the p^{th} line represents source terms $\Lambda^{(ms)}_{n,p}$ for layer p plotted against the geometries G_n as represented by the solar zenith angle variation. Quantities for a given line have been normalized to the values for geometry G_1 (first layer). The dependence is clearly highly linear, suggesting a linear or parabolic interpolation procedure. For the linear interpolation, we choose the end values $\Lambda^{(ms)}_{1,p}$ and $\Lambda^{(ms)}_{P,p}$ ($P = 60$), and for the parabolic case, we select an intermediate point $\Lambda^{(ms)}_{Q,p}$ ($Q = 20$ was chosen). Table 4.2 shows the the maximum interpolation errors obtained using these reference points and interpolating against the solar zenith angle. Linear interpolation (which requires only 2 calls to the RT model) gives errors no greater that 0.25%; the error is negligible for parabolic interpolation (which requires 3 calls to the RT model). Thus the sphericity correction can be implemented satisfactorily with just 1 or 2 additional calls to the RT model; there is no significant loss of accuracy. This is a very important performance consideration for the simulation of backscatter radiances and weighting functions in a retrieval scenario with wide off-nadir viewing geometry.

	4 stream	6 stream	20 stream
Linear	0.22410	0.23521	0.24039
Parabolic	2.1056E-03	2.8773E-03	3.3279E-03

Table 4.2: Maximum interpolation errors (%) for estimating multiple scatter layer source terms.

We note that since the sphericity correction for I^B by necessity involves a complete recalculation of the entire single scatter radiation field, it makes sense to use the Nakajima-Tanaka correction right from the outset whenever delta-M scaling has been applied to the discrete ordinate model. In the results that follow, we will adopt this strategy. We use expressions (4.124) for the radiance and results (4.126) and (4.127) for the weighting functions, remembering that different sets of geometries must be used as we sum layer contributions along the line of sight AB.

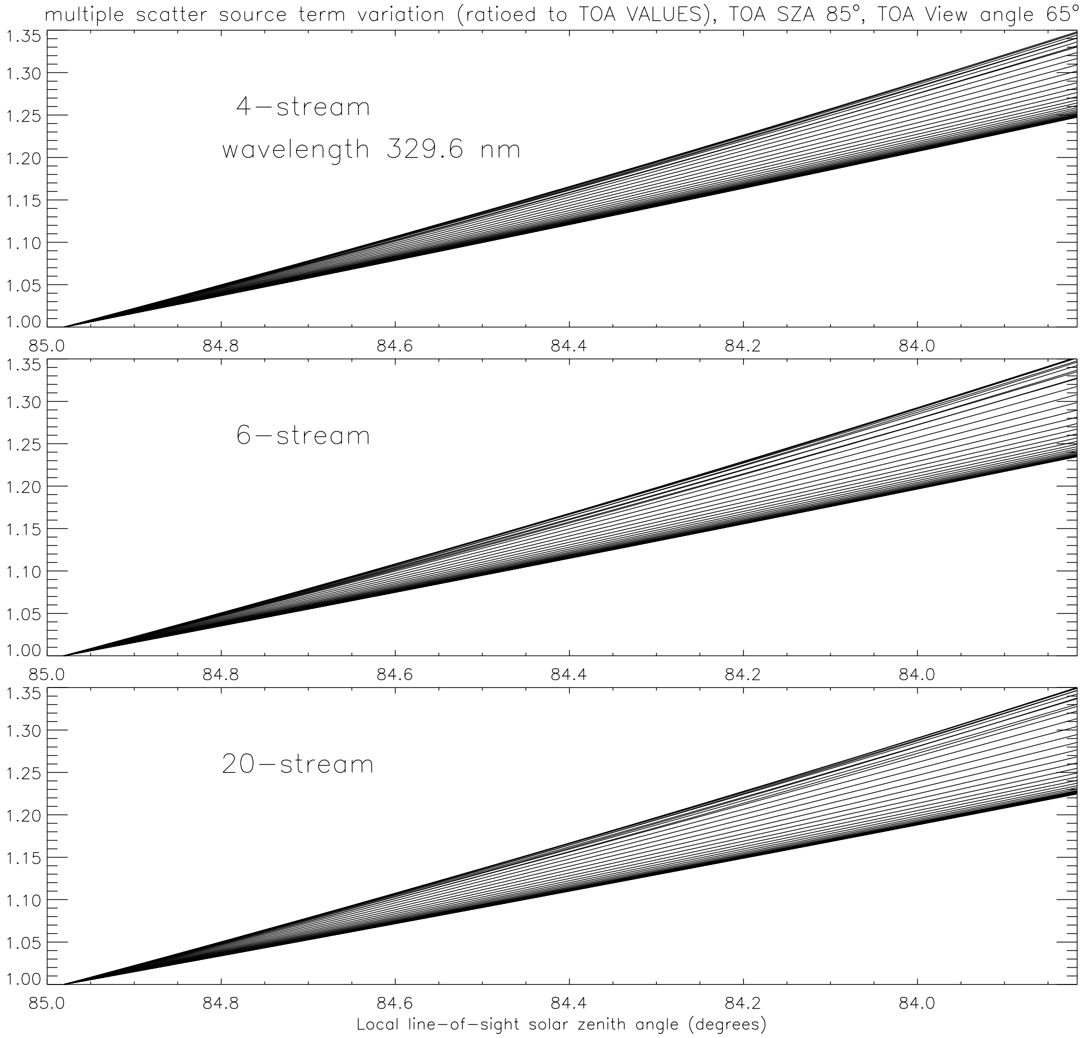

Figure 4.2: Dependence of multiple scatter layer source terms with solar angle along line of sight inclined at 65° to the nadir, with corresponding TOA solar zenith angle 85°. Wavelength as indicated, albedo 0.1, reference atmosphere.

4.5. 4/6-stream accuracy: comparisons with 20-stream output

In this section we compare 4 and 6 stream model output with results from LIDORT using 20 streams. Since the low-stream models are intended for use in a fast ozone profile retrieval scheme for a number of nadir viewing space instruments measuring in the UV/visible, we need to look at a wide range of viewing geometries and atmospheric optical properties in the appropriate wavelength range in order to characterize the forward model error. Following a summary description of the scenarios used in this investigation in Section 4.5.1 below, we then look at the close-to-nadir comparisons without the sphericity correction (Section 4.5.2), before moving on to the wide-angle viewing scenarios in Section 4.5.3.

4.5.1. Atmospheric setup and viewing scenarios

All calculations were performed on a 60-level grid from 0 to 60 km, with vertical resolution of 1 km throughout. Temperature, pressure and ozone volume mixing ratio profiles for the Tropical AFGL standard atmosphere were used [69]. Temperature-dependent cross sections for the ozone Hartley and Huggins absorption bands were taken from a standard data set [70]. Rayleigh scattering properties were determined using empirical formulae for the scattering coefficient and depolarization ratio [18] taken from the data of Bates [80]. A background aerosol distribution was taken from the MODTRAN database [71], with a maritime regime in the planetary boundary layer (visibility 25 km), and background loading and optical properties in the troposphere, stratosphere and mesosphere. Aerosol phase functions were approximated by the Henyey-Greenstein form, with asymmetry parameters also taken from the MODTRAN data set. The lower boundary of the atmosphere was treated as a Lambertian surface; four albedo values were chosen in this study (0.05, 0.1, 0.3 and 0.7).

This constitutes our clear-sky reference atmosphere. For cloud scenarios, we took a cloud layer of geometrical thickness 1.0 km between 3.0 and 4.0 km and varied the optical thickness (7 values of τ_{cloud} were chosen; 0.25, 0.50, 1.0, 2.0, 5.0, 10.0 and 20.0). The cloud particulate (water droplet) single scattering albedo was taken to be 0.999, with corresponding asymmetry parameter 0.85.

For the special cases involving optically thick particulate layers, we selected the following: (1) a Saharan dust scenario, consisting of a layer of dust 1 km thick between 6-7 km, with optical thickness 1.0, single scattering albedo 0.83 and asymmetry parameter 0.79, the latter two values taken from the MODTRAN dust model; (2) a volcanic ash scenario, with a layer of ash at 16-17 km, with extinction and scattering coefficients 0.05641 [km^{-1}] and 0.4494 [km^{-1}] respectively, and asymmetry parameter 0.7897; and (3) a polluted planetary boundary layer scenario, with a layer of particulates at 0-1 km with extinction coefficient 2.9462 [km^{-1}], scattering coefficient 1.893 [km^{-1}] and asymmetry parameter 0.7067. Optical properties for cases (2) and (3) were taken from the LOWTRAN aerosol data base, namely a “fresh volcanic” aerosol loading for case (2) and an “urban” planetary aoundary layer aerosol with visibility 2 km for case (3). Optical properties were taken be constant with wavelength (the values at 337.1 nm were used). All phase functions were treated using the Henyey-Greenstein form.

Calculations were performed for a wavelength range of 299 to 335 nm. Below 300 nm, multiple scattering effects are minor and the issue of RT model errors correspondingly less important owing to the strong ozone absorption and increasing predominance of the Rayleigh single scattering contribution. [Single scatter computations are entirely sufficient for RT simulations below 295 nm]. For the full-wavelength runs, a spectral resolution of $\sim$0.5 nm was adopted. For detailed studies, we selected six wavelengths spread over the Hartley-Huggins bands, from 309.5 nm to 335.5 nm at

$\sim$5.5 nm spacing. The range of solar zenith angles θ_0 used was 15-85°. For the relative azimuth angle $\phi_0 - \phi$ at TOA between the solar plane and the line-of-sight plane, we used the two values 0° (solar) and 180° (antisolar). For detailed studies using the close-to-nadir pseudo-spherical models without the sphericity correction, we chose values of the line-of-sight zenith angle from 0° to 40°. For investigations with the sphericity correction, some 34 values of the line-of-sight zenith angles were taken from -70° on the antisolar side to +70° on the solar side. This range is wide enough to include the extreme OMI and GOME-2 swath positions.

4.5.2. Close-to-nadir viewing: the Nakajima-Tanaka correction

We first look at the effect of the NT single scatter correction at one wavelength (329.0015 nm). Working with the clear sky reference atmosphere, we take an albedo of 0.1 and four solar zenith angles (20°, 50°, 70° and 80°), with a range of line-of-sight zenith angles from -40° on the antisolar side to +40° on the solar side. Figure 4.3 shows comparisons between 4 stream and 6 stream TOA radiance output against 20 stream LIDORT results, with and without the NT correction. Wave structures in the uncorrected output reflect preferential scattering which is not well accounted for by the uncorrected RT model. For the 4 stream case, these structures are damped upon application of the NT correction, and the overall error level is reduced by a factor of 2. However, there are still situations for which the 4/20 radiance difference has increased even after the correction. The situation is much improved with the 6 stream case; the wave structures have almost entirely disappeared and the error has been reduced to a constant low value of around 0.2 to 0.25%. Thus it is clear that there is a substantial improvement between 4 and 6 streams.

The situation for a sample of ozone volume mixing ratio weighting function profiles is shown in Figure 4.4. The scenario is the same as that used for Figure 4.3, except that we consider only one line-of-sight zenith angle (30° on the solar side). The first thing to notice is that the NT correction has little effect on the weighting function accuracy; this should not surprise us, since the weighting functions represent relative changes in the radiance with respect to changes in ozone distributions. A factor of 3 improvement in the error is apparent with the 6 stream case over the 4 stream values; 6 stream weighting functions are nowhere more than 2% distant from their 20 stream equivalents. Peak sensitivity for these weighting functions is around 25 km (this is a tropical atmosphere), and the absolute values of these weighting functions below the tropopause ($\sim$17.5 km) are small. Thus the major uncertainty in the weighting function profile occurring in the troposphere should not concern us unduly, as there is little information to be gained in the retrieval from this part of the atmosphere.

It is well known that Rayleigh scattering is dominant in this part of the UV, especially for shorter wavelengths. We would therefore expect in general that the effects of aerosol scattering will be small on the radiance differences, with the largest discrepancies occurring at higher wavelengths where aerosol scatter is more pronounced. Below 300 nm the magnitude of backscatter is controlled almost entirely by Rayleigh single scattering, and there is little contribution from surface reflected light and tropospheric scattered light because of strong ozone aborption in the Hartley bands (the total ozone absorption optical depth at 290 nm is typically $\simeq$12). For a Lambertian surface, the reflected (unscattered) direct solar beam is increasingly important for higher surface albedos, and we would expect 4/20 and 6/20 radiance differences to become smaller for high albedos.

We now consider more extensive comparisons for a wavelength range of 299 to 335 nm, and for 26 solar zenith angles from 15° to 85°. Figure 4.5 is a contour plot that shows both the 4 and 6 stream comparisons with and without the NT correction, for the reference atmosphere with an albedo of 0.1 and a viewing zenith angle of 20° in the solar direction. The most prominent feature in the

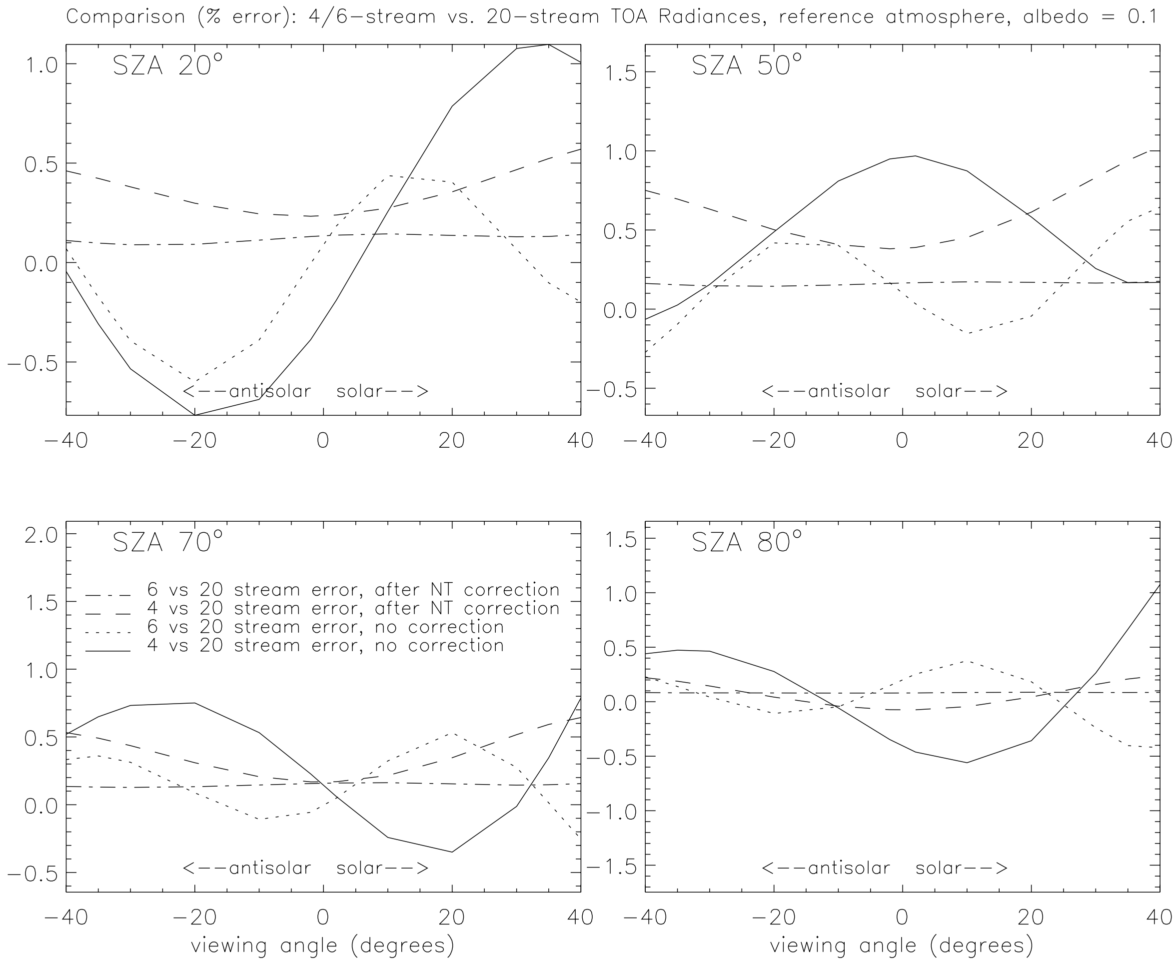

Figure 4.3: Comparison of 4/6 stream and 20 stream TOA upwelling radiances for a reference atmosphere with background aerosol loading; wavelength 329.002 nm, solar zenith angles as indicated.

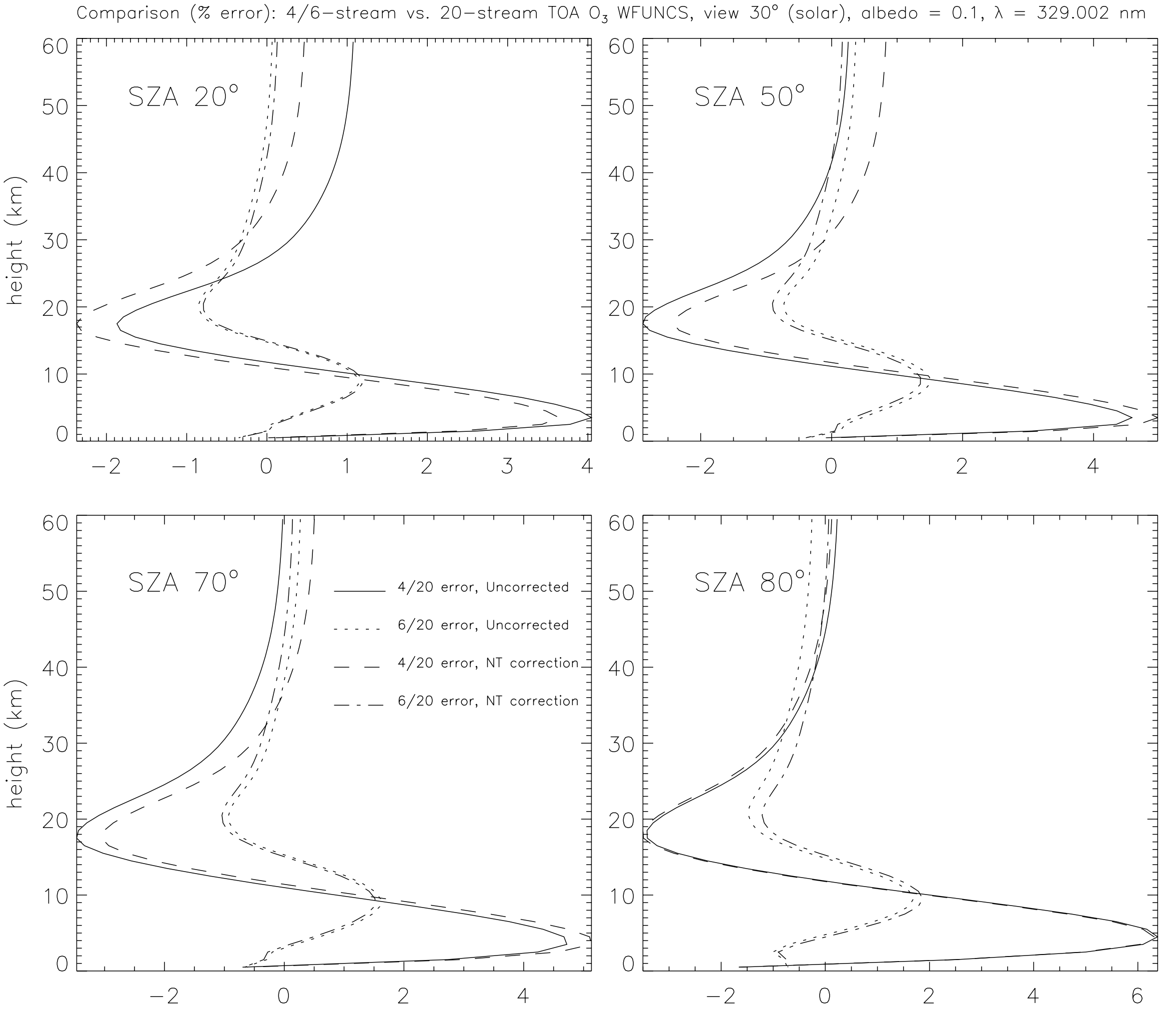

Figure 4.4: Comparison of 4/6 stream and 20 stream TOA upwelling ozone volume mixing ratio weighting functions for a reference atmosphere with background aerosol loading; wavelength 329.002 nm, solar zenith angles as indicated. Line of sight angle 30° on the solar side.

uncorrected 4/20 comparison (upper panel) is the broad maximum centered around solar zenith angle 35° and extending from 315 nm upwards. This is the preferential direction for combined molecular and aerosol single scattering in the atmosphere. Wave structures are apparent in both the uncorrected results, with the wave amplitude following the change in solar zenith angle. The preferential maximum and the wave structures are greatly reduced in the corrected 4 stream results, and almost totally absent for the 6 stream comparisons. We also observe that differences show some variation with the differential structure of the Huggins bands ozone absorption, particularly for high solar zenith angles. It is clear that differences are small for the shorter Rayleigh-dominated wavelengths.

We present detailed contour plots for two more scenarios. Figure 4.6 shows some 6 stream comparisons for an atmosphere with a cloud layer at 3-4 km, which has optical properties as noted above in Section 4.5.1. The scenario is for an off-nadir view of 20°, an albedo of 0.1 and a relative azimuth of 0°. Results for three cloud optical thickness values are shown. It is clear that once the optical depth reaches a certain value, the albedo effect kicks in and the cloud behaves increasingly like a reflecting surface - the 6 stream accuracy becomes greater the thicker the cloud (the same behavior was also found in the corresponding 4 stream comparisons). The optical depth value giving the highest level of error in this case is 2.0, with the maximum uncorrected error in excess of 2.0% for wavelengths greater than 325 nm and for solar zenith angles in the range 15-30° (center left panel). The wave structure is clear in the left-hand (uncorrected) panels. We note that for cloud layers closer to the surface, the effect will increasingly resemble that produced by a highly reflecting surface, so we would expect the 6/20 differences to be smaller in this case. By contrast, a particulate layer higher in the troposphere would be expected to produce more significant errors, and we observe this to be the case in the next scenario (Saharan dust).

In the ozone profile algorithms developed so far for GOME, SCIAMACHY and GOME-2, clouds have been treated in the independent pixel approximation, wherein the simulated TOA radiance for a partially cloudy scene is taken to be a weighted mean of two radiances for clear-sky and cloud-filled scenarios:

$$I_{total} = F_c I_{cloud} + (1 - F_c) I_{clear}. \tag{4.130}$$

F_c is the fractional cloud cover. For GOME scenes, F_c has been retrieved either by using reflectivity measurements in and around the O_2 *A* band [87, 88, 89], or by means of a thresholding algorithm based on GOME's broad-band polarization measurement devices [89]. O_2 *A* reflectivities can also yield information on cloud-top pressure values and cloud optical thickness, though it has not yet proved possible to obtain consistently reliable estimates of the latter quantity. In the FRESCO algorithm [88], clouds are treated as Lambertian reflectors with albedo 80%, and least-squares fitting of reflectivities in part of the O_2 *A* band yields a simultaneous retrieval of cloud fraction F_c and cloud-top pressure p_c. With the large GOME footprint, F_c and p_c must be regarded as *effective* values which in the context of ozone profile or column retrieval are used to correct for the trace gas distribution in the lower part of the atmosphere. These results from FRESCO are used in the Fast Delivery ozone processor at KNMI.

The previous example showed that the presence of an additional scatterer in one part of the atmosphere can introduce larger differences between 4/6 stream and 20 stream radiances, particularly if the layer has a critical optical depth. If the scatterer is optically thin in the chosen layer, then there will not be much difference from background results. On the other hand a really opaque particulate layer will act as a reflecting boundary with high albedo, in which case the change from 4/6 to 20 streams will be reduced for reasons given above. For the three special cases described in Section 4.5.1, we look at the same viewing conditions as in the cloud examples. In Figure 4.7 (top panels) results are shown for the Saharan dust layer scenario; the major positive error peak in the uncorrected results around

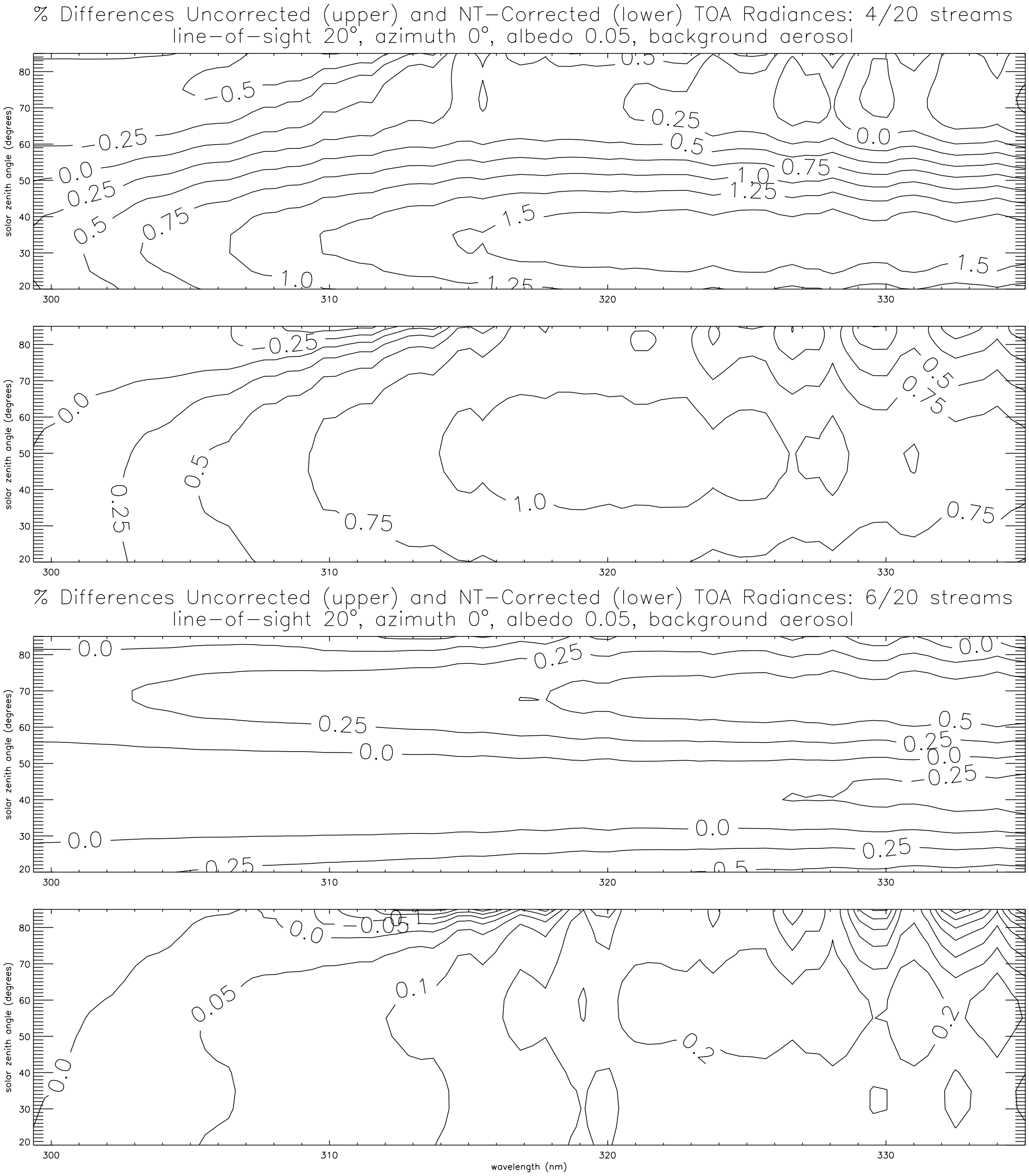

Figure 4.5: Comparison of 4/6 stream and 20 stream TOA upwelling radiances for a reference atmosphere with background aerosol loading; wavelength range 299-335 nm, solar zenith range 15-85°.

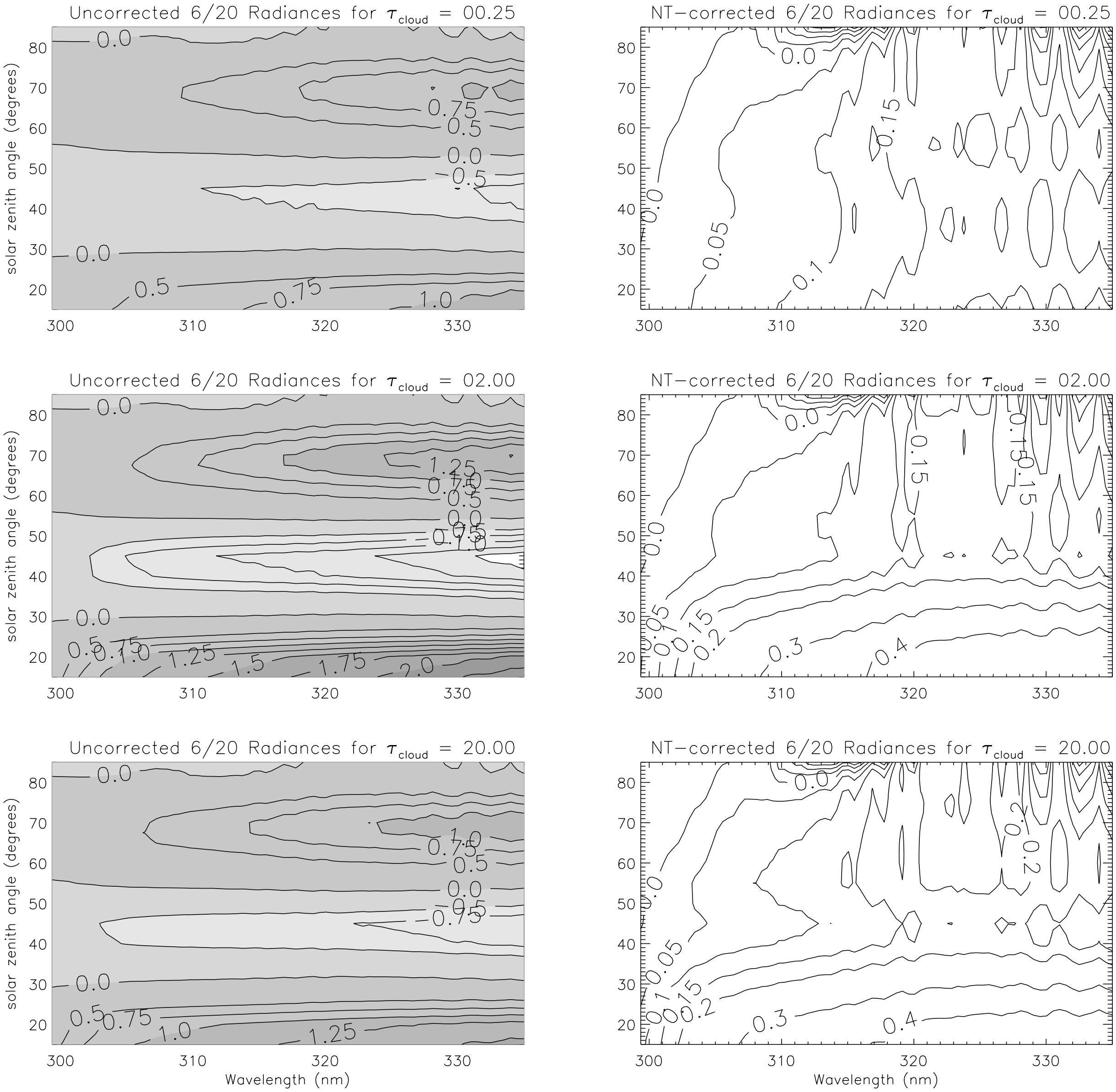

Figure 4.6: Differences (expressed as percentages) between 6 stream and 20 stream TOA upwelling radiances for a reference atmosphere with cloud layer between 3-4 km with 3 cloud optical thickness values as indicated. Viewing zenith 20°, azimuth 0°, albedo 0.1. Wavelength and solar zenith ranges as in Figure 4.5.

solar zenith angle 70° has increased to 2.2% by comparison with the cloud case (the corresponding number for the 4 stream comparison was greater than 3.5%). By contrast, the NT-corrected results (upper right) show little structure, with error levels below 0.5%. (Contour levels are at intervals of 0.5% for the uncorrected results, and generally at 0.1% for the NT-corrected comparisons). For the volcanic ash layer scenario, we would not expect 4/20 and 6/20 differences to be greatly in excess of those generated using the reference atmosphere. This remark follows from the consideration of optical depth; although the extinction coefficient for the volcanic layer is two orders of magnitude above background levels, the layer is still optically thin compared to the Saharan dust model. These remarks are borne out by the 6/20 stream comparisons in Figure 4.7 (middle panels).

For the planetary boundary layer scenario with an optically thick aerosol layer near the surface, we would expect this situation to resemble a reasonably highly reflecting surface. In Figure 4.7 (lower panels) the comparisons are done for 4 streams. The general error level is not greatly different from the clear sky case. The interesting thing to note here is that in contrast with the other two 6/20 stream comparisons in Figure 4.7, the NT-corrected 4/20 stream results in the lower right panel are actually worse than the uncorrected ones for sizeable ranges of wavelength and solar zenith angle. Geometry-dependent structures are present in both the lower panels, though the preferred direction has changed from uncorrected to NT-corrected. This example demonstrates clearly that 4 stream models should be used with caution; it is safer and more accurate with 6 streams.

Although the dust scenario is admittedly an extreme situation, it does help to establish accuracy limits for the low-stream models. This scenario has special significance in the ozone profile retrieval context. An algorithm to indicate the presence of absorbing aerosols in the lower atmosphere was first developed for the TOMS (Total Ozone Monitoring Spectrometer) instrument in order to look at anomalous ozone column results obtained in biomass burning (smoke aerosols) and dust-outbreak scenarios [90, 91, 92]. The algorithm examines the radiances at two different wavelengths and computes the spectral residue upon subtraction of the Rayleigh contribution to the backscatter. It turns out that this residue (the aerosol absorbing index) is a clear indicator for the presence of absorbing aerosols. The algorithm has now been applied to GOME measurements [93], and will also be used operationally for GOME-2 and SCIAMACHY. The point here is that if there is a clear indication of the presence of an absorbing aerosol layer in a given GOME or GOME-2 footprint, then we can use this information to switch from a 4 stream model to a 6 stream calculation of backscatter radiances and weighting functions required for an ozone (profile or column) retrieval.

Results for the reference and cloud-layer scenarios are summed up in Table 4.3, along with the abovementioned three special cases. The table gives an overview of the maximum and minimum differences to the 20 stream output, both for uncorrected and NT-corrected TOA radiance values. The first four reference scenarios (Ref 1 to Ref 4) are intended to examine the albedo dependence; as noted above the errors increase with decreasing albedo. The Ref 2 and Ref 5-7 scenarios together give an indication of the off-nadir viewing angle dependence; for the uncorrected results, both 4 stream and 6 stream errors increase as the viewing angle moves away from the nadir, but this dependence is absent for the NT-corrected equivalents. Cloud-layer scenarios show the cloud optical thickness dependence; all results show a clear peak in the maximum error values for optical thickness $\tau_{cloud} = 2.0$. Finally, we note that the Saharan dust scenario has the largest 6 stream error. In summary, we note that in all cases, the NT-corrected 6 stream results are within 0.65% of their 20 stream equivalents, and that in clear sky circumstances, these errors are mainly at the 0.25% level or below. For the corrected 4 stream results, the reference clear sky errors are in the 1.0-1.3% range and cloud-layer errors are roughly the same; however two of the special cases are still showing absolute errors at the 1.75% level.

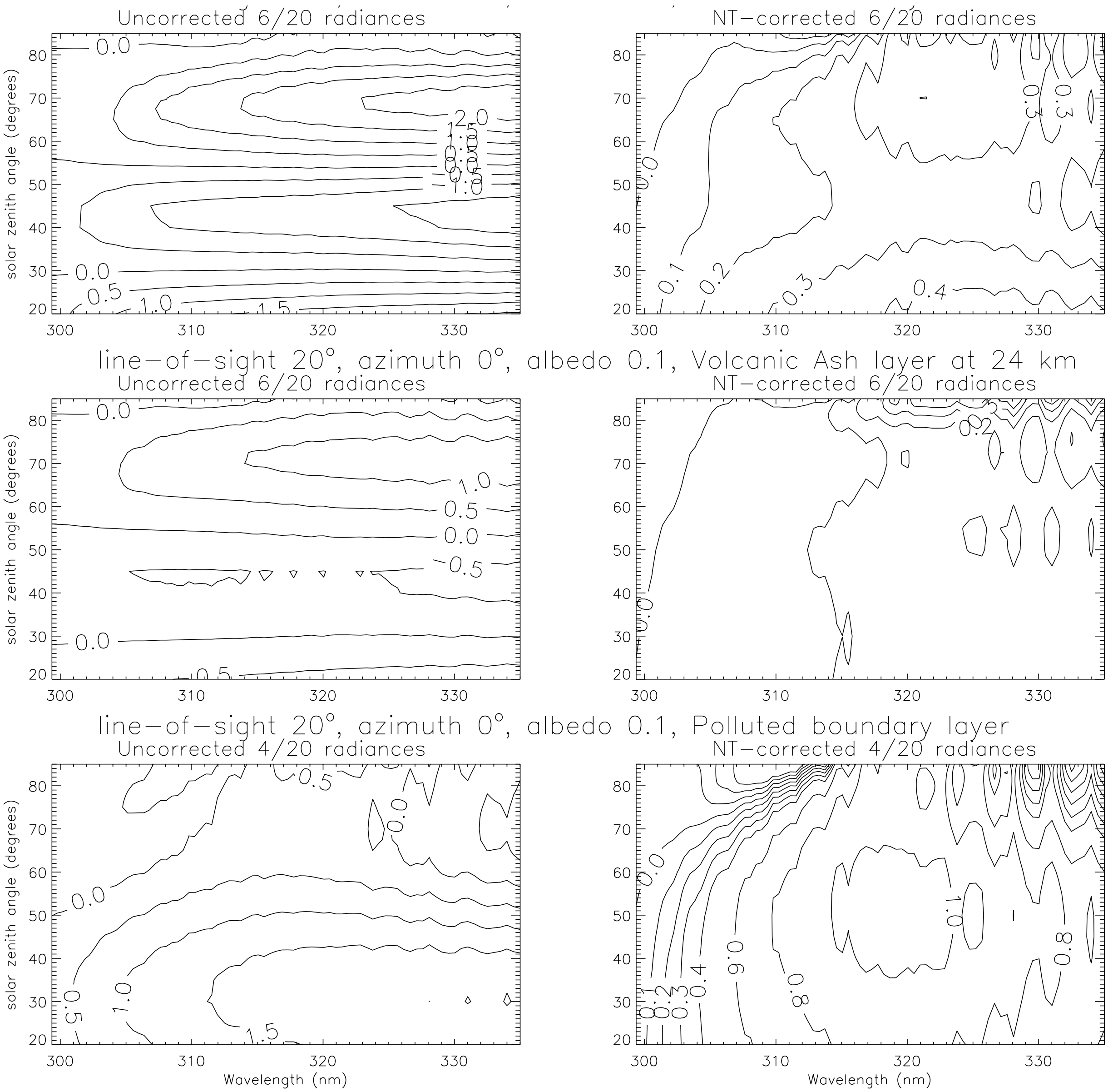

Figure 4.7: Comparison of TOA upwelling radiances for three special cases: (top panels) 6/20 differences with layer of desert dust at 6-7 km; (center panels) 6/20 differences with volcanic ash layer at 24 km; (lower panels) 4/20 differences with polluted boundary layer. Viewing zenith 20°, azimuth 0°, albedo 0.1. Wavelength and solar zenith ranges as in Figure 4.5.

Maximum and Minimum % errors for uncorrected and NT-corrected TOA radiance output											
				UNCORRECTED				NT-CORRECTED			
Scen	*Alb.* τ_{cloud}	*View*	*Azm*	*4 stream*		*6 stream*		*4 stream*		*6 stream*	
				Max	Min	Max	Min	Max	Min	Max	Min
Ref 1	0.05	20.0	0.0	1.721	-0.757	0.720	-0.362	1.139	-0.612	0.248	-0.217
Ref 2	0.10	20.0	0.0	1.596	-0.763	0.684	-0.337	1.069	-0.619	0.241	-0.216
Ref 3	0.30	20.0	0.0	1.208	-0.794	0.608	-0.303	0.834	-0.651	0.220	-0.214
Ref 4	0.70	20.0	0.0	0.732	-0.900	0.481	-0.287	0.565	-0.726	0.217	-0.207
Ref 5	0.10	2.0	0.0	1.416	-1.030	0.610	-0.224	0.860	-0.661	0.249	-0.234
Ref 6	0.10	10.0	0.0	1.504	-1.041	0.656	-0.267	0.891	-0.656	0.253	-0.230
Ref 7	0.10	30.0	0.0	1.622	-0.420	0.791	-0.735	1.300	-0.555	0.231	-0.200
Cld 1	00.25	20.0	0.0	2.120	-0.949	1.174	-0.867	1.074	-0.625	0.225	-0.212
Cld 2	00.50	20.0	0.0	2.554	-1.288	1.561	-1.226	1.050	-0.630	0.274	-0.208
Cld 3	01.00	20.0	0.0	3.077	-1.685	2.055	-1.564	1.010	-0.641	0.393	-0.203
Cld 4	02.00	20.0	0.0	3.415	-1.961	2.407	-1.659	1.041	-0.741	0.556	-0.196
Cld 5	05.00	20.0	0.0	3.054	-2.112	2.246	-1.404	1.176	-0.928	0.630	-0.189
Cld 6	10.00	20.0	0.0	2.476	-1.954	1.867	-1.151	1.011	-0.989	0.576	-0.189
Cld 7	20.00	20.0	0.0	2.051	-1.779	1.572	-0.986	0.757	-1.012	0.493	-0.190
Sahar	0.10	20.0	0.0	2.675	-4.172	2.439	-1.895	0.406	-1.778	0.452	-0.164
Volcn	0.10	20.0	0.0	2.049	-1.366	1.283	-0.641	1.721	-0.550	0.557	-0.086
Polld	0.10	20.0	0.0	2.025	-0.738	1.023	-0.476	1.091	-0.593	0.294	-0.216

Table 4.3: Maximum and Minimum % errors for uncorrected and NT-corrected TOA radiance output.

4.5.3. Wide-angle viewing: the sphericity correction

We wish to compare sphericity-corrected output for the path AB with regular pseudo-spherical RT calculations for a scattering path AC based on the geometry at point A. We will be comparing two sets of NT-corrected data in order to isolate the sphericity effect. This time we take line of sight viewing angles from -70° in the antisolar direction to +70° in the solar direction. Figure 4.8 shows results for the TOA radiance for the reference atmosphere with albedo 0.1, for a selection of 6 wavelengths and 4 solar zenith angles. Three separate RT model runs were done for the multiple scatter terms along AB, with parabolic interpolation used to determine intermediate values as described in Section 4.4.3 above. Note that the correction has the same sign for lower values of the solar zenith angle, but reverses for high solar zenith angles. This is a function of the sun's position in front or behind the line of sight. The correction is also much larger for high solar zenith angles, where attenuation along the direct solar beam is critical.

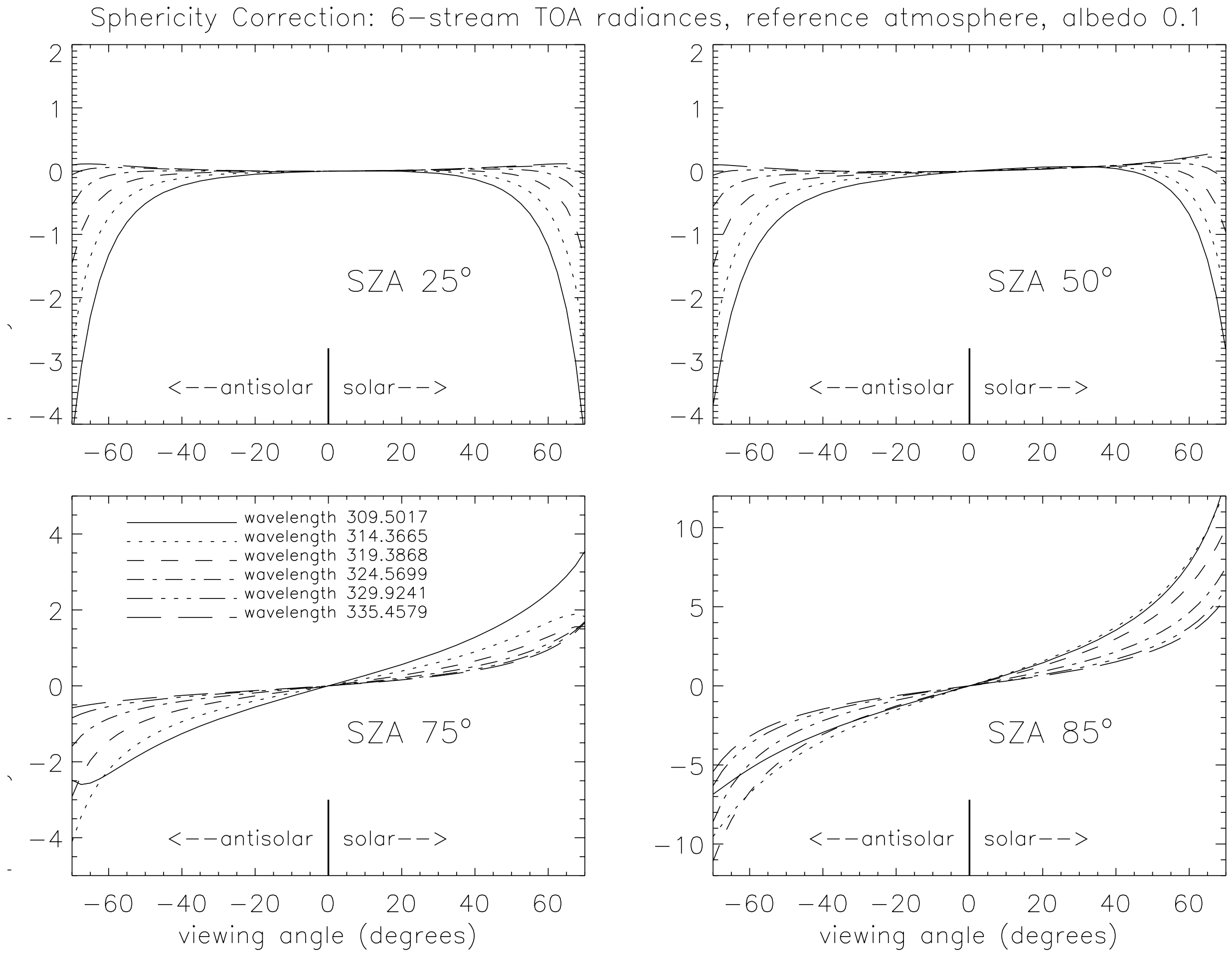

Figure 4.8: Sphericity correction 6 stream TOA upwelling radiances for a reference atmosphere with albedo 0.1. Viewing zenith angle range -20° to +40°. Wavelength and solar zenith ranges as indicated.

The magnitude of the sphericity correction is very much the same for 4, 6 and 20 stream calculations. This should not surprise us, since as already noted, its magnitude is strongly dependent on the single scatter calculations to point along the path AB. It is immediately obvious that this correction

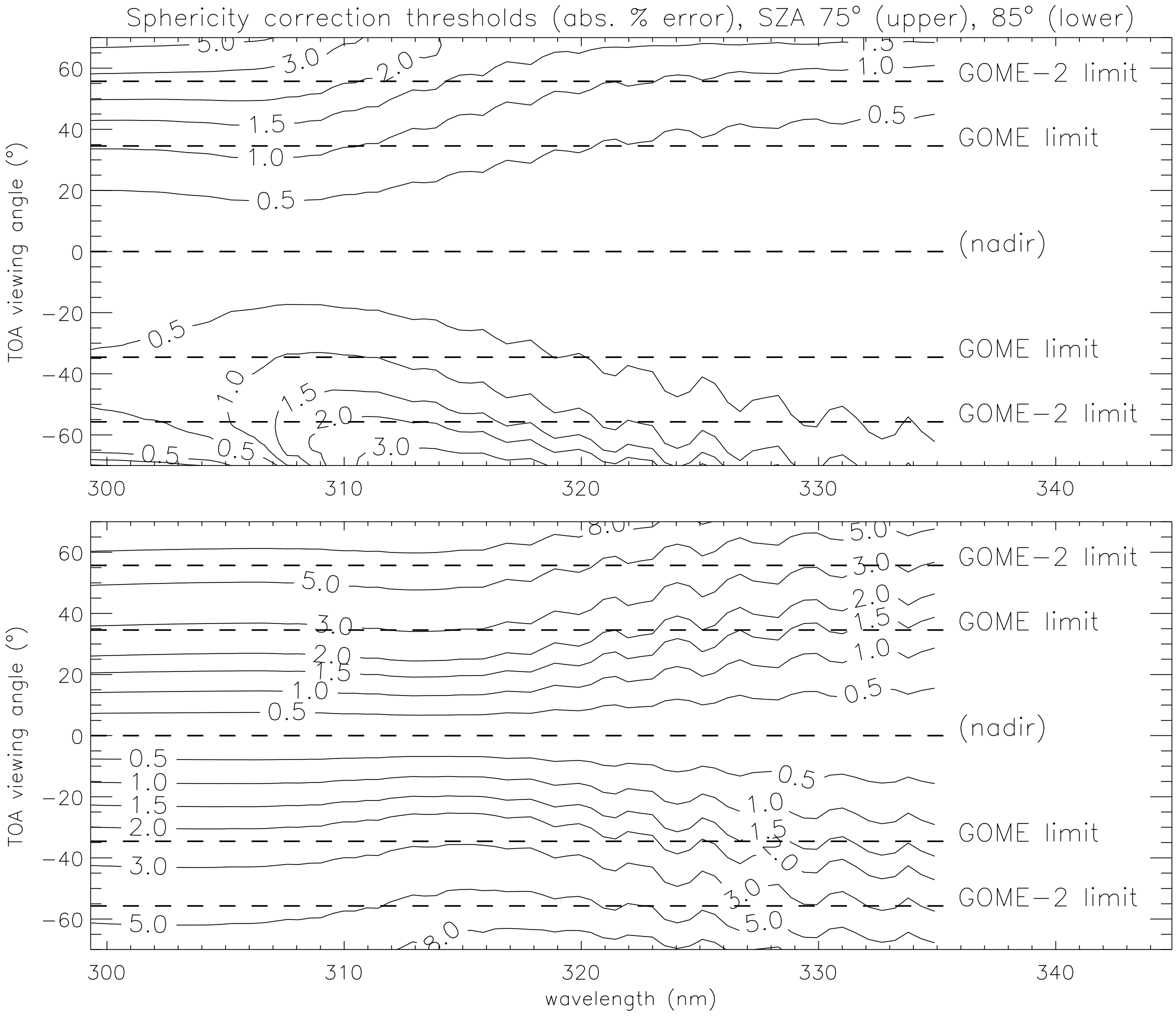

Figure 4.9: Sphericity correction thresholds for 6 stream TOA upwelling radiances for a reference atmosphere with albedo 0.1, and for 2 solar zenith zenith angles. Wavelength against line-of-sight viewing angle.

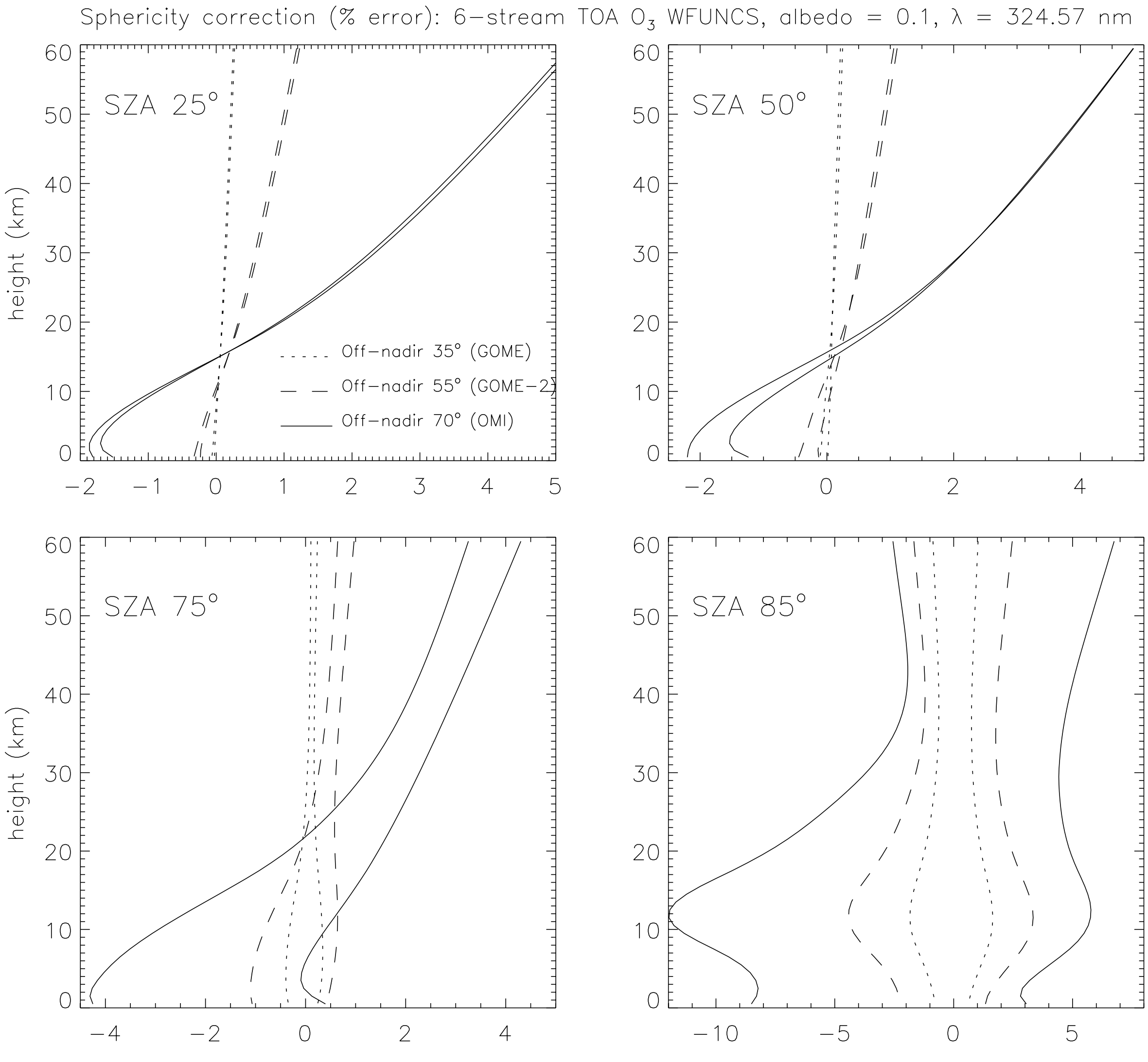

Figure 4.10: Sphericity correction for 6 stream TOA upwelling ozone volume mixing ratio weighting functions, for a reference atmosphere with albedo 0.1, for wavelength 324.57 nm. Solar zenith angles as in Figure 4.8.

is important for the wide angle view. Indeed for a solar zenith angle of 85°, the line-of-sight zenith angles are restricted to the range [$\pm$15.9°] at 319.4 nm if the sphericity correction is to be ignored at the 1% level. Even for a solar zenith angle of 50°, viewing paths outside the range [$+62.7°, -55.7°$] will be outside the 1% threshold for the sphericity correction. Another way of looking at these results is to plot thresholds for the absolute sphericity correction. In Figure 4.9, this is done for thresholds from 0.5% to 8.0% (contours as marked) and for a wide wavelength range. The GOME ($\sim$ 34.6°) and GOME-2 ($\sim$ 55.7°) swath limits are marked; the OMI swath limit is at $\sim$ 67.4°. Clearly the sphericity effect for GOME can be ignored to the 1% level for solar zenith angles up to 75°, but it becomes significant at the 2% level at sun angle 85°. For GOME-2, the sphericity correction is needed to the 2% level at SZA 75°, and at the 5% level at 85°. The situation with OMI is even more serious. Notice also the asymmetry between solar and antisolar directions, and at SZA 75° the change in sign of the correction for wavelengths near 300 nm. The increasingly high ozone absorption in this part of the UV can have a critical effect on the attenuation along both the solar beam and the line-of-sight path. Given this sort of variability, it is not an easy matter to decide when to implement the sphericity correction, and this will have consequences for the retrieval algorithm.

A similar picture pertains for the weighting functions. Since the sphericity effect is much the same no matter what the scattering accuracy, we focus on 6 stream output only, looking at weighting function profiles with respect to ozone volume mixing ratio in our reference atmosphere, again assuming an albedo of 0.1. Figure 4.10 shows results for 4 solar zenith angles at a wavelength of 329.5 nm, and for line-of-sight viewing angles corresponding to the GOME, GOME-2 and OMI swath limits. From the graphs, we see that for solar zenith angles up to 75°, the sphericity correction can be ignored for GOME at the 1% level, and for GOME-2 at the 2% level. At SZA 85°, weighting function errors due to the neglect of the sphericity correction are up to 2% for GOME and as high as 5% for GOME-2. The situation for OMI is more serious, with significant errors at all solar zenith angles, ranging from a +5% maximum at SZA 20°, to -12% at SZA 85°. In common with the results in Figure 4.8, the sphericity correction has the same sign for lower SZA values, but has the opposite sign for all off-nadir angles at SZA 85°.

4.6. Discussion: relevance to ozone profile retrieval

In this paper, we have determined analytic 4 and 6 stream solutions for radiance and 4 stream solutions for weighting functions using a linearized discrete ordinate model. In order to determine the model's suitability for use in a fast and accurate ozone profile retrieval algorithm using UV backscatter measurements from nadir viewing instruments such as GOME, GOME-2, SCIAMACHY and OMI, we have carried out a detailed investigation of the model accuracy for a range of atmospheric scenarios appropriate to this retrieval application. Comparisons for radiance and a limited number of weighting functions were carried out against the general model LIDORT operating in the 20 stream discrete ordinate approximation. We have shown that significant improvments to the accuracy can be gained by using a post-processing correction for the single scatter contribution to the upwelling radiance. Further, it was shown that a sphericity correction is an essential requirement for wide-angle off-nadir viewing, particularly for high solar zenith angles.

We show that with a few exceptions, the NT-corrected 4 stream model is accurate to 1.25% for the vast majority of clear sky scenarios likely to be encountered in the retrieval of ozone profiles from backscatter UV spectrometers in space. The major exceptions occur in the presence of additional moderately thick particulate layers at high levels in the troposphere. The template for this is the Saharan dust model. It is noted that this situation can be flagged in an operational environment provided that the presence of such a layer can be established by means of a suitable absorbing aerosol indexing algorithm. The single scatter corrected 6 stream model is shown to reproduce 20 stream radiance values to better than 0.65% for all scenarios considered, with corresponding weighting function accuracy to ±2% levels.

It is clear that the single scatter correction should be applied for all situations in order to achieve acceptable levels of accuracy. However the sphericity correction is only really needed for wide angle views and in general for high solar zenith angles. However, determining the range of viewing geometries for which this correction is required is not a straightforward manner, and further investigation is needed to establish limits of applicability which are consistent with the overall level of accuracy chosen for an operational ozone profile retrieval algorithm with global reach.

By allowing for an acceptable loss of accuracy, a large gain in speed may be obtained using 4/6 stream models. This has great consequence for the performance of operational near-real-time retrievals of ozone profiles, particularly for a high data-rate instrument such as OMI. The choice of an accuracy criterion for the RT model depends on the strategy adopted for the retrieval algorithm, and most importantly on the instrument measurement uncertainty. The aim is to achieve an accuracy level that is better than (or at least equal to) that of the measurements. A measurement accuracy of about 1.5% is in theory obtainable from the GOME, SCIAMACHY and GOME-2 instruments, the main limiting factor being the accuracy of the pre-launch radiometric calculation. Taking this number as a yardstick, the 4 stream model presented here can be expected to simulate radiances to about the same level of accuracy, with the 6 stream model providing a factor of three improvement on the overall accuracy of both radiances and weighting functions. It should be noted that the radiometric calibration error for GOME is actually much greater than 1.5%; additional sources of measurement error for GOME include the instrument degradation now apparent 5 years after launch, and the uncertainty inherent in the polarization correction (up to 10%). In the latter respect, GOME-2 is much better served than GOME; the latter has only 3 polarization measurement devices (PMDs), whereas GOME-2 has some 15 PMDs measuring in two directions of polarization.

We have attempted to quantify only the *forward model error* likely to be encountered in the ozone profile retrieval context; we have not considered other sources of error in the optical properties assumed in the calculation (for example uncertainties in the trace gas cross sections). The 4 and 6 stream models have been installed in an prototype operational algorithm at KNMI designed to retrieve ozone profile information from nadir UV/VIS backscatter measurements from the GOME and GOME-2 instruments. In the follow-up paper [77] to the present work, we carry out a feasibility study for the operational ozone profile retrieval for the GOME-2 instrument, based on the 4/6 stream models described in the present work. This study will examine the effect of all error sources (including those from the forward model) on the accuracy of the ozone profile retrieval.

Acknowledgments

R.V.O. was supported by The Netherlands Remote Sensing Board (BCRS) under the project *DORAS* 4.1/AP-05. R.J.D.S. was funded from an ozone SAF Visiting Scientist Grant (P-4799-2-00) at KNMI (Royal Dutch Meteorological Institute). The authors would like to thank Piet Stammes for many stimulating discussions on this work.

Chapter 5

Sensitivity and error assessment of operational ozone profile retrieval algorithms for the GOME and GOME-2 remote sensing spectrometers

This chapter is a nearly-complete working version of a paper that will be submitted for publication in the Journal of Geophysics Research (Atmospheres) in early summer 2001, and is co-authored by R.F. van Oss. It is anticipated that Section 6.3 of this chapter will be expanded into a companion paper (also to be submitted to JGR this summer) to be co-authored by N. Schutgens, R. van Oss, P. Stammes and R. Spurr.

Abstract

We use the optimal estimation method to investigate some sensitivity and error assessment issues for the operational retrieval of ozone profiles using backscatter measurements from moderate-resolution nadir-viewing remote sensing instruments such as GOME and GOME-2. Simulated radiances and analytically calculated weighting functions are determined from a linearized discrete ordinate radiative transfer forward model. We use the degrees-of-freedom-for-signal (DFS) diagnostic to investigate ozone profile accuracy as a function of the tropospheric temperature pattern. DFS is used to optimize the choice of an upper wavelength limit for the retrieval window; there is little new information to be gained from the inclusion of measurements above 323 nm. We examine model parameter errors, concentrating on uncertainties in profiles of temperature and aerosol optical thickness. Ozone profile accuracy is shown to be highly sensitive to temperature uncertainty; it is important to have accurate temperature input. It is shown that temperature-induced errors can be included easily in the optimal estimate solution covariance. Aerosol-induced errors in the optimal estimate are generally too large to be treated in this way; it is better to retrieve aerosol optical depth as an additional element in the state vector. Forward model errors are also investigated, first with respect to the number of discrete ordinate streams used in the radiative transfer, and secondly with regard to the neglect of polarization. We conclude that a 4-stream radiative transfer model is sufficiently accurate for wavelengths below 320 nm. The absence of polarization in the radiative transfer model is a more serious source of error. The accuracy of the polarization correction applied to GOME radiance data is also shown to be critically important for the retrieved profile uncertainty.

5.1. Introduction

A global and long-term measurement record of the vertical and horizontal distribution of ozone is an essential tool for monitoring the Earth's atmosphere and understanding its chemical and physical balance. This is especially important in the light of perceived changes to the global atmospheric system due to man's activities on the planet. Ozone is one of the most important atmospheric trace species, and scientific studies have focussed on topics such as the ozone hole phenomenon observed during the Austral spring over the south pole, the enhancement of ozone levels during severe tropospheric pollution events, and the role of ozone in global climate change. Space-based instruments on suitable orbits have the potential to deliver ozone measurements that are indispensable for this research.

The first algorithms for ozone profile retrieval from satellites were pioneered by Singer & Wentworth [94] and Twomey [9]. Twomey in particular demonstrated that the ozone profiles can be retrieved from a single earthshine spectrum. With the advent of backscatter ultraviolet (BUV) instruments in the 1970s, an operational ozone profile retrieval algorithm for UV nadir earthshine measurements was developed by NASA for the SBUV, SBUV/2 and SSBUV experiments. SBUV profiles comprise 12 partial columns of ozone, retrieved from 12 nadir-view radiance measurements between 255 and 340 nm (bandwidth 1.1 nm). The algorithm uses the optimal estimation retrieval technique; for a description and summary of the NASA developments, see [11]. In general, SBUV profile element precisions are 5-15% in the range 1-20 mbar; outside of this range, profile elements are heavily influenced by prior assumptions.

In April 1995, the nadir viewing Global Ozone Monitoring Experiment (GOME) instrument was launched on board the ESA satellite ERS-2; GOME delivers earthshine backscatter measurements in the UV, visible and near infrared (240 - 790 nm spectral range) [5]. GOME is an atmospheric chemistry instrument designed to measure column abundances of O_3 and a number of other trace species [7]. GOME has a spectral resolution of $\sim$0.2 nm in the UV channels where ozone absorption is prominent. Ozone profile retrieval algorithms for GOME have been reported in the literature [13, 15, 14, 16]. GOME stratospheric ozone profiles are now operationally available within 4 hours after observation via the KNMI GOME Fast Delivery service [95].

An improved version of the GOME instrument, GOME-2, will fly on three METOP satellites [6]; the first is scheduled for launch in 2005. The operational period for these platforms is 15 years, and this offers a unique opportunity to obtain a long-term, global ozone record. GOME-2 improvements include: (i) an extended set of polarization measurements, (ii) better spectral sampling ratio, and (iii) smaller ground pixels (40x40 km). GOME-2 will operate with a wide swath (1920 km, twice that of GOME). Retrieval algorithm development and validation for GOME-2 takes place within the framework of the Ozone Monitoring Satellite Application Facility (Ozone SAF) initiated by EUMETSAT in 1997. Among the nine participating institutes the Royal Netherlands Meteorological Institute (KNMI) has responsibility for the generation of ozone profile and aerosol products from GOME-2. Other instruments capable of delivering ozone profiles from nadir backscatter measurements are SCIAMACHY, due for launch in summer 2001 on the ESA-ENVISAT platform [96], and OMI (Ozone Monitoring Instrument) scheduled for launch on the EOS-AURA satellite in 2003 [8].

The potential of these four instruments to deliver ozone profiles (Level 2 data products) with the temporal and geographical sampling of the earthshine measurements (Level 1 products) can only be exploited if the ozone profile retrieval is fast enough to keep up with the data rate using up-to-date computer resources. It is highly desirable to develop algorithms which are as efficient as possible, and in particular to find the right balance between accuracy and speed in the operational environment.

A key component in the ozone profile retrieval problem is the *forward model*. Given appropriate observing conditions (solar and viewing angles), a choice of ozone profile and other atmospheric constituent distributions, and a suitable instrument response function, the forward model simulates the earthshine radiance measurements as measured by the instrument. This comprises a radiative transfer (RT) calculation followed by a convolution with the instrument response function. Also required in this problem is the computation of the Jacobian matrices of derivatives of these simulated measurements with respect to the retrieval parameters (of which the ozone profile variables are of primary importance). These Jacobians are usually referred to as the *weighting function* matrices, and they are generated through the *linearization* of the forward model. Formally we can write:

$$\vec{y} = F(\vec{x}) \quad \text{and} \quad K = \frac{\partial}{\partial \vec{x}} F\,, \tag{5.1}$$

where $\vec{y}$ is the vector of simulated earthshine radiances at different wavelengths, $\vec{x}$ is the *state vector* containing the parameters to be retrieved, F is the forward model and K is the matrix of weighting functions. The actual retrieval consists of an iterative series of linear inversions. Starting with a first-guess profile $\vec{x}_0$, the forward model is linearized through:

$$\vec{y} - \vec{y}_0 = K(\vec{x} - \vec{x}_0), \tag{5.2}$$

with $\vec{y}_0 = F(\vec{x}_0)$. Matrix K is the forward map from the space of state vectors to the measurement vector space; this is equivalent to the measurement itself, subject to the measurement error. The inverse map from measurement space to state space is determined using a linear inversion technique; the solution is the “second-guess” profile. Simulated earthshine measurements and associated weighting functions are then re-calculated using the updated profile and the linear inversion is repeated; the iteration stops when appropriate convergence criteria are satisfied.

In common with most work done on ozone profile retrieval, we will use *optimal estimation*. Here, the linear inversion step is based on Bayes’ theorem for the determination of the posterior probability density function (*pdf*) $P(\vec{x}|\vec{y})$ for state $\vec{x}$ given measurement $\vec{y}$, in terms of the *a priori* knowledge characterized by $P(\vec{x})$ and the conditional *pdf* $P(\vec{y}|\vec{x})$ for $\vec{y}$ given $\vec{x}$. The last quantity requires the forward model and measurement error statistics; we take the latter to be Gaussian. If the prior *pdf* also has Gaussian statistics, then the posterior *pdf* will be Gaussian. The optimal or *maximum a posteriori* (MAP) estimate is then the state vector that maximizes the posterior *pdf*.

The forward model should have the ability to deliver both simulated radiances and weighting functions. Weighting functions for the RT model can either be calculated numerically using finite-difference methods, or analytically by explicit differentiation of the radiance. The finite difference technique requires repeated calls to the RT model, and there are some concerns over the accuracy of the answers. From the point of view of both accuracy and algorithm efficiency, the analytic derivation of weighting functions is much to be preferred [1]. For a scattering atmosphere, only two RT models have been extended for the purpose of direct analytic derivation of weighting functions. These are the GOMETRAN model developed by Rozanov [40, 43] and the discrete ordinate LIDORT code developed by Spurr [75, 85]. In this work, we use the LIDORT model. This is a general purpose multiple scattering discrete ordinate radiative transfer code with the ability to deliver simultaneous fields of radiance and analytically accurate weighting functions. We use the model in its fast 4-stream formulation [77].

We address two important sensitivity issues in this paper. One is connected to the temperature dependence of the ozone absorption cross sections in the Huggins bands: how sensitive is the retrieval to the temperature profile in the troposphere? The other concerns the optimization of the choice of an upper wavelength limit in the Huggins bands beyond which little or no further improvement in the retrieved ozone profile is apparent. For these issues, we use a reformulation of the linear inversion step using singular value decomposition (SVD) analysis. This offers a clear interpretation of the inversion, and offers a convenient definition of two additional diagnostic tools: the DFS (degrees of freedom of signal) and the Information Content. We show in particular how the DFS diagnostic can give quantitative answers to these two issues.

In addition to measurement and *a priori* errors, the retrieval will also be affected by uncertainties inherent to the forward model itself, and by uncertainties about model atmospheric parameters that are inputs to the forward model. The ozone profile accuracy can be determined by linearizing the forward model about some state and using contribution functions to calculate the magnitude and expected values of the profile errors. We consider two kinds of forward model error: (1) due to the use of a fast 4-stream discrete ordinate model, and (2) due to the neglect of polarization. Forward model error will be treated as systematic. We also examine the effect of the polarization correction that is currently applied to GOME signals; this particular measurement error is a major source of profile uncertainty. For model parameter errors, we look at uncertainties in the aerosol optical thickness and temperature profiles, assuming Gaussian statistics for their error distributions. The forward model is able to deliver weighting functions with respect to these quantities, thus enabling model parameter errors to be included in the optimal estimate error covariance.

The plan of the paper is straightforward. In Section 5.2, we recapitulate the main elements of the optimal estimation inversion technique, including a description of the error sources, and an outline of the SVD reformulation. This section is based in large part on the publications of Rodgers [60, 4, 1]. In Section 5.3 we discuss forward model aspects; this includes a resumé of the LIDORT radiative transfer model and remarks on instrument response convolution and noise statistics. In Section 5.4 we describe the set-up for the retrieval and sensitivity studies; this includes the definition of our reference atmosphere, and a description of the state, *a priori* and model parameter vectors used in this study. Sections 5.5 and 5.6 contain the main results for the sensitivity study and the error assessment respectively. The paper concludes with some remarks on the consequences of these findings for an operational ozone profile retrieval algorithm.

5.2. Profile retrieval with optimal estimation

5.2.1. State vector updates

Optimal estimation provides a natural solution to the ill-conditioning problems typically found in remote sensing atmospheric retrieval applications; it combines information on the state vector contained in the measurement with *a priori* information on the state vector itself. Assuming Gaussian probability density functions (*pdf*) for both the *a priori* uncertainty and for the error statistics of the measurement vector, the optimal estimate is the state that maximizes the product of these two *pdf*'s. This product is called the posterior *pdf*, and it is also Gaussian. An explicit solution for its maximum value (the MAP or “optimal” estimate) is given by [1]:

$$\Delta\vec{x}_{\mathrm{OE}} = \Delta\vec{x}_{\mathrm{a}} + D_{\mathrm{y}}(\Delta\vec{y} - K\Delta\vec{x}_{\mathrm{a}}), \tag{5.3}$$

$$D_{\mathrm{y}} = S_{\mathrm{OE}}K^{\mathrm{T}}S_{\mathrm{y}}^{-1}, \tag{5.4}$$

$$S_{\mathrm{OE}} = \left(K^{\mathrm{T}}S_{\mathrm{y}}^{-1}K + S_{\mathrm{a}}^{-1}\right)^{-1}, \tag{5.5}$$

with $\Delta\vec{x}_{\mathrm{a}} = \vec{x}_{\mathrm{a}} - \vec{x}_0$, and $\Delta\vec{y} = \vec{y} - F(\vec{x}_0)$. Here $\vec{x}_{\mathrm{a}}$ is the *a priori* state vector, S_{a} the *a priori* error covariance, S_{OE} the posterior error covariance and S_{y} the measurement error covariance. The T-superscript denotes matrix transpose. The optimal estimate $\vec{x}_{\mathrm{OE}}$ follows from $\vec{x}_{\mathrm{OE}} = \vec{x}_0 + \Delta\vec{x}_{\mathrm{OE}}$. D_{y} is variously called the *gain matrix* or the matrix of *contribution functions*. These characterize the sensitivity of the retrieval to the measurement, and are important in the consideration of error sources. For linear inversion with Gaussian statistics, the optimal estimate is only equal to the maximum likelihood state or the minimum variance state (obtained by minimizing the cost function) in the absence of prior knowledge.

To deal with the non-linearity of the forward model, the optimal estimate of the linear system is used to calculate a new set of weighting functions, thereby creating a new linear inversion problem from which an updated optimal estimate is computed. This process is repeated until the relative change in optimal estimates between iterations is less than a specific amount for all components of the state vector. This is our primary convergence criterion. We also use a second criterion based on the relative change in the total cost function ("chi-square") between iterations:

$$\chi^2 \equiv \chi_{\mathrm{s}}^2 + \chi_{\mathrm{n}}^2 = (\vec{x} - \vec{x}_{\mathrm{a}})^{\mathrm{T}} S_{\mathrm{a}}^{-1} (\vec{x} - \vec{x}_{\mathrm{a}}) + [\Delta\vec{y}]^{\mathrm{T}} S_{\mathrm{y}}^{-1} \Delta\vec{y} \tag{5.6}$$

Note that the optimal estimation technique assumes a relatively small departure from linearity in the forward model to ensure that the posterior *pdf* is well approximated as Gaussian where it is non negligible [1]. Note also that the optimal estimation results can be obtained by Newton-Gauss methods (minimizing the cost function with respect to $\Delta\vec{x}$). The cost function in (5.6) has contributions χ_{s}^2, which is the functional based on $(\vec{x} - \vec{x}_{\mathrm{a}})$, and χ_{n}^2 based on the measurement noise functional. Ordinary least squares fitting involves minimization of χ_{n}^2 in the absence of prior knowledge.

5.2.2. Error sources in the retrieval

The error on $\Delta\vec{x}_{\mathrm{OE}}$ has four components: (1) measurement or retrieval error $\varepsilon_{\mathrm{M}}(\vec{x})$; (2) the smoothing error $\varepsilon_{\mathrm{A}}(\vec{x})$; (3) forward model error $\varepsilon_{\mathrm{F}}(\vec{x})$; and (4) model parameter error $\varepsilon_{\mathrm{B}}(\vec{x})$. We deal with each of these in turn, following the analysis of Rodgers [1].

Retrieval error

This is defined to be

$$\varepsilon_{\mathrm{M}}(\vec{x}) = D_{\mathrm{y}}\varepsilon_{\mathrm{y}}, \tag{5.7}$$

where ε_{y} is the measurement noise ($\vec{y} = F(\vec{x}) + \varepsilon_{\mathrm{y}}$) characterized by error covariance S_{y}, and D_{y} is the gain matrix of contribution functions. The error covariance for the optimal estimate of the state vector from this source of error is $S_{\mathrm{M}} = D_{\mathrm{y}} S_{\mathrm{y}} D_{\mathrm{y}}^{\mathrm{T}}$.

Smoothing error

This is given by

$$\varepsilon_{\mathrm{A}}(\vec{x}) = (A - E)\Delta\vec{x}_{\mathrm{a}}, \tag{5.8}$$

where E is the unit matrix in state vector space and A is the *averaging kernel* matrix, defined in terms of the Frechét derivative:

$$A \equiv \frac{\partial\vec{x}}{\partial\vec{x}_{\mathrm{true}}} \cong D_{\mathrm{y}} K \tag{5.9}$$

A represents the sensitivity of the retrieved state to its true value. Although the product $D_{\mathrm{y}}K$ is used to calculate A, this is strictly speaking only correct if $\vec{x}_{\mathrm{OE}}$ and $\vec{x}_{\mathrm{true}}$ are in the linear regime, that is:

$$\vec{x}_{\mathrm{OE}} - \vec{x}_{\mathrm{a}} \cong D_{\mathrm{y}}K\left(\vec{x}_{\mathrm{true}} - \vec{x}_{\mathrm{a}}\right) \tag{5.10}$$

in the absence of other error sources.

Since the true state is not known, we must estimate this error contribution using suitable statistics for an ensemble of states. It is usual to take $\vec{x}_{\mathrm{a}}$ and S_{a} for the mean and covariance of the ensemble, in which case the error covariance for the optimal estimate from this source is $S_{\mathrm{S}} = (A-E)S_{\mathrm{a}}(A-E)^{\mathrm{T}}$. It is straightforward to show that in the absence of other sources of error, $S_{\mathrm{OE}} = S_{\mathrm{M}} + S_{\mathrm{S}}$.

From (5.9), we see that the gain matrix D_y is a “fuzzy” inverse of the linearization map K. In a perfect retrieval, there is no ambiguity: A is then the unit matrix in state space. In a retrieval with state vectors consisting of profile elements, the rows (averaging kernels) of A are profiles which generally peak at the diagonal entry. The half-width of these peaked functions is a measure of the vertical resolution of the profile. In the ideal case, the peaks are delta-functions; for this reason the columns of A are sometimes referred to as the point spread functions (responses to delta-function perturbations of the state vector).

Forward model error

An additional source of error on the profile retrieval arises from approximations made in the forward model itself. We define the model error ΔF through:

$$F_{\mathrm{true}} = F_{\mathrm{app}} + \Delta F, \tag{5.11}$$

with F_{true} and F_{app} the true and the approximated forward models respectively. Then the error on $\vec{x}$ is:

$$\varepsilon_{\mathrm{F}}(\vec{x}) = \vec{x}_{\mathrm{app}} - \vec{x}_{\mathrm{true}} = D_{\mathrm{y}}\Delta F \tag{5.12}$$

where D_{y} is the contribution function matrix given in (5.4). $\vec{x}_{\mathrm{app}}$ is the estimate derived using the approximate forward model, and $\vec{x}_{\mathrm{true}}$ is the estimate based on the true forward model. We have assumed here that the error in the measurement is within the linearity limits of the forward model; that is, the same K (and hence the same D_{y}) holds for $\vec{x}_{\mathrm{app}}$ and $\vec{x}_{\mathrm{true}}$. Forward model error will be treated as systematic; its effect will be manifest as an offset on the retrieved state.

In Section 5.6 we use (5.12) to examine the effect of this error on the ozone profile optimal estimate. We look at forward model errors due to the use of a low number of streams in the discrete ordinate radiative transfer model. In [77], 4 and 6 stream forward model errors were characterized extensively by comparing radiance and weighting function output with accurate values obtained from a 20-stream model. In Section 5.6.2 we look at another source of forward model error due to the neglect of a vector radiative transfer treatment with polarization.

Model parameter error

In this case the error between the retrieved state and its true value is given by

$$\varepsilon_{\mathrm{B}}(\vec{x}) = D_{\mathrm{y}}\, K_{\mathrm{b}}\Delta\vec{b}, \tag{5.13}$$

where D_{y} is the contribution function matrix, and K_{b} is the sensitivity of the forward model to a set of model parameters $\vec{b}$ (that is, K_{b} is the matrix of derivatives of the forward model radiances $F(\vec{x})$ with respect the elements of $\vec{b}$). For a linearized RT model such as LIDORT that can deliver fast and accurate analytic weighting functions, it is straightforward to generate K_{b} along with the state vector Jacobians K. In this work we will assume that the uncertainties on $\vec{b}$ are characterized by Gaussian statistics with error covariance S_{b}. Then the error covariance for the optimal estimate will contain an additional term

$$S_{\mathrm{B}} = D_{\mathrm{y}} K_{\mathrm{b}} S_{\mathrm{b}} K_{\mathrm{b}}^{\mathrm{T}} D_{\mathrm{y}}^{\mathrm{T}} \tag{5.14}$$

which should be added to the posterior error covariance S_{OE} defined in (5.5). Of particular interest for us are the uncertainties in aerosol thickness and temperature profiles, and in Section 5.6 we will use weighting functions K_{b} in conjunction with simple estimates of S_{b} to investigate these error sources in more detail. We also consider cloud fractional cover, cloud-top pressure and cloud albedo as model parameter errors.

5.2.3. Singular value decomposition; DFS and Information Content

Following [1], we reformulate (5.3) by introducing the transformations:

$$\hat{x} = S_{\mathrm{a}}^{-\frac{1}{2}} \Delta\vec{x} \text{ and } \hat{y} = S_{\mathrm{y}}^{-\frac{1}{2}} \Delta\vec{y}. \tag{5.15}$$

In the transformed spaces, the *a priori* and measurement error covariances are now both unit matrices. The forward model linearization is $\hat{y} = \hat{K}\hat{x}$, where the transformed Jacobian is:

$$\hat{K} = S_{\mathrm{y}}^{-\frac{1}{2}} K S_{\mathrm{a}}^{\frac{1}{2}}. \tag{5.16}$$

A further reduction may be carried out with a singular value decomposition (SVD) of matrix $\hat{K}$:

$$\hat{K} = U \Lambda V^{\mathrm{T}}; \tag{5.17}$$

U and V are unitary matrices and Λ is diagonal. The columns of V form an orthonormal basis set in the space of state vectors, and the columns of U constitute a similar basis in measurement vector space. In our problem, all the elements of the state vector have some influence on the measurements; V is a square matrix, and there is no null space [1]. By introducing the unitary transformations $y' = U^{\mathrm{T}}\hat{y}$ and $x' = V^{\mathrm{T}}\hat{x}$ we find:

$$y' = \Lambda x'. \tag{5.18}$$

In terms of these variables, the optimal estimate is given by:

$$x'_{\mathrm{OE},i} = \frac{\lambda_i y'_i + x'_{i,\mathrm{a}}}{\lambda_i^2 + 1}. \tag{5.19}$$

Here, λ_i are the *singular values*, that is, the diagonal elements of Λ. $\vec{x}'_{\mathrm{a}}$ is determined from $\Delta\vec{x}_{\mathrm{a}}$ using the same transformations as those applied above to $\Delta\vec{x}$. The optimal estimate is then:

$$\Delta\vec{x}_{\mathrm{OE}} = S_{\mathrm{a}}^{\frac{1}{2}} V \vec{x}'_{\mathrm{OE}} \tag{5.20}$$

This reformulation using singular value decomposition has a clear interpretation. Mapping the state vector on to basis V and the measurement vector to basis U simplifies the forward model considerably: y'_i only depends on x'_i. For the optimal estimate the same situation holds: $x'_{i,\mathrm{OE}}$ depends only on y'_i. The singular values determine the relative weighting between *a priori* and measurement information in the optimal estimate. For those elements of the state and measurement vectors generating small singular values, the *a priori* contribution dominates the optimal estimate; for large singular values the measurement contribution is paramount. The role of the *a priori* vector in this analysis is clear; it regularizes the estimate when the measurement does not contain enough information to fully determine the state.

The SVD procedure has the further advantage that a number of important diagnostics may be established directly from the singular values. The improvement in knowledge of the state vector relative to the *a priori* due to the inclusion of the measurement can be quantified with the so-called *Information Content H*. This is defined in terms of information theory [97], and we establish its value by calculating the entropy of the posterior *pdf*. This can be done in measurement or state space; the results are the same. For a Gaussian distribution, this is a standard result [1]. In terms of the singular values, H can be written very conveniently:

$$H = -\frac{1}{2}\ln|E-A| = \sum_i \frac{1}{2}\ln\left(1+\lambda_i^2\right). \tag{5.21}$$

E is the unit matrix in state space. The degrees-of-freedom-for-signal (DFS) indicator d_s is another useful diagnostic for assessing the improvement in state vector precision; it is defined by:

$$d_\mathrm{s} = \mathrm{tr}(A) = \sum_i \frac{\lambda_i^2}{\lambda_i^2+1}. \tag{5.22}$$

This quantity can be interpreted as the number of independent linear combinations of the state vector that can be independently retrieved from the measurement. If N is the dimension of the state vector, we have $d_\mathrm{s} = N$ if the measurement completely determines the state, and $d_\mathrm{s} = 0$ if there is no information at all in the measurement. d_s is the expectation value of the cost function contribution χ^2_s for the optimal estimate. The degrees-of-freedom-for-noise (DFN) d_n is the counterpart of DFS; it is the expectation value of the noise contribution χ^2_n to the minimum value of the cost function. Since the expected value of χ^2_{min} equals the number of measurements M, it follows that $d_\mathrm{n} = M - d_\mathrm{s}$. The connections between H and d_s and the matrix A indicate the importance of averaging kernels in the discussion of information flow in the retrieval. Examples using these diagnostics will be given in Section 5.5.

5.3. Forward model aspects

5.3.1. Simulated measurements

The actual forward model consists of two operations: (i) the LIDORT radiative transfer computation for a set of wavelengths to simulate the spectrum before detection and (ii) an instrument simulation to compute the radiances as seen by the instrument detector pixels. We may write:

$$I_i = \int_{\mathrm{pixel}_i} d\lambda \int_0^\infty d\lambda' S(\lambda,\lambda') I(\lambda'). \tag{5.23}$$

Here, I_i is the radiance detected at spectral pixel i, $S(\lambda,\lambda')$ is the instrument slit function and $I(\lambda')$ is the LIDORT simulation of radiance at the entrance of the instrument. The outer wavelength integration is performed over the wavelength range of spectral pixel i. Invoking the linearization of the forward model, we have a similar expression for the weighting functions:

$$K_{ij} = \frac{\partial I_i}{\partial x_j} = \int_{\text{pixel}_i} d\lambda \int_0^\infty d\lambda' S(\lambda,\lambda') \frac{\partial I(\lambda')}{\partial x_j}, \tag{5.24}$$

where x_j is the j^{th} component of the state vector of parameters to be retrieved. A similar expression can be written down for weighting functions K_b with respect to model parameters $\vec{b}$. With the exception of the Ring scaling correction (see below), all of the derivatives $\partial I(\lambda')/\partial x_j$ in the integrand in (5.24) can be determined directly from the weighting function output of the linearized LIDORT model. The same applies to the derivatives $\partial I(\lambda')/\partial b_j$ for model parameters b_j which do not appear in the retrieval but will be considered as sources of error.

In this paper, radiance and irradiance measurements are simulated for the GOME-2 instrument. Solar irradiances are taken from the high resolution Kitt peak solar spectrum [18], which has resolution 0.01 nm. To make synthetic GOME-2 radiance measurements for a full retrieval, the RT model is used to calculate sun-normalized backscatter radiance at the resolution equal to or finer than that of the instrument. For full accuracy, RT calculations can be done at the resolution of the reference solar spectrum. For the GOME-2 instrument simulation, the spectral pixel size is 0.12 nm, with slit function resolution (FWHM) 0.24 nm [98]. A flat-topped slit function of the form $f(x) \sim 2^{-x^4}$ was used for the convolution. Radiance measurement errors were constructed using a combination of photon shot and electronic noise:

$$\Delta I(\lambda) = a\sqrt{\frac{I(\lambda)}{a} + b^2}, \tag{5.25}$$

where I is the radiance in absolute units, and parameters a and b are taken from GOME-2 specifications [98]. For wavelengths $\lambda < 307$ nm, $a = 10000$, $b = 2000$; for wavelengths $\lambda > 307$ nm, $a = 80000$, $b = 3000$. For the error analysis and sensitivity studies, it is sufficient to do RT simulations at the pixel resolution. For the solar spectrum, irradiance errors were modeled according to:

$$\Delta I_{sun}(\lambda) = a_{sun} I_{sun}(\lambda) + b_{sun}, \tag{5.26}$$

with $a_{sun} = 0.0014$ and $b_{sun} = 10^7$. Since we are dealing with sun-normalized radiance values $R = I/I_{sun}$, we require the relative error:

$$\frac{\Delta R(\lambda)}{R(\lambda)} = \sqrt{\left(\frac{\Delta I(\lambda)}{I(\lambda)}\right)^2 + \left(\frac{\Delta I_{sun}(\lambda)}{I_{sun}(\lambda)}\right)^2}, \tag{5.27}$$

Additive random-number noise can be added to (5.25), but this has not been considered in the present work. We now summarize the LIDORT output.

5.3.2. The LIDORT radiative transfer model

Molecular scattering tends to dominate in the UV spectral windows typically used for ozone profile retrieval; it is essential to use a radiative transfer model with a full multiple scattering capability. LIDORT uses the discrete-ordinate method to solve the RTE; derivatives are found by explicit analytical differentiation of the radiance with respect to atmospheric parameters of interest. LIDORT is a generic scattering formalism; it requires optical depth and single scatter albedos defined for a multilayer atmosphere, and for the derivatives, the variation of these inputs with respect to atmospheric parameters for which weighting functions are required. Once the radiance solution has been established, no further numerical computations are required for the weighting functions; the results are analytically exact, and hence all weighting functions will be computed to the same degree of accuracy as that specified for the radiance. A single call to LIDORT will return the radiance and all necessary weighting functions for an iteration step in the retrieval; the model is ideally suited to the kind of non-linear atmospheric retrieval algorithm exemplified in the present work. Details for the general N-stream formalism in the pseudo-spherical treatment may be found in Spurr [85].

Aside from the large advantages in efficiency to be gained by using analytical Jacobian determination, the speed of the RT code is also greatly increased by using a low number of discrete ordinate streams, though there is naturally some loss of accuracy. 4 and 6 stream versions of LIDORT are described in detail in [77]; the retrieval algorithm uses the 4-stream model. All RT simulations are done using the Nakajima-Tanaka single scatter correction procedure [37] in conjunction with the delta-M scaling [36, 34]; contributions to the TOA upwelling radiance from atmospheric single scatter are computed with exact forms of the phase functions. The weighting functions are similarly corrected [77].

In [77], the accuracy of the low-stream versions was investigated for a wide range of scenarios and viewing geometries appropriate to nadir-viewing satellite instruments measuring in the UV. These results can be used to establish one source of forward model error in the evaluation of ozone profile precision. Another source of forward model error derives from the neglect of polarization in the radiative transfer simulations. Polarized light scatter requires a Stokes-vector treatment of the RTE. It is known that in the absence of a polarization the use of a scalar (radiance-only) RT model can lead to significant sources of error [99, 48]. We used a doubling-adding vector RT model [41], running the code in vector and scalar modes to establish the magnitude of this source of error.

The state vector of ozone profile elements consists of a number of partial column densities (see below for details). Weighting functions with respect to these column densities may be established directly from the LIDORT 4-stream output; this is explained in detail in [77]. We make one further observation regarding the efficient computation of Jacobian matrices. In [77], it was noted that weighting functions with respect to column densities for trace gas g are proportional to the corresponding cross-sections σ_g. Thus, once partial column Jacobians have been established for O_3, column density weighting functions for any other species g can be determined quickly by simply scaling the O_3 values with the cross-section ratio $(\sigma_g/\sigma_{ozone})$. In our problem in the UV, NO_2 and SO_2 are the other significant absorbers. We note also that for any trace species, the weighting function with respect to the *total* atmospheric column is the sum of the partial column weighting functions. Further, when working with fixed pressure levels in a hydrostatic atmosphere, the temperature dependence of the radiation field is expressed only through the derivative of trace gas cross sections with respect to temperature ϑ. One can again use the O_3 partial column derivatives, but this time scaling them by factor $[\partial\sigma_{ozone}/\partial\vartheta]/\sigma_{ozone}$. Thus for our problem, four different sets of weighting functions (O_3, NO_2 and SO_2 partial columns, plus temperature) can be obtained from one template. This is an important saving of computational effort, and it allows model parameter errors for NO_2, SO_2 and temperature profiles to be incorporated in the O_3 state vector error covariance with little extra effort.

5.3.3. Layer subdivisions in the RT model

In general the forward model layering is finer than that defined by the fixed pressure grid used for the retrieval state vector. Subdivision of the atmosphere is driven by the requirement that optical properties do not vary too much with optical depth within any layer. Neglecting the small variation in the scattering phase function due to changing aerosol properties, it is mainly the variation of the single scattering albedo with optical depth that determines the degree of homogeneity in a layer. For the wavelength range employed in the ozone profile retrieval, absorption is dominated by ozone and scattering by air molecules. In this case, the single scattering albedo is approximately proportional to the inverse of the ozone VMR. The sub-layering is then determined by the VMR profile $V(P)$; for an atmosphere in hydrostatic equilibrium, we have:

$$V(P) = \frac{10^6}{gm_{\mathrm{air}}}\frac{dC(P)}{dP}, \tag{5.28}$$

with V in [ppm] units, m_{air} the molecular mass of air and g the gravitational acceleration (assumed constant over the layer). The sublayering works as follows: starting with a basic template of pressure levels, we first use (5.28) to find the relative VMR variation across the basic layers. We assume that $C(P)$ can be approximated by a cubic spline in P, thus producing a smooth derivative with respect to P and hence a smooth VMR. The VMR variation is compared to a threshold value of 20%; when this is exceeded, a number of sublayers are introduced for which the VMR variations are below 20%. The sublevels are placed at equal log-pressure intervals and the C values are computed using the cubic spline. The 20% threshold was found to give an error of $< 0.5\%$ for the radiance at TOA compared to calculations using even finer sublayering. For wavelengths in the UV below 300 nm, the atmosphere is optically thick, and the sublayering procedure is only followed for levels above a threshold value set by a cut-off value of 10 for the ozone absorption optical thickness.

5.4. Ozone profile retrieval: algorithm set-up

5.4.1. Reference atmosphere

We now define a reference atmospheric state used in the results of Sections 5.5 and 5.6. RT model simulations are done with the LIDORT model for a complete wavelength range of 270-340 nm. Ozone cross sections are from a standard data set [70]. Wavelength dependent Rayleigh cross-sections and depolarization ratios are taken from an empirical source [18, 80]. Ozone reference states are taken from climatology; we use the monthly zonal-mean global ozone data set of Fortuin and Kelder [17] (January data, mid-latitude). NO_2 profiles were interpolated from USA standard atmosphere values [69]; cross sections were extracted from the MODTRAN data set. Temperature profiles were taken from an ECMWF climatology [100]. The aerosol model is taken from the LOWTRAN data set [71], with rural boundary layer aerosol loading and extinction (visibility 25 km), and background tropospheric, stratospheric and upper atmosphere loading and optical properties. The surface albedo (Lambertian) was taken to be 0.5 for standard cases, with values 0.05 and 0.8 for low and high albedo scenarios respectively.

For a complete retrieval, the "true" ozone profile used to derive the synthetic measurement data is constructed in part from a Sonde profile (1000 to 10 mbar, 67 levels) and in part by interpolating data from climatology (0.1 to 10 mbar, 20 levels). January climatological data at latitude 53°N was selected to match the sonde profile. The true temperature profile was also taken from the same Sonde data (up to 10 mbar); values at higher levels were interpolated from ECMWF data appropriate to the season and latitude.

The reference state is the starting point for the retrieval, and we take it also to be the *a priori*. For the error assessment and sensitivity issues addressed in this study, we carry out a single inversion step by linearizing the forward model about the reference state vector. All runs were done for a GOME "East pixel", with the line-of-sight zenith angle ranging from 10.6° to 30.9° at the satellite, and a relative azimuth angle of 3° at the satellite. The solar zenith angle (SZA) was allowed to vary from 25° to 85°. Integration of RT model output over the line-of-sight zenith angle range was done by two-point quadrature.

5.4.2. Construction of state, *a priori* and model parameter vectors

The ozone profile elements of the state vector will be the 34 layer column densities $\Delta C_i = C_i - C_{i-1}$ between 35 fixed pressure levels $P_i, i = 1, \ldots, 35$. We use as a template the 19 pressure levels from Fortuin and Kelder: surface pressure, 700, 500, 300, 200, 150, 100, 70, 50, 30, 20, 10, 7, 5, 2, 1, 0.5, 0.3, 0.1 mbar. These levels appear to capture the global and inter-annual variations in the ozone profile. The remaining levels are chosen by examining the relative variation in O_3 VMR across the 18 basic layers, and introducing sublayers whenever this variation exceeds a 20% threshold; this is discussed above in section 5.3.3. The function C_i is defined as the ozone column density from level P_i to the top of the atmosphere (TOA), which is set at 0.1 mbar.

The spacing of pressure levels should be finer than the vertical resolution likely to be achieved in the retrieval; this ensures that the averaging kernels can be sufficiently well characterized to allow the vertical resolution to be established. This is analogous to the application of the Nyquist criterion to sampling issues in spectral measurements. In the context of the vertical sampling and resolution in the ozone profile retrieval, we can argue that the sampling (which we are free to choose) has to be a factor of 2-3 higher than the resolution (which is fixed by the measurement and the forward model). The ozone profile retrieval resolution from nadir UV/VIS TOA measurements appears to be such that six to eight independent ozone profile parameters can be derived from the data (depending on the signal-to-noise, atmospheric scenario and choice of window) [15]. The 34-layer sampling adopted here therefore obeys the Nyquist criterion. The vertical sampling was also chosen to satisfy the layer subdivision criterion discussed above in Section 5.3.3; for all wavelengths, RT simulations with the 34-layer sampling were found to be within 0.5% of values obtained using finer vertical layering.

There are a number of other parameters that could be included in the state vector in addition to the vertical ozone column densities. These auxiliary parameters describe other aspects of the atmosphere or the instrument that also influence the earthshine measurement but which are not known to a high enough accuracy. An important example is the surface reflectance; it is sufficient for our application to approximate this quantity with a Lambertian albedo. Weighting functions with respect to surface albedo may be determined directly from the 4-stream LIDORT model. Other auxiliary parameters that might be included in the state vector are the total NO_2 and SO_2 column densities, the total aerosol optical depth, and a number characterizing the magnitude of the Ring effect. Aside from the Ring parameter which is discussed separately below in Section 5.4.3, atmospheric variables other than O_3 can of course be treated as model parameter errors. The temperature profile will always be treated as a model parameter vector.

The presence of clouds is treated in the "independent-pixel approximation". Separate radiances I_{cloud} and I_{clear} are calculated for the fully cloudy and cloud-free scenarios, and a weighted average taken with respect to the cloud fractional cover f_c:

$$I_{total} = f_c I_{cloud} + (1 - f_c) I_{clear}. \tag{5.29}$$

A similar relation holds for the weighting functions. For the cloud-filled simulation, the cloud is treated as a Lambertian reflector (albedo 0.8) at cloud-top pressure. The two computations differ only in the bottom layer and the surface albedo; it is not necessary to repeat some of the calculations for layers above the cloud top. Forward model errors for cloud-filled scenarios have been investigated in [77]. In the present paper, we look first at the effect of forward model errors on O_3 profile precisions for partially cloud covered scenes. We also determine the effect of fractional cover f_c treated as a model parameter error source; weighting functions for I_{total} with respect to f_c may be established easily from (5.29). The effects of cloud-top pressure and cloud albedo parameter errors may also be investigated since the corresponding weighting functions are available from the linearized forward model. In the operational retrieval, effective values of cloud-top pressure and fractional cloud-cover will be retrieved from the FRESCO cloud fitting algorithm [88].

The *a priori* state vector elements $\vec{x}_a$ for the O_3 profile are taken from the Fortuin and Kelder climatology. Diagonal elements (variances) of the *a priori* error covariance matrix S_a are also specified in the climatology. Off-diagonal elements of this matrix are determined using a fixed correlation function which is Gaussian in log-pressure and has width $\Delta \log P = 0.2$. *A priori* state vector elements for auxiliary retrieval parameters are taken from climatology (NO_2 column and aerosol optical depth) or from a suitable data set (albedo) or set to an initial value (Ring). Variances for these auxiliary elements are set by hand; the parameters are loosely constrained. It is assumed that auxiliary *a priori* elements are uncorrelated with each other and also not correlated with *a priori* O_3 profile elements.

5.4.3. A note on the Ring effect

Although we will not deal with the Ring effect in the error assessments presented in this paper, it is necessary to allow for it in an operational context. The Ring effect is attributed to (inelastic) rotational Raman scattering (RRS) by air (N_2 and O_2) molecules [101, 19, 20]; energy exchange results in a wavelength shift of ± 0-2 nm in the UV for scattered photons. The Ring effect induces a small-amplitude distortion that follows the Fraunhofer lines in the atmospheric reflectance spectrum. This structure hampers the profile retrieval if it is not removed or treated in the forward model.

The structure is commonly dealt with by using a pre-calculated "Ring spectrum", defined as the logarithm of the ratio of radiances with and without RRS [18]. An amplitude for a selected Ring spectrum is included in the state vector. This is analogous to the treatment of absorbing constituents in the Beer-Lambert approximation used in DOAS-type algorithms [23] - the Ring spectrum has the signature of a “pseudo-absorber”. Since RRS also affects atmospheric absorption structures, notably those of ozone, a second Ring correction amplitude has to be used. This second correction scales with the ozone column for the longer wavelengths. Weighting functions for the Ring amplitudes follow in a straightforward fashion from their definitions.

A more accurate characterization of the Ring spectrum can be obtained by suitable forward model calculations [20, 19]. A look-up table of Ring spectra (classified by solar zenith angle and surface albedo) can then be used in the ozone profile retrieval algorithm. However it is possible to dispense with Ring parameter fitting altogether by performing the necessary RRS calculations “on-the-fly”, that is, as an integral part of the retrieval algorithm RT model. We intend to investigate this issue in a future paper.

5.5. Sensitivity analysis with DFS and Information Content

5.5.1. Temperature sensitivity for GOME-2 using DFS

Ozone absorption cross sections in the Huggins bands are strongly dependent on temperature. Since GOME and GOME-2 are able to resolve these absorption features, then knowledge of the temperature profile should enable the retrieval to generate additional ozone information in the lower atmosphere. To investigate the temperature sensitivity of the retrieval, we construct a series of tropospheric temperature profiles. The tropopause temperature is fixed at 220.7 K; this is value assigned for the 7th partial column (85 - 100 mbar). We allow the temperature in the lowest layer to vary from 220.7 K to 300 K; each tropospheric profile is linearly interpolated between the surface value and 220.7 K. For a surface temperature of 220.7 K, the profile is flat. This exercise is repeated for a number of solar zenith angles (30°, 50°, 70° and 80°) and for two albedos (0.05 and 0.75). The upper wavelength limit was taken to be 340 nm. In each case, the linearization is subject to an SVD analysis, and the corresponding DFS and Information Content diagnostics are computed from the formulae in Section 5.2.3.

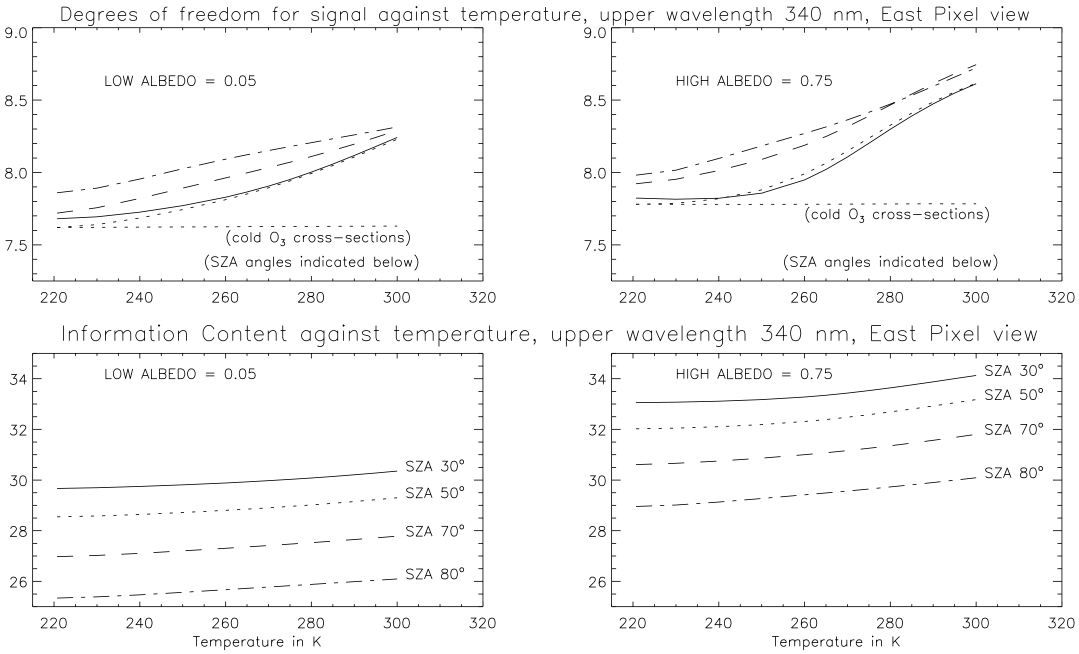

Figure 5.1: DFS (upper panels) and Information Content (lower panels) for two values of albedo (0.05 and 0.75) and four solar zenith angles as indicated. Upper wavelength limit 340 nm, GOME East pixel view.

The results for the two albedo cases are shown in Figure 5.1. DFS values range between 7.6 and 8.8. It is the slope of these graphs that indicates the temperature sensitivity. To see this, we compute DFS for all temperature regimes, but keeping ozone cross sections in the first 7 layers at values for temperature 220.7 K. This results in the two flat lines in the top panels of Figure 5.1 (only the DFS values for SZA 50° are shown). It is remarkable that the increase in DFS is due solely to the temperature sensitivity of *tropospheric* ozone absorption. In all cases, increasing DFS values show that the retrieval *precision* (that is, the measurement contribution to the profile accuracy) is improved with warmer tropospheric temperatures. Information Content is only weakly sensitive to the tropospheric temperature profile.

All values of DFS and Information Content are higher for the high albedo cases (right panels of Figure 5.1). The general continuum level in the measurement spectrum will be larger for higher albedos, thus increasing the overall signal to noise level and hence allowing more information to be gleaned from the measurements. The Information Content also shows a steady decrease with rising SZA. However the situation with DFS is different; measurements with the two higher SZA values generate slightly higher DFS, especially at lower temperatures.

DFS gradients are noticeably steeper for the high albedo case, and the slopes are also steeper for lower SZA values. These scenario-related effects are in general governed by the level of measurement noise. To investigate this further, we plot some of these slopes for a range of albedos (0.05 to 0.8) and SZAs (25° to 85°) in Figure 5.2. Here we look at increases (linear gradients) in DFS and Information Content going from a cold surface (240 K) to a warm one at 300 K. From left to right in the lower panel, contours of the Information Content are evenly spaced, with the 240/300 slopes increasing slowly over the range 2-3% as the albedo increases. The DFS gradients show more structure, especially for higher solar zenith angles. There is a marked drop in sensitivity beyond SZA 80°, especially for low albedos; at glancing solar incidence, surface reflected contributions fall off rapidly.

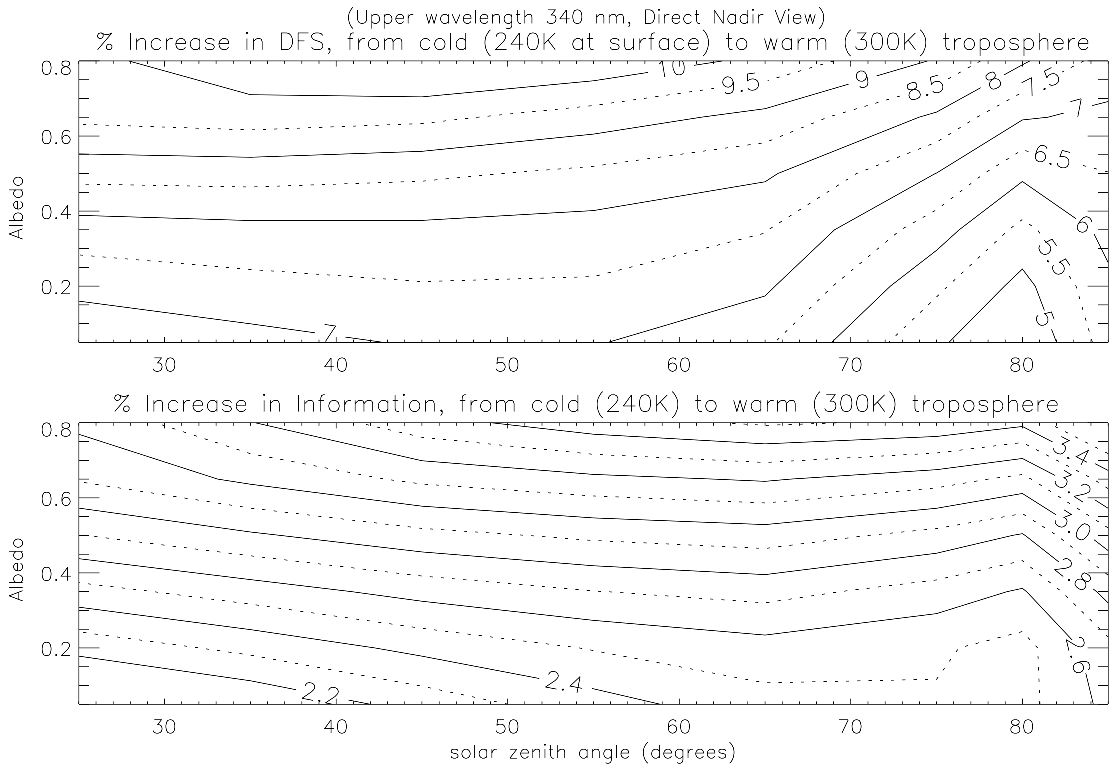

Figure 5.2: DFS (upper panel) and Information Content (lower panel) temperature sensitivity for albedos from 0.05 to 0.8, and for a range of solar zenith angles from 25° to 85°. Contour plots for the increase in diagnostics between a cold surface at 240 K and a warm surface at 300 K.

5.5.2. Temperature sensitivity and averaging kernels

For a given scenario, the total Information Content in the retrieval does not change greatly, but the information itself is redistributed: for higher tropospheric temperatures, more of it comes from the measurements, less from the *a priori*. Further, this increase in measurement information is manifested in increased precision in the tropospheric profile elements; stratospheric elements show little change in precision. To see this, we look at some averaging kernels (rows of matrix *A*), plotted in Figure 5.3 for SZA 30° and albedo 0.8, and for two surface temperatures: 220.7 K (the cold flat profile) and 300 K (warm troposphere). Kernels are shown for the lowest four levels of the retrieval and for a number of stratospheric levels. Kernels in the middle stratosphere have well-defined peaks; the full width half maximum (FWHM) is about 6 mbar, indicating a profile resolution of about 6.5 km in the 10 mbar region.

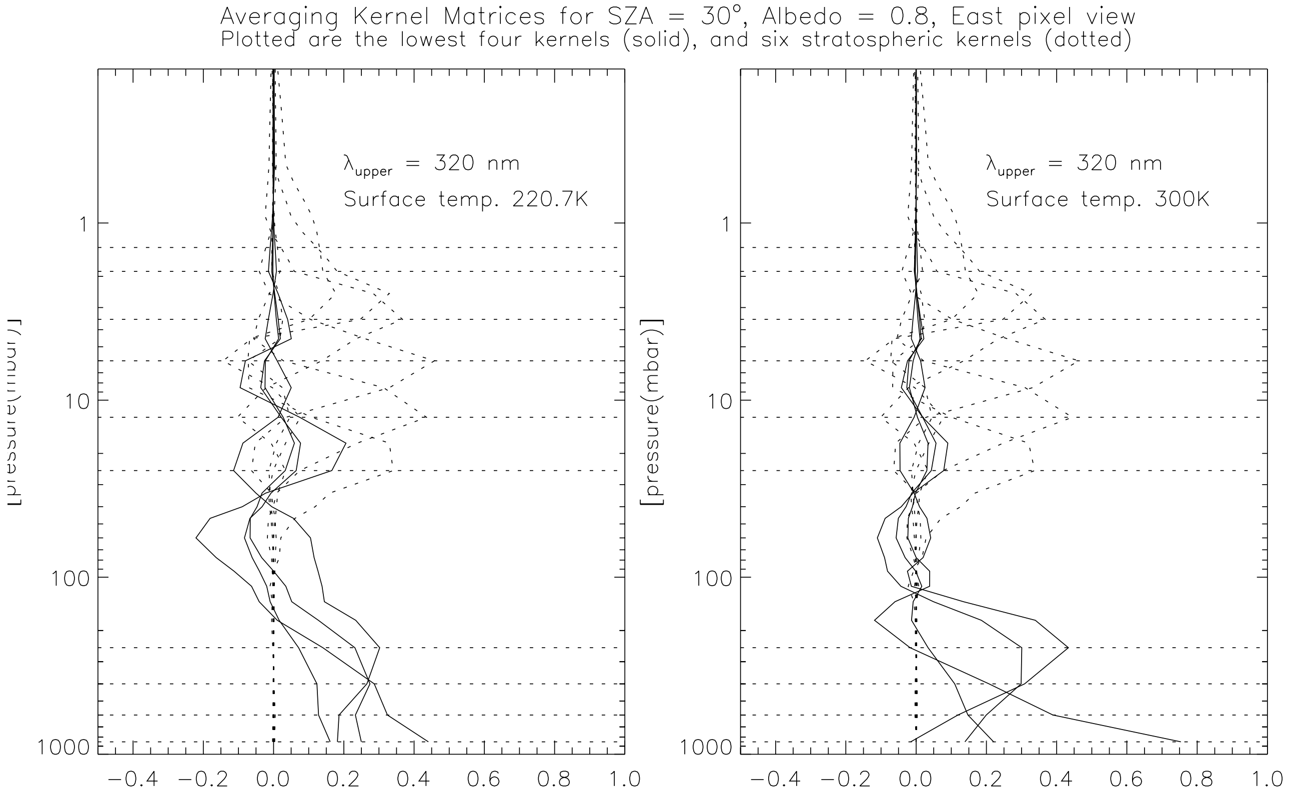

Figure 5.3: Selected averaging kernels for a cold troposphere with surface temperature 220.7 (left) and for a warm troposphere with the surface at 300 K (right). Upper wavelength limit 340 nm, solar zenith angle 30°, albedo 0.8.

With the flat temperature profile in the troposphere, the tropospheric averaging kernels have poorly defined or non-existent peaks and it is difficult to assign any FWHM values to get an idea of the vertical resolution (left panel in Figure 5.3). Another feature apparent in both graphs is that some of the kernels peak at pressures not equal to the retrieval values. There is also some mixing of tropospheric information in higher levels, mainly in the lower stratosphere (presence of several positive and negative lobes). Averaging kernels are more sharply defined in the troposphere for the warm temperature profile (right panel); the most pronounced improvement is actually for the lowest partial column of ozone. The spread of these kernels may be defined mathematically using the Backus and Gilbert function [102]:

$$s(z) = 12\frac{\int (z-z')^2 A^2(z,z')\mathrm{d}z'}{\left\{\int A^2(z,z')\mathrm{d}z'\right\}^2} \tag{5.30}$$

where the variable z is the logarithm of the pressure. Values of this spread function are shown in Table 5.1 for 22 averaging kernels, including the ones plotted in Figure 5.3 (these are denoted by asterisks). The layer average pressures are computed from the mid-point of the layer boundary log-pressures.

Although the results in Table 5.1 are suggestive, they should be used with caution. The variability in spread for the lowest 8 kernels is due in the main to the influence of *a priori* errors. The *a priori* ozone profile is tightly constrained (low standard deviation) at 500-700 mbar and again at 100-200 mbar. These variations are a reflection of our prior knowledge of the ozone (which comes from climatology). Despite the improvement in precision for a surface temperature of 300 K, it is not really possible to assign a meaningful figure to the vertical resolution of *all* profile elements below about 70 mbar. For profile element 4 at ~245 mbar, the kernel is well defined and has an FWHM of about 350 mbar (which translates to a vertical resolution of ~8.5 km).

Element	Average Pressure (mbar)	Spread Function T_{surf} = 240 K	Spread Function T_{surf} = 300 K
1 ∗	836.660	57.483	2.700
2 ∗	591.608	34.223	15.323
3 ∗	387.298	3.936	7.975
4 ∗	244.949	4.903	1.807
5	173.205	13.092	8.622
6	136.931	24.289	14.704
7	111.803	28.755	13.087
8	92.195	21.939	7.984
9	77.136	15.355	8.754
10	59.161	8.638	9.386
11	46.368	5.599	5.709
12	39.887	4.818	4.220
13 ∗	33.317	3.585	3.105
14	24.495	1.856	1.732
15 ∗	17.321	1.162	1.182
16	12.247	1.006	1.045
17 ∗	8.367	1.266	1.297
18	5.916	1.449	1.513
19 ∗	4.472	3.915	4.275
20	3.464	2.841	2.783
21 ∗	2.449	2.268	2.432
22	1.871	4.761	4.894

Table 5.1: Spread values for the averaging kernel matrices displayed in part in Figure 5.3.

If one chooses a loosely constrained *a priori* distribution with consistently high standard deviation in the troposphere, then one can make a better attempt at defining tropospheric vertical resolution.

However, too little regularization generates an optimal estimate that is heavily influenced by measurement errors, although the fit itself is good. In this case, the regularized state vector norm χ_s^2 in (5.6) swamps the residual noise norm χ_n^2. With over-strict regularization, the reverse happens: the fit is poor, and χ_n^2 dominates over χ_s^2. One can find an optimum level of regularization by examining the so called L-curve, which is a logarithmic plot of $\gamma\chi_s^2$ against χ_n^2 for various values of γ. The optimum choice of γ corresponds to the "corner" of the L-curve, and this can be determined as the point of maximum curvature [103]. The L-curve analysis is a standard feature of classical Phillips-Tikhonov regularization schemes, but it can easily be extended to the present situation.

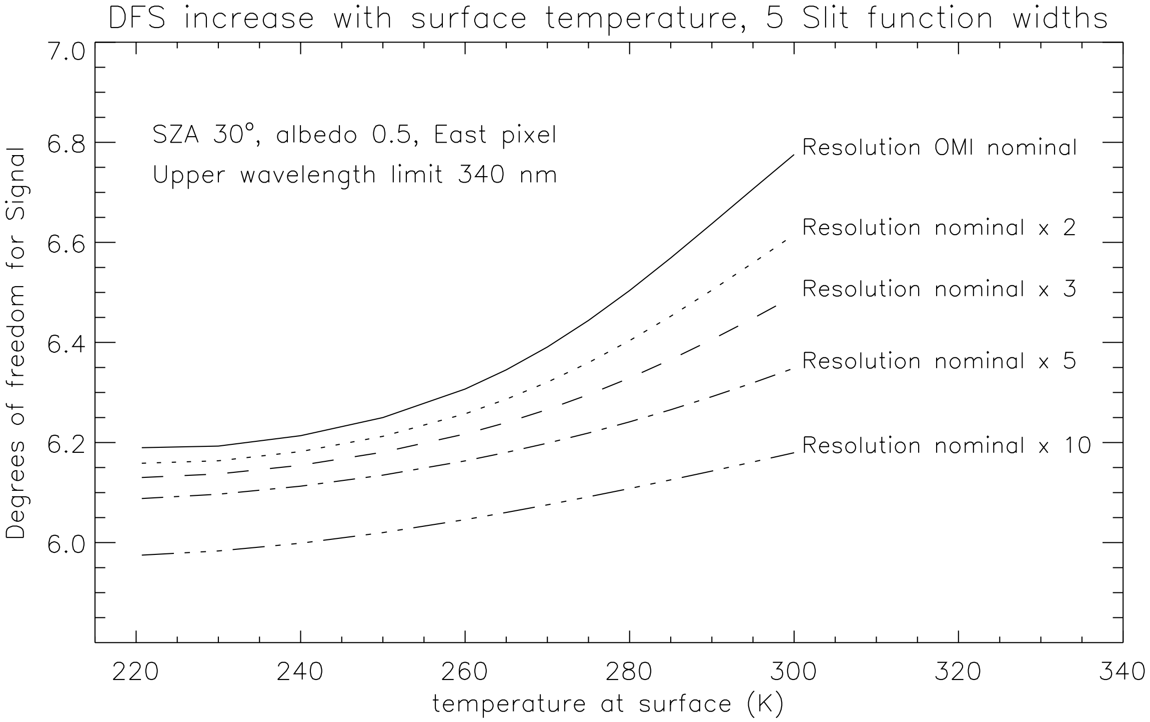

Figure 5.4: DFS values for OMI-type instrument with pixel resolution 0.32 nm and response function resolutions $\sim$ 0.45 nm (nominal) and factors of 2, 3, 5 and 10 times broader than the nominal value. Upper wavelength limit 340 nm, solar zenith angle 30°, albedo 0.5.

5.5.3. Temperature sensitivity for other instruments

The GOME, GOME-2, SCIAMACHY and OMI instruments are all capable of resolving the temperature structure of the ozone Huggins bands absorptions. GOME and SCIAMACHY have similar resolution to that of GOME-2. However the OMI instrument has pixel size 0.32 nm for its two UV channels, and response function resolutions of 0.42 and 0.45 nm for the two channels. Of interest here is the possible loss of temperature sensitivity with coarser spectral resolution. We repeat our calculations of DFS for various tropospheric temperature regimes for a number of slit functions, starting with the nominal OMI instrument parameters given above, and artificially increasing the slit FWHM by factors of 2, 3, 5 and 10. [Noise statistics for GOME-2 were used]. The results are shown in Figure 5.4. The general DFS level is much lower because of the relative paucity of observations ($\sim$40% that of GOME-2). However the increase in DFS is (for the nominal slit width) easily comparable to that for GOME 2 (about 8% from the value at 220.7 K to that at 300 K). It is only when the resolution becomes quite coarse that the DFS sensitivity is really poor; Huggins bands structures get smeared out.

5.5.4. Sensitivity to upper wavelength limit

In this case, we examine the improvement in accuracy of the profile for a number of different fitting windows. We vary the upper wavelength limit λ_{upper} from 300 to 340 nm, taking an albedo of 0.5 and SZA (30°). In the top panel of Figure 5.5, DFS is plotted against λ_{upper} for three surface temperatures (240 K, 275 K and 300 K). At 300 nm for the window limit, almost no light reaches the surface, and the three DFS curves converge - there is negligible tropospheric effect. The DFS rises steadily as more measurements are included, but there is little difference between the three curves up to about 313 nm. The temperature sensitivity becomes apparent with the inclusion of measurements in the approximate range 313-322 nm, but the use of measurements beyond 322 nm does not increase the DFS significantly. Another way of looking at this is to plot the decrease in DFS and Information Content for various limits λ_{upper} compared with the values of these diagnostics computed for a window with upper limit 340 nm (lower panels in Figure 5.5). Again we notice the lack of temperature sensitivity in the total information. The flatness in DFS for λ_{upper} beyond 322 nm is apparent for all temperatures considered.

These results are important for optimizing the window setting. It is clear that there is only a small improvement in DFS to be gained from the inclusion of measurements in the upper reaches of the ozone Huggins bands. Below in Section 5.6.2 we will see that the largest contribution to forward model error comes from precisely this region of the UV spectrum, and that 4-stream forward model errors for a full window out to 340 nm are unacceptably high. In the light of this remark, there is a strong case for leaving out measurements beyond a certain threshold λ_{thresh}. We could define this limit by using the 2% DFS contour in Figure 5.5 (center), in which case λ_{thresh} is about 323.1 nm. The choice of upper window limit has strong consequences for operational design and performance; a great deal of time can be saved by reducing the window to exclude measurements beyond λ_{thresh}.

5.6. Error assessment

5.6.1. Example of contribution functions

The contribution functions are central to the error assessment, and we display these in Figure 5.6, for a linearization about the reference state, with SZA 30° and an albedo of 0.5. These functions represent the sensitivity of the profile to the relative error on the measurement. There is little sensitivity at higher levels to the tropospheric measurements. For levels above 50 mbar (right panels), the first positive peak travels progressively towards higher wavelengths; this is the BUV effect (wavelength-dependent peak sensitivity in the strongly-absorbing Hartley bands is a measure of the effective scattering depth).

5.6.2. Forward model errors

Errors due to 4/6 stream discrete ordinate assumptions

For our reference atmosphere, we run the LIDORT RT model with 20 streams to get an accurate simulation of radiance, then repeat the calculations with 4 and 6 streams used for the discrete ordinate

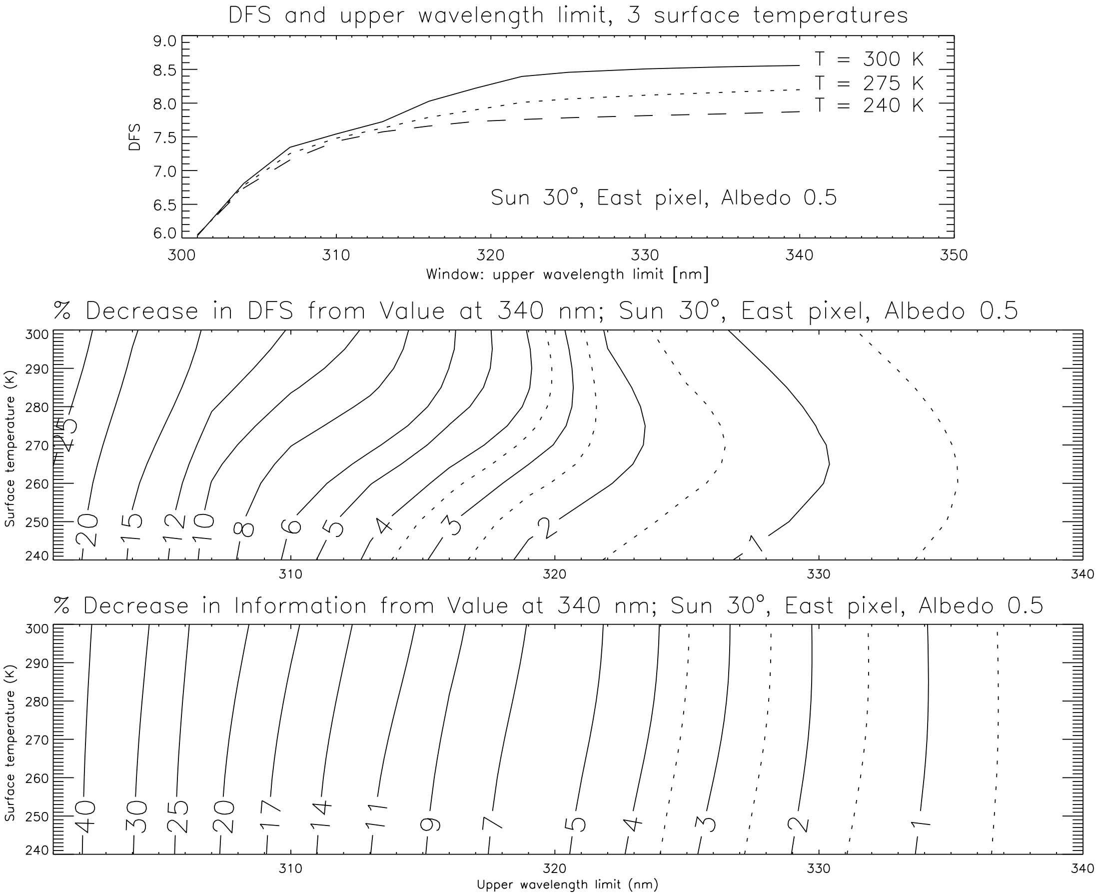

Figure 5.5: DFS and Information Content according to upper wavelength limit. (top) DFS for 3 surface temperatures; (middle) % decrease in DFS from its value computed for λ_{upper} = 340 nm, for various temperatures; (bottom) % decrease in Information Content from value for λ_{upper} = 340 nm. Solar zenith angle 30°, albedo 0.5.

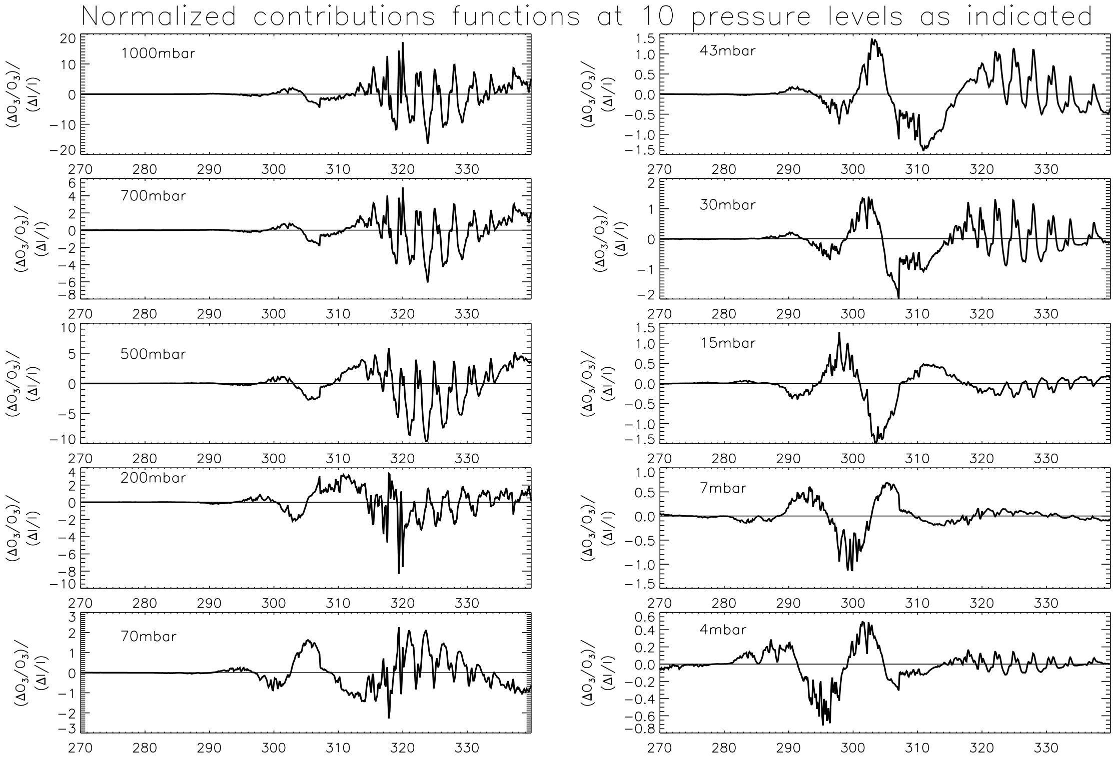

Figure 5.6: Normalized contribution functions in the range 270 to 340 nm, for linearization about a reference ozone profile with 34 elements. (Left panels) 5 tropospheric values at pressures indicated; (right panels) 5 stratospheric values as indicated.

approximation. The forward model errors are then $\Delta F_4 = R_{20} - R_4$ and $\Delta F_6 = R_{20} - R_6$, where R_N is the sun-normalized radiance for the N-stream approximation. We considered 2 solar zenith angles (30° and 80°) and 2 albedos (0.05 and 0.80) for the East pixel view used in this work. Since the single scatter correction in the model is independent of the stream number, the values of ΔF may be obtained by computing only the multiple scatter LIDORT radiances (this is however only true if the Delta-M scaling is switched off). Strictly speaking, one should use contribution functions calculated with the 6-stream model when assessing the 6/20 stream forward model error.

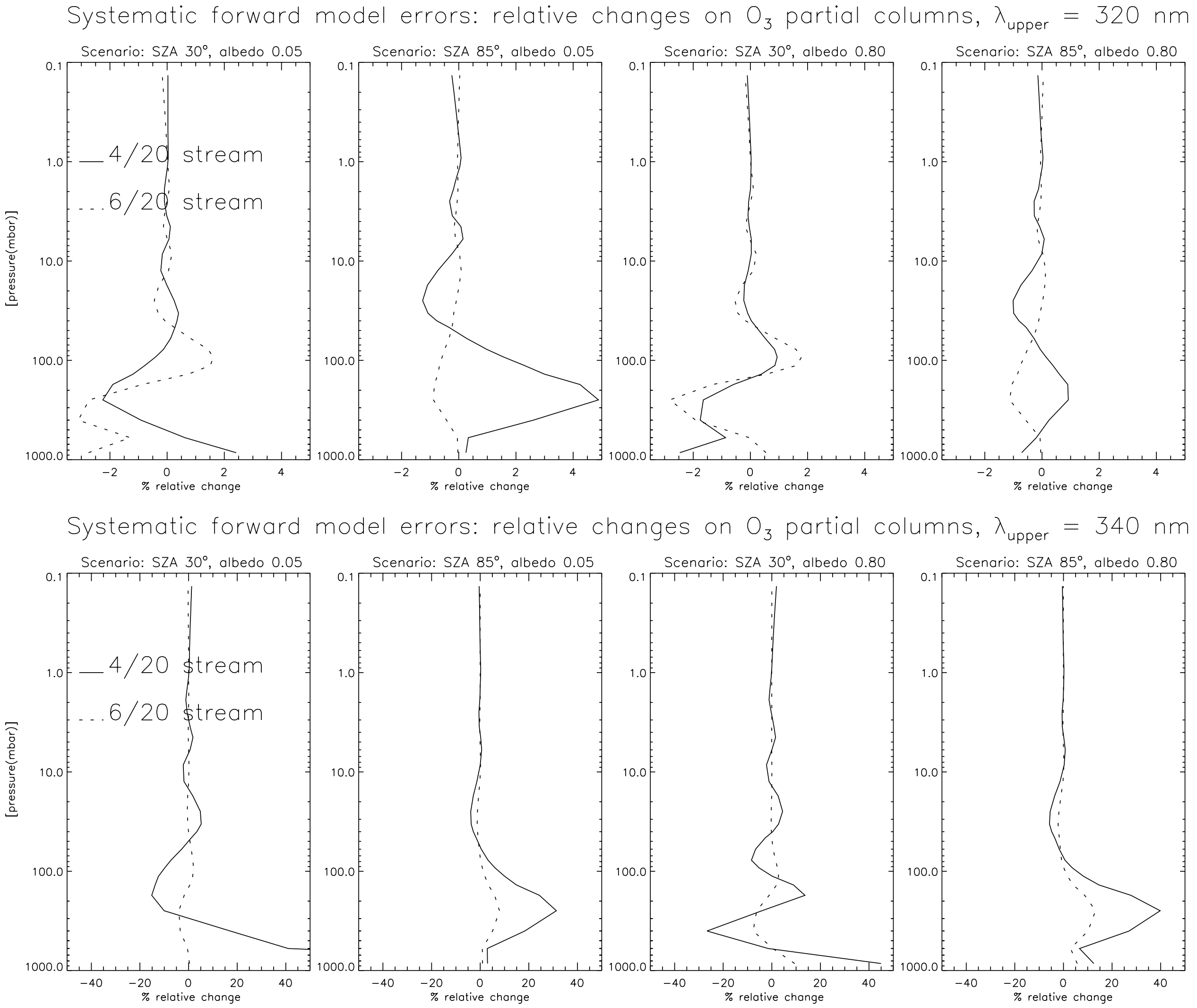

Figure 5.7: Effect of forward model errors on O_3 profile accuracy. (Upper panels) Four scenarios (SZA 30°, 80°, albedo 0.05, 0.8) with upper wavelength limit 320 nm; (Lower panels) the same four scenarios, this time with with upper wavelength limit 340 nm.

Figure 5.7 shows the relative changes $\Delta x_i / x_i$ in ozone profile elements obtained by multiplying ΔF by the 4-stream contribution functions according to (5.12). We show two sets of results, one for an upper wavelength limit of 320 nm, the second set for λ_{upper} = 340 nm. Apart from the high SZA, low albedo case (where very little light penetrates to the troposphere), these ΔF_4-induced changes are all below 2.5% for the smaller window λ_{upper} = 320 nm. The situation is very different for the larger window. With the rising importance of aerosol scattering at higher wavelengths, and the increasing penetration of light to the denser tropospheric layers, the low-stream approximations become increasingly inaccurate for wavelengths beyond 320 nm. Values of $\Delta x_i/x_i$ for the 4 stream forward model errors are above 5% even in the stratosphere (10-100 mbar), and the tropospheric levels are clearly unacceptable. In the longer-wavelength case, a large part of the profile error comes from poor forward model estimation beyond 320 nm. In all cases for λ_{upper} = 340 nm, there is a marked improvement when the 6-stream errors are used. These results indicate that the use of a 4-stream model will generate unacceptable levels of forward model error for larger windows.

Errors due to neglect of polarization

First we need to estimate the magnitude of this error before calculating its effect on profile accuracy. We look at output from an independent vector RT model with polarization [41]. We choose the same four scenarios used in the previous example. The error may be found simply by running the vector model in full Stokes vector mode (with polarization effects) and repeating the calculation in scalar-only mode (no polarization), then subtracting the results. Relative errors for wavelengths out to 340 nm are plotted in Figure 5.8. For SZA 30°, the error is not worse than 2%; this is comparable to the maximum value of the 4-stream error in the previous section. However, errors for the high solar zenith angle are much greater.

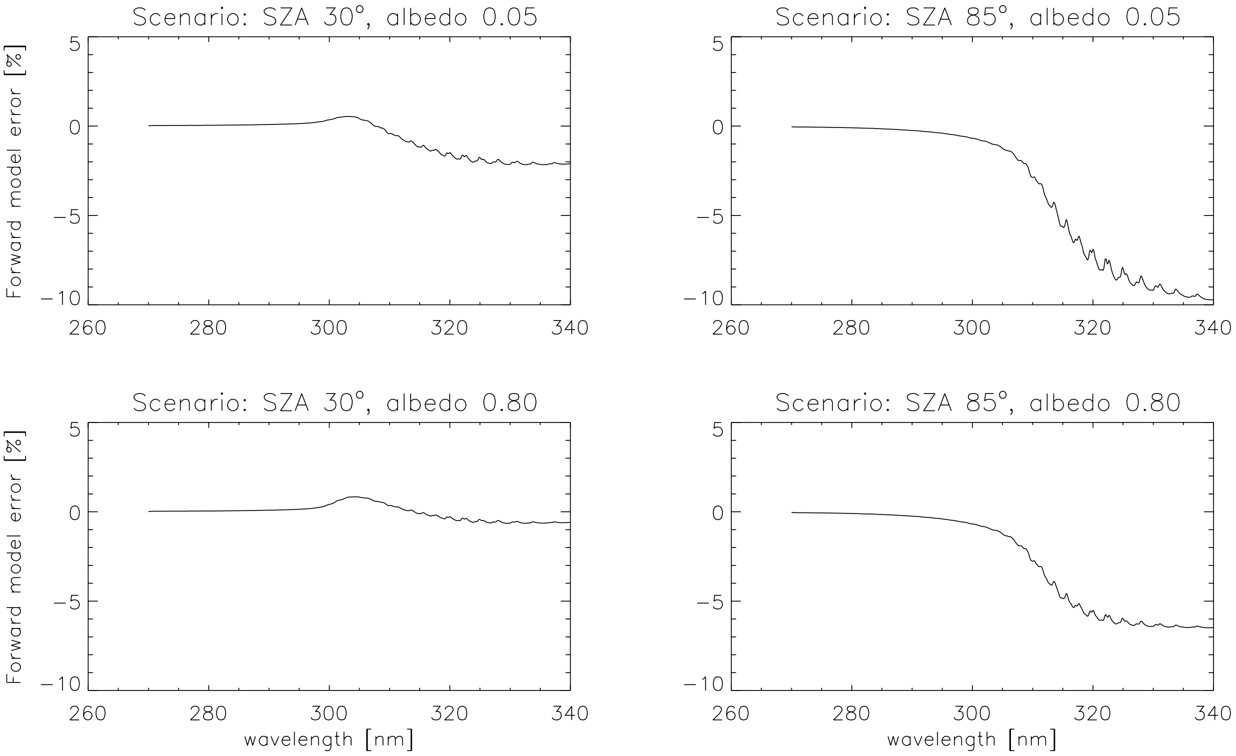

Figure 5.8: Forward model errors due to the neglect of polarization. Four scenarios (SZA 30°, 80°, albedo 0.05, 0.8) with wavelength limit 340 nm;

We now examine the effect of this error on profile accuracy. As before, the 4-stream forward model is linearized about the reference state $\vec{x}_0$, and we pre-multiply the above forward model errors by the contribution functions according to (5.12). The relative changes to ozone profile elements are shown in Figure 5.9 for the above four scenarios, and for upper wavelength limits of 320 nm (top panels) and 340 nm (lower panels). Results for SZA 30° are similar in magnitude to those in Figure 5.7 (4-stream) for both upper wavelength limits. Given the larger values of forward model errors in Figure 5.8 for SZA 85°, it is not surprising that the corresponding ozone profile relative errors are also greater for the low albedo case; the accuracy seems little affected when the albedo is high. It is clear that relative changes to tropospheric profile elements are once again unacceptably large when wavelength out to 340 nm are included in the inversion. The strong dependence of profile accuracy on solar zenith angle for this source of forward model error was also noted by [15]. They quoted a range of ±1% to ±5% on profile error, but did not provide any details by which a comparison could be made with the results in Figure 5.9.

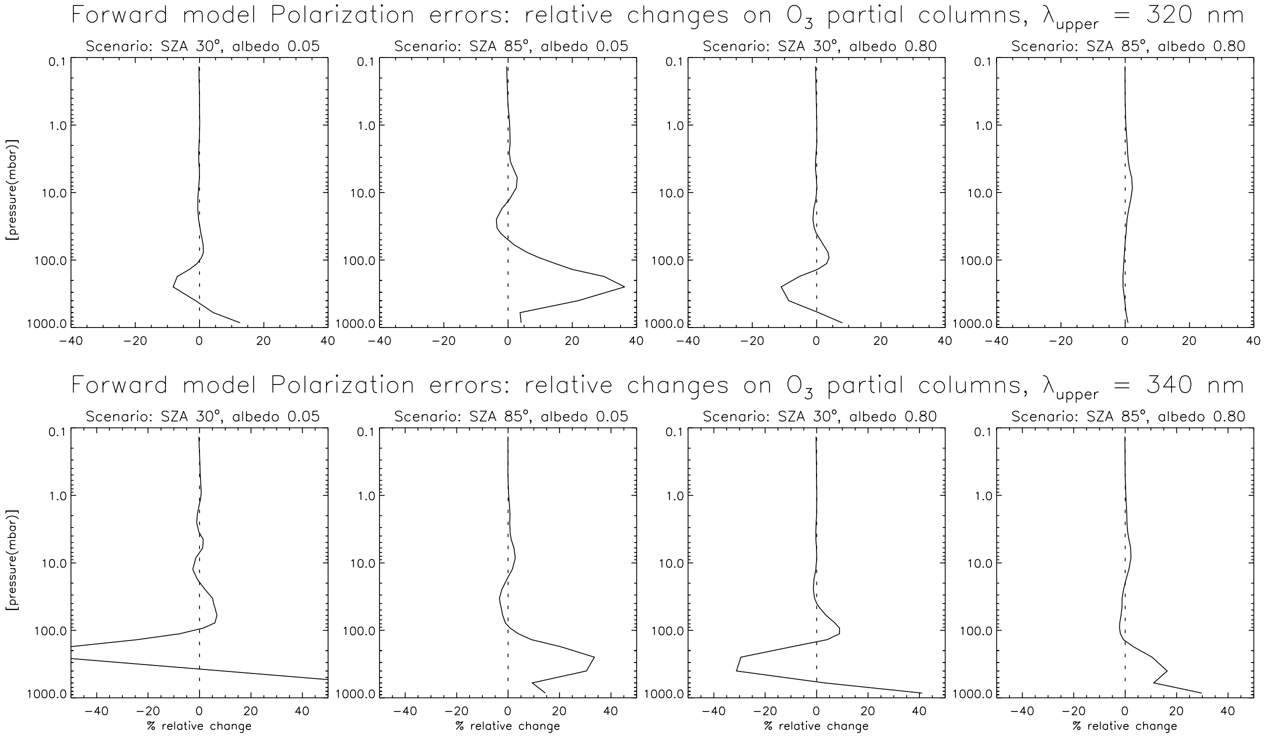

Figure 5.9: Effect on O_3 profile accuracy due to neglect of polarization in the forward model. East pixel, 4 scenarios as indicated. (upper panels) Errors on profile elements for upper wavelength limit 320 nm; (lower panels) the same for upper wavelength limit 340 nm.

5.6.3. Polarization errors in the measurement

We first remark on the polarization correction applied to GOME and GOME-2 radiance data. The regular radiance channels (pixel resolution ∼0.12 nm in the UV) observe polarized light with components parallel and perpendicular to the plane of the instrument slit. GOME and GOME-2 have a number of auxiliary broad-band detectors called Polarization Measurement Devices (PMDs). The 3 GOME PMDs are sensitive only to light polarized parallel to the instrument slit; the PMDs cover the ranges 300-400, 400-600 and 600-800 nm. Regular GOME signals from the array read-out detectors must be integrated over these ranges and combined with the PMD measurements to derive three independent values P_i ($i = 1,2,3$) of the degree of linear polarization P. For wavelengths less than $\sim$300 nm, P is treated as a constant value P_4 depending only on geometrical variables; it is evaluated from radiative transfer considerations in a single scatter Rayleigh atmosphere. These 4 values are then interpolated over wavelength to derive a polarization spectrum which is used to correct the radiance. This procedure is termed the polarization correction algorithm (PCA) [104]. If the radiance channel polarization sensitivity is $\eta(\lambda)$ (ratio of the spectral pixel's responses to light polarized perpendicular and parallel to the principal plane), then the relative radiance error derived from regular detector signals is [81]:

$$\varepsilon_P(\lambda) = \frac{\eta(\lambda)-1}{\eta(\lambda)+1}\left[P_{\text{true}}(\lambda) - P_{\text{PCA}}(\lambda)\right], \tag{5.31}$$

where $P_{\text{true}}(\lambda)$ is the real degree of linear polarization, and $P_{\text{PCA}}(\lambda)$ is the value from the PCA. With a limited set of available points for its determination, $P_{\text{PCA}}(\lambda)$ for GOME may be considerably in error from the true value. Efforts have been made to improve the PCA for GOME by incorporating information from a vector RT model and by using an improved interpolation scheme [21, 22].

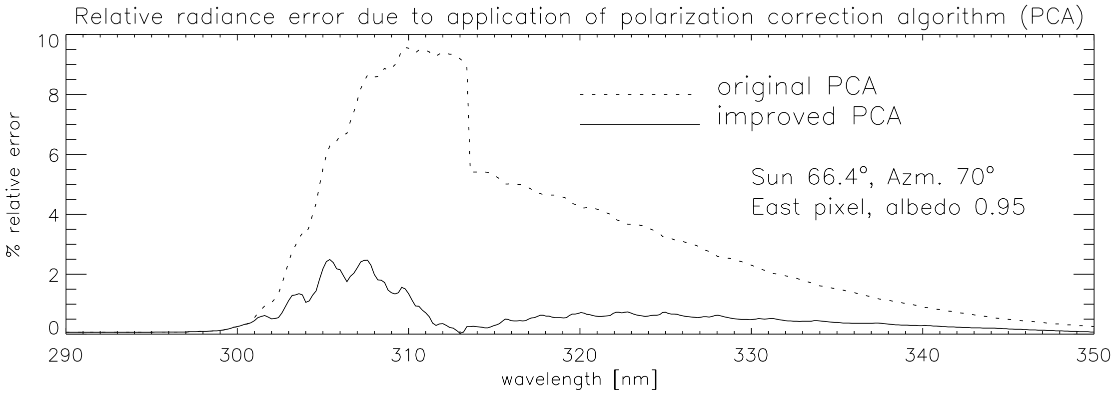

Figure 5.10: Relative radiance error on GOME measurements due to incorrect polarization correction, for East pixel with SZA 66.42°, Azimuth 70° and albedo 0.95.

To simulate the effect of this polarization correction, one can use high resolution calculations from the DAK (KNMI doubling-adding) vector RT model [105, 106, 107] and convolve them using the polarization responses and slit functions for the array detectors and PMD devices in GOME. The PCA is then applied to the simulated GOME data, and the corrected intensity compared with the full RT calculation [21, 22]. The dotted line in Figure 5.10 displays the error ε_P arising from an application of the PCA algorithm as currently used in the GOME operational data processor. $P_{\text{true}}(\lambda)$ has its strongest dependence on wavelength over the region 300-310 nm and the PCA error grows rapidly for measurements in this range. The jump at $\sim$313 nm corresponds to the change from GOME band 1b to GOME band 2; the two 1024-pixel array detectors have different polarization sensitivity response curves $\eta(\lambda)$. Results using the improved PCA algorithm are shown also in Figure 5.10; the general level of error is now below 2%. GOME-2 is much better equipped to deal with polarization correction; it has some 15 PMDs, several of which will cover relatively narrow bands in the critical 300-325 nm region. The GOME-2 PMDs are also serial read-out detectors, and will be capable of measuring light in two polarization directions [6].

pressure	Improved PCA	Original PCA
836.660	111.089	-94.502
591.608	19.221	-42.753
387.298	20.614	179.527
244.949	39.160	377.976
173.205	24.364	123.409
136.931	-0.713	-1.123
111.803	-14.604	-34.264
92.195	-20.025	-41.624
77.136	-21.512	-40.507
59.161	-16.895	-28.585
46.368	-11.327	-15.224

Table 5.2: Optimal estimate differences (%) induced by polarization correction algorithm errors on GOME measurements for the scenario in Figure 5.10. Values are shown for the improved and original PCAs.

For the profile algorithm which requires measurements straddling both the GOME 1b and 2 bands, the original PCA-induced error is a major source of uncertainty. We treat the error spectra in Figure 5.10 as the relative differences between measured and calculated radiances. We again linearize the forward model $\vec{y}_0 = F(\vec{x}_0)$ about the reference state $\vec{x}_0$, and for the difference radiance vector, we write $\Delta\vec{y} = F(\vec{x}_0)\varepsilon_P$. We compute the optimal estimate difference $\Delta\vec{x}_{\mathrm{OE}}$ for this linear inversion step. Table 5.2 compares values of these differences for the first 11 partial columns, for the original and improved PCA applications (results for higher columns do not differ greatly and are generally below 7%). Errors induced by the original PCA are clearly out of bounds. Even though the improved PCA reduces the measurement error by a factor of 5, there is still a substantial uncertainty in the profile estimate (second column); the lowest column still has an unacceptable error. This is admittedly an extreme case (snow surface), but it serves to illustrate the importance of accurate radiometric calibration on GOME measurements if they are to be used in the ozone profile retrieval problem.

We look at some results for the improved PCA in more detail in Figure 5.11. On the left are relative changes in the mid-stratospheric profile elements (down to 20 mbar), for a number of choices of upper wavelength limit in the inversion. Corresponding results for the tropospheric and lower stratospheric elements (20-1000 mbar) are shown at right. The upper wavelength limits were 330, 325, 323 and 320 nm. In general the stratospheric ozone profile accuracy is not greatly affected (4% level or less), though the inclusion of longer wavelength measurements tends to move the error levels around (λ_{upper} = 330 nm). However, lower stratospheric and tropospheric elements show wide variations in error, and it is only with the inclusion of measurements with some surface penetration that the overall accuracy in the lowest column reaches acceptable levels. Even though from Figure 5.10 the PCA error is at the 1% level or less beyond 313 nm, the presence of larger PCA errors between 300 and 313 nm is sufficient to maintain a profile uncertainty at the 20% level for the lower atmosphere. In general we can say that mid-stratospheric profile elements are not badly affected, but there are grave concerns that the accuracy of lower stratospheric and tropospheric profile elements is seriously compromised by this source of measurement error. We remark further on this in Section 5.7.

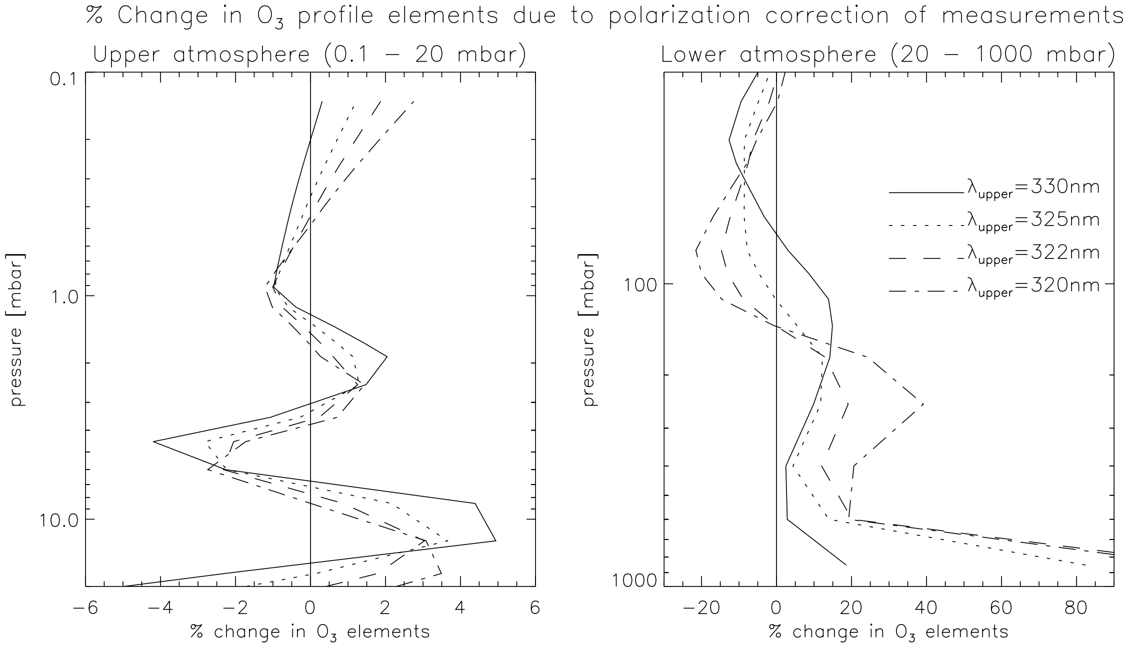

Figure 5.11: Effect on O_3 profile accuracy due to polarization correction algorithm applied to the measurements. Error spectrum from Figure 5.10. (Left) Errors on upper atmosphere profile elements for 4 upper wavelength limits as indicated; (right) corresponding errors on tropospheric and lower stratospheric elements (20-1000 mbar).

5.6.4. Model parameter errors

Temperature profile errors

We carry out a single inversion step, linearizing about the reference state defined earlier. The solar zenith angle is 30°, with albedo 0.5; this is a scenario with high temperature sensitivity. We assume first that errors on the temperature profile $\vec{b}$ are uncorrelated and the same at all levels. If the change in temperature is ΔT at all levels, then the error covariance S_b (assuming Gaussian statistics) is simply $(\Delta T)^2$ times the identity matrix. We choose 4 values for ΔT: 1 K, 2 K, 5 K and 10 K. From (5.14), we compute the corresponding solution error covariance matrix S_B using contribution functions and temperature profile weighting functions K_b. Expected values of the changes in ozone partial columns are simply the square roots of the diagonal elements of S_B.

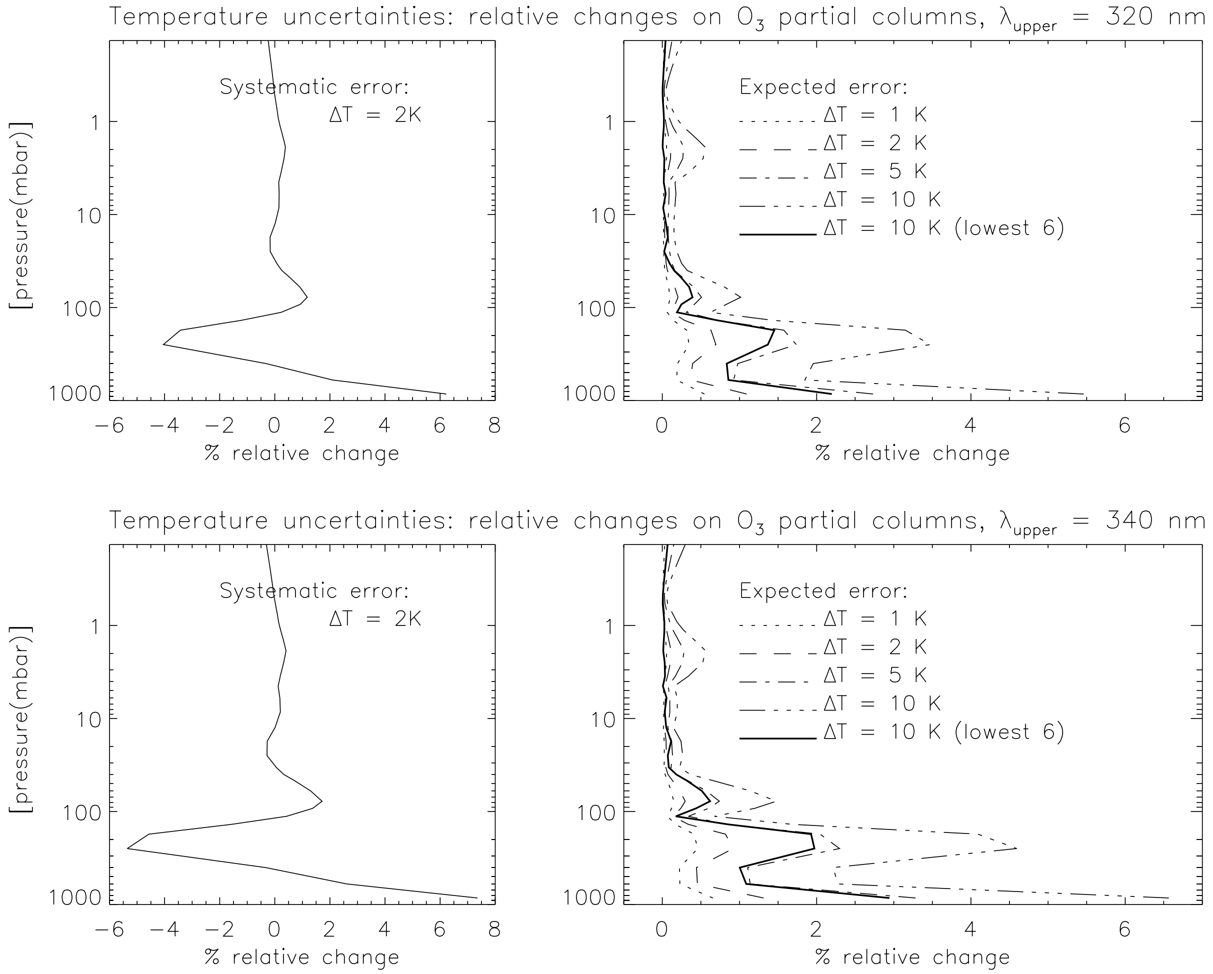

Figure 5.12: Effect of temperature profile model parameter errors on O_3 profile accuracy, for a scenario with SZA 30° and albedo 0.5. (Upper panels) Systematic and expected relative changes in ozone amounts for upper wavelength 320 nm; (lower panels) results for λ_{upper} = 340 nm.

These are plotted for the above four values of ΔT in the two right-hand panels of Figure 5.12 corresponding to the two choices of upper wavelength limit (λ_{upper} = 320 nm and 340 nm). The systematic change from an assumed true O_3 profile is plotted for ΔT = 2 K in the left panels; this is computed from (5.13). [Values for other temperatures scale linearly]. A further test was done by assuming an error $\Delta T = 10$ K for the lowest six partial columns in the troposphere and assuming no errors for the remaining (stratospheric) columns; results for this case are also plotted in Figure 5.12.

There are several interesting associations. First, we note that results for the larger window are not a great deal worse that those for $\lambda_{upper} = 320$ nm. Secondly, it is clear that the stratospheric part of the retrieval is not so sensitive to temperature uncertainty; for $\Delta T = 2$ K, both systematic and expected errors are at the 1% level or below for columns above 100 mbar. Thirdly, that accurate knowledge of stratospheric temperatures considerably reduces the expected ozone profile uncertainty in the lower atmosphere; this we deduce from the $\Delta\vec{x}$ profile determined using temperature uncertainty in just the lowest 6 tropospheric columns. Fourthly, the magnitudes of the $\Delta\vec{x}$ components mirror the swings in the *a priori* covariance values in the troposphere.

We can probe deeper into this source of uncertainty by analyzing the posterior error covariance matrix S_P. In the presence of model parameter errors, this is the sum of three terms S_M, S_S and S_B corresponding to the retrieval noise (measurement error), the smoothing error and the model parameter error respectively. In operational retrieval algorithms for ozone profiles, it is customary to output standard deviations for the optimal estimate error (square roots of the diagonal entries of S_P). Although this is useful for interpretation, a more sophisticated analysis of the error covariance may be carried out by looking at *error patterns* that emerge from an eigenvalue analysis of S_P [1]. Here we restrict ourselves to an analysis of the variance contributions to this matrix.

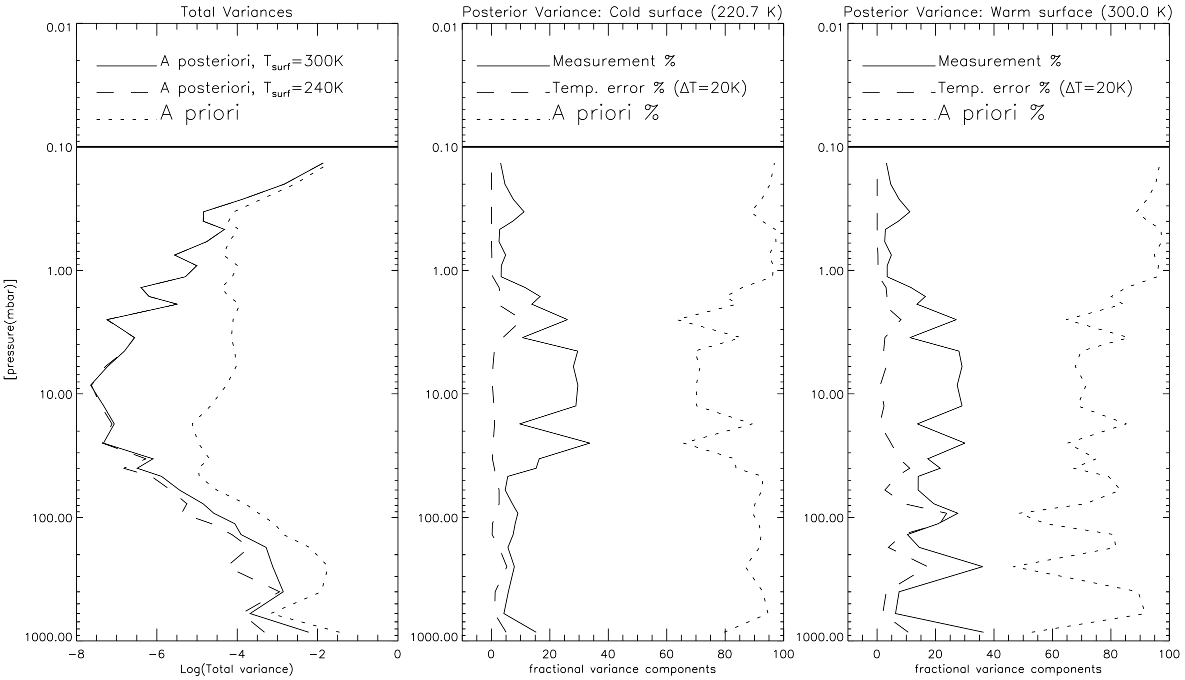

Figure 5.13: Variance contributions to the posterior ozone profile covariance matrix for two temperature scenarios. (Left) Total posterior variances and *a priori* variances; (center) variance breakdown for the cold tropospheric regime; (right) variance breakdown for the warm troposphere. SZA 30° and albedo 0.5. $\lambda_{upper} = 340$ nm.

In Figure 5.13 we examine the variance contributions for the contributing matrices S_M, S_S and

S_B. Two temperature regimes are used for the troposphere. In the left panel, we plot total posterior variances for the optimal estimate for a warm ($T_{surface}$ = 300 K) and cold ($T_{surface}$ = 240 K) tropospheric regimes; the *a priori* variance is shown for reference. In the center and right panels of this figure, the variance percentages are shown for the two tropospheric regimes. An error level of 20 K in the temperature was assumed to hold for the whole atmosphere. Results for the cold troposphere show that total variance is dominated by the *a priori* term above 1 mbar and below about 50 mbar; there is little information from the measurements in these regions. The warm troposphere variance distributions clearly show the information gain in the troposphere from the measurement. The large bulge in the low troposphere still follows the *a priori*. Of especial interest in this last panel are the magnitudes of the model parameter variances $\mathrm{var}_i(S_B)$; they are nearly equal to the measurement variances at 100 mbar and generally comparable at other points in the troposphere. It is not acceptable when the gain in measurement precision of the ozone profile elements is counter-balanced by equally large temperature-induced uncertainties.

The temperature should be known to a certain level of accuracy in order to obtain precision estimates that exceed temperature-induced standard deviations by an acceptable degree. We may investigate this by examining the ratios of two standard deviations:

$$Q_i^{(1)} = \sqrt{\frac{var(S_B)_i}{var(S_M)_i}} \quad \text{and} \quad Q_i^{(2)} = \sqrt{\frac{var(S_B)_i}{var(S_P)_i}}. \tag{5.32}$$

Loosely speaking, $Q^{(1)}$ compares temperature-induced errors with measurement precision, and $Q^{(2)}$ compares temperature-induced errors with the accuracy of the retrieval. We take a warm troposphere with surface temperature 300 K, with a fitting window extending to 340 nm; calculations were done for the East pixel geometry and albedo values used in Figure 5.13. We consider four regimes of temperature uncertainty: (R1) T-errors for the whole atmosphere (34 elements); (R2) T-errors only in the stratosphere (profile elements 10 to 25); (R3) T-errors only in the troposphere (profile values 1 to 9); (R4) T-errors only in the planetary boundary layer (profile element 1). For a given level of error ΔT we compute the maximum values of $Q^{(1)}$ and $Q^{(2)}$ for the atmosphere. Since we are using diagonal matrices for S_b, we can determine the magnitude of ΔT that will give rise to a certain threshold value for $\max(Q^{(1)})$ and $\max(Q^{(2)})$.

Table 5.3 summarizes these temperature accuracy levels for various maximum values of the ratios threshold values (5.32) from 1% to 50%. The results were obtained with *a priori* for the reference state. The table indicates the importance of having accurate stratospheric temperatures (column 2). Assuming no errors in the stratosphere, then the tropospheric temperature error thresholds are less severe (column 3). The first column is indicative of the whole atmosphere. For example, taking a 10% level for temperature-induced errors compared with the total profile accuracy, then we require temperature errors ΔT to be less than 3.6 K everywhere in the atmosphere. In Table 5.4 the values correspond to *a priori* with covariance S_a scaled up by a factor of 5. (This loosens the regularization but preserves the correlation statistics of the prior knowledge). In the second table, the accuracy levels are slightly tighter; with an improved fit, there is less scope for temperature uncertainty if the overall level of profile accuracy is to be maintained. Thus the whole-atmosphere results require temperature to be known to better that 3.1 K if the temperature-induced error is to be less than 10% of the accuracy as a whole.

These are stringent requirements on the temperature accuracy; they become more stringent as the *a priori* constraint is relaxed. From this table we conclude that it is of the utmost importance that the temperature profile be known accurately in this sort of retrieval. We have noted already that temperature weighting functions in a hydrostatic atmosphere are obtained by simple scaling of the

Temperature error thresholds (K), prior covariance S_a				
	Regime 1	Regime 2	Regime 3	Regime 4
$\max(Q^{(1)})$				
1%	0.197	0.253	0.398	0.990
2%	0.394	0.505	0.795	1.981
5%	0.985	1.264	1.989	4.952
10%	1.971	2.527	3.977	9.903
20%	3.942	5.054	7.954	19.806
50%	9.855	12.635	19.886	49.516
$\max(Q^{(2)})$				
1%	0.358	0.439	0.719	1.567
2%	0.716	0.878	1.439	3.134
5%	1.791	2.199	3.601	7.843
10%	3.595	4.414	7.229	15.745
20%	7.302	8.964	14.682	31.977
50%	20.652	25.355	41.528	90.446

Table 5.3: Temperature thresholds ΔT (in K) required to achieve levels of precision and accuracy indicated in the left columns. Four regimes are: (1) T-errors in the whole atmosphere; (2) T-errors in stratosphere; (3) T errors in troposphere; (4) T-errors only for the bottom layer.

Temperature error thresholds (K), prior covariance 5.S_a				
	Regime 1	Regime 2	Regime 3	Regime 4
1%	0.190	0.252	0.391	1.099
2%	0.381	0.504	0.782	2.197
5%	0.952	1.259	1.954	5.493
10%	1.903	2.518	3.909	10.987
20%	3.806	5.036	7.817	21.974
50%	9.516	12.590	19.544	54.934
$\max(Q^{(2)})$				
1%	0.309	0.386	0.628	1.978
2%	0.618	0.773	1.257	3.956
5%	1.546	1.935	3.146	9.900
10%	3.105	3.884	6.316	19.874
20%	6.305	7.889	12.829	40.364
50%	17.834	22.313	36.285	114.168

Table 5.4: Same as Table 5.3, but with *a priori* covariance 5S_a.

ozone profile Jacobians; thus the computation of S_B requires little extra effort. This requires the input temperature data supplied to the retrieval to be specified with error statistics S_b. If this is the case, then it is possible to include the temperature-induced standard deviations $\sqrt{var(S_B)_i}$ in the product diagnostics, along with the usual accuracy estimate $\sqrt{var(S_P)_i}$; the additional computational effort is minimal.

Aerosol optical thickness profile

The analysis is similar to that for the temperature. We confine our attention to the smaller window ending at 320 nm, using a solar zenith angle of 30° and an albedo of 0.5. We assume that errors on the aerosol optical thickness profile τ_{aer} are uncorrelated and the same at all levels where they exist. We take values of $\Delta\tau_{aer}/\tau_{aer}$ at 2%, 5%, 10%, 25% and 50%. Again from (5.14), we compute the corresponding solution error covariance matrix, this time using aerosol optical depth weighting functions for K_b. From (5.13) we get the systematic error. Expected values of the changes in ozone partial columns are plotted in Figure 5.14 (top right); the systematic relative profile differences for a 10% aerosol optical depth change are plotted in Figure 5.14 (top left). More tests were done with aerosol errors assumed only for the lowest 6 and lowest 2 levels of the troposphere (lower panels in Figure 5.14). Stratospheric O_3 profiles are not sensitive to aerosol uncertainties. All the results in Figure 5.14 show that the lowest partial column element is highly sensitive to uncertainties in the aerosol optical thickness of the planetary boundary layer. The expected change in this column grows very rapidly for aerosol optical thickness uncertainties above 20%. Without prior knowledge of the lower atmosphere aerosol, this is a major source of error for the lower tropospheric column.

The analysis of standard deviation used above for characterizing temperature-induced error contributions may be extended to the case of aerosols. We again compare ratios of standard deviations for various levels of aerosol optical thickness error. We use the four regimes as noted in the previous section. The calculations are similar, only we now tabulate the level of aerosol optical thickness uncertainty $\Delta\tau_{aer}$ as a percentage (instead of the magnitude ΔT of the temperature error); thus in Table 5.5 the aerosol optical thickness at all levels should be known to better than 1.5% if the model parameter standard deviation is to be within 5% of the accuracy at all levels in the atmosphere. Looking at stratospheric aerosol errors alone (column 2), there is much more latitude, with a profile error of 18% producing less than 2% standard deviation when compared to the overall result.

As with the temperature, these requirements are very stringent, and apart from the stratospheric part, it is impossible in practice to achieve these levels of aerosol accuracy. In any case there is a major difficulty in establishing statistics for the assumed profile of aerosol optical thickness values. With the smooth spectral signature of aerosols in the UV, the backscatter spectrum is not likely to yield more than one piece of information on aerosols. We can either fit the total atmospheric aerosol optical thickness (AOT) or the thickness of the planetary boundary layer (PBL) aerosol. The scattering contribution of this layer of aerosol is hard to distinguish from the reflected surface term, and it may be better to dispense with assumptions about PBL aerosol and subsume it in the albedo retrieval (the albedo is then regarded as an effective quantity). Thus, though it is possible to include this source of model parameter error in the solution covariance, we recommend including the tropospheric aerosol column as an additional parameter in the retrieval.

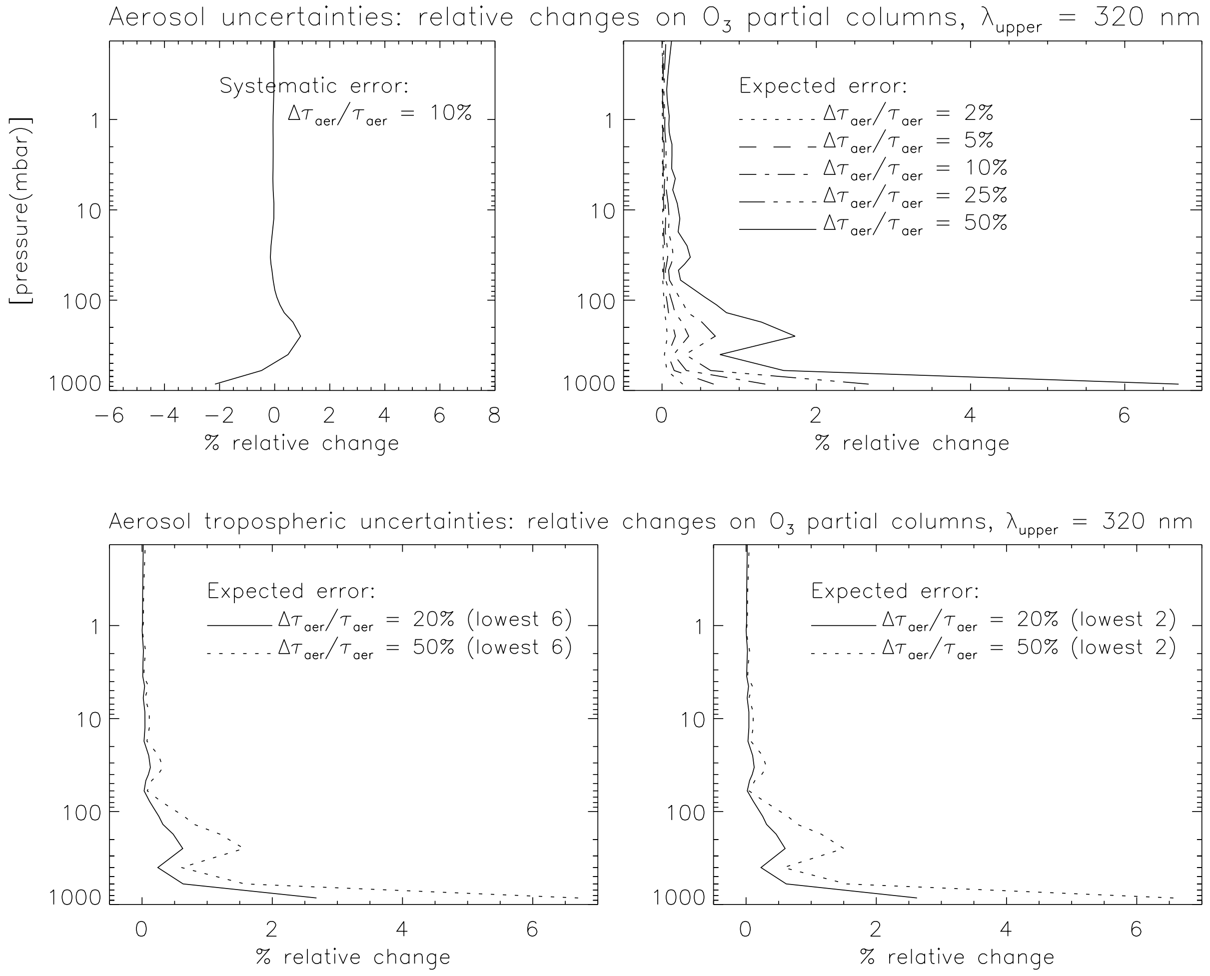

Aerosol uncertainties: relative changes on O_3 partial columns, λ_{upper} = 320 nm

Aerosol tropospheric uncertainties: relative changes on O_3 partial columns, λ_{upper} = 320 nm

Figure 5.14: Effect of aerosol profile model parameter errors on O_3 profile accuracy, for a scenario with SZA 30° and albedo 0.5, upper wavelength 320 nm. (Upper panels) Systematic and expected relative changes in ozone amounts due to relative layer aerosol optical thickness changes at all levels as indicated; (lower panels) results for aerosol uncertainties in the lower atmosphere only.
]

Aerosol optical thickness error thresholds (%)				
	Regime 1	Regime 2	Regime 3	Regime 4
$\max(Q^{(1)})$				
1%	0.192	4.663	0.315	0.242
2%	0.384	9.326	0.630	0.484
5%	0.960	23.315	1.575	1.211
10%	1.920	46.629	3.151	2.422
20%	3.841	93.258	6.301	4.845
50%	9.601	233.146	15.753	12.112
$\max(Q^{(2)})$				
1%	0.301	9.455	0.494	0.380
2%	0.602	18.913	0.987	0.759
5%	1.506	47.333	2.471	1.900
10%	3.023	95.024	4.961	3.814
20%	6.141	192.995	10.075	7.746
50%	17.368	545.873	28.496	21.910

Table 5.5: Aerosol optical thickness error thresholds (in %) required to achieve levels of precision and accuracy indicated in the left columns. Regimes 1-4 as for Table 5.3. *A priori* covariance S_a from climatology.

5.7. Concluding remarks

In this paper we have investigated a number of sensitivity and error issues for the GOME-2 ozone profile retrieval algorithm. The DFS and Information Content diagnostics were used to investigate temperature sensitivity and limits on the fitting window. The DFS shows a significant (~10%) increase from cold to warm tropospheric temperature regimes, with a corresponding increase in the precision of the ozone profile elements in the troposphere. The Information Content is less sensitive to temperature. DFS increase is still significant even for an instrument such as OMI with coarser resolution. Most of the temperature-sensitive DFS increase is related to measurements in the range 316-322 nm; DFS remains rather flat for upper wavelength limits beyond 322 nm.

Systematic errors on the profile elements due to the forward model assumption of 4 discrete ordinate streams are restricted to the 2% level provided the upper window limit is restricted to 320 nm. Inclusion of measurements out to 340 nm worsens these errors to an unacceptable degree. Forward model errors due to the neglect of polarization in the RT model are larger, and the corresponding profile error is at the 10% level for a window limit of 320 nm, though there appear to be scenarios for which this limit is exceeded. Measurement calibration errors due to the correction of polarization are shown to be a major source of uncertainty for profile elements in the lower stratosphere and troposphere. We remark in passing that other sources of measurement calibration error have been identified for ozone profile retrieval [95], but the polarization sensitivity is still paramount.

Model parameter errors from temperature profile uncertainty were also investigated. Fairly stringent limits should be set on the temperature profile error in order to maintain an acceptable level of ozone profile accuracy ($\Delta T \sim 3.5$ K at the 10% level, for example). This source of error can be included in the covariance matrix of the optimal estimate with little extra effort. Model parameter errors due to aerosol optical thickness profile uncertainty generate large sources of error in the ozone profile, most notably for tropospheric aerosol uncertainty. Limits on aerosol profile uncertainty are too stringent to be useful in an overall assessment of ozone profile accuracy; it is better to regard the tropospheric aerosol optical depth as an additional parameter to be included in the retrieval state vector.

There are a number of consequences for the operational implementation of this algorithm. Many of the results in this work have shown that it is inadvisable to include measurements beyond a certain limit of about 320-322 nm; beyond this limit, increased ozone profile precision is very limited (flat DFS) and any advantage to be gained is easily offset by increasingly large forward model errors as one goes out to 340 nm. We therefore recommend that the upper wavelength limit be set somewhere in the 319-322 nm range. A more precise value will be found by further examination of the forward model polarization error which is the critical factor. We further recommend that the input temperature profiles provided to the operational algorithm should be known to a high level of accuracy, and that these profiles should be accompanied by some error statistics in order that this source of error may be identified in the ozone profile solution covariance. Our recommendation is to use ECMWF temperature profiles.

Much work still needs to be done to properly characterize error and sensitivity for this algorithm. The most serious concern is the polarization-induced error in the profile, both from the forward model point of view, and from the measurement error induced by the polarization correction algorithm. In the next paper we will introduce a version of this retrieval that contains an explicit linearized *vector* RT model. This is the only way to eliminate the forward model error implicit in a scalar radiative transfer treatment. In addition, such a model would permit the retrieval to be done with a combined set of regular GOME-2 serial readout spectral measurements and coincident PMD measurements, thus avoiding calibration errors due to the correction of polarization.

Acknowledgments

R.V.O. was supported by The Netherlands Remote Sensing Board (BCRS) under the project *DORAS* 4.1/AP-05. R.J.D.S. was funded from an ozone SAF Visiting Scientist Grant (P-4799-2-01) at KNMI (Royal Dutch Meteorological Institute). Special thanks to Nick Schutgens for providing the polarization data in Section 5.6.3. The authors would like to thank Piet Stammes, Ronald van der A, Johan de Haan and Henk Eskes for stimulating discussions on this work.

Chapter 6

Summary and outlook

6.1. Summary of the thesis

The main focus of this study has been on the development of a discrete ordinate radiative transfer model that will simultaneously generate radiances and weighting function fields as required in iterative multi-parameter atmospheric retrieval problems. The main application in this study has been the use of this forward model for the investigation and optimization of prototype algorithms for ozone profile retrieval from nadir viewing remote sensing instruments.

Although there are many accurate radiative transfer models that compute radiances in a multilayer multiply scattering atmosphere, less attention has been paid to the computation of weighting functions (derivatives of the radiance field with respect to atmospheric parameters to be considered in a retrieval algorithm). Most such retrieval algorithms are iterative, based on a sequence of linear inversion steps. Weighting functions represent the linearization of the forward model used in the retrieval process. In the Introduction (Chapter 1) and in the introductory sections to the main thesis chapters, weighting functions are shown to be of crucial importance for such algorithms. Traditional methods to compute radiance derivatives have relied on time-consuming finite difference estimates; this technique requires repeated calls to radiative transfer models that are only able to return radiance output. The need for a radiative transfer forward model that will make simultaneous and accurate computations of both radiances and weighting functions provides the main motivation behind this study.

The discrete ordinate method for solving radiative transfer equations was first developed by Chandrasekhar in the 1940s. The method is based on a Fourier cosine series decomposition for the azimuth dependence of the radiance field, together with the use of Gauss-Legendre quadratures (the eponymous “discrete ordinates”) to evaluate multiple scatter integrals over the polar direction. The discrete ordinate method is a scattering formalism that requires only as input the specification of (i) a vertical optical depth grid, (ii) layer single scattering albedos and (iii) phase function expansion moments; the user will determine these quantities from detailed physical knowledge of the atmospheric constituent distributions particular to the application for which the discrete ordinate RT model is being used. The DISORT radiance model based on this method is the most widely used numerical package available to the atmospheric physics community. Given the motivation behind this study, the aim was first to extend discrete ordinate theory to develop an analytic formulation of weighting functions, and secondly to develop a general purpose discrete ordinate radiative transfer package with the simultaneous capability for radiance and weighting function output.

The first development is reported in Chapter 2. The investigation here is restricted to the upwelling radiation field at the top of an atmosphere treated as a plane-parallel medium. The discrete ordinate radiance solution is broken down into its component parts: (1) homogeneous solutions to the RTE in the absence of source terms, determined by means of eigensolution methods; (2) particular solutions due to the presence of external light sources (solar beam, thermal emission); (3) boundary conditions at the top and bottom of the atmosphere and continuity at intermediate layer boundaries; and (4) the post-processing source function integration step for the derivation of TOA output in arbitrary polar directions away from the quadrature streams. The analysis is carried out for both the thermal emission source and for the solar beam source in a plane-parallel medium. A general bidirectional reflecting surface boundary condition is used.

A perturbation analysis is used to carry out the linearization for weighting functions. The starting points for this analysis are perturbations of the input optical properties that control the discrete ordinate solution (here, the single scattering albedos and the layer optical thickness values); these quantities establish the perturbation rules. First-order perturbation analysis is then carried out for each of the above four stages in the RTE problem; it is shown how perturbations of the input properties translate explicitly into perturbations for the homogeneous and particular discrete ordinate solutions and subsequently to perturbations of the integration constants that result from the boundary conditions. Weighting functions at arbitrary polar direction are determined by perturbing the source function integration used in the post-processing function. Albedo weighting functions are also derived by perturbing albedo-dependent contributions to the discrete ordinate field. A hypothetical 5-layer atmosphere is constructed in order to carry out the first validation of weighting functions. This is done using a finite difference estimate with a very small finite difference step. A further example is taken from a more realistic terrestrial atmosphere in the UV and visible; weighting functions for ozone volume mixing ratios and temperatures are calculated for a number of wavelengths in the Hartley-Huggins absorption bands. Output is compared with results from another model. It is also shown that a perturbation analysis can be carried out on the original full-space quadrature solution developed by Chandrasekhar for the multiple scattering discrete ordinate solution in a given layer. LIDORT Version 1.1 was the outcome of this work.

The development of weighting functions is carried several steps further in Chapter 3. The emphasis is changed from perturbation analysis to a direct differentiation of the various components of the discrete ordinate solution; the approaches are equivalent owing to the linearity of the discrete ordinate differential equations. We introduce the linearization operator for the discrete ordinate solution. Starting points for the linearization are now the derivatives of the input optical properties (single scattering albedo and optical depth) with respect to the atmospheric parameters for which weighting functions are desired. The linearization proceeds by chain-rule differentiation of each part of the discrete ordinate solution, starting with homogeneous solutions, working through the particular solutions, the direct linearization of the boundary value problem (which determines derivatives of the integration constants), and finally the derivatives of the post-processing step. As with the perturbation analysis adopted in the first paper, the process is entirely analytic, requiring no additional numerical steps. In particular it is not necessary to re-solve the boundary conditions for each weighting function; since the original boundary value problem is linear, the matrix inversion involved in its solution need not be repeated. It is simply a matter of back-substitution for each derivative of the integration constants.

The main extension in Chapter 3 is to the pseudo-spherical approximation, wherein the direct solar beam attenuation is calculated for a curved atmosphere, with all scattering processes treated for a plane-parallel medium. This approximation is good for solar zenith angles up to 90° provided the line-of-sight is not too far from the vertical. The pseudo-spherical treatment is vitally important for the high solar zenith angles encountered in many remote sensing scenarios. A number of parameterizations for the solar beam attenuation are discussed, and their accuracies compared. The simplest such parameterization is the average secant approximation whereby slant path attenuations are exact at the layer boundaries. Since the solar beam attenuation no longer has the simple $\exp[-\tau/\mu_0]$ form used for the plane-parallel case, care must be taken to ensure that cross-layer derivatives are properly accounted for when dealing with the particular solution linearization. It is shown that the particular solution for a pseudo-spherical beam source can be solved by two independent methods; (1) with the original formulation due to Chandrasekhar and (2) with the powerful Green's function method which expresses the particular solution as a linear combination of the homogeneous solutions.

The complete theory is generalized to develop output at arbitrary optical depth and viewing geometry, for both upwelling and downwelling radiation. This extends the range of the model to ground-based atmospheric sounding applications as well as remote sensing from space. A further correction is developed to deal with sphericity effects present in wide-angle off-nadir viewing pertinent to remote sensing instruments such as GOME-2 and OMI (swaths 1920 km and 2600 km respectively). This involves a source function integration along the line of sight; transmittances in the viewing and solar paths are treated in a curved atmosphere so that a precise calculation is made of the single scatter contributions to the upwelling radiance. Multiple scatter contributions are calculated using model output appropriate to local viewing geometries along the line-of-sight view through the atmosphere. A number of examples of radiance and weighting functions are presented for both satellite upwelling and bottom of the atmosphere downwelling simulations. Comparisons are made with plane-parallel output in order to highlight the importance of the pseudo-spherical treatment. An example is given of the limitations of the average secant parameterization to the solar beam attenuation; errors of up to 3.5% are possible for a high-atmosphere optically thick layer at glancing solar incidence. We look also at the effect of neglecting refraction. We look at the effect of the line-of-sight sphericity correction for wide angle viewing; it is shown that radiance errors can be up to 5% for GOME-2 at the swath limits, and up to 8% for OMI. This work culminated in the release of LIDORT Version 2.1.

In Chapter 4 we look at the application of LIDORT to an important retrieval issue for nadir viewing backscatter instruments such as GOME, GOME-2, SCIAMACHY and OMI, namely the retrieval of ozone profiles. We focus in particular on the use of fast and accurate forward models for use in the retrieval. With its ability to calculate simultaneous radiances and analytically-accurate Jacobians, LIDORT is well suited to this problem, and there is a trade-off between forward model accuracy and performance. We are interested in particular in fast 4-stream and 6-stream models; with a low number of streams, analytic results for the homogeneous and particular solutions and their parameter derivatives were obtained without recourse to numerical methods. Additional weighting functions with respect to parameters (such as aerosol asymmetry parameter) that govern the angular distribution of scattering are also noted; the controlling inputs for these quantities are the derivatives of the input layer phase function moments. It is shown that the entire discrete ordinate solution is explicitly differentiable.

Single scatter corrections may be made by considering an accurate form of the phase function, and the single scatter correction in a delta-M scaled atmosphere is implemented, both for radiances (as originally developed by Nakajima and Tanaka [NT]) and in the present work, for analytic weighting functions. With this correction, it is only necessary for the LIDORT model to calculate the multiple scatter contributions to the TOA radiance and weighting function fields. Since the Fourier cosine azimuth series converges more rapidly for these contributions when compared with the total radiance computation, a further time saving becomes apparent. The sphericity correction developed in the previous chapter is investigated further, where it is shown that the LIDORT multiple scatter contributions do not need to be calculated for every viewing condition along the line-of-sight. It is only necessary to make a small number of calls to the model for two or three geometries along this path; straightforward interpolation of these contributions to other viewing conditions does not introduce any significant additional error. This makes for a fast and expeditious computation for the wide angle case. These two corrections enable the complete range of geometries for GOME-2 and OMI to be considered.

4/20 and 6/20 stream comparisons are presented for a wide range of solar and line-of-sight viewing conditions, in the solar and antisolar positions. A wavelength range of 299-335 nm was used for the comparisons. A reference clear sky atmosphere with Rayleigh scattering, background aerosol absorption and scattering and ozone trace gas absorption is used. Special scenarios were constructed by inserting additional layers with heavy particulate loading; this includes a cloud layer in the troposphere for a number of cloud optical thickness values, and three aerosol scenarios (desert dust, volcanic and polluted planetary boundary layer). We look first at the NT correction for a regular pseudo-spherical calculation (no sphericity correction). For the reference atmosphere, the NT-uncorrected 4-stream radiance results are 1.0-1.5% different to NT-uncorrected 20-stream values; the differences vary with viewing and solar geometry. Application of the NT single scatter correction reduces these differences by a factor of 2, but does not remove the geometrical variation. A similar variation is apparent in the uncorrected 6/20 stream differences, but this vanishes with the use of the NT correction; the error is reduced to the 0.2-0.25% level. This error level is much lower than the radiometric calibration error of GOME-2 and related instruments. Single scatter corrections are less noticeable for scenes with high surface albedo and low solar zenith angle; the direct beam reflectance is prominent here. For the special atmospheric scenarios, the same sort of geometry-dependent differences are seen in the uncorrected results. For the cloud scenes, it is shown that the largest differences occur for a cloud of moderate optical thickness; really opaque clouds tend to behave like highly reflecting surfaces. Error limits are tabulated for all the scenarios considered in this Chapter; the largest 6/20 stream NT-corrected differences was 0.65% for the desert dust scenario.

Model comparisons were then computed for off-nadir wide-angle viewing scenarios using the sphericity correction. This correction has the same sign and very similar magnitude for all streams. It was shown that for GOME and SCIAMACHY, the 6-stream uncorrected radiances were generally less than 2% away from the sphericity-corrected values at the maximum swath positions. However for GOME-2, sphericity-corrected radiances were up to 5% different from uncorrected values at extreme swath and high solar zenith angles (85°), and for the OMI instrument, the figure was 8%. Weighting functions computed without the sphericity correction show comparable differences to the corrected values. From the results of Chapter 4, we can establish the magnitude of the forward model error that contributes to the ozone profile accuracy.

In Chapter 5, we investigate the effect of a number of different error sources on the accuracy of the ozone profiles to be retrieved from a prototype operational algorithm for the GOME-2 instrument. We look also at two sensitivity issues, namely the dependence of the retrieval information on temperature distributions in the troposphere, and the information content as a function of the upper wavelength limit of the fitting window. Synthetic measurements are created for a wavelength range 270 to 340 nm. We use the optimal estimation formalism for the retrieval, with a priori information to regularize the fitting. We emphasize in particular the use of singular value decomposition methods in order to establish the information content and the number of degrees of freedom to be obtained from the retrieval. The retrieval state vector comprises a number of partial columns of ozone, with one additional parameter (surface albedo). For a full retrieval, the iteration converges when all state vector elements change between iterations by less than a prescribed small amount, and when the change in the total cost function (chi-square) is less than a prescribed value.

Both GOME and GOME-2 are able to resolve temperature-dependent ozone absorption features in the Huggins bands. Knowledge of the temperature profile is expected to yield additional information on ozone profile elements in the troposphere. We investigate this temperature sensitivity quantitatively for a number of tropospheric temperature regimes and for various scenarios; the increase in DFS is of the order of 10% going from a cold troposphere extreme to a warm troposphere. Absolute values of DFS are scenario dependent and also depend on the degree of regularization; we discuss these issues in the context of averaging kernel matrices. It is seen that there is a reasonable increase in profile precision in the troposphere for the warm temperature regimes. We repeat the retrieval for a selection of windows, each time extending the upper wavelength limit further into the Huggins bands. the information content and degrees of freedom for signal (DFS) are not improved significantly for upper limits beyond about 322 nm, irrespective of the temperature regime in the lower atmosphere.

Using the kind of forward model errors characterized in the previous chapter, we use contribution functions to calculate the systematic error induced on the ozone profile elements. For 4/20 stream forward model error, relative profile errors are generally at the 2% level for an upper wavelength limit of 320 nm, but are unacceptably large for an upper limit of 340 nm. We also look at the neglect of polarization as a source of forward model error; for an upper wavelength limit of 320 nm, corresponding relative profile errors are typically 5-10%. This figure is much larger if more measurements are included in the inversion. Another source of error (this time on the measurements) is due to the polarization correction algorithm (PCA) applied to GOME data as part of the level 0 to 1 calibration. This is seen to be a serious source of error on the profiles, even with an improved PCA that reduces the measurement error by a factor of 5 compared with the current PCA implemented operationally for GOME. Polarization errors are the largest source of uncertainty for the profile retrieval.

We consider model parameter uncertainties in quantities such as temperature and aerosol optical thickness which are not retrieved. Using Gaussian statistics on these error sources, we examine the magnitude of their contributions to the expected profile accuracy and measurement precision. The retrieval is sensitive to temperature profile uncertainty, and stringent requirements on the level of temperature uncertainty are required to ensure that ozone profile accuracies are not affected strongly by this source of error. Aerosol uncertainties (particularly in the troposphere) are shown to generate unacceptable levels of ozone profile error, and it is best include aerosol optical depth as an auxiliary parameter in the retrieval rather than treat it as a model parameter error.

6.2. Main conclusions of this work

The main conclusions from this work are:

(1) that the general pseudo-spherical discrete ordinate solution for radiance at arbitrary direction and optical depth in a multiply-scattering stratified atmosphere is completely differentiable in an analytic fashion; analytically accurate weighting functions can thus be derived for any atmospheric parameter that affects optical depths, single scattering albedos and phase function Legendre moments;

(2) that on the strength of this differentiability, a generic and flexible numerical software package (LIDORT) suitable for a wide range of atmospheric retrieval applications can be developed for the simultaneous and accurate output of both radiances and weighting functions;

(3) that LIDORT can be used effectively as the RT component of the forward model in operational ozone profile retrieval algorithms for nadir-viewing remote sensing backscatter instruments. In conjunction with optimal estimation methods, one can investigate error assessment issues such as forward model error and parameter uncertainties and their effects on the accuracy of the retrieved profile, plus sensitivity issues such as the effect of tropospheric temperature and upper wavelength limits on the information content of the retrieval.

6.3. Outlook and future work

6.3.1. Remote sensing applications for LIDORT

Total columns. Although DOAS-type fitting algorithms for nadir viewing remote sensing applications have yielded good results for trace gas column abundances, there are some unanswered questions, mainly concerning the Air Mass Factor (AMF) conversion from fitted slant columns to vertical amounts. There are problems with the basic logic behind this conversion: how is it possible to retrieve a vertical column when one has to make an assumption about the profile in order to simulate the AMF in order to get a vertical column? In addition, the Lambert-Beer assumption for the whole atmosphere is only really valid for optically thin absorbers; ozone in the Huggins bands does not really fit this category. It is well known that for optically thin species such as NO_2 and HCHO, AMF values are extremely sensitive to abundances of these gases in the planetary boundary layer.

Improved AMF values for HCHO have been calculated, based on profile shape factors provided by a geochemical model in conjunction with LIDORT weighting function output to give so-called scattering weights [108].

In the long run, total column retrieval should really be viewed as an adjunct to a nadir-view profile retrieval algorithm. The retrieved state vector of trace species partial column amounts can be simply summed to get the overall total vertical column; total column weighting functions are the sum of partial column values. For optically thin species with small absorption features close to instrument noise levels, it is usually only possible to extract a single piece of information (the total column) from a suitable fitting window of backscatter measurements; in that case, geochemical models can provide the profile shape factors which can be adjusted as the total column amount is fitted iteratively. For these cases (and also to a certain extent for the total ozone column) what is really required is a stripped-down profile algorithm with full forward model calculations of radiance and weighting functions to be used iteratively in a non-linear fitting scheme. This will at least get the physics right and avoid the assumptions inherent to DOAS-type algorithms. Although DOAS-type retrieval is quick (particularly if one uses look-up tables for the AMFs), computers are now so powerful that the use of “on-the-fly” full RT simulations of radiance and weighting functions is becoming a viable proposition from an operational viewpoint. With a stripped-down profile algorithm based on the LIDORT as the forward model, it is intended to make a theoretical reassessment of the accuracy of trace gas column retrievals from nadir backscatter instruments measuring in the UV and visible.

Profiles. The application of LIDORT to the ozone profile retrieval algorithm has been discussed at length in this thesis. A further application of LIDORT is to be found in the limb backscatter algorithms to be implemented in 2001 for the operational SCIAMACHY data processor. Studies have shown that multiple scattering cannot be ignored in the limb backscatter modeling [38]. This argues against onion-peeling methods; one really needs a global fitting algorithm [59]. One approach adopted for the SOLSE/LORE instruments is to use look-up tables for multiple scatter contributions, and ignore weighting functions for these contributions; the single scatter calculations are done accurately with full ray tracing. The reflected diffuse light contribution from the surface is taken out by using ratios of scan measurements [109]. For SCIAMACHY the approach will be similar: single scattering will be modeled exactly, with multiple scatter contributions computed "on-the-fly" using 4 or 6 stream LIDORT; in this way, a complete set of radiances and weighting functions can be generated for a whole scan sequence making up the global measurement vector. The lower atmosphere below the lowest usable tangent height is treated with a number of homogeneous layers characterized by a small number of “effective” parameters, the principal among which is the assumed surface albedo. For more details see the SCIAMACHY ATBD [110]. A similar approach to limb radiance modeling has been adopted for the ODIN/OSIRIS instrument [111].

Aerosols. LIDORT has the capability to deliver weighting functions not only with respect to the amount or degree of aerosol scattering and attenuation (optical depth single scattering albedo), but also with respect to quantities such as the asymmetry parameter which affect the angular distribution of scattering. There is in theory no limit to the aerosol retrieval applications using LIDORT; this includes the retrieval of microphysical quantities such as size parameters and refractive indices. As was demonstrated in Chapter 4, it is just a matter of determining the derivatives of the LIDORT input parameters (total single scatter albedo, total phase function moments, total extinction or optical thickness) with respect to parameters for which one requires weighting functions. In general though, the retrieval of aerosol properties from GOME and related nadir-viewing instrument is limited because of the smoothness of the spectral signatures. Some success has been reported using a non-linear least squares algorithm with selected GOME radiances from spectral regions free of trace gas signatures [112]. The algorithm only works with clear sky scenes and is sensitive to the assumed surface albedo; the best results have been obtained for Saharan dust outbreaks advected over the subtropical Atlantic ocean. Aerosol Absorbing Index (AAI) algorithms provide an indication of the presence of soot-type aerosols; however it has proved difficult to obtain any reliable estimates of physical aerosol properties from these algorithms [113]. The situation regarding aerosol retrieval with polarized data is much more promising - see the discussion below on vectorized LIDORT.

Coupled ocean-atmosphere studies. The retrieval of chlorophyll concentrations and related ocean properties from space has been the focus of intense interest. Retrieval algorithms to date have used a separate atmospheric simulation to subtract the atmospheric contribution from the surface upwelling radiance; ocean substance amounts are then determined from the water-leaving radiances ([114] and references therein). This procedure is a major source of error for the SeaWiFS data processing [115, 116]. One solution to this problem is to use a coupled ocean-atmosphere RT model to ensure that the physics is correctly modeled. Such a model exists [117, 34] and is currently undergoing further development [118] as a prelude to the use of fitting methods to simultaneously retrieve ocean properties and atmospheric corrections (principally aerosol optical properties in the planetary boundary layer). Using this model, studies on the optical remote sensing of marine constituents have demonstrated the feasibility of this approach [119, 120]. This approach to ocean color retrieval would be greatly facilitated with the use of a linearized RT model capable of delivering weighting function fields for the coupled media.

6.3.2. Vectorized LIDORT model (with polarization)

Until recently, interest in using radiative transfer models with polarization in remote sensing retrieval applications has been limited, partly owing to the complexity and slowness of the vector models, and also in part to the lack of suitable instrumentation. This latter situation is changing; a new generation of space-based instruments such as POLDER [121] have the capability to generate multispectral polarization data. POLDER was flown in space on ADEOS-1 (1996-1997) and a second POLDER device will be on board ADEOS-2 scheduled for launch in 2001.

The GOME polarization correction is critical for the ozone profile retrieval algorithm. Improved polarization correction algorithms have been developed for GOME to remedy the large uncertainty in radiance calibration due to this source [22]. Studies have also shown that the accuracy of the GOME polarization correction is important for retrievals based on spectral fitting in and around the O_2 A band [81]. It is well known that under certain circumstances, the assumption of a scalar model for the backscatter computation of intensities can lead to significant differences with values computed using a vector model [48]. The GOME-2 instrument will deliver a lot of potentially useful polarization data, and a reassessment of the ozone profile algorithm is needed in the light of this new information. This is not just a question of improved polarization corrections; it should be possible to combine measured radiance data in different polarization directions and (with the help of a vectorized version of LIDORT) extract additional information from the optimal estimation retrieval. In this way it might be possible to achieve a higher profile resolution in the troposphere than that currently obtained from GOME measurements.

Polarization data is particularly useful for determining the scattering and microphysical properties of aerosols and clouds. It is well known that the degree of linear polarization for aerosol single scattering events is highly sensitive to microphysical properties such as refractive index and size parameter [122]. A feasibility study for the EOSP instrument has shown the value of polarization measurements in obtaining high degrees of precision for the simultaneous retrieval of aerosol optical thickness and microphysical parameters (effective radius and refractive index) [82]. In recent years, a lot of effort has been devoted to the retrieval of aerosol characteristics from space and ground-based instruments, and some sophisticated retrieval methods have been developed (see for example [123] and [124]). Polarization measurements from POLDER have been used to distinguish aerosol and surface contributions to backscatter [83]. In addition, recent research using POLDER/ADEOS-1 data has demonstrated the potential of multi-angle polarization measurements for the retrieval of aerosol and cloud microphysical properties from space [125, 126, 127]. We note also that the UV polarization measurements of GOME have been used to determine cloud-top presssure [128].

As is the case for scalar models, there are many ways of solving the vector RTE. Following the pioneering work of Dave [129] and Hovenier [130], the mathematical treatment of Mueller scattering matrices has become more sophisticated [131, 132, 133, 47, 134]. Plane-parallel models have been developed using the F-N method [135], a generalized spherical harmonics method [136], the doubling and adding technique [41] and also with discrete ordinate theory [72, 73, 84]. High levels of accuracy are now attainable with these codes [84, 137]. A recent treatment [84] has incorporated the powerful Green's function technique for particular integral determination in vector discrete ordinate theory. A multi-dimensional discrete ordinate code has also been investigated for polarized light [138]. Other solution methods include matrix-operator techniques [139], successive iteration of the auxiliary radiative transfer equation [140, 12], a full spherical treatment based on Gauss-Seidel iteration [141, 142], a backward Monte-Carlo approach [38, 143], and the use of Fourier transform techniques [144].

There are no vector models with a linearization capacity for weighting function calculations; any such weighting functions must be estimated by finite differencing. Most retrieval studies using vector RT models have used phase-space diagrams and look-up tables; iterative techniques often use simplex methods [82]. There is a clear need to develop a vector radiative transfer linearization in order to harness the power and flexibility of fitting techniques such as optimal estimation; this will greatly increase the range and performance of polarization data retrievals. This work is already under way for the LIDORT model. The vector LIDORT model will use the discrete ordinate methodology developed in [84]; linearization will follow the same steps used for the scalar model and described at length in this thesis. The vector model will be generic enough to include output at arbitrary optical depth and viewing geometry, and will include a pseudo-spherical treatment. This last point is particularly important, since many current models are limited to plane-parallel media (one exception is the Dave-Mateer code [140, 12], but this is technically only valid for a Rayleigh atmosphere). The single scatter corrections (sphericity and Nakajima-Tanaka) developed in Chapter 4 for the scalar LIDORT model may be incorporated in the vector version without difficulty.

Chapter 7

Appendices

7.1. Remote-sensing instruments considered in this study

GOME

GOME (Global Ozone Monitoring Experiment) is a nadir-viewing spectrometer on board the ERS-2 satellite launched in April 1995 [5]. The orbit is 100-minute sun-synchronous, with a local equator crossing time of 10.30h. The instrument has some 3584 spectral channels from 240 to 790 nm, with a moderate resolution of 0.2 to 0.4 nm, and a typical footprint size of 320x40 km for a 1.5 second read-out; the maximum swath is 960 km. The detectors are silicon array linear read-out devices. GOME also has a Pt-Ne-Cr lamp for on-board wavelength calibration, and also a diffuser plate for the determination of solar irradiance from space. Besides the four serial read-out detectors, GOME has 3 broad-band (resolution > 100 nm) Polarization Measurement Devices (PMDs) measuring light in a direction parallel to the slit. The PMDs' main purpose is to generate a polarization correction for the level 1 (calibrated and geolocated) radiance spectra [5].

GOME is an atmospheric chemistry instrument, its mission to detect and measure trace gas distributions in the Earth's atmosphere, with particular emphasis on ozone [5, 7]. GOME has been operating successfully for six years. The main operational Level 2 product is the global distribution of total vertical column amounts of ozone; the retrieval algorithm uses the DOAS technique. PMDs are read out 16 times more frequently than the silicon detectors; the sub-pixel resolution allows them to be used in thresholding and RGB filtering algorithms to assign fractional cloud cover for the GOME footprints [89]. Cloud cover and effective cloud-top pressure have also been retrieved from fitting algorithms based on measurements in and around the O_2 *A* band [87, 88]. The detection of soot-type absorbing aerosols has also been carried out with GOME UV data [93], using an "Absorbing Aerosol Index" algorithm similar to that developed for the TOMS instrument [90].

As noted in the thesis, a number of studies have been carried out on the retrieval of ozone profiles from GOME measurements in Channel 1b (282-305 nm) and Channel 2a (305-350 nm). It is now possible to generate ozone profiles on a global scale, and a fast delivery near-real-time algorithm has been developed [95]. Most of these retrievals are based on optimal estimation; many of them rely on a two-stage algorithm. The first step retrieves a stratospheric profile from the large-footprint long-readout Channel 1b data using the BUV method developed for the SBUV instruments [10, 11]; the resulting profile is then used as *a priori* for retrievals at higher spatial resolution using normal-readout channel 2 data. This process is critically dependent on the radiometric accuracy of GOME Level 1 data. This is currently much the largest source of error in the retrieval, with major uncertainties due to the implementation of the polarization correction and also to increasingly large degradation effects in solar irradiance measurements taken by means of the on-board diffuser plate.

GOME-2

GOME-2 is an improved version of the GOME instrument; the mission objectives are similar. The first GOME-2 is scheduled for launch in 2005/2006 on board the first METOP satellite [6]; two further missions with this instrument are planned. Like GOME, GOME-2 has four silicon array detectors covering a similar spectral range with comparable resolution. The instrument has a diffuser plate and in-flight wavelength calibration lamp; there is an additional internal white-light lamp to ensure that the instrument's radiometric calibration accuracy is stable. GOME-2 is much better equipped than GOME to deal with polarization; there are 15 PMDs. These have much narrower band-widths than the GOME devices; several of them are concentrated in the 300-340 nm range where the earthshine polarization signature shows strong non-linear dependence on wavelength. The GOME-2 PMDs are also serial read-out detectors; they will take measurements in two (orthogonal) polarization directions. This should greatly improve the polarization correction for Level 1 radiance data; the expected radiometric calibration error is 1.5-2%. GOME-2 will operate with a wide swath of 1920 km (twice the GOME value), corresponding to a maximum scan angle of $\sim 55.7^\circ$ at the satellite.

A large part of the geophysical level 1 to level 2 data processing will be done at KNMI under the Ozone-SAF program. This includes the DOAS-style retrieval of total column amounts, the installation of an aerosol absorbing index algorithm and the inclusion of a dedicated cloud retrieval algorithm. Of central importance in the SAF program is the development of an ozone profile algorithm with a fast delivery capability. This algorithm will use the LIDORT model developed in this thesis, and the research carried out in Chapters 4 and 5 of this thesis was done for the GOME-2 ozone profile algorithm studies as part of the Ozone-SAF program.

OMI

OMI (Ozone Monitoring Instrument) is a joint Dutch-Finnish contribution to NASA's EOS-CHEM satellite scheduled for launch in 2003 [8]. It has a spectral range limited to UV and visible (270-500 nm), with resolution $\sim$0.45 nm in the two UV channels and $\sim$0.63 nm in the visible. Unlike the other three instruments mentioned above, OMI has CCD-array readout technology, with a "push-broom" mode of operation to provide a greatly enhanced spatial resolution (pixel size 13x24 km for wavelengths greater than 310 nm) in addition to the moderate spectral resolution. The nominal CCD read-out time is 0.4 seconds, with a co-adding factor of 5. OMI uses a scrambler to generate unpolarized light. It has a wide swath of some 2600 km, corresponding to a maximum scan angle of $\sim 57.0^\circ$ at the satellite (height $\sim$705 km). Top priority will be the retrieval of ozone columns and profiles, and OMI will also be able to generate additional trace species distributions and aerosol products. As with GOME-2, sphericity effects will be important in OMI forward model simulations for the wide-angle off-nadir views, and the studies in chapters 4 and 5 apply to both instruments. 4-stream LIDORT will be used in the forward model component of the ozone profile retrieval algorithm for OMI currently under development at KNMI.

SCIAMACHY

The SCIAMACHY (SCanning Imaging Absorption spectroMeter for Atmospheric CHartographY) is an atmospheric chemistry instrument to be launched on board the ENVISAT platform in October 2001 [76]. SCIAMACHY has 8 array detectors, with a spectral range from 240 to 2380 nm. The first 4 detectors cover the range 240-790 nm with similar resolution to that for GOME; indeed, the SCIAMACHY concept actually pre-dates GOME and the latter was envisioned as a smaller version of SCIAMACHY. The two most important infra-red detectors cover ranges 1940-2040 nm and 2265-2380 nm with moderately high spectral resolution (1024 pixels). The nadir swath is 1000 km, encompassing four forward scans of 1 second read-out time (GOME with a 960 km swath has three forward scans each with 1.5 second read-out). SCIAMACHY also has an along-track limb-viewing mode which (under normal operating conditions) will alternate with the nadir scan, the object being to replicate air mass coverage for the two scan modes. There is a second (azimuthal) scan mirror which will allow limb viewing to follow the earth's curvature as the elevation angle changes. SCIAMACHY will be able to take solar occultation measurements for short periods prior to the diffuser-plate solar calibration measurements. SCIAMACHY has an on-board white light lamp for radiometric calibration. There are six broad-band PMDs covering the SCIAMACHY spectral range and designed to correct for the degree of linear polarization; a seventh PMD will provide an additional measurement for the direction of polarization (azimuth scanning only).

In its nadir-view mode in the UV/visible out to 790 nm, SCIAMACHY has similar mission objectives to GOME; in the infra-red, the target species are CO, N_2O and CH_4 (Channel 8), CO_2 and H_2O (channels 6-8), and there will be additional opportunities for aerosol and cloud retrieval. As with GOME, DOAS-type algorithms will be used for the total column retrievals of trace species absorbing in the UV/visible; related fitting algorithms have been developed for the NIR and IR species [145, 146]. The top priority for limb retrieval will be O_3 profiles in the UV; profiles for other trace species will also be considered (NO_2, possibly BrO, and CO, N_2O and CH_4 in the infrared, the latter three being signal-to-noise limited). Limb backscatter measurements in channel 7 (CO_2 absorption around 2000 nm) and in channel 4 (O_2 *A* band) will also be used to retrieve temperature and pressure profiles in the stratosphere. The LIDORT model will be used to simulate multiple-scatter contributions to simulated limb backscatter measurements [110].

7.2. Notes on the numerical model LIDORT Version 2.3

In this appendix we present some notes on the LIDORT software package. This is intended to give a flavor of the scope and structure of the model. More details can be found in the User's Guide, which can be downloaded from the SAO ftp site (ftp cfa-ftp.harvard.edu, cd pub/lidort/v2/). LIDORT is written in FORTRAN 77; all the code uses double precision arithmetic. Version 2.3 of the LIDORT package is separated into two parts: an "intensity-only" model (Version 2.3S) and an "extended" model with the additional weighting function capability (Version 2.3E). Apart from the three highest-level modules, all code in the "S" package is a subset of that used in the "E" package; the extended versions have been constructed around the core of the "S" packages. Version 2.3E has the following features:

1. Pseudo-spherical (average secant) and plane-parallel treatments for an external beam source;
2. Particular integral solution using the classical technique or the Green's function method;
3. Bi-directional reflectance at the lower boundary, including surface thermal emission (isotropic);
4. Intensity output at arbitrary optical depth, for any set of azimuth and elevation angles, for upwelling and/or downwelling directions;
5. Additional options for mean value output (flux, mean intensity) at arbitrary optical depth;
6. Additional options for layer-integrated multiple scatter source terms and their weighting functions;
7. Weighting function output at arbitrary optical depth, for any set of azimuth and elevation angles, for upwelling and/or downwelling directions;
8. Weighting functions with respect to layer atmospheric variables (including phase function quantities) defined by the user, weighting functions for albedo and surface emission.
9. The Nakajima-Tanaka single scatter correction module for both intensities and weighting functions, to be used in conjunction with the delta-M scaling method.

LIDORT package organization

The LIDORT package is organized in six directories orgainzed as follows:

Version V2.3S	Version V2.3E
src_v23s_master	src_v23e_master
src_standard	src_standard
include_s	include_s
	include_e
	src_extension

The two “include” directories contain all the structure files: these contain variable or parameter declarations and a storage facility (in FORTRAN 77, block COMMON statements are used for the latter). The structures in include_s contain variables used to compute the radiance itself; only this directory is required for the intensity-only calculations in V2.3S. The second group of structures contain variables for weighting function calculations; both groups (include_s and include_e) are required for the weighting function applications in V2.3E. The most important structure file is LIDORT.PARS in directory include_s. This contains constants, fixed indices and symbolic dimensioning numbers. All source-code modules in LIDORT include this file; it must also be included in the environment modules that call LIDORT. The dimensioning parameters control the size of the object modules and executables. If there is a requirement for more streams or more atmospheric layers, then the respective dimensioning parameters inside LIDORT.PARS should be changed to ensure that there are no declaration mismatches (dimensioning is checked internally by LIDORT itself). Once this is done the entire code can be compiled and linked according to the installation instructions.

The directory src_v23e_master contains three high-level master modules which control the execution of the extended model (directory src_v23s_master is similar). The three high-level modules are:

LIDORT_V23E_INPUT.

This module carries out an initialization file-read to assign input control variables; it is called directly from a user-defined environment. This is an *optional* module; input variables can be set directly in the user environment without the need for a file-read.

LIDORT_V23E_MASTER.

This is the main module, again called directly from a user-defined environment.

LIDORT_V23E_FOURIER.

This is the master module for calculation of a single Fourier component of the intensity and weighting function output. It is called directly in LIDORT_V23E_MASTER as part of the Fourier loop, but the call will not be present in the user-defined environment.

The directory src_standard contains all core code for the standard version; there are 11 modules in all. We list them with a brief note on function. The first 8 are called in the order in which they appear in the main and/or the Fourier master modules; the remaining 3 are auxiliary modules.

LIDORT_CHECKINPUT.f

Checks all control, model and geophysical inputs for consistency.

LIDORT_DERIVEINPUT.f
: This is an internal assignation of model variables that are not declared explicitly as part of the file-read or in an external environment. Includes tasks like sorting the stream angles input, sorting and assigning masks for the arbitrary optical depth output.

LIDORT_MISCSETUPS.f
: Only called for Fourier component $m = 0$. A number of set-up operations including the Delta-M scaling and the preparation of all optical depth exponentials that can be pre-calculated.

LIDORT_RTSOLUTION.f
: Solution of the discrete ordinate radiative transfer equation. Returns the eigensolutions and separation constants from the homogeneous equation, plus the particular (beam) solution vectors for both the classical solution technique and the Green function method.

LIDORT_BVPROBLEM.f
: Set-up and solution of the boundary-value problem (constants of integration) in a multi-layer atmosphere. This requires the L-U decomposition (matrix inversion).

LIDORT_INTENSITY.f
: Computation of intensities at user-defined optical depths and stream angles; this is the post-processing (source function integration).

LIDORT_MULTIPLIERS.f
: Computation of multipliers required for the layer source terms that form the heart of the source function integration technique.

LIDORT_CONVERGE.f
: Examines convergence of Fourier series for all intensities; upgrades the intensity Fourier series.

LIDORT_WRITEMODULES.f
: Four modules for writing outputs to file. Outputs are: full intensity results, Fourier components of intensity, a scenario description and a summary of the input data.

LIDORT_AUX.f
: Standard numerical routines for eigenproblem solution (ASYMTX as used in DISORT is preferred, though LAPACK software is available), and linear algebra modules (LAPACK band storage and L-U decomposition modules). Legendre polynomial and Gauss quadrature evaluation. Includes an input file-read tool.

LIDORT_INPUTREAD.f
: Sequential read of all standard control and model variables in the initialization file (use optional).

The directory `src_extension` contains all internal modules that are additionally required for the extended version; there are 9 modules in all, and they are all concerned with aspects of weighting function generation. The first 7 are called in the order in which they appear in the main and/or the Fourier master modules; the remaining 2 are auxiliary modules. The naming is chosen so that the tasks executed by these additional modules are equivalent to those tasks defined for the original (intensity-only) modules.

LIDORT_L_CHECKINPUT.f
: Checks additional control and geophysical inputs for consistency.

LIDORT_L_MISCSETUPS.f

Only called for Fourier component $m = 0$. A number of additional set-up operations including the Delta-M scaling for variational inputs and the preparation of all optical depth exponentials that can be pre-calculated.

LIDORT_L_RTSOLUTION.f

Linearization analysis of the discrete ordinate radiative transfer equation. Returns the derivatives of the eigensolutions and separation constants, plus the particular (beam) solution vectors with respect to atmospheric parameter variations.

LIDORT_L_BVSETUPS.f

Column vector set-up for the linearized boundary value problem. The actual matrix back substitution which returns the linearized integration constants is done in LIDORT_V23E_FOURIER.

LIDORT_L_WFCALC.f

Computation of weighting functions at user-defined optical depths and stream angles. This is the post-processing (source function integration) technique; the routine is modeled along the same lines as LIDORT_INTENSITY.

LIDORT_L_MULTIPLIERS.f

Computation of derivatives of the multipliers required for the layer source terms that form the heart of the source function integration technique.

LIDORT_L_FOURIERADD.f

Upgrades the weighting function Fourier series.

LIDORT_L_WRITEMODULES.f

Modules for writing additional (weighting function) outputs to file. Outputs are: full weighting function results, Fourier components, additional scenario descriptions and a summary of supplementary input data.

LIDORT_L_INPUTREAD.f

Read of all extended control variables in the initialization file (optional).

Schematic computational sequence

This "pseudo-code" example deals with a simple wavelength loop calculation. LIDORT names and variables are given in upper case letters. LIDORT execution is controlled by a single module LIDORT_V23E_MASTER for (extended) Version 2.3E, and LIDORT_V23S_MASTER for Version 2.3S (intensity-only). Both these modules must be called from a user-defined environment, once for each wavelength. Note that within the wavelength loop, the call to the master module is preceded by the user-defined preparation module "user_prepare_geophys" which will assign values to *geophysical* input variables in the appropriate structure files (these are called LIDORT_GEOPHYS.VARS and LIDORT_L_GEOPHYS.VARS). In most cases the user must call "user_prepare_geophys" before the LIDORT master module call.

The main call is preceded by a call to LIDORT_V23E_INPUT (extended version). which will read the appropriate input from file (in this case the file is called "LIDORT.INP" and passed as a subroutine argument). File-read errors will be written to an error file name "LIDORT.ERR" (also passed as a subroutine argument). If the STATUS_INPUTREAD integer output is not equal to the index

LIDORT_SUCCESS, the program should stop and the user should examine the error file. A similar output (STATUS_INPUTCHECK) is available for the checking of the input data once the file-read is complete (this checking is internal to LIDORT). Geophysical inputs are also checked internally. After each call to the master module, the STATUS_CALCULATION integer output is examined, and the program stopped if there is a failure. Any errors arising in the master modules will be traced and written to the error file passed as an argument to the module. Note that LIDORT_V23E_INPUT is optional - it is possible for the user to dispense with this kind of input set-up and assignment and simply assign input variables explicitly.

```
main user_lidort

/* Fixed structures
include LIDORT.PARS, LIDORT_L.PARS
/* input structures
include LIDORT_CONTROL.VARS, LIDORT_GEOPHYS.VARS
include LIDORT_MODEL.VARS
include LIDORT_L_CONTROL.VARS, LIDORT_L_GEOPHYS.VARS
/* output structures
include LIDORT_RESULTS.VARS, LIDORT_L_RESULTS.VARS
/* status declarations
INTEGER STATUS_INPUTREAD, STATUS_INPUTCHECK, STATUS_CALCULATION

/* Define output in the way you want!
–> Declare output arrays

/* File-read variables in the input structures
call LIDORT_V23E_INPUT (“LIDORT.INP”,“LIDORT.ERR”,STATUS_INPUTREAD)
if (STATUS_INPUTREAD = LIDORT_SERIOUS) write message and abort

/* Start wavelength loop
for i = 1, n_user_wavelengths, begin
/* Assign variables in LIDORT_GEOPHYS.VARS and LIDORT_L_GEOPHYS.VARS
call user_prepare_geophys
/* LIDORT master call and error check
call LIDORT_V23E_MASTER
(STATUS_INPUTCHECK,STATUS_CALCULATION)
if (STATUS_INPUTCHECK=LIDORT_SERIOUS) error message and abort
if (STATUS_CALCULATION=LIDORT_SERIOUS) error message and abort
copy LIDORT output to user-defined output arrays
/* End wavelength loop
end for

/* finish
write user-defined output arrays
stop and end of program
```

7.3. Abbreviations and Acronyms

The following is a list of acronyms and abbreviations used in this thesis.

AAI	Absorbing Aerosol Index
ADEOS	ADvanced Earth Observing System
AMF	Air Mass Factor
BOA	Bottom Of the Atmosphere
BUV	Backscatter Ultra Violet
CCD	Charge Couple Detectors
DFS	Degrees of Freedom of Signal
DLR	Deutsches Forschungszentrum fuer Luft und Raumfahrt
DOAS	Differential Optical Absorption Spectroscopy
DISORT	DIScrete Ordinate Radiative Transfer
ECMWF	European Center for Medium-range Weather Forecasts
ENVISAT	ENVIronmental SATellite
ERS	Environmental Research Satellite
ESA	European Space Agency
EOS	Earth Observing System
EUMETSAT	EUropean METeorological SATellite
FWHM	Full Width Half Maximum
GOME	Global Ozone Monitoring Experiment
KNMI	Koninklijk Nederlands Meteorologisch Instituut (Royal Netherlands Meteorological Institute)
LIDORT	LInearized Discrete Ordinate Radiative Transfer
MAP	Maximum A Posteriori
METOP	METeorological OPeration
NASA	North American Space Agency
NT	Nakajima-Tanaka
OE	Optimal Estimation
OMI	Ozone Monitoring Instrument
OSIRIS	Optical Spectrograph and InfraRed Imager System
PBL	Planetary Boundary Layer
PCA	Polarization Correction Algorithm
pdf	probability density function
PMD	Polarization Measuring Device
POLDER	POLarization and Directionality of the Earth’s Reflectances
RGB	Red-Green-Blue
RRS	Rotational Raman Scattering
RT	Radiative Transfer
RTE	Radiative Transfer Equation
SAF	Satellite Application Facility
SAO	Smithsonian Astrophysical Observatory
SBUV	Solar Backscatter Ultra Violet
SCIAMACHY	SCanning Imaging Absorption spectroMeter for Atmospheric CHartographY
SeaWiFS	Sea-viewing Wide Field of view Sensor
SSBUV	Shuttle Solar Backscatter Ultra Violet

SZA	Solar Zenith Angle
TOA	Top Of the Atmosphere
TOMS	Total Ozone Mapping Spectrometer
UV	Ultra Violet
VMR	Volume Mixing Ratio

Bibliography

1. C.D. Rodgers. *Inverse methods for atmospheric sounding*. World Scientific Publishing Pte Ltd, New York, 2000.

2. D.W. Marquardt. An algorithm for least squares estimation of nonlinear parameters. *J. Soc. Indust. Appl. Math.*, 2:431–441, 1963.

3. H.W. Engel, M. Hanke, and A. Neubauer. Regularization of inverse problems. In *Mathematics and its applications*, volume 375. Kluwer Academic Publishers, 1996.

4. C.D. Rodgers. Characterization and error analysis of profiles retrieved from remote sounding experiments. *J. Geophys. Res.*, 95:5587, 1990.

5. ESA/ESTEC, Noordwijk, The Netherlands. *GOME Users Manual*, 1998.

6. J. Callies, E. Corpaccioli, M. Eisinger, A. Lefebvre, and A. Hahne. Ozone Monitoring by GOME-2 on the METOP satellites. In *Atmospheric Ozone, Proceedings of the Quadrennial Ozone Symposium*, Sapporo, Japan, 2000.

7. J.P. Burrows, M. Weber, M. Buchwitz, V.V. Rozanov, A. Ladstaetter-Weisenmeyer, A. Richter, R. de Beek, R. Hoogen, K. Bramstadt, K.-U. Eichmann, M. Eisinger, and D. Perner. The Global Ozone Monitoring Experiment (GOME): mission concept and first scientific results. *J. Atmos. Sci*, 56:151–175, 1999.

8. P. Stammes, P. Levelt, J. de Vries, H. Visser, B. Kruizinga, C. Smorenburg, G. Leppelmeier, and E. Hilsenrath. Scientific requirements and optical design of the Ozone Monitoring Instrument on EOS-CHEM. In *SPIE Conference on Earth Observing Systems IV, SPIE Vol. 3750, 221-232*, Denver, USA, 1999.

9. S. Twomey. On the deduction of the vertical distribution of ozone by ultraviolet spectral measurements from a satellite. *J. Geophys. Res.*, 66:2153–2162, 1961.

10. K.F. Klenk, P.K. Bhartia, A.J. Fleig, V.G. Kaveeshwar, R.D. McPeters, and P.M. Smith. Total ozone determination from backscattered (BUV) ultraviolet experiment. *J. Appl. Meteorol.*, 21:1672–1684, 1982.

11. P.K. Bhartia, R.D. McPeters, C.L. Mateer, L.E. Flynn, and C. Wellemeyer. Algorithm for the estimation of vertical ozone profiles from the backscattered ultraviolet technique. *J. Geophys. Res.*, 101:18793–18806, 1996.

12. J.J. DeLuisi and C.L. Mateer. On the application of the optimum statistical inversion technique to the evaluation of umkehr observations. *J. Appl. Meteorol.*, 10:328–324, 1971.

13. K. Chance, J. P. Burrows, D. Perner, and W. Schneider. Satellite measurements of atmospheric ozone profiles, including tropospheric ozone, from UV/visible measurements in the nadir geometry: a potential method to retrieve tropospheric ozone. *J. Quant. Spectrosc. Radiat. Transfer*, 57:467–476, 1997.

14. R. Munro, R. Siddans, W. J. Reburn, and B. J. Kerridge. Direct measurement of tropospheric ozone distributions from space. *Nature*, 392:168–171, 1998.

15. R. Hoogen, V. Rozanov, and J. Burrows. Ozone profiles from GOME satellite data: algorithm description and first validation. *J. Geophys. Res.*, 104:8263–8280, 1999.

16. R.J. van der A, R.F. van Oss, and H. Kelder. Ozone profile retrieval from GOME data. In J.E. Russell, editor, *Remote Sensing of Clouds and the Atmosphere III, Proceedings of SPIE Vol. 3495*, pages 221–229, 1998.

17. J.P.F. Fortuin and H. Kelder. An ozone climatology based on ozonesonde and satellite measurements. *J. Geophys. Res.*, 103:31709–31734, 1999.

18. K. Chance and R.J.D. Spurr. Ring effect studies: Rayleigh scattering, including molecular parameters for rotational Raman scattering, and the Fraunhofer spectrum. *Applied Optics*, 36:5224–5230, 1997.

19. J. Joiner, P.K. Bhartia, R.P. Cebula, E. Hilsenrath, R.D. McPeters, and H. Park. Rotational Raman scattering (Ring effect) in satellite backscatter ultraviolet measurements. *Applied Optics*, 34:4513–4525, 1995.

20. M. Vountas, V.V. Rozanov, and J.P. Burrows. Ring effect: Impact of rotational raman scattering on radiative transfer in earth's atmosphere. *J. Quant. Spectrosc. Radiat. Transfer*, 60:943–961, 1998.

21. N.A.J. Schutgens and P. Stammes. Characterising top-of-atmosphere ultraviolet polarisation from radiative transfer calculations. In *Proceedings of the ERS-ENVISAT Symposium 2000, European Space Agency*, Gothenburg, Sweden, 2000.

22. N.A.J. Schutgens and P. Stammes. Assessment and improvement of the polarisation correction algorithm for GOME. In *Proceedings of the ERS-ENVISAT Symposium 2000, European Space Agency*, Gothenburg, Sweden, 2000.

23. U. Platt. Differential optical absorption spectroscopy (DOAS). In M. Sigrist, editor, *Air monitoring by spectroscopic techniques, Chem. Anal. Ser., 127, 27-84*, 1994.

24. K. Chance. Analysis of BrO measurements from the Global Ozone Monitoring Experiment. *Geophys. Res. Lett.*, 25:3335–3338, 1998.

25. D. Loyola, B. Aberle, W. Balzer, K. Kretschel, E. Mikusch, H. Muehle, T. Ruppert, C. Schmid, S. Slijkhuis, R. Spurr, W. Thomas, T. Wieland, and M. Wolfmueller. Ground Segment for ERS-2 GOME Data Processor. In *3rd Symposium on Space in the Service of our Environment*, Florence, Italy, 1997.

26. K. Chance, P.I. Palmer, R. Spurr, R.V. Martin, T.P. Kurosu, and D.J. Jacob. Satellite observations of formaldehyde over North America from GOME. *Geophys. Res. Lett.*, 27:3461–3464, 2000.

27. W. Thomas, E. Hegels, S. Slijkhuis, R. Spurr, and K. Chance. Detection of trace species in the troposphere using back-scatter spectra obtained by the GOME spectrometer. *Geophys. Res. Lett.*, 25:1317–1320, 1998.
28. A. Richter, F. Wittrock, M. Eisinger, and J.P. Burrows. GOME observations of tropospheric BrO in the northern hemispheric spring and summer 1997. *Geophys. Res. Lett.*, 25:2683–2686, 1998.
29. T. Wagner and U. Platt. Satellite mapping of enhanced BrO concentrations in the troposphere. *Nature*, 395:486–490, 1998.
30. T. Wagner, C. Leue, K. Pfeilsticker, and U. Platt. Monitoring of the stratospheric chlorine activation by GOME OClO measurements in the austral and boreal winters 1995 through 1999. *J. Geophys. Res.*, 106:4971–4986, 2001.
31. M. Eisinger and J.P. Burrows. Tropospheric sulfur dioxide observed by the ERS-2 GOME instrument. *Geophys. Res. Lett.*, 25:4177–4180, 1998.
32. A.N. Maurellis, R. Lang, W.J. van der Zande, I. Aben, and W. Ubachs. Precipitable water column retrieval from GOME data. *Geophys. Res. Lett.*, 27:903–906, 2000.
33. S. Noel, M. Buchwitz, H. Bovensmann, R. Hoogen, and J.P. Burrows. Atmospheric water vapor amounts retrieved from GOME satellite data. *Geophys. Res. Lett.*, 26:1841–1844, 1999.
34. G.E. Thomas and K. Stamnes. *Radiative Transfer in the Atmosphere and Ocean*. Cambridge University Press, 1st edition, 1999.
35. A. Dahlback and K. Stamnes. A new spherical model for computing the radiation field available for photolysis and heating at twilight. *Planet. Space Sci.*, 39:671–683, 1991.
36. W.J. Wiscombe. The delta-M method: rapid yet accurate radiative flux calculations for strongly asymmetric phase functions. *J. Atmos. Sci.*, 34:1408–1422, 1977.
37. T. Nakajima and M. Tanaka. Algorithms for radiative intensity calculations in moderately thick atmospheres using a truncation approximation. *J. Quant. Spectrosc. Radiat. Transfer*, 40:51–69, 1988.
38. L. Oikarinen, E. Sivhola, and E. Kyrola. Multiple scattering radiance in limb viewing geometry. *J. Geophys. Res.*, 104:31261–31275, 1999.
39. B.R. Barkstrom. A finite difference method of solving anisotropic scattering problems. *J. Quant. Spectrosc. Radiat. Transfer*, 16:725–739, 1976.
40. V.V. Rozanov, D. Diebel, R.J.D. Spurr, and J.P. Burrows. GOMETRAN: A radiative transfer model for the satellite project GOME - the plane parallel version. *J. Geophys. Res.*, 102:16683–16695, 1997.
41. J.F. de Haan, P.B. Bosma, and J.W. Hovenier. The adding method for multiple scattering of polarized light. *Astron. Astrophys.*, 183:371–391, 1987.
42. J. Lenoble, editor. *Radiative Transfer in Scattering and Absorbing Atmospheres*. Deepak publishing, Hampton, VA, USA, 1985.

43. V. Rozanov, T. Kurosu, and J. Burrows. Retrieval of atmospheric constituents in the UV/visible: A new quasi-analytical approach for the calculation of weighting functions. *J. Quant. Spectrosc. Radiat. Transfer*, 60:277–299, 1998.

44. A.V. Rozanov, V.V. Rozanov, and J.P. Burrows. Combined differential-integral approach for the radiation field computation in a spherical shell atmosphere: Nonlimb geometry. *J. Geophys. Res.*, 105:22937–22942, 2000.

45. O.P. Hasekamp and J. Landgraf. Ozone profile retrieval from backscattered ultraviolet radiances: The inverse problem solved by regularization. *J. Geophys. Res., in press*, 2001.

46. S. Chandrasekhar. *Radiative Transfer*. Dover Publications Inc., New York, 1960.

47. J.W. Hovenier and C.V.M. van der Mee. Fundamental relationships relevant to the transfer of polarized light in a scattering atmosphere. *Astron. Astrophys.*, 128:1–16, 1983.

48. A.A. Lacis, J. Chowdhary, M.I. Mischenko, and B. Cairns. Modelling errors in diffuse-sky radiation: Vector vs. scalar treatment. *Geophys. Res. Lett.*, 25:135–138, 1998.

49. S. Chandrasekhar. *Selected Papers*, volume 2. University of Chicago Press, New York, 1989.

50. L.B. Barichello, R.D.M. Garcia, and C.E. Siewert. Particular solutions for the discrete-ordinates method. *J. Quant. Spectrosc. Radiat. Transfer*, 64:219–226, 2000.

51. K.N. Liou. Analytic two-stream and four-stream solutions for radiative transfer. *J. Atmos. Sci.*, 31:1473–1475, 1974.

52. K. Stamnes and R. A. Swanson. A new look at the discrete ordinate method for radiative transfer in anisotropically scattering atmospheres. *J. Atmos. Sci.*, 38:387–399, 1981.

53. K. Stamnes and H. Dale. A new look at the discrete ordinate method for radiative transfer in anisotropically scattering atmospheres II: Intensity computations. *J. Atmos. Sci.*, 38:2696, 1981.

54. K. Stamnes. On the computation of angular distributions of radiation in planetary atmospheres. *J. Quant. Spectrosc. Radiat. Transfer*, 28:47, 1982.

55. K. Stamnes. Reflection and transmission by a vertically inhomogeneous planetary atmosphere. *Planet. Space Sci.*, 30:727, 1982.

56. K. Stamnes and P. Conklin. A new multi-layer discrete ordinate approach to radiative transfer in vertically inhomogeneous atmospheres. *J. Quant. Spectrosc. Radiat. Transfer*, 31:273, 1984.

57. K. Stamnes. The theory of multiple scattering of radiation in plane parallel atmospheres. *Rev. Geophys.*, 24:299, 1962.

58. K. Stamnes, S.-C. Tsay, W. Wiscombe, and K. Jayaweera. Numerically stable algorithm for discrete ordinate method radiative transfer in multiple scattering and emitting layered media. *Applied Optics*, 27:2502–2509, 1988.

59. M. Carlotti. Global-fit approach to the analysis of limb-scanning atmospheric measurements. *Applied Optics*, 27:3250–3254, 1988.

60. C.D. Rodgers. Retrieval of atmospheric temperature and composition from remote measurements of thermal radiation. *Rev. Geophys. Space Phys.*, 14:609–624, 1976.

61. W.P. Chu, M. McCormick, J. Lenoble, C. Brogniez, and P. Pruvost. SAGE II inversion algorithm. *J. Geophys. Res.*, 94:8339–8351, 1989.

62. M.A. Berk, L.S. Bernstein, and D. Robertson. MODTRAN: A moderate resolution model for LOWTRAN7. Technical Report GL-TR-89-0122, Geophysics Laboratory, Hanscomb AFB, MA, 1989.

63. J.M. Dlugach and E. G. Yanovitskij. The optical properties of Venus and the Jovian planets. II. Methods and results of calculations of the intensity of radiation diffusely reflected from semi-infinite homogeneous atmospheres. *Icarus*, 22:66–81, 1974.

64. T. Kurosu, V.V. Rozanov, and J.P. Burrows. Parameterization schemes for terrestrial water clouds in the radiative model GOMETRAN. *J. Geophys. Res.*, 102:21809–21823, 1997.

65. E. Anderson, Z. Bai, C. Bischof, J. Demmel, J. Dongarra, J. Du Croz, A. Greenbaum, S. Hammarling, A. McKenney, S. Ostrouchov, and D. Sorensen. *LAPACK User's Guide*. Society for Industrial and Applied Mathematics, Philadelphia, 2nd edition, 1995.

66. C.E. Siewert. A concise and accurate solution to Chandrasekhar's basic problem in radiative transfer. *J. Quant. Spectrosc. Radiat. Transfer*, 64:109–130, 2000.

67. W.H. Press, S. A. Teukolsky, W. T. Vetterling, and B. P. Flannery. *Numerical Recipes in Fortran 77*. Cambridge University Press, 2nd edition, 1992.

68. R.M. Goody and Y.K. Yung. *Atmospheric radiation*. Oxford University Press, 2nd edition, 1989.

69. R. McClatchey, R. W. Fenn, J. E. Selby, F. E. Volz, and J. S. Garing. Environ. res. pap. 411. In *Optical properties of the atmosphere*. Air Force Cambridge Res. Lab., Bedford, Mass., 3rd edition, 1972.

70. A.M. Bass and R.J. Paur. The UV cross-sections of ozone: 1. Measurements in atmospheric ozone. In *Proceedings of the Quadrennial Ozone Symposium*, pages 606–616, Halkidiki, Greece, 1985.

71. E.P. Shettle and R. W. Fenn. Models of the aerosols of the lower atmosphere and the effects of humidity variations on their optical properties. Technical Report AFGL-TR-79-0214, Geophysics Laboratory, Hanscomb AFB, MA 01732, 1979.

72. F.M. Schulz, K. Stamnes, and F. Weng. VDISORT: an improved and generalized discrete ordinate method for polarized (vector) radiative transfer. *J. Quant. Spectrosc. Radiat. Transfer*, 61:105–122, 1999.

73. F.M. Schulz and K. Stamnes. Angular distribution of the Stokes vector in a plane-parallel vertically inhomogeneous medium in the vector discrete ordinate radiative transfer (VDISORT) model. *J. Quant. Spectrosc. Radiat. Transfer*, 65:609–620, 2000.

74. K.N. Liou. A numerical experiment on Chandrasekhar's discrete-ordinate method for radiative transfer: applications to cloudy and hazy atmospheres. *J. Atmos. Sci.*, 30:1303, 1973.

75. R.J.D. Spurr, T.P. Kurosu, and K.V. Chance. A linearized discrete ordinate radiative transfer model for atmospheric remote sensing retrieval. *J. Quant. Spectrosc. Radiat. Transfer*, 68:689–735, 2001.

76. J.P. Burrows, K. Chance, P. Crutzen, H. van Dop, J. Geary, T. Johnson, G. Harris, I Isaksen, G. Moortgat, C. Muller, D. Perner, U. Platt, J.-P. Pommereau, H. Rodhe, E. Roeckner, W. Schneider, P. Simon, H. Sundquist, and J. Vercheval. SCIAMACHY: A European proposal for atmospheric remote sensing from the ESA polar platform. Max- Planck Institut für Chemie, Mainz, Germany, 1988.

77. R. van Oss and R.J.D. Spurr. Ozone profile retrieval using fast 4 and 6 stream linearized radiative transfer models. *unpublished*, 2000.

78. T.R. Caudill, D.E. Flittner, B.M. Herman, O. Torres, and R.D. McPeters. Evaluation of the pseudo-spherical approximation for backscattered ultraviolet radiances and ozone retrieval. *J. Geophys. Res.*, 102:3881–3890, 1997.

79. A. Kylling and K. Stamnes. Efficient yet accurate solution of the linear transport equation in the presence of internal sources: The exponential-linear-in-depth approximation. *J. Comp. Phys.*, 102:265–276, 1992.

80. D.R. Bates. Rayleigh scattering by air. *Planet. Space Sci.*, 32:785–790, 1984.

81. D. Stam, J.F. de Haan, J.W. Hovenier, and I. Aben. Detecting radiances in the O2 *A* band using polarization sensitive satellite instruments, with application to GOME. *J. Geophys. Res.*, 105:22379–22392, 2000.

82. M.I. Mischenko and L.D. Travis. Satellite retrieval of aerosol properties over the ocean using polarization as well as intensity of reflected sunlight. *J. Geophys. Res.*, 102:16989–17013, 1997.

83. J.L. Deuzé and F.M. Bréon and P.Y. Deschamps and C. Devaux and M. Herman and A. Podaire and J.L. Roujean. Analysis of the POLDER (POLarization and Directionality of Earth's Reflectances) airborne instrument observations over land surfaces. *Remote Sens. Environ.*, 45:137–154, 1993.

84. C.E. Siewert. A discrete-ordinates solution for radiative-transfer models that include polarization effects. *J. Quant. Spectrosc. Radiat. Transfer*, 64:227–254, 2000.

85. R.J.D. Spurr. Simultaneous radiative transfer derivation of intensities and weighting functions in a general pseudo-spherical treatment. *J. Quant. Spectrosc. Radiat. Transfer, in press*, 2001.

86. K. Stamnes, S.-C. Tsay, and I. Laszlo. DISORT: a General Purpose Fortran Program for Discrete-Ordinate-Method Radiative Transfer in Scattering and Emitting Layered Media: Documentation of Methodology. NASA internal report.

87. A.K. Kuze and K.V. Chance. Analysis of cloud top height and cloud coverage from satellites using the O_2 *A* and *B* bands. *J. Geophys. Res.*, 99:14481–14491, 1994.

88. R.B.A. Koelemeijer and P. Stammes. A fast method for retrieval of cloud parameters using oxygen A-band measurements from the Global Ozone Monitoring Experiment. *J. Geophys. Res.*, 106:3475–3490, 2001.

89. T.P. Kurosu, K.V. Chance, and R.J.D. Spurr. CRAG – Cloud Retreival Algorithm for ESA's Global Ozone Monitoring Experiment. In *Proceedings of the European Symposium on Atmospheric Measurements from Space (ESAMS), WPP-161, 513-521*, Noordwijk, The Netherlands, 1999.

90. N.C. Hsu, J.R. Herman, P.K. Bhartia, C.J. Seftor, O. Torres, J.F. Gleason, T.F. Eck, and B.N. Holben. Detection of biomass burning smoke from TOMS measurements. *Geophys. Res. Lett.*, 23:745–748, 1996.

91. J.R. Herman, P.K. Bhartia, O. Torres, N.C. Hsu, C.J. Seftor, and E. Celarier. Global distribution of absorbing aerosols from Nimbus 7/TOMS data. *J. Geophys. Res.*, 102:16911–16921, 1997.

92. J.F. Gleason, N.C. Hsu, and O. Torres. Biomass burning smoke measured using backscattered ultraviolet radiation: SCAR-B and Brazilian smoke interannual variability. *J. Geophys. Res.*, 103:31969–31978, 1998.

93. R.F. van Oss. Aerosol retrieval with GOME. In *Proceedings of the European Symposium on Atmospheric Measurements from Space (ESAMS), WPP-161, 581-583*, Noordwijk, The Netherlands, 1999.

94. S.F. Singer and R.C. Wentworth. A method for the determination of the vertical ozone distribution from a satellite. *J. Geophys. Res.*, 62:2299–2308, 1957.

95. R.J. van der A, A.J.M. Piters, R.F. van Oss, P.J.M. Valks, J.H.G.M. van Geffen, H.M. Kelder, and C. Zehner. Near-real time delivery of GOME ozone profiles. In *ESA-ENVISAT Symposium, October 2000*, Gothenburg, Sweden, 2000.

96. H. Bovensmann, J.P. Burrows, M. Buchwitz, J. Frerick, S. Noel, V.V. Rozanov, K.V. Chance, and A.P.H. Goede. SCIAMACHY: Mission objectives and measurement modes. *J. Atmos. Sci.*, 56:127–150, 1999.

97. C.E. Shannon and W. Weaver. *The Mathematical Theory of Communication*. Paperback Edition, University of Illinois Press, Urbana, Illinois, 1962.

98. ESA/EUMETSAT. *EPS/METOP System - Single Space Segment - GOME-2 Requirements Specification*, 1999.

99. M.I. Mischenko, A.A. Lacis, and L.D. Travis. Errors induced by the neglect of polarization in radiance calculations for rayleigh-scattering atmospheres. *J. Quant. Spectrosc. Radiat. Transfer*, 51:491–510, 1994.

100. G. Konstandinidis and J. Hennessy. Meteorological archive and retrieval system m1.9/2, mars user guide (for data retrieval), revision 11. Technical report, ECMWF Computer Bulletin B6.7/2, Reading, U.K., 1995.

101. J.F. Grainger and J. Ring. Anomalous fraunhofer line profiles. *Nature*, 193:762, 1962.

102. G.E. Backus and J.F. Gilbert. Uniqueness in the inversion of inaccurate gross earth data. *Phil. Trans. Roy. Soc. London*, 266:123, 1970.

103. P.C. Hansen and D.P. O'Leary. The use of the L-curve in the regularization of discrete ill-posed problems. *SIAM J. Sci. Comput.*, 14:1487–1503, 1993.

104. Gome level 0 to 1 algorithms description. Technical Report Report ER-TN-DLR-GO-0022, Deutsches Forschungszentrum für Luft und Raumfahrt (DLR), DLR, Oberpfaffenhofen, Germany, 1995.

105. P. Stammes, J.F. de Haan, and J.W. Hovenier. The polarized internal radiation field of a planetary atmosphere. *Astron. Astrophys.*, 225:239–259, 1989.

106. P. Stammes. Errors in UV reflectivity and albedo calculations due to neglecting polarisation. In *SPIE Proceedings Vol. 2311, "Atmospheric Sensing and Modelling"*, 1994.

107. P. Stammes. Spectral radiance modelling in the UV-Visible range. In A. Deepak Publ., editor, *IRS 2000: Current problems in Atmospheric Radiation*, Hampton (VA), 2000.

108. P.I. Palmer, D.J. Jacob, K.V. Chance, R.V. Martin, R.J.D. Spurr, T.P. Kurosu, I. Bey, R. Yantosca, A. Fiore, and Q. Li. Air-mass factor formulation for spectroscopic measurements from satellites: application to formaldehyde retrievals from GOME. J. Geophys. Res., *in press*, 2000.

109. D.E. Flittner. Private communcation, 1999.

110. ENVISAT, Noordwijk, The Netherlands. *SCIAMACHY ATBD*, 2000.

111. E. Griffioen and L. Oikarinen. LIMBTRAN: A pseudo three-dimensional radiative transfer model for the limb-viewing imager OSIRIS on the ODIN satellite. *J. Geophys. Res.*, 105:29717–29730, 2000.

112. F. Torricella, E. Cattani, M. Cervino, R. Guzzi, and C. Levoni. Retrieval of aerosol properties over the ocean using Global Ozone Monitoring Experiment measurements: Method and application to test cases. *J. Geophys. Res.*, 104:12085–12098, 1999.

113. O. Torres, P.K. Bhartia, J.R. Herman, Z. Ahmad, and J.F. Gleason. Derivation of aerosol properties from satellite measurements of backscattered ultraviolet radiation: Theoretical basis. *J. Geophys. Res.*, 103:17099–17110, 1998.

114. H.R. Gordon. Atmospheric correction of ocean color imagery in the Earth Observing System era. *J. Geophys. Res.*, 102:17081–17106, 1997.

115. D.A. Siegel, M. Wang, S. Maritorena, and W. Robinson. Atmospheric correction of satellite ocean color imagery: the black pixel assumption. *Applied Optics*, 39:3582–3591, 2000.

116. K.G. Ruddick, F. Ovidio, and M. Rijkeboer. Atmospheric correction of SeaWiFS imagery for turbid coastal and inland waters. *Applied Optics*, 39:897–912, 2000.

117. Z. Jin and K. Stamnes. Radiative transfer in nonuniformly refracting layered media: atmosphere-ocean system. *Applied Optics*, 33:431–442, 1994.

118. K. Stamnes. Private communication, 2000.

119. O. Frette, J.J. Stamnes, and K. Stamnes. Optical remote sensing of marine constituents in coastal waters: a feasibility study. *Applied Optics*, 37:8318–8326, 1998.

120. O. Frette, S.R. Erga, J.J. Stamnes, and K. Stamnes. Optical remote sensing of waters with vertical structure. *Applied Optics*, 40:1478–1487, 2001.

121. P.Y. Deschamps, F.M. Bréon, M. Leroy, A. Podaire, A. Bricaud, J.C. Buriez, and G. Seze. The POLDER mission: instrument characteristics and scientific objectives. *IEEE Trans. geosci. Remote Sens.*, 32:598–614, 1994.

122. J.E. Hansen and L.D. Travis. Light scattering in planetary atmospheres. *Space Sci. Rev.*, 16:527–610, 1974.

123. O. Dubovik and M.D. King. A flexible inversion algorithm for retrieval of aerosol properties from Sun and sky radiance measurements. *J. Geophys. Res.*, 105:20673–20696, 2000.

124. A. Vermeulen, C. Devaux, and M. Herman. Retrieval of the scattering and microphysical properties of aerosols from ground-based optical measurements including polarization. *Applied Optics*, 39:6207–6220, 2000.

125. F.M. Bréon and P. Goloub. Cloud droplet effective radius from spaceborne polarisation measurements. *Geophys. Res. Lett.*, 25:1879–1882, 1998.

126. J.L. Deuzé and F.M. Bréon and C. Devaux and P. Goloub and M. Herman and B. Lafrance and F. Maignan and A. Marchand and F. Nadal and G. Perry and D. Tanré . Remote sensing of aerosols over land surfaces from POLDER/ADEOS-1 polarised measurements. *J. Geophys. Res.*, 106:4913–4926, 2001.

127. L. C.-Labonnote, G. Brogniez, J.-F. Gayet, M. Doutriaux-Boucher, and J.C. Buriez. Modeling of light scattering in cirrus clouds with inhomogeneous hexagonal monocrystals. Comparison with in-situ and ADEOS-POLDER measurements. *Geophys. Res. Lett.*, 27:113–116, 2000.

128. W.J.J. Knibbe, J.F. de Haan, J.W. Hovenier, D.M. Stam, R.B.A. Koelemeijer, and P. Stammes. Deriving terrestrial cloud top pressure from photopolarimetry of reflected light. *J. Quant. Spectrosc. Radiat. Transfer*, 64:173–199, 2000.

129. J.V. Dave. Intensity and polarization of the radiation emerging from a plane-parallel atmosphere containing monodispersed aerosols. *Applied Optics*, 9:2673–2684, 1970.

130. J.W. Hovenier. Multiple scattering of polarized light in planetary atmospheres. *Astron. Astrophys.*, 13:7–29, 1971.

131. C.E. Siewert. On the equation of transfer relevant to the scattering of polarized light. *Astrophysics. J.*, 245:1080–1086, 1981.

132. C.E. Siewert. On the phase matrix basic to the scattering of polarized light. *Astron. Astrophys.*, 109:195–200, 1982.

133. P. Vestrucci and C.E. Siewert. A numerical evaluation of an analytical representation of the components in a fourier decomposition of the phase matrix for the scattering of polarized light. *J. Quant. Spectrosc. Radiat. Transfer*, 31:177–183, 1984.

134. W.A. de Rooij and C.C.A.H. van der Stap. Expansion of mie scattering matrices in generalized spherical functions. *Astron. Astrophys.*, 131:237–248, 1984.

135. R.D.M. Garcia and C.E. Siewert. The f_n method for radiative transfer models that include polarization effects. *J. Quant. Spectrosc. Radiat. Transfer*, 41:117–145, 1989.

136. R.D.M. Garcia and C.E. Siewert. A generalized spherical harmonics solution for radiative transfer models that include polarization effects. *J. Quant. Spectrosc. Radiat. Transfer*, 36:401–423, 1986.

137. W.M.F. Wauben and J.W. Hovenier. *J. Quant. Spectrosc. Radiat. Transfer*, 47:491–000, 1992.

138. J.L. Haferman, T.F. Smith, and W.F. Krajewski. A multi-dimensional discrete ordinates method for polarized radiative transfer. Part 1: Validation for randomly oriented axisymmetric particles. *J. Quant. Spectrosc. Radiat. Transfer*, 58:379–398, 1997.

139. G.N. Plass, G.W. Kattawar, and F.E. Catchings. Matrix Operator Theory of Radiative Transfer I. Rayleigh Scattering. *Applied Optics*, 12:314–329, 1973.

140. J.V. Dave. Meaning of successive iteration of the auxiliary equation in the theory of radiative transfer. *Astrophysics J.*, 140:1292–1303, 1964.

141. B.M. Herman, A. Ben-David, and K.J. Thome. Numerical technique for solving the radiative transfer equation for a spherical shell atmosphere. *Applied Optics*, 33:1760–1770, 1994.

142. B.M. Herman, T.R. Caudill, D.E. Flittner, K.J. Thome, and A. Ben-David. A comparison of the Gauss-Seidel spherical polarized radiative transfer code with other radiative transfer codes. *Applied Optics*, 34:4563–4572, 1995.

143. L. Oikarinen. Polarization of light in uv-visible limb radiance measurements. *J. Geophys. Res.*, 106:1533–1544, 2001.

144. D.W. Mueller and A.L. Crosbie. Three-dimensional radiative transfer with polarization in a multiple scattering medium exposed to spatially varying radiation. *J. Quant. Spectrosc. Radiat. Transfer*, 57:81–105, 1997.

145. R.J.D. Spurr and K.V. Chance. BIAS : An Algorithm for the Retrieval of Tracegas Vertical Columns from Near Infra-red Earthshine Measurements by the SCIAMACHY Satellite Spectrometer. In *Proceedings of IEEE IGARSS 98*, Seattle, Washington, 1998.

146. M. Buchwitz, V.V. Rozanov, and J.P. Burrows. A near infrared optimized DOAS mothod for the fast global retrieval of atmospheric CH_4, CO, CO_2, H_2O and N_2O total column amounts from SCIAMACHY/ENVISAT-1 nadir radiances. *J. Geophys. Res.*, 105:15231–15245, 2000.

Samenvatting

Ozon is een van de belangrijkste sporengassen is de aardatmosfeer. Het absorbeert in sterke mate straling in het ultraviolette gedeelte van het elektromagnetisch spectrum. De aanwezigheid van ozon in de atmosfeer voorkomt dat deze schadelijke straling het aardoppervlak kan bereiken. Verder is ozon een belangrijk bestanddeel van de luchtvervuiling in de lagere atmosfeer en speelt het gas een belangrijke rol bij het zogeheten *broeikaseffect*. Het bekende *ozongat* fenomeen in de Zuidpool lente vormt een significante verstoring van de ozonlaag; deze grootschalige ozonafbraak is gerelateerd aan de aanwezigheid van chemicaliën die door de mens in de stratosfeer zijn gebracht. Het is essentieel om de verdeling van ozon te bepalen en te monitoren op een globale schaal en gedurende een lange periode. Dit kan het beste worden uitgevoerd met *remote sensing* satelliet instrumenten, die op verschillende manieren stralingsmetingen aan de atmosfeer kunnen doen: metingen aan gereflecteerd zonlicht in het ultraviolet, zichtbaar en nabij-infrarood, of van thermische emissiespectra in het infrarood en verder tot aan de radio-golflengtes. In dit werk is de belangrijkste toepassing de bepaling van verticale profielen van ozon door middel van metingen aan het door de aarde gereflecteerde zonlicht in het ultraviolet. Deze metingen worden gedaan met satelliet instrumenten zoals GOME (gelanceerd in 1995), GOME-2 (vanaf 2005), SCIAMACHY (vanaf 2001) en OMI (vanaf 2003). Al deze instrumenten kijken recht naar beneden de atmosfeer in (*nadir*), met een kleine variatie naar iets schuinere blikken. Dit in tegenstelling tot satelliet instrument die in *limb*, onder een schuine hoek door de atmosfeer heen kijken.

De bepaling van atmosferische profielen uit atmosferische spectra staat bekend als *retrieval*. Een retrieval algoritme gebaseerd op stralingsmetingen bestaat uit een onderdeel waarmee de spectra (stralingssterktes voor een bepaald bereik van golflengtes) kunnen worden gesimuleerd en een module waarmee de gemeten en gesimuleerde spectra tot overeenstemming kunnen worden gebracht. Voor de simulatie is een model (het voorwaartse model) nodig waarmee een theoretische berekening kan worden gedaan van het stralingsveld dat door de satelliet is gemeten. Een belangrijk onderdeel van dit model is de stralingstransport-berekening waarin de verstrooiing en absorptie van zonlicht in de aardatmosfeer wordt beschreven. Er wordt een initiële aanname gemaakt voor het ozon profiel, maar ook voor de verdelingen van andere atmosferische variabelen (zoals temperatuur, aërosolen, grondreflectie enzovoort). De afhankelijkheid van het voorwaartse model voor het ozon profiel is complex en niet-lineair; de retrieval moet worden uitgevoerd met een geschikte optimalisatie, of *fitting* methode. Gegeven dat de afhankelijkheid redelijk lineair is, kan de retrieval geschieden door middel van een iteratief schema van lineaire inversie stappen. Elk van deze stappen vergt een lineairisatie van het voorwaartse model rond een gegeven atmosferische situatie: we hebben niet alleen het gesimuleerde spectrum nodig voor deze situatie, maar ook de gevoeligheid van het spectrum voor variaties in het ozon profiel. Gegeven een initiële waarde voor het profiel, hangt de volgende schatting niet alleen af van het gesimuleerde spectrum en de voornoemde gevoeligheid, maar ook van de meetfout en de aanname voor de vooraf beschikbare informatie over het profiel (de *a priori* informatie). Het iteratieve proces wordt voortgezet totdat aan een geschikt convergentie criterium is voldaan.

De gevoeligheden zijn een essentieel onderdeel van elke retrieval: ze worden gewichtsfuncties genoemd. In feite zijn het de afgeleiden van het stralingsveld naar de atmosferische parameter die worden ge-retrieved (in ons geval de ozon waarden). We hebben dus een voorwaarts model nodig die ons twee zaken levert: een simulatie van het gemeten spectrum en de gewichtsfuncties voor een brede variatie van atmosferische parameters. De meeste stralingstransport modellen zijn alleen geschikt om er een spectrum mee te bepalen. De gewichtsfuncties moeten dan numeriek worden bepaald door het effect van kleine verstoringen door te rekenen. Dit kost veel rekentijd, zeker wanneer we te maken hebben met een groot aantal parameters. Verder zijn deze methoden vaak te onnauwkeurig.

In dit proefschrift is een stralingstransport model ontwikkeld dat specifiek het probleem van meervoudige verstrooiing in de atmosfeer in het ultraviolet oplost. Het is speciaal ontwikkeld om niet alleen de stralingssterkte, maar ook alle mogelijke gewichtsfuncties op een nauwkeurige en snelle manier te berekenen. In het model wordt het stralingsveld bepaald door een discretisatie toe te passen van de hoekafhankelijkheid van de meervoudig verstrooide straling. Naast verstrooiing wordt ook de absorptie van het licht meegenomen. Het stralingsveld wordt opgelost voor een aantal (N) discrete polaire hoeken ten opzichte van de nadir richting. Met behulp van een slim interpolatie-schema wordt hierna de stralingssterkte voor elke gewenste hoek berekend. Dit vormt de basis van de discrete ordinaten methode. In het proefschrift wordt aangetoond dat voor een realistische atmosfeer bestaande uit meerdere homogene lagen het stralingsveld, zoals dat met de *discrete ordinate* methode is bepaald, geheel differentieerbaar is naar elke atmosferische variabele die bijdraagt aan de verstrooiing of absorptie in de atmosfeer. Hierdoor is het mogelijk om gewichtsfuncties op een analytische manier te bepalen met dezelfde nauwkeurigheid als het berekende stralingsveld. De gelijktijdige berekening van gewichtsfuncties levert een enorme besparing op in de tijd die een computer nodig heeft om de berekeningen te volbrengen. Gezien het feit dat de methode analytisch is, is er geen sprake van ad-hoc benaderingen die typisch zijn voor numerieke pertubatie methoden.

De inhoud van het proefschrift is als volgt samen te vatten.

Na een introductie volgt in Hoofdstuk 2 een uitleg over de bepaling van radianties en gewichtsfuncties voor de verstrooide zonnestraling die de top van een vlak-gelaagde atmosfeer verlaat. Gewichtsfuncties kunnen worden berekend voor elke atmosferische parameter: hoeveelheden ozon, andere gassen, temperatuur en druk, aërosol optische eigenschappen, maar ook de reflectie eigenschappen van het oppervlak. In dit hoofdstuk wordt ook de thermische straling behandeld. In Hoofdstuk 3 wordt het model op een aantal belangrijke onderdelen veralgemeniseerd. Er wordt aangetoond dat de gewichtsfuncties kunnen worden berekend voor elke hoogte, niet alleen voor de top van de atmosfeer. Dit is van belang voor stralingsmetingen aan de grond of vanuit vliegtuigen. Verder is het model toepasbaar voor elke kijkhoek en zonnestand. In de belangrijke pseudo-sferische benadering wordt de uitdoving van de nog-niet-verstrooide zonnebundel exact voor een sferische atmosfeer (in plaats van een vlak-gelaagde) berekend. Met deze benadering wordt het model toepasbaar voor situaties met een lage zonnestand. Verder is het nu mogelijk met de methode om het stralingspad langs de gezichtslijn voor de correcte sferische geometrie mee te nemen. Dit is van belang voor instrumenten zoals GOME-2 en OMI waarmee onder een vrij schuine hoek (tot ongeveer 50^0)de atmosferische straling wordt gemeten. Een verdere verbetering in de berekeningen is behaald door de enkelvoudige verstrooide deel van de stralingssterkte en de gewichtsfuncties exact mee te nemen, buiten de *discrete-ordinate* benadering en geheel voor een sferische atmosfeer. Het software pakket LIDORT (*LInearized Discrete Ordinate Radiative Transfer*) is geconstrueerd op basis van de theorie in de Hoofdstukken 1 en 2.

Het pakket omvat een algemeen toepasbare stralingstransport-computer-code voor de berekening van stralingssterkte en gewichtsfuncties. Het software pakket is zonder kosten of restricties te downloaden van http://cfa-www.harvard.edu/lidort. Het omvat tevens een test-dataset en een *Users Guide*.

In een gecompliceerd retrieval algoritme, zoals dat voor ozonprofielen, zijn vele stralingstransport simulaties nodig. De snelheid en de nauwkeurigheid van deze simulaties worden voornamelijk bepaald door het aantal discrete polaire hoeken, of stromen, die in het model worden gebruikt. Een aanzienlijke besparing van rekentijd kan worden verwezenlijkt door slechts 4 of 6 stromen te gebruiken, maar dit heeft een verlies aan nauwkeurigheid tot gevolg. In Hoofdstuk 4 wordt deze afweging tussen snelheid en nauwkeurigheid voor de ozonprofiel-retrieval onderzocht door 4- en 6-stromen resultaten te vergelijken met berekeningen met 20 stromen. Deze berekeningen worden uitgevoerd voor een brede variatie aan specifieke waarneem-condities, zoals die gelden voor de GOME, GOME-2 en OMI instrumenten, en voor een aantal atmosferische scenario's. Hierbij worden ook wolken en zwaar-vervuilde aërosol-lagen op verschillende hoogtes meegenomen. Op deze wijze wordt de fout in de stralingstransport-berekening ten gevolge van de 4 of 6 stromen benadering in kaart gebracht. In het algemeen blijken de fouten voor de 4-stromen benadering tot ∼2.0-2.5% op te lopen binnen het golflengte interval van 270 tot 320 nm. De 6-stromen benadering geeft fouten binnen de ∼0.5-0.7% voor hetzelfde interval. Deze waarden zijn vergelijkbaar tot beter dan de nauwkeurigheid van de satellietmetingen zelf, die wordt bepaald door de instrument-calibratie.

In Hoofdstuk 5 worden een aantal foutenschattingen en gevoeligheidstudies gepresenteerd voor een operationeel ozonprofiel retrieval-algoritme voor GOME-2. Ozon absorptie in het ultraviolet is sterk temperatuur-afhankelijk. In de studies is gekeken naar het effect van deze afhankelijkheid voor op de nauwkeurigheid van het ozonprofiel en op de hoeveelheid informatie die uit de satellietmeting kan worden afgeleid. Er wordt aangetoond dat er een aanzienlijke toename in de nauwkeurigheid van het troposferische profiel plaatsvindt voor hogere temperaturen in de troposfeer. Een typisch spectraal interval waarbinnen de spectrale metingen worden gebruikt voor de retrieval is 270 tot 320 nanometer. In het hoofdstuk is aangetoond dat een uitbreiding van dit interval naar 340 nanometer geen grote verbetering in de nauwkeurigheid en in de informatie geeft. Voor de foutenanalyse is gekeken naar factoren als temperatuur en aërosol concentraties die beide niet zijn meegenomen in de retrieval, maar die toch van invloed zijn op het atmosferisch stralingstransport. We laten zien dat de nauwkeurigheid van het ozonprofiel gevoelig is voor de onzekerheid van de temperatuur in de gehele atmosfeer en van de aërosol-verdeling in de lagere delen van de atmosfeer. Verder is aangetoond dat polarisatie-effecten een belangrijke invloed hebben op de fout op het profiel. Dit betreft zowel de fout in de instrument calibratie voor de correctie van de polarisatie-gevoeligheid van het instrument, als de fout in het stralingstransport-model ten gevolge van het niet meenemen van de polarisatie van de straling.

Curriculum Vitae

Robert James Duncan Spurr was born in London (UK) in 1954. He was educated at Trinity College, Cambridge University (UK) (1972-1975), receiving a B.A. in 1975 (first class Honors, Mathematics) and M.A. in 1979. He did postgraduate work in Cambridge (UK) 1975-76, and at the Department of Astrophysics, Oxford University, UK (1976-78). He was a mathematics teacher in Oxford (1979-1981). From 1981 to 1987 he was a Higher Scientific Officer in the UK Meteorological Office, and served for a number of years as an operational weather forecaster in the UK, mainly at the London Weather Center but also with spells at Lerwick (Shetland Islands), Aberdeen (Scotland), and on the North Sea oil platforms. He travelled widely in Australia, New Zealand and North America in the years 1988-90.

For the past 10 years, Robert Spurr has been a research scientist closely involved with the GOME and SCIAMACHY instruments. During the GOME algorithm development phase, he worked at the Max Planck Institute for Chemistry, Mainz, Germany (1991-1992); the Institute of Remote Sensing, University of Bremen, Germany (1992-1994); and as the chief consulting scientist for GOME level 1 to 2 data processing at DLR (Deutsches Zentrum fuer Luft- und Raumfahrt), Wessling, Germany, before moving to the USA in September 1995. Since then, he has continued to work first on GOME post-launch data processing (1995-96), then on SCIAMACHY algorithm development (1997-2000). Recently he has been an Associated Scientist for the Ozone SAF project at KNMI, The Netherlands.

He is a member of the European Space Agency Global Ozone Monitoring Experiment Scientific Advisory Group; the GOME Data and Algorithm subcommittee; the SCIAMACHY Scientific Advisory Group and the SCIAMACHY scientific working subgroup for Algorithm Development and Data Usage. He is Fellow of the Royal Meterological Society (UK), and a member of the American Geophysical Union and the American Association for the Advancement of Science.

Publications

Goede, A., C. Gunsing, T. Kamperman, J. de Vries, R. Spurr, J.P. Burrows and K. Chance, GOME instrument simulation, *SPIE Meeting on Optical Methods in Atmospheric Chemistry*, Berlin, Germany, 1992.

Burrows, J.P., V. Rozanov, Y. Timofeyev, A. Polyakov, R. Spurr and K. Chance, A study of the accuracy of atmospheric trace gas vertical profile retrieval from satellite-based occultation measurements, in *Proceedings of the International Radiation Symposium*, Tallinn, Eds. Keevallik and Kaerner, p. 398, Deepak publishing, 1993.

Spurr, R., D. Diebel and J. Burrows, Forward model considerations and precision estimates for the retrieval of atmospheric profiles, in *Optical Methods in Atmospheric Chemistry,* Proc. SPIE 1715, 573-584, 1993.

Loyola, D., B. Aberle, W. Balzer, K. Kretschel, E. Mikusch, H. Muehle, T. Ruppert, C. Schmid, S. Slijkhuis, R. Spurr, W. Thomas, T. Wieland and M. Wolfmueller, Ground segment for ERS-2 GOME sensor at the German D_PAF, *Proc. 3rd ERS Symposium, SP-414*, 591-596, 1997.

Spurr, R., Development of a prototype algorithm for the operational retrieval of height-resolved products from GOME, *Proc. 3rd ERS Symposium, SP-414*, 621-628, 1997.

Chance, K., and R.J.D. Spurr, Ring effect studies: Rayleigh scattering, including molecular parameters for rotational Raman scattering, and the Fraunhofer spectrum, *Appl. Opt. 36*, 5224-5230, 1997.

Rozanov, V., D. Diebel, R. Spurr and J. Burrows, GOMETRAN: A radiative transfer model for the satellite project GOME - the plane parallel version, *J. Geophys. Res. 102,* 16,683-16,695, 1997.

Thomas, W., E. Hegels, S. Slijkhuis, R. Spurr and K. Chance, Detection of biomass burning combustion products in Southeast Asia from backscatter data taken by the GOME spectrometer, *Geophys. Res. Lett. 25*, 1317-1320, 1998.

Kurosu, T.P., K.V. Chance and R.J.D. Spurr, CRAG – Cloud Retreival Algorithm for ESA's Global Ozone Monitoring Experiment, *Proceedings of the European Symposium on Atmospheric Measurements from Space (ESAMS),* WPP-161, 513-521, Noordwijk, The Netherlands, 1999.

Spurr, R.J.D., T.P. Kurosu, K.V. Chance, R.F. van Oss, P. Stammes, H. Kelder, W. Thomas, U. Boettger, W. Balzer and K. Stamnes, The LIDORT package: a generic forward-model radiative transfer tool for the simultaneous generation of intensities and weighting functions for atmospheric retrieval, ERS-ENVISAT Symposium 2000, Gothenburg, Sweden.

Spurr, R.J.D., T.P. Kurosu and K.V. Chance, A linearized discrete ordinate radiative transfer model for atmospheric remote sensing retrieval*, J. Quant. Spectrosc. Radiat. Transfer 68,* 689-735, 2001.

Chance, K., P.I. Palmer, R.J.D. Spurr, R.V. Martin, T.P. Kurosu and D.J. Jacob, Satellite observations of formaldehyde over North America from GOME, *Geophys. Res. Lett. 27*, 3461-3464, 2000.

Palmer, P.I., D.J. Jacob, K.V. Chance, R.V. Martin, R.J.D. Spurr, T.P. Kurosu, I. Bey, R. Yantosca, A. Fiore and Q. Li, Air-mass factor formulation for spectroscopic measurements from satellites: application to formaldehyde retrievals from GOME *J. Geophys. Res. in press*, 2000.

Kurosu, T.P., K.V. Chance, and R.J.D. Spurr, Cloud retrieval algorithm for the European Space Agency's Global Ozone Monitoring Experiment, *Proc. S.P.I.E. (EUROPTO), Satellite Remote Sensing of Clouds and the Atmosphere III, 3495,* 17-25, 1998.

Chance, K.V., R.J.D. Spurr, and T.P. Kurosu, Atmospheric trace gas measurements from the European Space Agency's Global Ozone Monitoring Experiment, *Proc. S.P.I.E. (EUROPTO), Satellite Remote Sensing of Clouds and the Atmosphere III, 3495,* 230-234, 1998.

Kurosu, T.P., K.V. Chance and R.J.D. Spurr, CRAG – Cloud Retreival Algorithm for ESA's Global Ozone Monitoring Experiment, *Proceedings of the European Symposium on Atmospheric Measurements from Space (ESAMS),* WPP-161, 513-521, Noordwijk, The Netherlands, 1999.

Acknowledgements

First, I would like to offer special thanks to my team of thesis advisors and sponsors from KNMI (sponsor Hennie Kelder, co-sponsor Piet Stammes and advisor Roeland van Oss) for their enthusiasm and support all the way from the time I first approached them with the idea for this thesis. Biggest thanks go to my main collaborator Roeland for numerous stimulating discussions on the theory and applications of LIDORT. This collaboration has been (and continues to be) a really fruitful meeting of minds. Piet deserves tremendous credit for his thorough reviews and penetrating comments; such precise and careful feedback is enormously useful when presenting new work. Hennie's enthusiasm and interest is tremendously infectious. It is always a pleasure to visit KNMI and talk to these guys!

I have been very fortunate to have the support and interest of Knut Stamnes (the "father of DISORT") as my external sponsor and reviewer. There is a commonality of interest which I have enjoyed very much in our discussions. I am very grateful for his support and recommendations on the organization of this material.

It was Thomas Kurosu who remarked casually in March 1999 that it would be nice to get weighting functions from a discrete ordinate model; his skills in LateX were of immense help in the organization and write-up of the work. Werner Thomas of DLR gave some very valuable assistance in the quality control of the software.

Wolfgang Balzer of DLR has been a true friend throughout. His support during the dark time was a great asset. Thanks also to my old friend John Pezzey, now in Australia, who knows what it's like to get a thesis later in life. I am happy that these two guys agreed to be my paranymphs!

It is sometimes not possible to see the wood for the trees, and the perspectives offered by users of the model are very helpful. In particular I would like to thank Ute Boettger, Kelly Chance, Ahellis Maurellis and Paul Palmer for their user feedback. Thanks also to many other colleagues at DLR for their interest in this work (Albrecht von Bargen, Mihai Datcu, Peter Fuchs, John How, Klaus Kretschel, Diego Loyola, Tom Rother, Franz Schreier, Sander Slijkhuis and Uli Steinbrecher). I have also enjoyed discussions with Ronald van der A, Ilse Aben, Bingquan Chen, Henk Eskes, Dave Flittner, Jim Gleason, Johan de Haan, Dan Jacob, Robert Koelemeijer, Jochen Landgraf, Pieternel Levelt, Rose Munro, Ankie Piters, Larry Rothman, Nick Schutgens, Richard Siddans and Pieter Valks.

Lastly, there aren't enough thanks I can give Diane; she is always there for me.

Funding for this work was through:

1. SCIAMACHY Data Processor Development, Contract number 332/60570480,
   Deutsches Zentrum fuer Luft und Raumfahrt (DLR),
   Postfach 1116, D82230 Wessling, Germany.
   (April/May 1999, July 1999 - July 2000)

2. Ozone SAF Visiting Scientist Grants, P-4799-2-00 and P-4799-2-01,
   KNMI (Royal Dutch Meteorological Institute),
   P.O. Box 201, 3730 AE De Bilt, The Netherlands.
   (August 2000 - March 2001).

3. Smithsonian Astrophysical Observatory (internal funds),
   60 Garden Street, Cambridge, MA 02138, USA. (May/June 1999).